Quantitative Analysis of 2D and 3D Models for Epidermal Growth Factor Receptor-Dependent Cell Migration in the Context of the Extracellular Microenvironment

by

Hyung-Do Kim

B.S, Biomedical Engineering
Johns Hopkins University, 2003

SUBMITTED TO THE DEPARTMENT OF BIOLOGICAL ENGINEERING
IN PARTIAL FULFILLMENT OF THE REQUIREMENTS FOR THE DEGREE OF

DOCTOR OF PHILOSOPHY IN BIOLOGICAL ENGINEERING

AT THE
MASSACHUSETTS INSTITUTE OF TECHNOLOGY
FEBRUARY 2009

Signature of Author: _____
Department of Biological Engineering
December 18, 2008

Certified by: _____
Douglas A. Lauffenburger
Whitaker Professor of Biological Engineering, Chemical Engineering, and Biology
Thesis Advisor

Certified by: _____
Frank B. Gertler
Professor of Biology
Thesis Advisor

Approved by: _____
Alan J. Grodzinsky
Professor of Biological Engineering, Electrical Engineering, and Mechanical Engineering
Chair, Graduate Committee

THESIS COMMITTEE

Approved by: _____

Roger D. Kamm
Germeshausen Professor of Biological Engineering and Mechanical Engineering
Chair, Thesis Committee

Approved by: _____

Forest M. White
Mitsui Career Development Associate Professor of Biological Engineering

Approved by: _____

Douglas A. Lauffenburger
Whitaker Professor of Biological Engieering, Chemical Engineering, and Biology

Approved by: _____

Frank B. Gertler
Professor of Biology

Quantitative analysis of 2D and 3D models for EGF receptor-mediated cell migration in the context of the extracellular microenvironment

by

Hyung-Do Kim

Submitted to the Department of Biological Engineering on December 18, 2008
in partial fulfillment of the requirements for the degree of
Doctor of Philosophy in Biological Engineering

ABSTRACT

Major therapeutic efforts have been devoted to targeting the epidermal growth factor receptor (EGFR), which is aberrantly expressed in many cancers and is correlated with tumor progression and invasiveness. In the current tumor progression paradigm, individual invasive carcinomas arise upon epithelial-mesenchymal transition (EMT) and migrate through a complex tumor microenvironment to successfully metastasize. While the activation of EGFR enhances invasiveness in vivo, it is still unclear which downstream molecular changes caused by EMT contribute to the invasive phenotype and subsequently, how the invasive cell integrates downstream biophysical processes to invade through a three-dimensional (3D) extracellular matrix (ECM).

This thesis addresses these questions from a quantitative, engineering perspective, that cell migration in the context of the invasion microenvironment is an inherently multivariate biochemical and biophysical problem. As such, we developed various carefully controlled, but biologically relevant, *in vitro* experimental systems with an emphasis on the extracellular microenvironment. These systems were combined with quantitative data-driven parameterization of signaling components and subsequent modeling of migration phenotypes via various 2D and 3D single cell tracking assays.

By measuring 2D cell migration of immortalized human mammary epithelial cells conferring pre- or post-EMT states, we respectively identified physiologically relevant, EMT-dependent collective and individual migration modes. A comprehensive systems modeling approach identified the novel activation of a downstream kinase, which acts in a switch-like manner to differentially regulate epithelial, EGFR-dependent migration versus mesenchymal migration. Next, the subsequent mesenchymal migration in 3D, as modeled by a human glioblastoma cell line, was assessed via a quantitative biophysical analysis. EGF-enhanced 3D migration arose from a balance between a cell-intrinsic regulation of cell speed and a matrix- and proteolysis-dependent, extrinsic regulation of directional persistence. Lastly, we quantified fibroblast migration in a porous scaffold of varying pore sizes and stiffness to model contact-guided quasi-3D migration. We surprisingly found that the micro-architecture of guidance structures alone influenced cell speed.

Therefore, the combination of biologically relevant experimental systems and quantitative models provided novel mechanistic insights pertinent to early stages of tumor metastasis. The experimental approaches and biological mechanisms in this thesis hold potential in guiding therapeutic targeting of the biophysical responses prompted by the extracellular microenvironment.

Thesis Supervisor: Douglas A. Lauffenburger
Title: Whitaker Professor of Biological Engineering, Chemical Engineering, and Biology

Thesis Supervisor: Frank B. Gertler
Title: Professor of Biology

BIOGRAPHICAL NOTE

Hyung-Do Kim received his Bachelor of Science in Biomedical Engineering with concentration in Chemical Engineering in 2003 from the Johns Hopkins University in Baltimore, MD. While at Johns Hopkins, Hyung-Do was introduced to biomedical research in the laboratory of Dr. James Hildreth studying the role of CXCR4 antagonists in inhibiting HIV-cell entry. Hyung-Do completed his senior thesis in the laboratory of Dr. Denis Wirtz studying the role of tensin in actin cross-linking using rheological methods. Hyung-Do received academic honors and research awards, and he became a member of Alpha Eta Mu Beta and Tau Beta Pi honor societies.

Hyung-Do started his graduate thesis in the Department of Biological Engineering at MIT in the fall of 2003. Under the joint supervision of Drs. Douglas Lauffenburger and Frank Gertler, Hyung-Do pursued his doctoral thesis entitled, "Quantitative Analysis of 2D and 3D Models of Epidermal Growth Factor Receptor-Dependent Cell Migration in the Context of the Extracellular Microenvironment". While at MIT, Hyung-Do was supported by graduate fellowships from the National Cancer Institute Integrative Cancer Biology Program and from the Ludwig Institute for Cancer Research. Hyung-Do also completed a minor in Biotechnology Entrepreneurship through his coursework at the Sloan School of Management.

ACKNOWLEDGEMENTS

A whole chapter can be devoted to my indebtedness to my thesis advisors who each provided unique and far-reaching visions to the science I love. Douglas Lauffenburger left an everlasting imprint on me by demonstrating his unsurpassable commitment to the education of biological engineers. I am privileged to have been a part of a professional, collegial, and intellectually stimulating laboratory environment and a uniquely diverse and talented department, in which his inspirational qualities are inscribed. My scientific development as a quantitative biologist is owed to him and these unique environments. Doug displayed indescribable patience and mentorship to an undeserving student from the beginning; and despite his duties as a mentor to hundreds of students and scholars, Doug always gave me the illusion of devoting 100% of his time to me. I am immensely grateful for his insightful personal discussions and for his participation at my wedding. I owe my 'biological' advisor Frank Gertler my new-found perspective on interdisplinary science. In addition to the unwavering support in my interests, he supplied with exceptional rigor and expertise and taught me to 'accelerate' and 'steer' through the world of biology. I may never become a true biologist, but he branded my engineering mindset with a rare education in the value of a biological mindset and in the necessity to have fun in biology.

I would also like to acknowledge James Hildreth, my first undergraduate advisor, who has initially introduced me to biomedical research and to the importance of mentorship in scientific development of young scholars. His selfless dedication to the public health and scientific minorities will always guide me through my career path.

This work would not have been possible without the support of the members of the M.I.T. community, especially the guidance of my thesis committee members Roger Kamm, Paul Matsudaira, and Forest White. The past and present members of the Lauffenburger and the Gertler groups have defined the amazing working atmosphere. I would like to acknowledge Neil Kumar, Muhammad Zaman, and Lisa Joslin as my initial mentors shaping my thesis projects, who were instrumental collaborators in the development of quantitative methods in chapter 2. I was blessed with the expertise of Brendan Harley, who provided the initial design of the project, material design, and cellular solids modeling expertise in chapter 5. In addition, Shannon Alford, Benjamin Cosgrove, Erik Dent, Pamela Kreeger, Matthew Lazzara, Leslie Mebane, Megan Palmer, Ulrike Philippar, Elaine Pinheiro, Justin Pritchard, Irina Shapiro, Yana Wang, and Alejandro Wolf-Yadlin have provided experimental and computational training during this thesis. In addition, I am also thankful for helpful discussions with Kevin Janes, Nick Marcantonio, Shelly Peyton, Manu Platt, and Andrea Tentner. James Evans, Eliza Vasile, Al Davis, and Aran Parillo have provided support in the microscopy facilities and associated image analysis and data management. Also, expert lab management by Christina Lewis, Stacey Pawson, JoAnn Sorrento, and Jose Medrano greatly facilitated my progress. I have also had the privilege of advising numerous talented undergraduate students. Especially, work in chapter 4 is indebted to Angela Wu, Tiffany Guo, and Jordan Raphel.

I would like to single out the close friendships formed with Lisa Joslin, Neil Kumar, Megan Palmer, Elaine Pinheiro, Matthew Lazzara, Neil Kumar, and Andrea Tentner, as well as my housemate David Appleyard. In addition to these individuals and the members of BE class of 2003, my best friends and 'scientific' guides Brian Cook and Ben Cosgrove made a substantial impact on my personal development during my tenure at MIT.

Lastly, I thank my family for their unwavering support and display of pride. The love of my parents and my sister provided strength throughout my education. Most importantly, I am grateful to the unwavering support and love of my wife, Erin, who is my greatest friend and cheerleader, has been the joyful pillar during the fight against the challenges posed by this thesis, and sacrificed more than I can describe by allowing me to finish my thesis at MIT.

TABLE OF CONTENTS

LIST OF FIGURES AND TABLES

CHAPTER 1

Introduction

This chapter is not only intended to introduce the thesis work described in this thesis but also emphasize the rationale for the unique approaches taken in this thesis for the study of the biology of cell motility. As such, the motivation of regarding the cell motility process in the context of the microenvironment is given, followed by the background helpful for understanding the work in subsequent chapters.

1.1. Overview: the complexity of the tumor invasion microenvironment

1.1.1. A brief introduction to cell migration

The fascinating phenomenon of cell locomotion has first been observed in leukocytes as early as 1863 [1]. As a readily observable phenomenon, cell migration has been studied with great interest since then; particularly, the advances in imaging technologies have led to numerous insights into the fundamental biology of cell motility. Today, we know that cell migration is a carefully orchestrated phenomenon consisting of cycles of biophysical processes from protrusion, cell-matrix adhesion, polarization, contraction, and rear detachment (see section 1.2.2 for a detailed discussion of their molecular players) [2, 3]. In metazoans, cell migration is highly conserved, intricately regulated, and critical in diverse physiological processes, including embryogenesis, wound healing, and immune function [3]. The migratory potential is highly cell-type dependent, with leukocytes, fibroblasts, and other mesenchymal cells displaying inherent migratory potential while others, such as cells of epithelial origin may require appropriate transformations to become motile [4, 5]. Growth factors and cytokines, as well as over-expression of their receptors are known to stimulate cell motility, which often lead to dysregulation of the motility process [6].

Tumor invasion and metastasis, the leading cause of fatality in cancers, is the most prominent example of pathological dysregulation of the motility process [7-9]. Above transformations and changes in gene expression that often occur during tumor progression are known to confer non-motile carcinomas the ability to move and invade neighboring tissues or disrupt the control of physiological migration in case of fibrosarcomas or other mesenchymal tumor types. In either case, invasive cells are endowed with the ability to upregulate genes responsible for degradation of the surrounding extracellular matrix (ECM), to detach from the primary lesion, and to respond to chemotactic cues present in the invasion environment.

Both physiological and pathological migratory processes are dependent on the stimulatory extracellular cues as well as many intracellular regulators [3, 6]; therefore, a great degree of attention has been paid to developing therapeutics against tumor invasion and metastasis by targeting growth factor receptors or intracellular regulators to inhibit the migration machinery [10, 11]. Their limited success suggests that our current understanding of the migratory process is very limited [12].

Recent studies range from phenomenological *in vivo* studies that identify critical genes and proteins in the invasive processes to controlled *in vitro* studies allowing systematic assessment of various stimulations and molecular manipulations on particular migratory processes. The latter includes the qualitative assessment of the role of ECM proteins or other cell types [13, 14], as well as the role of substrate mechanical properties in regulating migratory behavior (some of which is discussed in section 1.2.2.). While these *in vitro* studies attempt to draw conclusions to physiologically relevant settings, many of them have been performed in two-dimensional substrates or artificially engineered settings. The development of physiologically relevant *in vitro* models for biological studies is a relatively recent movement [15, 16].

1.1.2. Cancer in its microenvironmental context

The existence of the extracellular tumor microenvironment (ME) has been widely acknowledged long before the seminal works by Cairns and Nowell in the 1970s, which characterize cancers as evolutionary entities with inherent heterogeneities arising from the

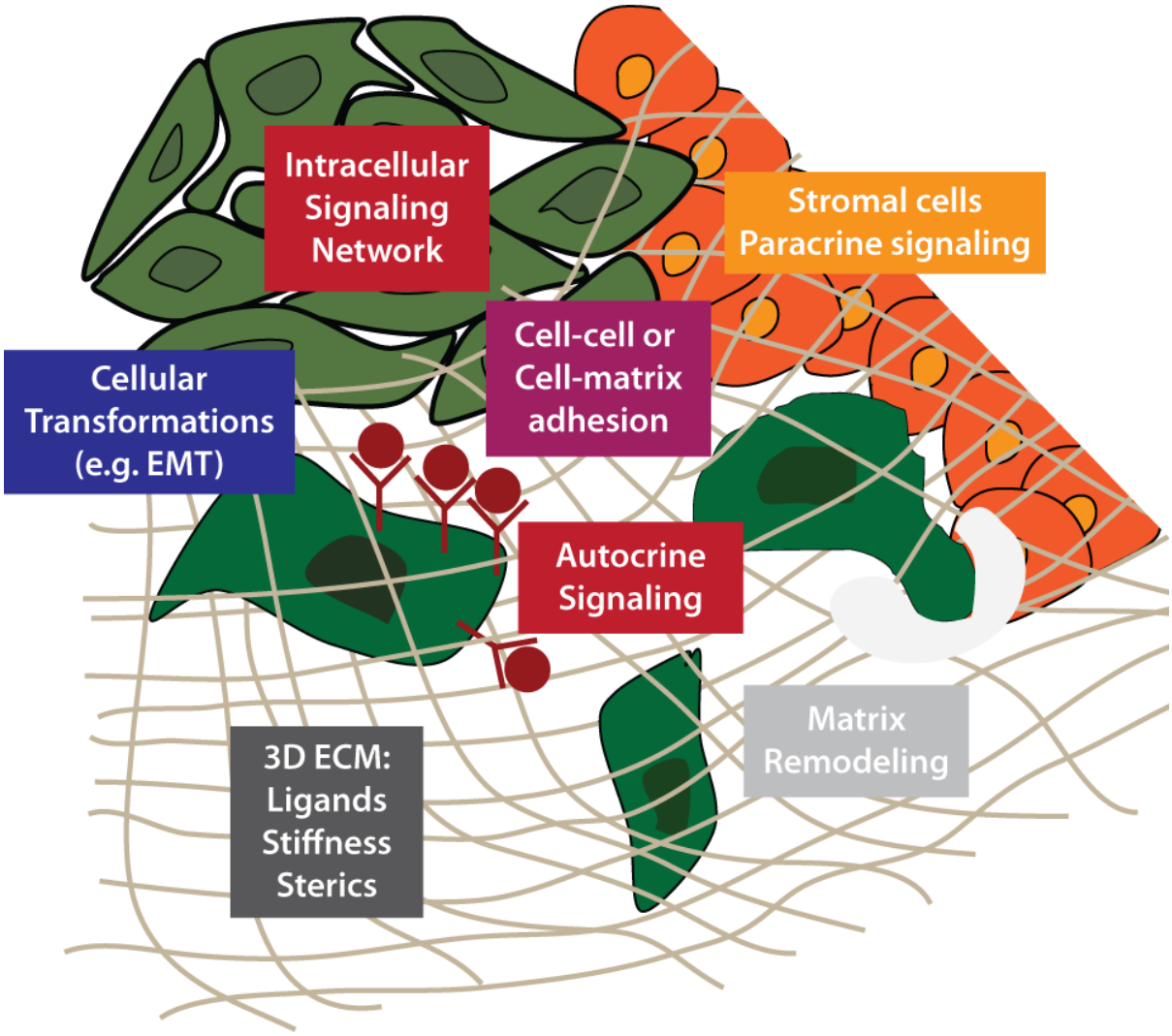

Figure 1-1 – Simplified multi-parameter conceptualization of the tumor invasion microenvironment. Depicted are tumor cells in green in a 3D ECM environment (grey) with stromal cells (orange). All these biological phenomena are parameters that affect the balance of tumor cell migration.

competition for resources provided by the tumor microenvironment (ME) [17-19]. In addition to the stromal cells intended to provide resource support the surrounding tissue, the major constitueents of the extracellular ME (from the perspective of the tumor) are the constantly remodeled extracellular matrix (ECM), the growth factors and cytokines secreted by tumor or stromal cells in an autocrine or paracrine fashion, other environmental factors such as nutrients, and the microvasculature and its constituents such as endothelial cells or cells of the immune system [16]. Some of these factors are

illustrated in Figure 1-1. While these factors are intended for homeostasis of the tissue, they also play a critical role in the dynamic processes of physiology and disease, such as tumor cell invasion and metastasis. Especially, the dynamic interplay of the tumor microenvironment with the primary tumor lesions or the invading/metastasizing cells presumably determines the degree of tumor progression.

Perhaps due to the extraordinary complexity presented by the ME – beyond the genetic and molecular components of the tumor cells themselves – the ME has traditionally received disproportionately little attention in cancer research. Recent ME-related work mainly investigate the effects of hypoxia on tumor progression and discuss stromal cells as therapeutic media [20]. However, ME-centric studies particularly focusing on tumor invasion are still at their infancies. Conceivably, the most prominent in this category are the ongoing elegant intravital imaging studies by the Condeelis group, which observe dynamic tumor invasion processes in their native ME and are able to identify genes and proteins upregulated in invasive subpopulations [21]. These studies have suggested the prominent role of macrophages and their paracrine secretion of chemotactic EGF in recruiting tumor cells towards blood vessels and have demonstrated the preferential migration of tumor cells along migratory collagen fibers (see section 1.2.1. for more discussion).

1.1.3. The microenvironment as a composite source for extracellular cues

Macrophages, collagen fibers, and EGF chemotactic gradients constitute factors that regulate the cell migration processes in an equal extent as the upregulation and over-expression of genes and proteins. The roles of these individual factors in regulating cell migration is clearer due to existing *in vitro* studies investigating them. For example, quantitative analyses of chemotactic gradients have led to insights into the role of precise concentrations of chemotactic agents in regulating receptor-mediated chemotaxis [22]. Even in absence of a chemotactic gradient (therefore during chemokinesis, not chemotaxis), homogeneous stimulation of cells with chemotactic agents are known to induce cell migration [23].

Numerous studies have been performed on the effects of ECMs on cell migration, either investigating the role of diverse ECM types, such as fibronectin, laminin, or collagens,

or the role of varying ligand densities in regulating the migratory behavior [24, 25]. First quantitative studies regarding cell-substrate adhesions demonstrated that adhesion strengths must be properly balanced with the contractile forces generated to produce motion [26, 27]. As adhesion strengths are dependent on substrate ligand density, the ligand density non-trivially contributes to the biophysical balance involved in cell motility. Recent studies indicate that the ECM mechanical properties are varied with ECM ligand densities both in 2D and 3D substrates and affect cell locomotion speeds *in vitro* [28, 29].

The presence of diverse cell types in the ME suggests the presence of diverse soluble extracellular cues that in concert activate downstream signaling pathways eliciting cellular responses [30, 31]. Again, precise levels of these extracellular cues have been shown to play an important role as they elicit different levels of downstream activations [32]. In addition, as discussed in section 1.2.2. and 1.2.3., there are numerous intracellular regulators of the biophysical processes in cell migration. While they are not microenvironmental cues in the precise sense, they also contribute to the complexity of biological systems in the ME.

1.1.4. Limited therapeutic success against invasion suggest the need for novel experimental systems

These studies suggest that the process of cell migration and invasion is not a cell-centric process, but it is a balanced process between the diverse extracellular cues and diverse signals (Figure 1-1). These balances exist in the context of gene expression changes and cellular transformations, concentrations of soluble factors and ECMs, as well as mechanical cues. Many strides have been made in parsing the effects of individual cues and signals on the migratory processes using diverse, elegant *in vitro* systems with qualitative and sometimes quantitative variation of one variable. Perhaps due to the lenient scientific environment at the time, however, these *in vitro* experimental systems have often lacked additional components of the ME, which may ignore the importance of the biochemical and biophysical balance existent in the ME. Importance of microenvironmental multi-factor studies was demonstrated a decade ago by elucidating the effects of EGF stimulation on fibroblast movement in varying levels of 2D ECM densities. EGF stimulation only elicited a stimulatory response at medium ECM densities, while extreme ECM densities did not,

exemplifying the existence of a biochemical-biophysical balance [33]. Ignoring such balances could lead to misleading conclusions and questionable relevance of findings.

Perhaps this can be supported in part by the relatively limited therapeutic success of molecular interventions targeting tumor invasion and metastasis or by the resistance of invasive cells to standard chemotherapy, most notable in gliomas [34]. A prominent example for failed molecular interventions is the therapeutic targeting of ECM degrading enzymes, including matrix-metalloproteinases (MMPs; discussed in section 1.2.2 and 1.2.3). Although upregulation of MMPs are highly correlated with poor prognosis [35, 36], clinical trials of MMP inhibitors have been extremely disappointing. While the promiscuity of the inhibitors was initially blamed [37], recent studies indicate that in a 3D context, some tumors such as fibrosarcoma cells, can undergo mesenchymal-amoeboid transition that allows invasion without the need for MMPs [38]. We also offer an explanation in chapter 4, which emphasizes the importance of balance between ECM properties and the degree of matrix proteolysis and has been made possible by a more relevant experimental system.

In summary, we argue that novel experimental systems that take into account the diversity of microenvironmental cues are necessary to uncover previously unknown balances, which in turn are required for a comprehensive understanding of the migratory process and the relevance of therapeutic opportunities. As discussed in chapter 2, quantitative approaches are powerful in discovering these balances, as cell migration is a process with a biophysical emphasis. As the studies become more multivariate, future approaches compel the need for high-throughput technologies. We attempt to systematically address these challenges in this thesis by demonstrating the use of novel experimental systems in different biological problems.

1.2. Background

1.2.1. The epidermal growth factor receptor in tumor invasion

The members of the ErbB family receptor tyrosine kinases are ErbB1 (predominantly called EGFR or Her1), ErbB2 (often referred to as Her2 or neu), ErbB3 (Her3), and ErbB4

(Her4). Although in this thesis, we only make use of two ErbB ligands, there are more than 10 known ligands for the ErbB receptors [39]. Most notable ligands include the epidermal growth factor (EGF), transforming growth factor-α (TGF-α), Heparin-binding EGF (HB-EGF), betacellulin, amphiregulin, epiregulin, neuregulins 1a/b (heregulin-α/β), 2a/b , 3, 4, and epigen. Some ligands have high specificity towards a single ErbB receptor, such as EGF and neuregulin 4 towards EGFR and ErbB4, respectively. On the other hand, some ligands exhibit receptor-binding promiscuity [40]. Their implications in physiology and pathology are recorded in numerous publications, and their combinatorial opportunities due to the promiscuities provide an intriguing layer of regulatory possibilities.

The most well known regulatory layer is achieved by downstream signal propagation initiated by the activation of ErbB receptors. These receptors are type I trans-membrane receptors that each consist of (1) a similar cysteine-rich extracellular domain and (2) a cytoplastmic domain partly encoding the tyrosine kinase and partly containing numerous tyrosine phosphorylation sites. The ErbB signaling cascade is triggered by the binding of the ligand to the receptor, followed by homo- or hetero-receptor dimerization and transactivation of the receptor tyrosine kinases resulting in the autophorphorylation of cytosolic tyrosine sites. Subsequent binding of adaptor proteins (such as Shc and Grb2), and direct activation of downstream signaling components (such as Sos, Ras) leads to activation of many well elucidated (and other not well known) signaling pathways including the MAPK, PI3K and the PLC-γ pathways [41, 42] (see section 1.2.3.). One additional layer of regulatory control is achieved by multifaceted trafficking events – namely, internalization, recycling, and receptor complex degradation – that determine the duration and extent of signal relay. We depict these layers of ErbB activity regulation in Figure 1-2.

EGFR is one of the most well studied growth factor receptors. They have been found to be essential for embryonic development and physiological homeostasis, as most ErbB knockouts are non-viable [43]. Their dysregulation results in various pathologies from schizophrenia and heart disease [44, 45]. ErbB receptor kinases are a major area for therapeutic targeting as they are aberrantly expressed in more than 15 different types of cancers and are associated with tumor progression [43].

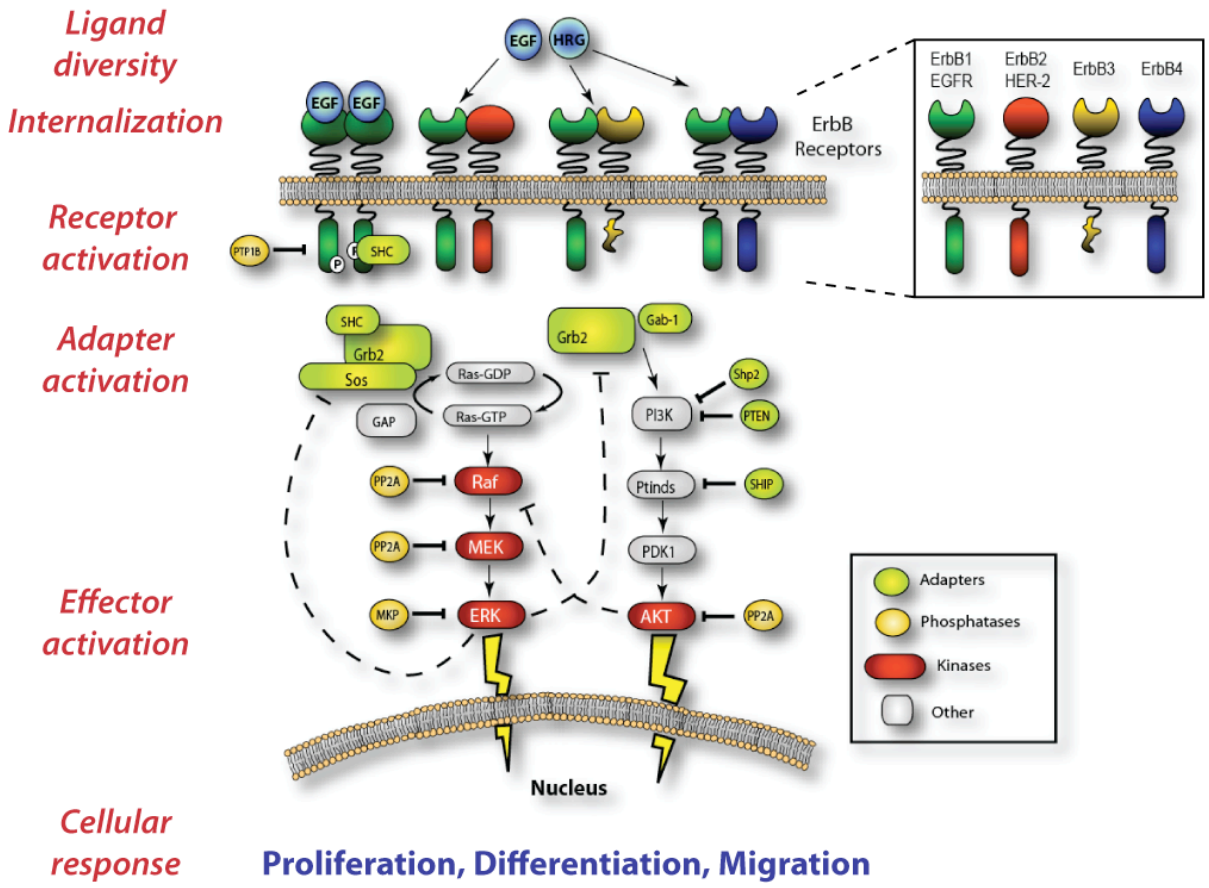

Figure 1-2 – Simplified schematic for the regulation of ErbB receptor tyrosine kinases and their downstream signals. Potential ErbB receptor homo- and hetero-dimerizations formed upon binding of EGF and heregulin (HRG) are illustrated. The layers of control (red, left) determine the extent and duration of signal propagation and eventual cellular responses triggered (blue). Intracellular kinases, phosphatases, and adapter proteins are involved in transmitting ErbB activated signals. Figure obtained from Dr. Paul Jasper.

During tumorigenesis and tumor progression, many different growth factors and their receptors are upregulated, with EGFR being the most frequent in human tumors [46]. In homeostasis, epithelial cells express EGFR and its ligands – predominantly EGF and TGF-α. But the expression of the receptors and ligands is spatially segregated – receptor expression is dominant at the basolateral surface whereas ligand release occurs at the apical membranes. This segregation is maintained by cell-cell junctions [47]. However, neoplastic epithelium exhibit weakened junctions causing inappropriate autocrine signaling. This signaling loop is thought to be responsible for active receptor activation and

internalization, accounting for the upregulation of EGFR signaling in carcinomas [48]. This is further supported by co-expression of EGFR and TGF-α in varieties of cancers and by the correlation of TGF-α expression with poor prognosis [49, 50].

Numerous transcription and protein level studies with primary glioblastomas, bladder carcinomas, gastric and colon carcinomas have demonstrated strong correlations between EGFR (and other growth factor receptors) signaling and the invasive step [51-56]. EGFR overexpression in DU-145 prostate tumor cells significantly increases their invasiveness *in vitro* and *in vivo*, which was diminished upon inhibition of EGFR activity [57, 58]. This result was validated in bladder and breast carcinoma lines *in vitro* [59]. Additionally, many upregulated growth factors and addition of exogenous EGF stimulate cell motility by increasing cell speed. However, it has been suggested that they also decrease the cell's directional persistence resulting in greater dispersion and sampling of a greater area, perhaps allowing cells to find advantageous cues embedded in matrix during tissue regeneration and development [33]. This strategy is suitable for carcinomas to find more penetrable regions of a matrix barrier and factors necessary for growth.

As alluded to in section 1.1., more recent studies by the Condeelis group show that an invasive subpopulation of previously injected tumors can be collected by inducing its chemotaxis towards a needle containing EGF [50, 60]. Their work provide compelling argument for macrophages expressing EGF and creating an EGF gradient towards the vasculature [61], while macrophages exhibit chemotaxis towards colony stimulating factor 1 (CSF-1) secreted by carcinomas. Gene expression studies of the invasive sub-population indicate that cells exhibiting EGF chemotaxis contain distinct genes that are upregulated (and downregulated), many of which include cytoskeletal proteins [21]. This further establishes the importance of downstream of signaling network in regulating cell migration.

It is interesting here to note that EGFR-induced cell locomotion may be a predominantly epigenetic phenomenon [6] since much of the motility phenomena can occur with the existing proteome and in absence of genetic mutations. Unlike naïve fibroblasts, tumor cells can translocate immediately upon exposure to growth factors [62, 63]. Although sustained migration requires long-term transcriptional and translational activity [64], genetic alterations in tumors can only partly explain the induced motility

during tumor invasion. Thus, understanding induced cell motility requires a complete understanding of the biophysical processes involved in locomotion as well as their molecular regulators downstream of EGFR that are activated by extracellular cues.

1.2.2. Biophysical decomposition of cell migration

Active cell motility is a delicately regulated process consisting of a series of biophysical steps [2]. After reorganization of the cytoskeleton to enable subsequent structural changes, the cell displays lamellipodial extensions and membrane ruffling at the leading edge to create directed or spontaneous new adhesions. The process of adhesion is accomplished by interactions between the cell surface adhesion receptors – integrin and non-integrin – and specific extracellular matrix domains [65]. These interactions can occur in the form of very close and structured focal adhesions or weaker focal contacts. The roles of different types of interactions are unclear, partly due to the fact that both new attachments (at the front) and detachment (at the rear) has to occur for productive motility; fibroblasts respond to exposure to EGF by losing their focal adhesions and regaining them later [63, 66] whereas mammary carcinoma cells display the opposite response [67].

Active locomotion is mediated by contraction via myosin-based molecular motors of the cell. These contractile forces are likely to be initiated near by the leading edge [2]. They are required in both pulling the cell body to the leading edge and eliminate adhesions at the rear end. Different myosin isoforms have been implicated in generation of contraction [68]; myosin II is important for both lamellipod extension and uropod retraction whereas myosin V is localized only in the lamellipod.

The final step of motility is rear detachment, which can occur in multiple ways. Fibroblasts and epithelial cells have shown to sever focal contacts from the cytoskeleton to the substratum [69, 70]. They have also shown to disperse focal adhesions and contacts by endocytic or membrane-directed recycling to the leading edge [2, 71]. Fast moving cells preferentially exhibit the endocytic recycling mechanism suggesting a relationship between the inherent cell speed and the detachment mode [6].

Above insights have been derived from *in vitro* experiments on 2D substrata with partial validation *in vivo*. Therefore, it is not surprising that most figures depicting the

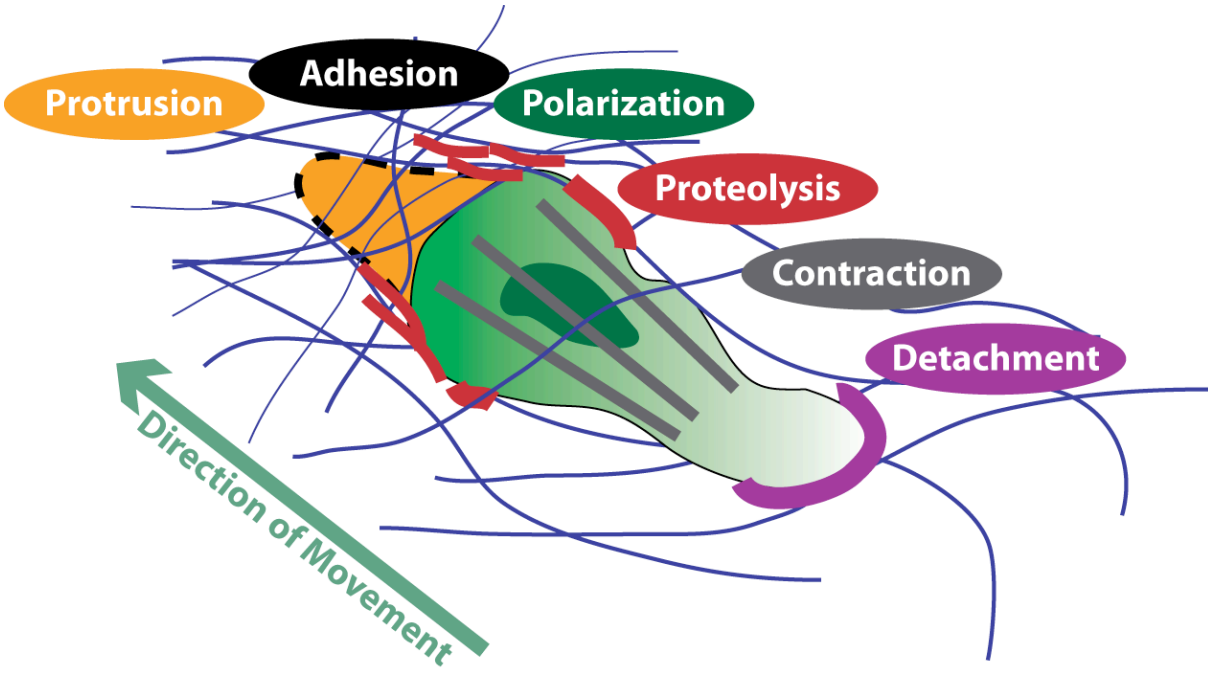

Figure 1-3 – Current model for the biophysical processes of cell migration in 3D ECMs. Depicted is a migrating cell (green) in 3D ECM fibers (blue). A careful spatio-temporal regulation of protrusion, adhesion, polarization, proteolysis, contraction, and detachment is required for productive cell migration.

biophysical steps of cell migration processes still depict a cell on a 2D surface. While these insights are still valid, recent studies spearheaded by the Friedl group and others in the field of matrix metalloproteinases (MMPs) suggest that there exist an additional biophysical step in cell migration in the context of the 3D environment [72]. The presence of a 3D ECM requires the clearance of a path for productive motility. Upon protrusion into the pores of ECM fibers, integrin-mediated cell-matrix adhesion, and establishment of proper polarization, cells are required to recruit and secrete surface proteases to ECM contacts, with focalized proteolysis occuring at the periphery of the cell, slightly behind the nascent adhesion sites (Figure 1-3). This step is required prior to the acto-myosin contractility generation for productive migration.

Slight differences between 2D and 3D migration may also exist in the formation of cell-matrix adhesions. It has been long assumed that cell movement in 3D environments may not be governed by same molecular dynamics as in 2D. Characterization of the composition and function of adhesions in 3D matrices [73] demonstrated that so-called

"3D-matrix adhesions" within *ex vivo* tissue and artificial matrices differ in their contents of integrins, paxillin, phosphorylated FAK, and other cytoskeletal components compared to 2D focal or fibrillar adhesions.

Lastly, the biophysical processes of cell migration in 3D environments are more prominently affected by mechanical and steric properties of the ECM. Pioneering work in an attempt to quantitatively understand cell migration in 3D integrated three-dimensional space, the biochemistry of integrin-matrix adhesions, matrix compliance, and matrix remodeling activity due to proteolysis computationally and experimentally. The results demonstrate a biphasic dependence of cell speed on substratum adhesivity and ligand concentration (as previously shown in 2D [25, 74]), as well as an intriguing biphasic dependence on matrix stiffness. These findings reiterate the multivariate nature of cell motility and the presence of a multivariate balance in the context of the relevant environment [75].

1.2.3. EGFR downstream regulators of biophysical processes of cell migration

Biophysical processes described above require precise biochemical regulation by the cellular signal transduction machinery for constructive locomotion. Understanding the signaling pathways associated with motility and their role in controlling intra- and extracellular biophysical processes is crucial for elucidating and predicting motility response behavior and identifying therapeutic targets. The following transduction components have been identified as representative key intracellular regulators of growth factor-induced motility and are summarized here with help of an excellent review [6, 76].

Phospholipase C-γ (PLC-γ): PLC-γ, an isoform of the PLC family directly activated by receptor tyrosine kinases, subsequently hydrolyzes phosphatidylinositol 4,5-biphosphate (PIP_2), and generates two second messengers, inositol triphosphate (IP_3) and diacylglycerol (DAG) [77, 78]. IP_3 then releases stored intracellular calcium from the endoplasmic reticulum, and DAG activates protein kinase C (PKC) isoforms. Thus, PLC-γ controls a diverse response signals downstream of EGFR.

PLC-γ has been speculated to be a rate-limiting step in EGF-induced cell motility [79]; it has been shown to be required for a full EGFR-mediated motility response [80],

whereas pharmacological and genetic diminution of PLC-γ activity leads to significantly decreased migration and invasion of prostate tumor and breast cancer cell lines *in vitro* and *in vivo* [59, 64]. Furthermore, sustained activation of PLC-γ through EGFR overexpression led to significantly higher invasive capability [57]. Similar requirement of PLC-γ has been observed in PDGF- [81], IGF-1- [82], and HGF-induced [83] motility. Nonetheless, PLC-γ activity alone is not sufficient for induced motility since inhibition of MEK prevents EGF-induced motility [66]; this is not surprising considering the signaling complexity involved in migration.

Interestingly, PLC-γ is not required for EGF-induced cell proliferation [64] indicating that EGFR serves as the control node for diverging proliferation and motility pathway activation. It is suggested that differential activation of effector molecules is responsible for the regulation of distinguished phenomena.

The most elucidated component downstream of PLC-γ concerns PIP_2. Actin binding proteins (ABP) and modulators of actin polymerization and cytoskeletal reorganization – like gelsolin, profilin, and cofilin – are bound to membrane PIP_2 in their inactive, immobile state [84]. Upon hydrolysis of PIP_2 by PLC-γ, localization of mobile ABPs assists lamellipod organization through sequestering, severing, capping, and polymerizing actin molecules. Vinculin, talin, and alpha-actinin have also been shown to bind to membrane PIP_2 and bridge focal adhesions and the actin cytoskeleton [85, 86] and to loosen attachments for membrane ruffling. Thus, PLC-γ regulates EGF-mediated reorganization of the actin cytoskeleton and establishes cellular asymmetry and lamellipod formation and extension [87, 88]. However, the precise role of PLC-γ signaling in these processes remains unknown until other required elements are elucidated [79].

Protein Kinase C-δ (PKC-δ): The PKC family of molecules consists of at least 11 isoforms. They are activated by phospholipids, DAG, fatty acids, and calcium depending isoforms. PKC-δ belongs to the group of the novel PKC, which are activated by DAG but are calcium independent [76]. PKC-δ is the most strongly phosphorylated isoform during EGF-stimulated motility. It has been shown that EGF requires phosphorylation of PKC-δ for inducing myosin II heavy chain and myosin light chain (MLC) activation for increasing contractile force [89]. Furthermore, inhibition of MEK and PI3K had no effect on PKC-δ

activation, suggesting that PKC-δ is potentially upstream of these pathways. However, inhibition of PLC-γ signaling led to delayed PKC-δ activation indicating that PLC-γ is required for promoting the acute phase of EGF-induced MLC activation [76].

Extracellular signal-regulated kinase (ERK): Raf, MEK, and ERK are tyrosine kinases of the mitogen-activated protein kinases (MAPK) cascade. The Raf-MEK-ERK cascade is typically triggered by growth factor-induced Ras activation. Interestingly, this particular cascade is very modular in that MEK-activation of ERK and Raf-activation of MEK are highly specific. In context of motility, ERK is activated upon integrin binding/clustering and growth factor occupancy [90]. It is proposed that ERK phosphorylates MLCK, which in turn phosphorylates myosin light chain inducing cell contraction. Furthermore, ERK has been implicated in phosphorylation of integrins resulting in reduction in their avidity to the ECM [91]. The fact that blocking of focal adhesion disassembly leads to both unstimulated and stimulated EGF-induced cell motility is explained by the ERK cascade [66]. The ERK pathway is shown to be required both for haptokinetic and chemokinetic cell motility [66, 90].

Matrix metalloproteinases (MMP): proteolytic activity is a cell's response to overcome the matrix barrier and is inherent to 3D migration although release of matrix-degrading proteases may also occur in 2D. Cells release a cocktail of substrate specific matrix-metalloproteases (MMPs) including MMP-2, MMP-9, and membrane-type MT-MMPs. The regulation of MMP expression is not very clear; but interestingly, their activation seems to be regulated among MMPs and tissue inhibitor of metalloproteases (TIMP) with highly regulated feedback loops [5]. Detailed interactions between MMPs and TIMPs are reviewed elsewhere [96]. In context of induced motility, EGF has shown to increase levels of a number of different proteases [97-99]. Interestingly however, some zymogram studies showed that EGF has no significant effect on secreted proteolytic activity. Collagenolytic activity has also been shown not to correlate with invasiveness [58].

1.3. Thesis overview

The work described in this thesis presents a survey of the combined use of novel experimental models and quantitative biology to advance the understanding of EGF receptor-mediated tumor cell migration. As such, this thesis not only describes development of experimental methods and models, but also emphasizes the importance of considering the complexity of biochemical and biophysical cues, provided by the tumor invasion microenvironment, in the design of quantitative experimental model systems. The demonstration begins in chapter 2 with the rationales for quantitative analyses for effective cell migration research. For an analysis of population migration dynamics, quantitative, increased-throughput, microscopy-based methodologies were developed. We then discuss the application of available mathematical models for a multivariate analysis of biochemical and biophysical processes. Chapter 3 is dedicated to a cue-signal-response analysis of EGF receptor-mediated cell migration upon epithelial-mesenchymal transition. Using an immortalized human mammary epithelial cell system and keeping a therapeutic purpose in mind, we combined a rigorous, yet relevant 2D migration system with multivariate data-driven modeling techniques. This approach aided in gaining novel insights into the migratory behavior defined by epithelial and mesenchymal cell states. The story continues in chapter 4 with the examination of physiologically relevant, EGF-stimulated tumor cell migration of mesenchymal origin by introducing a 3D experimental system. This work exploits the power of rigorous quantitative analysis of human glioblastoma population dynamics with a particular focus on the resulting biophysical effects that are potentially relevant to therapeutic targeting. Lastly in chapter 5, we challenge the notion of a physiologically relevant model system by exploring another 3D model system by using a 'quasi-3D' tissue engineering construct. The role of the microarchitecture of the extracellular matrix on mouse fibroblast migration is explored. The thesis is concluded in chapter 6 with our interpretation of the results, their impact, and the rationale for (1) engineering experimental systems with a comprehensive biological perspective and (2) the study of biology with a quantitative, biological engineering mindset.

1.4. References

1. Friedl, P., Y. Hegerfeldt, and M. Tusch, *Collective cell migration in morphogenesis and cancer.* Int J Dev Biol, 2004. **48**(5-6): p. 441-9.
2. Lauffenburger, D.A. and A.F. Horwitz, *Cell migration: a physically integrated molecular process.* Cell, 1996. **84**(3): p. 359-69.
3. Ridley, A.J., et al., *Cell migration: integrating signals from front to back.* Science, 2003. **302**(5651): p. 1704-9.
4. Yang, J. and R.A. Weinberg, *Epithelial-mesenchymal transition: at the crossroads of development and tumor metastasis.* Dev Cell, 2008. **14**(6): p. 818-29.
5. Friedl, P., K.S. Zanker, and E.B. Brocker, *Cell migration strategies in 3-D extracellular matrix: differences in morphology, cell matrix interactions, and integrin function.* Microsc Res Tech, 1998. **43**(5): p. 369-78.
6. Wells, A., *Tumor invasion: role of growth factor-induced cell motility.* Adv Cancer Res, 2000. **78**: p. 31-101.
7. Wang, W., et al., *Tumor cells caught in the act of invading: their strategy for enhanced cell motility.* Trends Cell Biol, 2005. **15**(3): p. 138-45.
8. Yamaguchi, H., J. Wyckoff, and J. Condeelis, *Cell migration in tumors.* Curr Opin Cell Biol, 2005. **17**(5): p. 559-64.
9. Kassis, J., et al., *Tumor invasion as dysregulated cell motility.* Semin Cancer Biol, 2001. **11**(2): p. 105-17.
10. Carapancea, M., et al., *Growth factor receptors signaling in glioblastoma cells: therapeutic implications.* J Neurooncol, 2008.
11. Grant, S.K., *Therapeutic Protein Kinase Inhibitors.* Cell Mol Life Sci, 2008.
12. Behmoaram, E., et al., *Early stage cancer cell invasion: signaling, biomarkers and therapeutic targeting.* Front Biosci, 2008. **13**: p. 6314-25.
13. Weigelt, B. and M.J. Bissell, *Unraveling the microenvironmental influences on the normal mammary gland and breast cancer.* Semin Cancer Biol, 2008. **18**(5): p. 311-21.
14. Seftor, E.A., et al., *The epigenetic reprogramming of poorly aggressive melanoma cells by a metastatic microenvironment.* J Cell Mol Med, 2006. **10**(1): p. 174-96.
15. Debnath, J. and J.S. Brugge, *Modelling glandular epithelial cancers in three-dimensional cultures.* Nat Rev Cancer, 2005. **5**(9): p. 675-88.
16. Griffith, L.G. and M.A. Swartz, *Capturing complex 3D tissue physiology in vitro.* Nat Rev Mol Cell Biol, 2006. **7**(3): p. 211-24.
17. Cairns, J., *Mutation selection and the natural history of cancer.* Nature, 1975. **255**(5505): p. 197-200.
18. Nowell, P.C., *The clonal evolution of tumor cell populations.* Science, 1976. **194**(4260): p. 23-8.
19. Merlo, L.M., et al., *Cancer as an evolutionary and ecological process.* Nat Rev Cancer, 2006. **6**(12): p. 924-35.
20. Abbott, D.E., et al., *Exploiting the convergence of embryonic and tumorigenic signaling pathways to develop new therapeutic targets.* Stem Cell Rev, 2007. **3**(1): p. 68-78.
21. Wang, W., et al., *Identification and testing of a gene expression signature of invasive carcinoma cells within primary mammary tumors.* Cancer Res, 2004. **64**(23): p. 8585-94.

22. Narang, A., K.K. Subramanian, and D.A. Lauffenburger, *A mathematical model for chemoattractant gradient sensing based on receptor-regulated membrane phospholipid signaling dynamics.* Ann Biomed Eng, 2001. **29**(8): p. 677-91.
23. Maheshwari, G. and D.A. Lauffenburger, *Deconstructing (and reconstructing) cell migration.* Microsc Res Tech, 1998. **43**(5): p. 358-68.
24. Friedl, P. and E.B. Brocker, *The biology of cell locomotion within three-dimensional extracellular matrix.* Cell Mol Life Sci, 2000. **57**(1): p. 41-64.
25. Palecek, S.P., et al., *Integrin-ligand binding properties govern cell migration speed through cell-substratum adhesiveness.* Nature, 1997. **385**(6616): p. 537-40.
26. Kharait, S., et al., *Decision tree modeling predicts effects of inhibiting contractility signaling on cell motility.* BMC Syst Biol, 2007. **1**: p. 9.
27. Gupton, S.L. and C.M. Waterman-Storer, *Spatiotemporal feedback between actomyosin and focal-adhesion systems optimizes rapid cell migration.* Cell, 2006. **125**(7): p. 1361-74.
28. Zaman, M.H., et al., *Migration of tumor cells in 3D matrices is governed by matrix stiffness along with cell-matrix adhesion and proteolysis.* Proc Natl Acad Sci U S A, 2006. **103**(29): p. 10889-94.
29. Zaman, M.H., et al., *Computational model for cell migration in three-dimensional matrices.* Biophys J, 2005. **89**(2): p. 1389-97.
30. Janes, K.A., et al., *A systems model of signaling identifies a molecular basis set for cytokine-induced apoptosis.* Science, 2005. **310**(5754): p. 1646-53.
31. Gaudet, S., et al., *A compendium of signals and responses triggered by prodeath and prosurvival cytokines.* Mol Cell Proteomics, 2005. **4**(10): p. 1569-90.
32. Schoeberl, B., et al., *Computational modeling of the dynamics of the MAP kinase cascade activated by surface and internalized EGF receptors.* Nat Biotechnol, 2002. **20**(4): p. 370-5.
33. Ware, M.F., A. Wells, and D.A. Lauffenburger, *Epidermal growth factor alters fibroblast migration speed and directional persistence reciprocally and in a matrix-dependent manner.* J Cell Sci, 1998. **111 (Pt 16)**: p. 2423-32.
34. Nakada, M., et al., *Molecular targets of glioma invasion.* Cell Mol Life Sci, 2007. **64**(4): p. 458-78.
35. Orlichenko, L.S. and D.C. Radisky, *Matrix metalloproteinases stimulate epithelial-mesenchymal transition during tumor development.* Clin Exp Metastasis, 2008. **25**(6): p. 593-600.
36. Shiomi, T. and Y. Okada, *MT1-MMP and MMP-7 in invasion and metastasis of human cancers.* Cancer Metastasis Rev, 2003. **22**(2-3): p. 145-52.
37. Overall, C.M. and O. Kleifeld, *Towards third generation matrix metalloproteinase inhibitors for cancer therapy.* Br J Cancer, 2006. **94**(7): p. 941-6.
38. Wolf, K., et al., *Compensation mechanism in tumor cell migration: mesenchymal-amoeboid transition after blocking of pericellular proteolysis.* J Cell Biol, 2003. **160**(2): p. 267-77.
39. Harris, R.C., E. Chung, and R.J. Coffey, *EGF receptor ligands.* Exp Cell Res, 2003. **284**(1): p. 2-13.
40. Jones, J.T., R.W. Akita, and M.X. Sliwkowski, *Binding specificities and affinities of egf domains for ErbB receptors.* FEBS Lett, 1999. **447**(2-3): p. 227-31.

41. Gschwind, A., O.M. Fischer, and A. Ullrich, *The discovery of receptor tyrosine kinases: targets for cancer therapy.* Nat Rev Cancer, 2004. **4**(5): p. 361-70.
42. Jorissen, R.N., et al., *Epidermal growth factor receptor: mechanisms of activation and signalling.* Exp Cell Res, 2003. **284**(1): p. 31-53.
43. Yarden, Y. and M.X. Sliwkowski, *Untangling the ErbB signalling network.* Nat Rev Mol Cell Biol, 2001. **2**(2): p. 127-37.
44. Lee, K.F., et al., *Requirement for neuregulin receptor erbB2 in neural and cardiac development.* Nature, 1995. **378**(6555): p. 394-8.
45. Mei, L. and W.C. Xiong, *Neuregulin 1 in neural development, synaptic plasticity and schizophrenia.* Nat Rev Neurosci, 2008. **9**(6): p. 437-52.
46. Aaronson, S.A., *Growth factors and cancer.* Science, 1991. **254**(5035): p. 1146-53.
47. DeWitt, A.E., et al., *Quantitative analysis of the EGF receptor autocrine system reveals cryptic regulation of cell response by ligand capture.* J Cell Sci, 2001. **114**(Pt 12): p. 2301-13.
48. Glynne-Jones, E., L. Goddard, and M.E. Harper, *Comparative analysis of mRNA and protein expression for epidermal growth factor receptor and ligands relative to the proliferative index in human prostate tissue.* Hum Pathol, 1996. **27**(7): p. 688-94.
49. Modjtahedi, H., et al., *EGFR blockade by tyrosine kinase inhibitor or monoclonal antibody inhibits growth, directs terminal differentiation and induces apoptosis in the human squamous cell carcinoma HN5.* Int J Oncol, 1998. **13**(2): p. 335-42.
50. Salomon, D.S., et al., *Epidermal growth factor-related peptides and their receptors in human malignancies.* Crit Rev Oncol Hematol, 1995. **19**(3): p. 183-232.
51. Barrack, E.R., *TGF beta in prostate cancer: a growth inhibitor that can enhance tumorigenicity.* Prostate, 1997. **31**(1): p. 61-70.
52. Chicoine, M.R. and D.L. Silbergeld, *Mitogens as motogens.* J Neurooncol, 1997. **35**(3): p. 249-57.
53. Libermann, T.A., et al., *Amplification, enhanced expression and possible rearrangement of EGF receptor gene in primary human brain tumours of glial origin.* Nature, 1985. **313**(5998): p. 144-7.
54. Neal, D.E., et al., *Epidermal-growth-factor receptors in human bladder cancer: comparison of invasive and superficial tumours.* Lancet, 1985. **1**(8425): p. 366-8.
55. Schlegel, J., et al., *Amplification of the epidermal-growth-factor-receptor gene correlates with different growth behaviour in human glioblastoma.* Int J Cancer, 1994. **56**(1): p. 72-7.
56. Yasui, W., et al., *Expression of epidermal growth factor receptor in human gastric and colonic carcinomas.* Cancer Res, 1988. **48**(1): p. 137-41.
57. Turner, T., et al., *EGF receptor signaling enhances in vivo invasiveness of DU-145 human prostate carcinoma cells.* Clin Exp Metastasis, 1996. **14**(4): p. 409-18.
58. Xie, H., et al., *In vitro invasiveness of DU-145 human prostate carcinoma cells is modulated by EGF receptor-mediated signals.* Clin Exp Metastasis, 1995. **13**(6): p. 407-19.
59. Kassis, J., et al., *A role for phospholipase C-gamma-mediated signaling in tumor cell invasion.* Clin Cancer Res, 1999. **5**(8): p. 2251-60.
60. Goswami, S., et al., *Breast cancer cells isolated by chemotaxis from primary tumors show increased survival and resistance to chemotherapy.* Cancer Res, 2004. **64**(21): p. 7664-7.

61. Goswami, S., et al., *Macrophages promote the invasion of breast carcinoma cells via a colony-stimulating factor-1/epidermal growth factor paracrine loop.* Cancer Res, 2005. **65**(12): p. 5278-83.
62. Segall, J.E., et al., *EGF stimulates lamellipod extension in metastatic mammary adenocarcinoma cells by an actin-dependent mechanism.* Clin Exp Metastasis, 1996. **14**(1): p. 61-72.
63. Maheshwari, G., et al., *Biophysical integration of effects of epidermal growth factor and fibronectin on fibroblast migration.* Biophys J, 1999. **76**(5): p. 2814-23.
64. Chen, P., et al., *Epidermal growth factor receptor-mediated cell motility: phospholipase C activity is required, but mitogen-activated protein kinase activity is not sufficient for induced cell movement.* J Cell Biol, 1994. **127**(3): p. 847-57.
65. Hynes, R.O., *Integrins: bidirectional, allosteric signaling machines.* Cell, 2002. **110**(6): p. 673-87.
66. Xie, H., et al., *EGF receptor regulation of cell motility: EGF induces disassembly of focal adhesions independently of the motility-associated PLCgamma signaling pathway.* J Cell Sci, 1998. **111 (Pt 5)**: p. 615-24.
67. Bailly, M., J.S. Condeelis, and J.E. Segall, *Chemoattractant-induced lamellipod extension.* Microsc Res Tech, 1998. **43**(5): p. 433-43.
68. Verkhovsky, A.B., T.M. Svitkina, and G.G. Borisy, *Myosin II filament assemblies in the active lamella of fibroblasts: their morphogenesis and role in the formation of actin filament bundles.* J Cell Biol, 1995. **131**(4): p. 989-1002.
69. Huttenlocher, A., et al., *Regulation of cell migration by the calcium-dependent protease calpain.* J Biol Chem, 1997. **272**(52): p. 32719-22.
70. Yamaguchi, R., et al., *Unphosphorylated and tyrosine-phosphorylated forms of a focal adhesion protein, paxillin, are substrates for calpain II in vitro: implications for the possible involvement of calpain II in mitosis-specific degradation of paxillin.* FEBS Lett, 1994. **356**(1): p. 114-6.
71. Palecek, S.P., et al., *Physical and biochemical regulation of integrin release during rear detachment of migrating cells.* J Cell Sci, 1998. **111 (Pt 7)**: p. 929-40.
72. Friedl, P. and K. Wolf, *Tumour-cell invasion and migration: diversity and escape mechanisms.* Nat Rev Cancer, 2003. **3**(5): p. 362-74.
73. Cukierman, E., et al., *Taking cell-matrix adhesions to the third dimension.* Science, 2001. **294**(5547): p. 1708-12.
74. DiMilla, P.A., K. Barbee, and D.A. Lauffenburger, *Mathematical model for the effects of adhesion and mechanics on cell migration speed.* Biophys J, 1991. **60**(1): p. 15-37.
75. Zaman, M.H., et al., *Computational Model for Cell Migration in Three- Dimensional Matrices.* Biophys J, 2005.
76. Iwabu, A., et al., *Epidermal growth factor induces fibroblast contractility and motility via a protein kinase C delta-dependent pathway.* J Biol Chem, 2004. **279**(15): p. 14551-60.
77. Berridge, M.J. and R.F. Irvine, *Inositol phosphates and cell signalling.* Nature, 1989. **341**(6239): p. 197-205.
78. Alberts, B., *Molecular biology of the cell*. 4th ed. 2002, New York: Garland Science. xxxiv, 1463, [86] p.
79. Wells, A., et al., *Epidermal growth factor receptor-mediated motility in fibroblasts.* Microsc Res Tech, 1998. **43**(5): p. 395-411.

80. Ji, Q.S., et al., *Epidermal growth factor signaling and mitogenesis in Plcg1 null mouse embryonic fibroblasts.* Mol Biol Cell, 1998. **9**(4): p. 749-57.
81. Kundra, V., et al., *Regulation of chemotaxis by the platelet-derived growth factor receptor-beta.* Nature, 1994. **367**(6462): p. 474-6.
82. Bornfeldt, K.E., et al., *Insulin-like growth factor-I and platelet-derived growth factor-BB induce directed migration of human arterial smooth muscle cells via signaling pathways that are distinct from those of proliferation.* J Clin Invest, 1994. **93**(3): p. 1266-74.
83. Derman, M.P., et al., *An 11-amino acid sequence from c-met initiates epithelial chemotaxis via phosphatidylinositol 3-kinase and phospholipase C.* J Biol Chem, 1996. **271**(8): p. 4251-5.
84. Chen, P., J.E. Murphy-Ullrich, and A. Wells, *A role for gelsolin in actuating epidermal growth factor receptor-mediated cell motility.* J Cell Biol, 1996. **134**(3): p. 689-98.
85. Sechi, A.S. and J. Wehland, *The actin cytoskeleton and plasma membrane connection: PtdIns(4,5)P(2) influences cytoskeletal protein activity at the plasma membrane.* J Cell Sci, 2000. **113 Pt 21**: p. 3685-95.
86. Ling, K., et al., *Type I gamma phosphatidylinositol phosphate kinase targets and regulates focal adhesions.* Nature, 2002. **420**(6911): p. 89-93.
87. Chen, P., H. Xie, and A. Wells, *Mitogenic signaling from the egf receptor is attenuated by a phospholipase C-gamma/protein kinase C feedback mechanism.* Mol Biol Cell, 1996. **7**(6): p. 871-81.
88. Mouneimne, G., et al., *Phospholipase C and cofilin are required for carcinoma cell directionality in response to EGF stimulation.* J Cell Biol, 2004. **166**(5): p. 697-708.
89. Straussman, R., L. Even, and S. Ravid, *Myosin II heavy chain isoforms are phosphorylated in an EGF-dependent manner: involvement of protein kinase C.* J Cell Sci, 2001. **114**(Pt 16): p. 3047-57.
90. Klemke, R.L., et al., *Regulation of cell motility by mitogen-activated protein kinase.* J Cell Biol, 1997. **137**(2): p. 481-92.
91. Hughes, P.E., et al., *Suppression of integrin activation: a novel function of a Ras/Raf-initiated MAP kinase pathway.* Cell, 1997. **88**(4): p. 521-30.
92. Glading, A., D.A. Lauffenburger, and A. Wells, *Cutting to the chase: calpain proteases in cell motility.* Trends Cell Biol, 2002. **12**(1): p. 46-54.
93. Franco, S., B. Perrin, and A. Huttenlocher, *Isoform specific function of calpain 2 in regulating membrane protrusion.* Exp Cell Res, 2004. **299**(1): p. 179-87.
94. Glading, A., et al., *Epidermal growth factor activates m-calpain (calpain II), at least in part, by extracellular signal-regulated kinase-mediated phosphorylation.* Mol Cell Biol, 2004. **24**(6): p. 2499-512.
95. Carragher, N.O., et al., *Cleavage of focal adhesion kinase by different proteases during SRC-regulated transformation and apoptosis. Distinct roles for calpain and caspases.* J Biol Chem, 2001. **276**(6): p. 4270-5.
96. Egeblad, M. and Z. Werb, *New functions for the matrix metalloproteinases in cancer progression.* Nat Rev Cancer, 2002. **2**(3): p. 161-74.
97. Jarrard, D.F., et al., *Effect of epidermal growth factor on prostate cancer cell line PC3 growth and invasion.* Prostate, 1994. **24**(1): p. 46-53.

98. Matrisian, L.M. and B.L. Hogan, *Growth factor-regulated proteases and extracellular matrix remodeling during mammalian development.* Curr Top Dev Biol, 1990. **24**: p. 219-59.
99. Yoshida, K., et al., *Induction of growth factor-receptor and metalloproteinase genes by epidermal growth factor and/or transforming growth factor-alpha in human gastric carcinoma cell line MKN-28.* Jpn J Cancer Res, 1990. **81**(8): p. 793-8.

CHAPTER 2

Quantitative *in vitro* methods for analyzing cell migration with a perspective towards microenvironment-relevant biophysics

This chapter is devoted to the detailed descriptions of methodologies used in subsequent chapters. It focuses on the development of quantitative experimental and mathematical methods to analyze migratory behavior in 2D and 3D environments necessary for a systematic, biophysical emphasis. Data-driven modeling methods are described to connect the signaling network to the migratory phenotype.

2.1. Introduction

2.1.1. Cell migration is a biochemically and biophysically intertwined problem compelling the use of quantitative methods

Analysis of cellular responses – from proliferation, apoptosis, to differentiation – is a complex problem regardless of the response being analyzed as all responses are controlled by the complex signaling network. However, as alluded to in chapter 1, the analysis of the motility processes is even more complex since the laws of physics intuitively play an integral role in the outcome of this particular cellular response. These laws do not only extend to the extracellular substrata within which cell migration occurs, but also in the cellular processes that are in turn controlled by the ever changing cell signaling dynamics [1]. Only when a balance between the extracellular substrata and the biophysical processes is achieved, does the cell obtain productive motion.

The detailed mechanism of how this balance is maintained by the individual cell will be researched for years to come. But recent advances suggest that differential signaling pathways are responsible for regulating certain aspects of the motility process. For example, certain pathways are responsible for the generation of locomotion, while others

are involved in determining directionality of motion [2, 3]. However, many of these studies were qualitative where quantitation was used as a measure of objectiveness. Moreover, the findings often do not consider the obvious importance of physical and mechanical effects.

As described in chapter 1, many high-profile studies have assessed the effects of substrate stiffness and cytoskeletal biophysics on the migratory process [4-6]. Often the use of de novo mathematical and computational models was necessary to describe biological entities in a mathematical language and to appropriately interpret experimental data. For example, the regulation of DU-145 prostate cancer cell locomotion in 3D Matrigel was highly matrix property-dependent and the variation of cell-matrix adhesions yielded unexpected results. They were only explained by developing a mathematical model with subsequent validation [7, 8]. Due to the relevance of physics and mechanics in the migratory process, the use of mathematical insights is often helpful in understanding the role of biochemistry in regulating cell migration.

Accordingly, quantitative analysis does not only serve functions in the traditional sense; namely, the concise, objective description of migratory behavior and its associated processes for the purpose of communicating the results and of testing hypotheses regarding the effects of molecular treatments or interventions on the migratory behavior [9]. But in the perspective of the biophysical processes, quantitative analyses can aid in the derivation and development of mathematical models – based either on statistical intuition or physical laws – that can lead to previously unknown mechanisms of motility [10].

2.1.2. Technological advances address the need for quantitation in understanding cell motility

In addition to the biology-oriented perspective of the field, technological limitations contributed to the relatively low integration of quantitative analyses in understanding cell migration. For the assessment of qualitative migratory phenotypes, two assays in particular have been widely used. The first is the Boyden chamber assay and their modified versions [11]. The Boyden chamber was originally developed to study leukocyte chemotaxis and consists of a chamber of two media separated by a microporous filter membrane. Cells are seeded on one side of the membrane, and the other side of the

membrane is filled with a chemotactic agent allowing the cells to migrate through the porous membrane. After a period of incubation, often 24 to 48 hours, the membrane is fixed and stained; the number of cells migrated to the other side of the membrane indicates the level of the population migratory potential. These assays are often modified by coating the membranes with ECMs. The second widely used assay is the scratch wound healing assay, where a 'wound' is induced by physically scratching a strip of cells away in a monolayer of cells. The cellular repopulation of the wound is indicative of the migratory potential of the cell under a treatment condition [12]. Although both of these assays can provide reliable measures for the motility of a cell line under certain treatments, these assays are endpoint assays, and the results are dependent on the time when the endpoints are taken. Most relevantly, the results – number of cells that migrated or the wound area closed – have little correlation to the biophysical processes of cell migration or the physical properties of the extracellular environment, rendering mathematical correlation of the parameters to motility processes difficult. As cell migration is a dynamic process, a comprehensive analysis of the motility process requires dynamic measurement techniques. As such, time-lapse microscopy for live-cell imaging has been adopted in many instances to capture cell speed as a more time-point independent parameter [13].

Recent advances in imaging technologies and their increased adaptation in research laboratories facilitate the high-throughput time-lapse image acquisition, which is often needed for efficient capture of dynamics of large cell populations. Large samples are required to generate sufficient statistics, not only for the confidence measurement, but also to analyze multiple, biophysically relevant parameters.

2.1.3. Quantitative analysis in the context of the migration microenvironment

Although the focus of this section was largely placed on the biophysical aspect of cell migration, this thesis does not contain detailed studies of migration biophysics, based on force balances, for instance. While studies addressing the physical phenomena of migratory processes by force-based measurements or single-molecule mechanics [14, 15] contribute greatly to the fundamental understanding of cell migration, they often use experimental setups that do not resemble the physiologically relevant migration environments. In fact, quantitatively minded experimental setups rarely recapitulate a

biologically relevant environment. For example, while micropatterned surfaces and constructs provide informative tools for measuring physically relevant parameters [15], they are seldom coated with extracellular matrices that may be prevalent in the microenvironment. Furthermore, certain quantitatively measured parameters may not be applicable to physiological processes. For instance, it is still to be investigated what significance directional persistence time of chemokinetic migration holds in the context of the *in vivo* migration microenvironment where the cues are predominantly present as chemotactic ones.

Lastly, we emphasize the importance of properly connecting the signaling network to their control of biophysical processes of cell migration. According to the systems biology paradigm [16, 17], quantitative methods can aid in understanding and expressing the migratory parameters as a function of the activities of intracellular signals, which are often sampled by assessing activities of only a few key intracellular regulators.

In this chapter, we attempt to address some aspects of the problem posed by the study of cell migration via the application of a biological engineering mindset to devise quantitative cell migration assays and appropriate quantitative methods. These assays and methods emphasize the importance of biological relevance of measurements and the interpretation of the results by integrating multi-cellular migration, as well as the challenges posed by the consideration of a three-dimensional extracellular matrix environment.

2.2. Quantitation of wound closure dynamics in a high-throughput format

One of the most high-throughput assays available to assess the migratory potential under large number of biological interventions is the scratch wound healing assay. Wound healing assays have been utilized in many settings not only for fibroblasts, but also for non-wound healing relevant cells such as mammary epithelial cells [18, 19]. These assays, however, have only been used as endpoint assays with images taken at initial and final time points. These endpoint assessments disregard the dynamics present in wound closure,

such as the relevance of the rate of wound closure. In this section, we describe the use of a high-throughput wound closure assay and the development of a MATLAB-based image processing software to quantify wound closure dynamics [20].

2.2.1. Image capture of wound closure dynamics

Cells were initially seeded in monolayers in a 96-well plate format, and a wound was induced by scratching each cell monolayer with a glass-pipette tip. Time-lapse microscopy of fluorescently labeled cells was utilized to observe cell movement into the wound area (Figure 2-1). Fluorescently labeled cells were used to increase contrast for facilitated image analysis. Image capture can be performed either with a Cellomics Kinetiscan imaging setup already designed to handle 96-well plates in an environmentally controlled manner, or with a custom-built, environmentally controlled microscope (as described below in section 2.3.). Most of the assay development has been reported in [20].

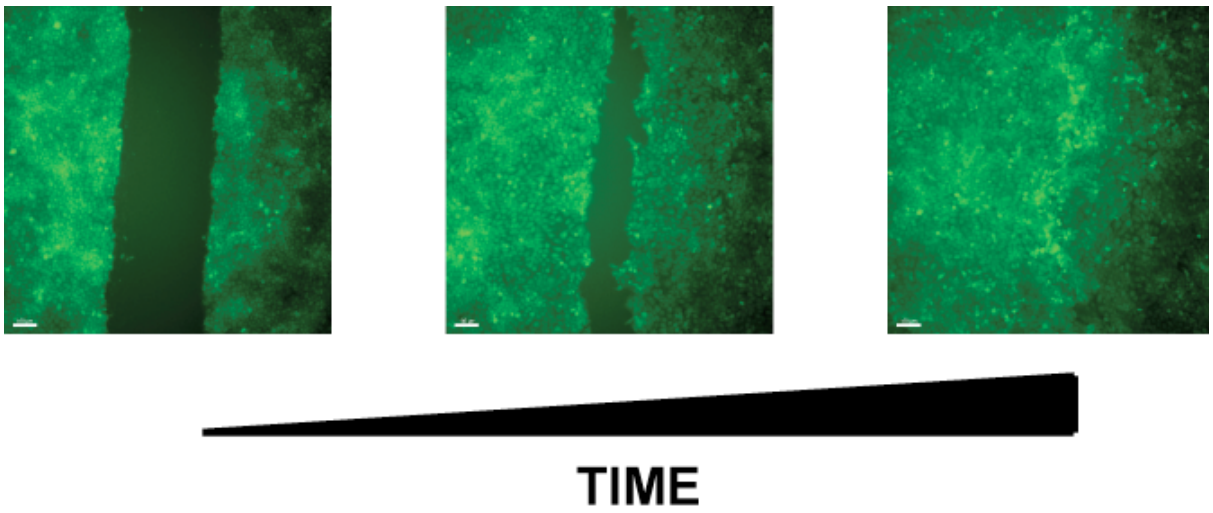

Figure 2-1 – Dynamic images of 184A1 human mammary epithelial cells in a scratch wound healing assay. 184A1 cells were labeled with CMFDA and seeded confluently before mechanically scratching a wound of ~650 μm width. Depicted are images at 0 h (left), 6 h (middle) and 12 h (right) time points. Figure is reprinted from [20] with permission by the Biophysical Society.

2.2.2. Quantitation of wound area using WoundGUI

High-throughput image analysis is non-trivially challenging due to the uneven, well-dependent fluorescent illuminations in a 96-well plate (or other multi-well formats). Furthermore, the heterogeneity of cell labeling contributes to inconsistent quantitation, usually requiring a great degree of manual work. To alleviate these problems, the following image processing procedures were applied to the fluorescent images to obtain wound area:

1. Image filling – fills the empty pixels within fluorescent pixels
2. Background subtraction – subtracts background calculated on all images
3. Contrast enhancement
4. Linear scaling – scaling images to enhance signal
5. Noise removal via median filtering
6. Image binarization
7. Image erosion and dilation – morphological structuring of binarized images
8. Manual selection of a wound area
9. Quantitation of time-lapse wound area sequences

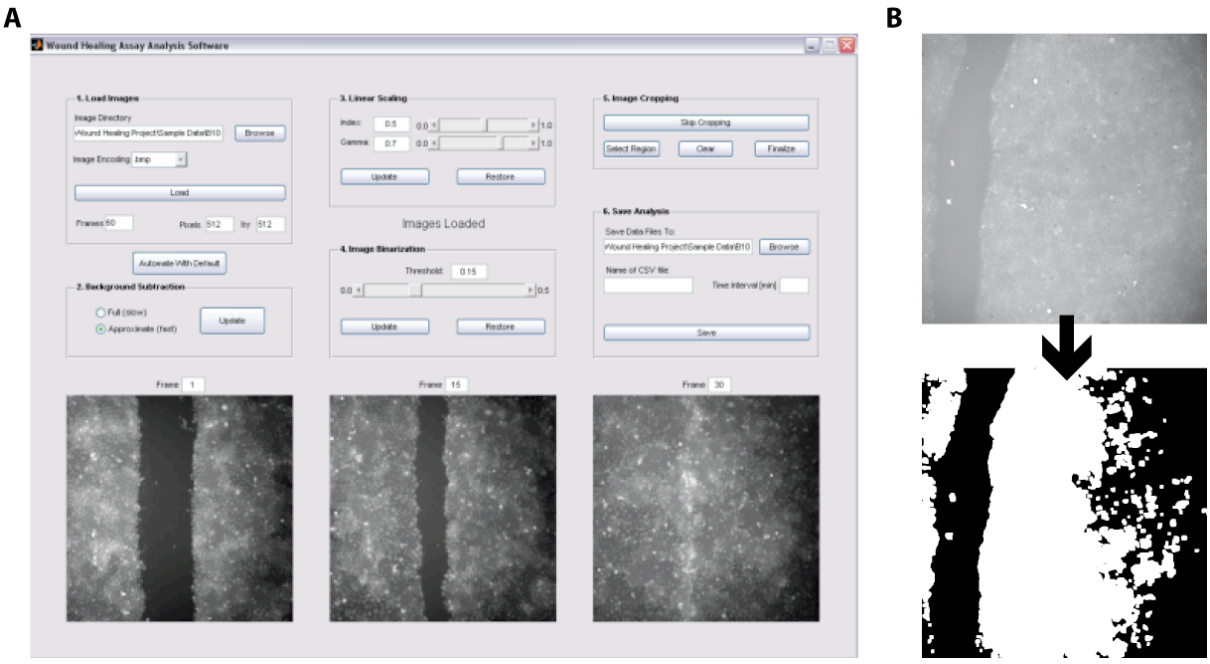

Figure 2-2 – Layout of WoundGUI, a graphical user interface for analyzing dynamic scratch wound assay images. (A) Graphical user interface for WoundGUI. **(B)** Original fluorescent image turned into a binarized image for wound area quantitation performed by WoundGUI.

These processing sequences have been implemented in a graphical user interface using MATLAB (Figure 2-2). Current version allows only handling of individual image sets, but future versions in currently in the works will contain handling of multiple images and vastly improved processing times. We included the MATLAB code for WoundGUI in Appendix A.

Data analyzed from woundhealing assays using 184A1 human mammary epithelial cells under different treatment conditions take the form of Figure 2-3 and have been published elsewhere [20, 21]. The data shows that the slope of wound closure is essentially similar during the first 2 hours after stimulation. After 2 hours, the slope is

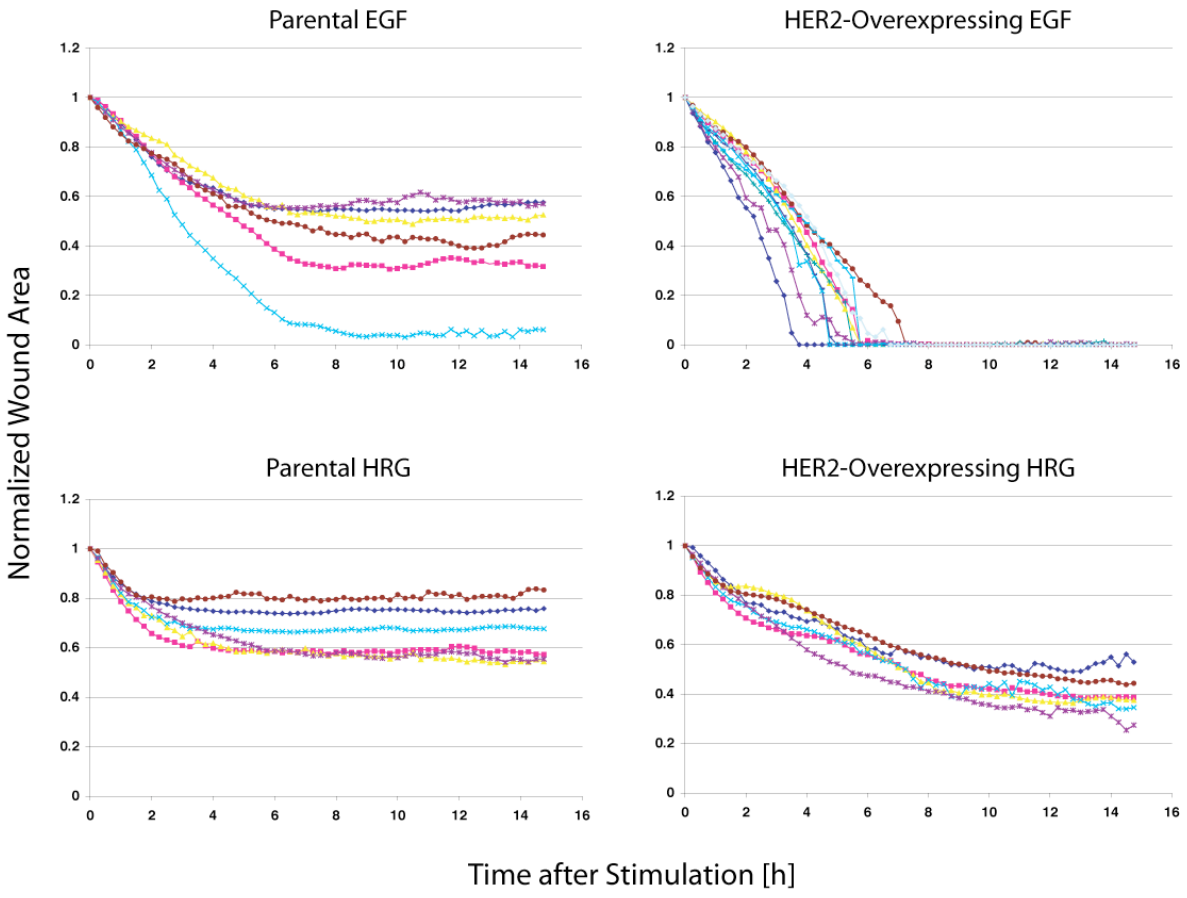

Figure 2-3 – Quantified wound areas over time exhibit cell line- and treatment-dependent wound closure rates. 184A1 parental (left) or HER2-overexpressing (right) cells were stimulated either with epidermal growth factor (EGF, top) or heregulin (HRG, top) after creating a wound through mechanical scratching. Wound closure was quantified with WoundGUI. Figure was modified and reprinted from [20] with permission from the Biophysical Society.

highly dependent on the stimulatory conditions. These datasets were used in a study to correlate signaling measurements to migration data by entering the rate of wound closure into a data-driven computational model [21].

Due to the questionable physiological relevance of wound healing assays for tumor cells, however, we will no longer consider their use in this thesis, which is focused on assessing migration behavior in the context of the tumor ME. Nevertheless, this high-througput image analysis platform allows the quick assessment of the migratory behaviors of multiple cell lines under multiple treatments.

2.3. 2D and 3D single cell tracking for quantitative analysis of cell migration via the persistent random walk model

While traditional endpoint assays or dynamic wound healing assays can provide the necessary throughput to measure multiple conditions at once, they lack the ability to quantify parameters that truly identify with the biophysical processes of cell migration. Cell speed and directional persistence are two parameters, which relate to the biophysical balance of protrusion, adhesion, polarization, contraction, and proper rear release. Their experimental measurements, however, necessitate proper spatio-temporal resolution. In this section, we describe the development of single cell tracking assays that are suited to assess context-dependent cell migration and are appropriate for higher throughput assessments. Finally, we describe the application of mathematical models to obtain cell speed and persistence time. These parameters are particularly well suited to model the migratory behavior of individual metastatic cells that have detached from the primary lesion and are of particular interest for successful therapy.

2.3.1. Use of fluorescence in 2D single cell tracking

Traditionally, time-lapse video microscopy has been used in brightfield mode to obtain single cell tracks [22, 23] to avoid potential phototoxicity presented by fluorescent labeling [24, 25]. Brightfield cell tracking is hindered by the cumbersome image analysis, which often requires arduous tracing of the cell outline in the low contrast image. Thus, the rate-

limiting step in high-throughput cell tracking experiments becomes the image analysis, and not image acquisition. Here, we introduce the use of cytoplasmic fluorescent labeling for single cell tracking, not only to increase the throughput of analysis, but also to track cells to measure cell migration in various cellular contexts.

In this thesis, we use CellTracker Green dye (5-chloromethylflouorescein diacetate; CMFDA) from Molecular Probes (Invitrogen; Carlsbad, CA) to label the cytoplasm cells. The labeling procedure has been optimized such that cells did not exhibit any noticeable phototoxicity when cells were migrating sparsely in a 2D environment over 18 hours (see section 3.2. for detailed description of methods). While no quantitative assessments have been performed, labeled cells migrated similarly to unlabeled cells in these low light exposure conditions. Cell viability in sparse cell migration assays was more dependent on seeding density than the existence of fluorescent labels.

The use of fluorescence enabled the benefit of commercially available image analysis software, which exploit the high contrast fluorescent images to generate cell tracks. Since fluorescent object recognition is essentially automated, cell tracks are obtained in greater throughput (pending manual validation of cell tracks). The shift of the rate-limiting step of the single cell tracking experiment from image analysis to image acquisition allows the simultaneous assessment of multiple conditions in a multi-well format by using a motorized stage (96-well as in [26] or 24-well as in chapter 3).

Further advantage of fluorescent labeling arises in the development of assays for collective cell movement. Mammalian cells often display the ability to move collectively within a monolayer. For example collective movement can be observed during fibrosarcoma invasion or during development [27, 28]. But *in vitro* quantitation of such movement is limited by available image analysis software. As described in chapter 3 and in [20, 26], CMFDA-labeled cells and unlabeled cells were seeded in a monolayer at a ratio of 1:20, and the movement of individual cells representing that of a monolayer were tracked using the same commercially available software as above (see Figure 3-4). This assay can also be combined with wound healing assays described in section 2.2. to obtain single cell parameters during wound closure [20, 29]. We note here that single cell tracking in monolayers was only used for obtaining cell speed and not directional persistence, as the

meaning of persistence in a monolayer is obscured and the applicability of the persistent random walk model is questionable.

2.3.2. Development of 3D time-lapse confocal microscopy

Single cell tracking assay is equally powerful for assessing migratory behavior of cells in a 3D environment. 3D single cell tracking have often been performed using brightfield imaging of cells embedded in a 3D extracellular matrix [22, 30]. Brightfield images yield tracks resolved only in x and y directions. While this may suffice for a qualitative assessment of migratory behavior, the lack of z-directional data results in the underestimation of cell speeds, whose accurate measurement is essential for a rigorous biophysical analysis of 3D cell movement. Therefore, in previous studies out of the Lauffenburger group, cell movement was captured using 3D time-lapse confocal microscopy, which used the ability of confocal microscopy to resolve images along the z-axis [7].

When performing time-lapse microscopy experiments lasting anywhere between 6-18 hours with an expensive shared instrument, time becomes of the essence and image acquisition throughput becomes important. However, previous setup located in the Whitehead-MIT BioImaging Center was not suited for capturing large amounts of images. In this section, we briefly describe the issues with developing a higher throughput 3D time-lapse microscopy setup on a custom-built confocal microscope, as this optimization process was surprisingly non-trivial.

Phototoxicity and photobleaching by excitation source and fluorescent labeling

Use of confocal microscopy for cell tracking has the disadvantage that cells must be labeled fluorescently. Current confocal microscopes are equipped with high power lasers for sample excitation (up to 1W) that alone may readily cause phototoxicity since chemical dyes are known to generate high amounts of reactive oxygen species enhancing DNA damage [31]. In addition, acquiring 80-100 images per field will render the phototoxicity generated a non-trivial issue. The extent of phototoxicity may be dependent on the cell type used as cells were labeled with CMFDA in previous assays [7] and in chapter 5 and

were robust to 3D time-lapse confocal microscopy. However, CMFDA causes cell death in 184A1 human mammary epithelial cells only after 6 hours (data not shown).

To minimize the phototoxicity, cells were cells were virally transduced with cytoplasmic green fluorescent protein (GFP) whenever possible, as shown in chapter 4. Continuous GFP expression not only diminishes phototoxicity, but also alleviates photobleaching since chemical dyes in 3D confocal assays exhibit photobleaching within a short amount of time rendering image analysis difficult. Lastly, the assay required an optimization to minimize phototoxcity and photobleaching and to maximize signal intensity by adjusting laser power and exposure times.

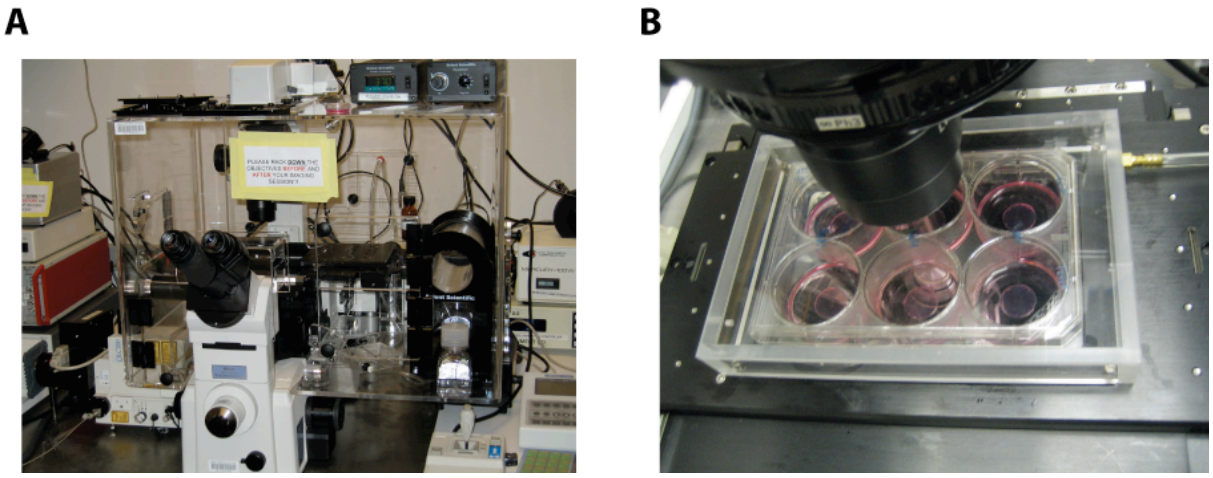

Figure 2-4 – Design of medium-throughput 3D time-lapse microscopy. (A) The confocal microscope equipped with a Solent environment chamber with controlled incubation temperature. **(B)** CO_2 environment chamber for multi-well plate point-revisiting experiment.

Environment control and stage revisiting

Perhaps because cell migration is such a delicately balanced process, the environment during imaging requires careful control. For this purpose, the confocal microscope was equipped with an environment chamber maintaining 37°C and 5% CO_2 (Figure 2-4, A). Plus, the microscope was equipped with a linearly encoded X-Y stage to enable medium-throughput setups. The Z-focus was controlled by the microscope focus control. For point revisiting experiments, it was imperative that an air-medium objective was used to avoid physical contact with the sample holder. Currently, for capturing 80 z-slices, 12 separate

fields can be imaged simultaneously during a 15 minute interval across a 6-well plate (Figure 2-4, B).

Choice of extracellular matrix

The choice of the extracellular matrix (ECM) is perhaps the most important aspect of the design of the 3D single cell tracking assay. Since our quantitative analysis serves the purpose of answering biological questions (see chapter 4 and 5), we have limited ourselves to naturally available ECMs. While synthetic constructs [32] provide well-controlled environments with robust variation of substrate parameters, their physiological relevance for understanding the effects of molecular manipulations on the migratory behavior is often questioned in biology. The type of ECM also determines the migratory behavior and the ability to record significant movement. For example, Matrigel, a commercially available ECM mixture secreted by mouse tumors, induces some motility in DU-145 prostate cancer cells [7], but interestingly provides an unhealthy environment for 184A1 human mammary epithelial cells (data not shown). Furthermore, collagen I abrogated most migratory behavior in DU-145 cells while it maintained viability for 184A1 cells (data not shown). We posit that this may be due to a combination of biochemical and mechanical stimuli, as Matrigel often exhibit significantly lower elastic moduli than collagen I matrices ([7] and chapter 3). Even migration of HT-1080 human fibrosarcoma cells in collagen I occurred with relatively low speeds, especially at high collagen concentrations. For the studies in chapter 4, we searched for a cell line/ECM combination that allowed sufficient cell migration across varying concentrations of ECM to extract directional persistence. We found that U87MG glioblastoma cells in a collagen I matrix exhibited the degree of migration over a relatively short period of time that allows cell track analysis with the persistent random walk model (Figure 4-1). While collagen I is not the ideal matrix for glioblastomas, the lack of a standard in vitro matrix for 3D glioblastoma studies [33] facilitated the justification for this cell/matrix combination.

2.3.3. Foundations of the persistent random walk model

Migratory paths obtained from spatio-temporally resolved single cell tracking assays codify large amounts of data regarding many aspects of cell migration. There have been many

methods developed to quantify the long-term migratory behavior [9, 34]. While cell displacement and cell speed have been a popular parameters to quantify degree of cell locomotion, the control of directionality have been found to be of interest since directional asymmetry is controlled by distinct signaling pathways. The simplest calculation to assess directionality is the 'D/T' ratio – total distance traveled over the total path length. However, this parameter is an endpoint measure that is dependent on the duration of the track and will often ignore the large data content provided by cell tracks. While there are other methods to assess chemokinetic directionality [35], persistent random walk (PRW) model and the directional persistence time parameter perhaps provides the most interesting measure of cell-intrinsic measure of persistence. PRW model quantifies a cell track by parsing it into two independent parameters, – cell speed and directional persistence time – which together fully describes a migratory track. An interesting analogy would be that, in essence, the gas pedal and the steering wheel of a car would be able to fully control the car. PRW model, therefore, not only provides a descriptive measure for the cell movement, but an intuitive measure for the cell's control of movement. This and other advantages are discussed below, after the derivations of the model.

The PRW model is based on the considerations of the statistical mechanics of Brownian motion, where, according to Einstein and Smoluchowski [36], the mean squared displacement (MSD) of a moving particle is directly proportional to the time interval assessed (MSD = $a\,t$, where a is a constant often containing the diffusion coefficient and a correction factor for the dimensionality). However, this relationship is only an approximation, which disregards the directional movement of a particle when assessing the sufficiently small time scales. For the movements of biological entities, the time scale during which directionality matters is sufficiently large, such that directional persistence can be considered as an additional parameter to be modeled.

The PRW model can be derived several different ways [37-39] and the underlying assumptions vary slightly according to the derivations. The simplest description of the PRW model was achieved by Ornstein [40] by solving the Langevin equation, in answer to a question raised by Smoluchowski about the role of inertia in Brownian motion. The Ornstein-Uhlenbeck (O-U) process is a Markov model descriptive of an auto-correlated random walk, where the velocity vector $\mathbf{v}(t)$ follows the stochastic infinitesimal equation:

$$d\mathbf{v}(t) = -a \cdot \mathbf{v}(t)dt + b \cdot d\mathbf{W_t} \qquad \text{(Eq. 1)}$$

where a and b are positive constants and $\mathbf{W_t}$ describes a two-dimensional Brownian motion. The first term on the right-hand side is called the infinitesimal drift and describes the resistance to motion of the magnitude a, while the second term depicts the random fluctuations with the magnitude of b. The root mean squared speed can then be calculated as $\sqrt{b^2/a}$ while directional persistence time derives to be $1/a$. This description is often used in Monte-Carlo models taking advantage of the stochastic nature of migratory processes, but is less intuitive than other descriptions since mainly the physical meaning of the Langevin equation cannot be transferred to cell movement. Therefore, we will leave the discussion of the O-U process to other available publications, including its first use for the description of cell movement [9].

The first statistical mechanics description of the PRW model and its application for describing cell movement were reported by Fürth in 1919. But meanwhile, other more elegant derivations have been reported [39]. Here, we will describe the derivation offered by Alt using a velocity autocorrelation function [38]. The function assumes that the cell velocity vectors between short time intervals are correlated, but at long time intervals become uncorrelated. This is apparent if the velocity vector at any time t is described in complex vector notation:

$$\mathbf{V}(t) = S(t) \cdot \Theta(t) = S(t) \cdot e^{i\alpha(t)} \qquad \text{(Eq. 1)}$$

where $S(t)$ and $\Theta(t)$ indicate two (more or less) independent processes in control of the velocity. $S(t) = |\mathbf{V}(t)|$ and refers to the control of the cell locomotion speed and $\Theta(t)$ to the control of the change of direction and $\alpha(t)$ is the angle between $\mathbf{V}(t)$ and the x-axis. The complex autocorrelation function between two velocity vectors of subsequent time points is defined as

$$G_V(\tau) = \langle \mathbf{V}(t+\tau) \cdot \mathbf{V}(t) \rangle \qquad \text{(Eq. 2)}$$

with τ as the time interval between the two vectors. At this point, we define directional persistence time (P) as

$$P = \lim_{\tau \to 0} \frac{2\tau}{\left\langle \left(\alpha(t+\tau) - \alpha(t) \right) \right\rangle} \qquad \text{(Eq. 3)}$$

With this definition and after considerable simplifications as well as assumptions described elsewhere [38], one can arrive at the intuitive equation for the real part of G_V

$$G_V(\tau) = S^2 e^{\tau / P} \qquad \text{(Eq. 4)}$$

which indicates that the correlation between two velocity vectors decays exponentially as a function of τ. Generally, the main objective of the model is to obtain cell speed and directional persistence time from trajectories obtained from time-lapse images. Therefore, of primary interest is to relate the displacements between time intervals ($\boldsymbol{d}(t)$) is related to S and P. The mean-squared displacement, $\left\langle d^2(t) \right\rangle$ can be related to the velocity autocorrelation function as

$$\left\langle d^2(t) \right\rangle = \left\langle \mathbf{d}(t) \cdot \mathbf{d}(t) \right\rangle = 2 \int_0^t dt' \int_0^{t'} G_V(\tau) d\tau \qquad \text{(Eq. 5)}$$

Together with Eq. 4, this equation then yields the well-known PRW equation used throughout this thesis:

$$\left\langle d^2(t) \right\rangle = 2S^2 P \left[t - P(1 - e^{-t/P}) \right] \qquad \text{(Eq. 6)}$$

where t here refers to the time intervals between displacements. This equation yields interesting limits for two extreme time intervals t:

For $0 < t << P$, $\qquad \left\langle d^2(t) \right\rangle \to S^2 t^2 \qquad \text{(Eq. 7)}$

Hence, displacement between short time intervals is described by a unidirectional motion without random turning.

For $t >> P$,

$$\left\langle d^2(t) \right\rangle \rightarrow 2S^2P \qquad \text{(Eq. 8)}$$

where $\left\langle d^2(t) \right\rangle$ becomes linearly proportional to t, as previously described by Einstein and Smoluchowski. Analogous to the molecular diffusion coefficient, a random motility coefficient, μ, can be defined from this limit:

$$\mu = \lim_{t \to \infty} \frac{\left\langle d^2(t) \right\rangle}{2n_d t} = \frac{S^2P}{n_d} \qquad \text{(Eq. 9)}$$

where n_d is the number of dimensions of $\boldsymbol{d}(t)$. It is to be noted that Eq. 6 is valid for both 2D and 3D environments.

2.3.4. Practical issues in implementing PRW for modeling experimental data

While the previous section concerned the mathematical derivation of the PRW model, this section explores the practical outlook in implementing the model. Although the mathematical derivations are established, there exist practical issues in using this model for experimental data. The first issue we discuss is the method of obtaining the mean-squared displacement (MSD). To properly fit Eq. 6 from the previous section, MSDs need to be calculated for various time intervals. There exist two methods as proposed by Dickinson and Tranquillo [41]. The first method samples all displacements for a particular time interval. For example, if the track consists of 9 time points and we are sampling all displacements over 3 time intervals, we average tracks between time points 0 – 3, 1 – 4, and 2 – 5, etc. The average squared displacements from overlapping time intervals for i time intervals, n_i displacement samples, and n total time points, yields

$$\bar{x}_i = \frac{1}{n_i} \sum_{k=1}^{n_i} x_{ik} \qquad \text{where } n_i = (n - i) \qquad \text{(Eq. 1)}$$

The second method samples only non-overlapping intervals. For the above example, we only yield 3 non-overlapping displacements of 3 time intervals. Hence, the number of

displacement samples reduces drastically as defined by following average squared displacement calculation:

$$\bar{x}_i = \frac{1}{n_i}\sum_{k=1}^{n_i-1} x_{i,1+ki} \qquad \text{where } n_i = \left[\frac{n-i}{i}\right] \qquad \text{(Eq. 2)}$$

In this thesis, we consistently use the method of non-overlapping intervals as the method of overlapping intervals oversamples the displacement such that $\bar{x}_i$ in Eq. 1 consists of averages of dependent values. While we sacrifice the number of samples for fit, we consistently find that PRW modeling with the method of non-overlapping intervals yields reasonable fit of the experimental data.

We implemented the PRW model with the method of non-overlapping intervals in MATLAB to calculate cell speed and directional persistence time. The MATLAB code is included in Appendix B. Figure 2-5 shows some graphs generated when fitting the PRW model to a 3D trajectory. The PRW model implementation calls for a two-parameter fitting of cell speed and directional persistence time. Two-parameter fitting using ordinary least squares fitting method (as shown in Figure 2-5, D) results in very high uncertainties (data not shown). One result of the two-parameter fitting is often the consistent yield of unreasonably high persistence times. One remedy is to use a generalized least squares method as described in [41]. However, we have resorted to calculating the average cell speed via averaging the instantaneous cell speed between each time intervals and only fitting for a single parameter, directional persistence time (Figure 2-5, C). We find that this estimation of persistence time is more reasonable when inspecting the actual trajectory.

2.3.5. Validity of PRW model in 3D environments

Like the Brownian motion model, the PRW model assumes an independently moving body in a homogeneous, isotropic environment without external physical forces applied on the body. These assumptions can be reasonably applied to cells in 2D environments when cells are seeded sufficiently sparsely, and the secretion of own extracellular matrices and autocrine growth factors – the latter establishing chemotactic

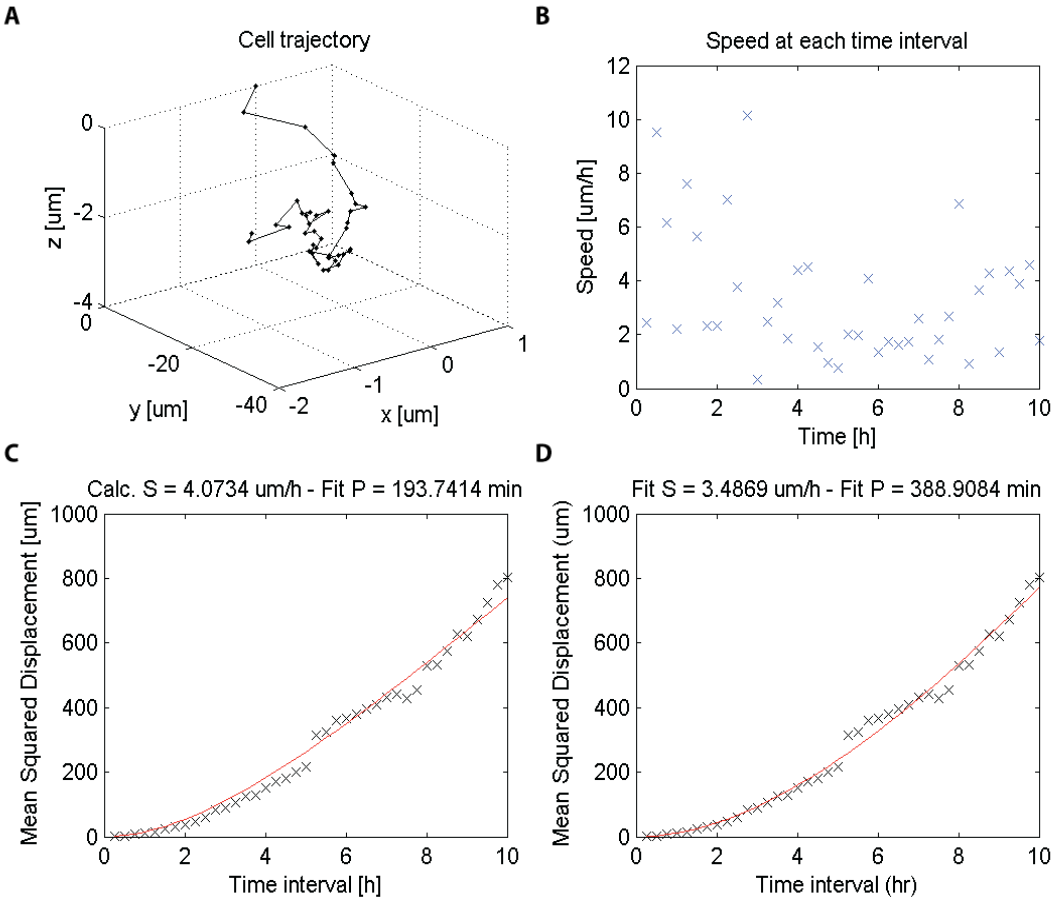

Figure 2-5 – Implementation of PRW model to a 3D cell track. (A) Three-dimensional cell track generated using 3D time-lapse confocal microscopy. **(B)** Instantaneous cell speeds over time. **(C)** and **(D)** Cell speed and persistence time was calculated by fitting mean squared displacement over various time intervals, using one-parameter (C) or two-parameter fitting (D).

gradients – is ignored. Unlike cells in 2D, which are submerged in a relatively homogeneous medium over the course of the experiment, cells in a 3D *in vitro* migration assay are embedded in a 3D extracellular matrix, which is constantly remodeled even within a short time scale. Recent observations of collagen degradation by fibrosarcoma cells indicate that there exists a significant heterogeneity of matrix sterics [42], and the heterogeneous distributions of physical forces provided by the matrix barrier pose a challenge to apply the PRW model for 3D cell movement. Furthermore, we have previously referred to the inherent ability of extracellular matrix proteins to bind growth factors and cytokines [43]. Unlike the homogeneous aqueous extracellular environment of 2D assays,

the diffusion of cytokines and growth factors is significantly hindered and potentially creates more pronounced heterogeneity.

Furthermore, as described in chapter 4 and seen in Figure 4-10, A, collagen matrices are relatively homogeneous when compared to the size of the mammalian cell. However, upon cellular remodeling, collagen fibers can realign themselves to facilitate contact-guided migration. We attempt to model contact guidance along aligned fibers via the use of porous scaffolds in chapter 5. While the porous scaffold does not expose the cell to the steric hindrances, the fibrous environment is not homogeneous. Thus, we note that we applied the PRW model in chapter 4 and 5, even though its assumptions are clearly violated.

It is important to note this violation, since the meaning of directional persistence as quantified by persistence time is drastically changed in a 3D environment. In 2D environments, the persistence time measured may indicate the inclination of a cell to migrate directionally productive or randomly (as long as the assumptions are valid within the experimental setup). However, as we lay out in chapter 4, the resulting persistence in 3D arises from both cell-intrinsic and -extrinsic effects – where the latter effect have not been taken into account by the derivations of the model. Cell migration along a fiber ('quasi-3D) was modeled using the PRW model under the understanding that the persistence time does not describe the intrinsic inclination to move directionally. The parameter served purely as an indicator for resulting directional motion, as guided by the physical properties of the scaffold fiber.

We conclude here that the PRW model is not an ideal model for describing cell movement in 3D, but is sufficient to describe the migratory phenomenon as long as the violation of assumptions are taken into account. At times, these violations can be quantified to serve to obtain further biological insights, as shown in Figure 4-10.

2.4. Data-driven correlation of signaling dynamics and migratory parameters via PCA/PLSR

As described in previous sections, a great number of proteins regulate cell function; the robust integration of activation and deactivation signals contribute to the complex

regulation of one or more phenotypic aspect, such as cell migration. While this complexity is fascinating, it poses a challenge to the discovery of unknown regulators. Despite this inherent challenge, in chapter 3, we attempt to discover the importance of hidden activities of key intracellular regulators by correlating the quantitatively measured migration phenotype to the signaling dynamics that govern the biophysical processes of cell migration.

2.4.1. Quantitative measurements of protein phosphorylation to generate cell signaling dataset

As a mechanism to spatio-temporally regulate protein activity to transduce extracellular cues into cellular phenotype, biology has evolved diverse mechanisms [44]. The most well understood mechanism is the phosphorylation certain specific amino acid residues (tyrosine, serine, and threonine), which introduces novel capabilities in a protein, including conformational changes of the protein itself or novel binding sites for other proteins required for their activation. Generally speaking, phosphorylation of certain sites are required for the diverse activity of proteins and their levels are often correlated with the activity of a kinase [44].

In chapter 3, we attempt to correlate protein activity to the migratory phenotypes. To do so, we measure phosphorylation levels of various proteins, and the phosphorylation sites measured have been known to confer activity (see chapter 3). This section is intended to provide a brief description of quantifying cell signaling activities. Quantitative measurements of protein phosphorylation levels have been described previously in various theses and publications out of the Lauffenburger laboratory [21, 26, 45] and will therefore be introduced only briefly in this section.

Availability of phospho-antibodies determines the feasibility and quality of the quantitative assay. Fluorescent bead-based ELISA assays originally developed by Luminex and available through Biorad and other companies have gained popularity for multiplexed quantitative measurements [46]. The use of fluorescently coded beads with unique capture antibodies allows the measurement of multiple proteins in one experiment. The availability of both a capture antibody and a phospho-site-specific antibody, which generally serve the binding of the protein to the bead and the quantitation of the

phosphorylation site, respectively, determines the feasibility of the quantitative assessment of a protein. Lack of significant cross-reactivity between the various antibodies is essential for multiplexing and has been validated to a certain extent by the manufacturers. Out of the 16 proteins measured in chapter 3, 10 proteins were measured by bead-based ELISAs.

The remaining 6 proteins were measured by quantitative Western Blot since the development of a Bioplex assay is limited by the commercial interest in a protein phosphorylation site. Simple assays of many key regulators of migratory processes are unavailable due to low customer base. Thus, traditional, low-throughput Western Blot technique is used to identify bands with known molecular weights where quantitation is performed by densitometry of the bands using highly quantitative infrared dye-conjugated secondary antibodies.

Despite the availability of these assays, their quantitative capabilities require validation, as phosphorylation levels too low can fall below the limit of detection while

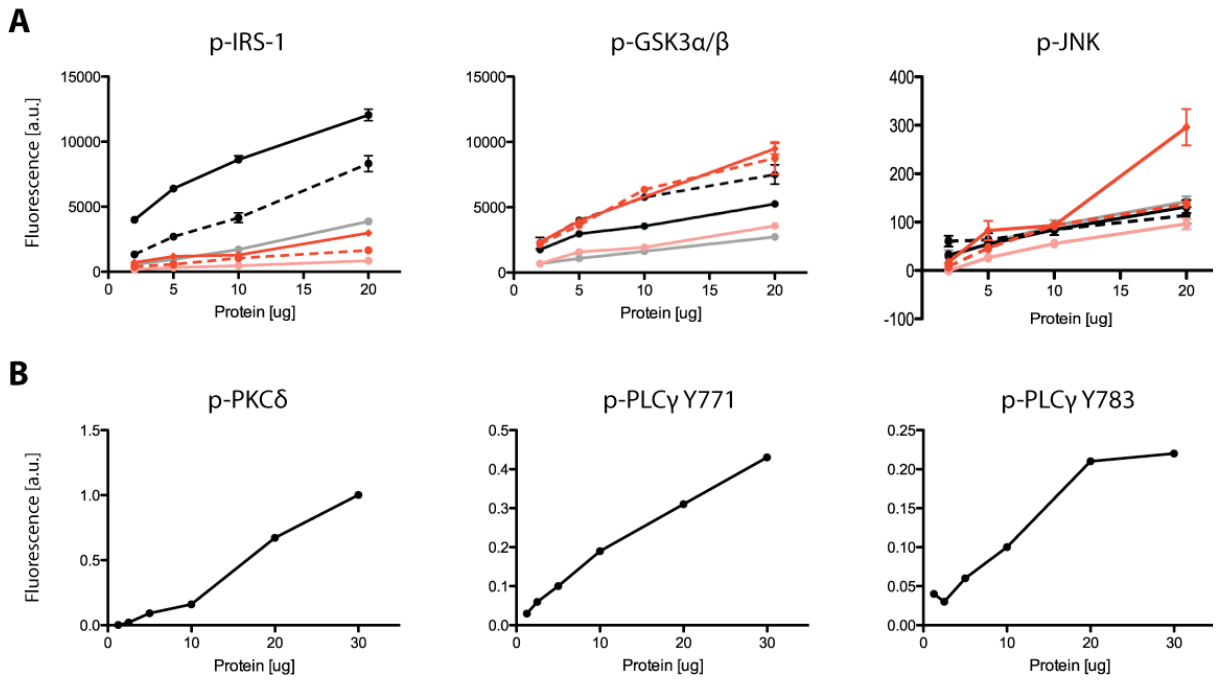

Figure 2-6 – Assessment of phospho-protein assay linearity. Various bead-based ELISA assays **(A)** or quantitative Western Blot assays **(B)** were tested for signal to specific phospho-protein mass linearity. Total of 18 assays were developed and tested for linearity. See chapter 4 for the quantitative analysis of cell signaling network.

levels too high can lead to signal saturation. Therefore, there exists a regime where the assay exhibits linearity. This linearity regime was tested by plotting signal intensity against protein mass loaded in an assay well (Figure 2-6). Low signal intensities (such as low 100's for Bioplex assays) indicate the need to load higher protein amounts, whereas high signal intensities and flat linearity curves indicate the need to load lower protein amounts. For example, while phospho-IRS-1 and phospho-GSK3α/β Bioplex assays show robust linearity with high signals between the protein loadings of 2 and 20 μg, phospho-JNK signals are relatively low. These results invoke the need for loading at least 20 μg for a robust phospho-JNK signal, while 5 μg may be required for phospho-IRS-1 and phospho-GSK3α/β assays to avoid saturation. Hence, the ability to multiplex assays is often hindered by assay saturation. For Western blot assays, phospho-PKCδ and phospho-PLCγ at site Y771 show robust linearity, phospho-PLCγ at site Y783 show saturation at even very low signal indicating that the latter assay may not be suited for quantitation.

As described in chapter 3, each of the 16 assays were validated for the presence of the linearity regime and the optimal protein mass per assay well determined. Finally, to account for assay-to-assay variability, a large stock of control lysates have been generated, which are loaded in each assay as a standard. For a detailed materials and methods description, see chapter 3.

2.4.2. Introduction to principal component analysis/partial least squares regression

The ultimate goal of signaling measurements is to assess molecular mechanism of action by identifying signals whose activities correlate with the interesting phenotypes. When the number of signaling candidates that regulate these phenotypes are large, as the current network-centric systems biology view often calls for (as opposed to the traditional protein-centric view), pure categorical inspection of signaling data becomes inefficient in correlating signaling datasets to the migration datasets. This inherent difficulty posed by multidimensional datasets (with multiple signaling candidates, multiple treatments, time courses, etc.) necessitates multivariate data analysis approaches that (1) can identify co-variation of signaling activities and response parameters and (2) can properly correlate signaling and response datasets as cause-effect relationships.

One additional difficulty also arises from the fact that the number of proteins that can be experimentally assessed are limited and the knowledge of the protein-protein interactions leading to the regulation of migratory processes are vastly incomplete, generally requiring a highly abstract approach for a comprehensive signal-response analysis. The underlying assumption of this analysis would be that the cellular response, such as migration, could be described as a function of the cellular signals.

When we assume that this function is a linear combination of the cellular signals, Principal component analysis (PCA) and partial least squares regression (PLSR) enables such correlation through linear mapping of one multi-dimensional dataset onto another [47]. PCA/PLSR is an abstracted tool that takes advantage of linear algebra and the statistical power of linear regression and offers an approximate function describing the cellular responses given a linear combination of cellular signals. The overall goal of PCA/PLSR is then to utilize linear regression of the two datasets to identify a set of parameters that project the matrix consisting of the signaling dataset onto a matrix consisting of the response dataset. This set of parameters (as denoted by the vector **b** in the next section) enables the transformation of signals to the response via linear projection and may aid in revealing the governing rules for how proteins and kinases coordinate. These parameters will also aid in identification of a cluster of co-varying signals through an algorithm that decomposes the multidimensional space into a lower dimensional one for a simpler interpretation of the clusters. In addition, the parameters will provide for an a priori prediction of cell behavior under a new treatment condition, given the availability of experimental signaling dataset. Nevertheless, it is to be noted that PCA/PLSR only yields useful insights in the boundaries of the training dataset (under the concept of garbage in = garbage out), and interpretations should be made with caution within the limits of the power of statistical correlation.

In this thesis, while the clustering capability of PCA/PLSR yielded useful insights, we have not yet taken full advantage of the predictive capability of the PLSR model derived from our dataset, but will regard it as an avenue for future research.

2.4.3. Principles of PCA/PLSR

Implementation of PLSR has the ultimate goal to solve the following linear regression problem (with a slight modification as described below) [48]:

$$\mathbf{Y} = \mathbf{Xb} \qquad \text{(Eq. 1)}$$

relating **Y**, which contain the response parameters, such as cell speed in one column and persistence in another, to **X**, which contain the phosphorylation levels of signaling components, via a regression vector **b** (or regression matrix if **Y** has more than one column), which maps the signaling matrix to the response space. Eq. 1 can be solved for **b**:

$$\mathbf{b} = (\mathbf{X}^T\mathbf{X})^{-1}\mathbf{X}^T\mathbf{Y} \qquad \text{(Eq. 2)}$$

When solving this equation, we find ourselves facing a linear problem with a large number of variables, where the uncertainty of estimated parameters is unacceptably high and is the dominating factor in the solution [48]. One powerful method to alleviate this problem is to reduce the dimensionality associated with each data matrix increasing the correlative and predictive power of the resulting model.

The dimensionality reduction is performed through single value decomposition (SVD) or PCA, which refer to the same technique [49] but whose derivations are often described differently. The mathematical details will be left to the excellent books available in this field [49]. SVD is a critical component of the PCA/PLSR algorithm and is especially well suited for the study of experimental data in biology as biology often yields rank-deficient matrices. The matrix containing the signaling measurement, **X**, has the dimensions of M x N corresponding to M cellular treatment conditions and N protein measurements for each treatment condition. For example, phosphorylation measurement at one time point (e.g. phospho-Erk at 5 min time point) for each treatment may populate one column, while a growth factor treatment for one particular cell line (EGF treatment for epithelial cell line) may populate a row. As currently available technologies using cell lysates for protein measurements cause the number of treatment condition to be rate-limiting and the number of unique protein measurements (~100 – 1000 measurements)

often exceed the number of treatment conditions (~5 – 20), **X** typically results in a rank-deficient, multi-dimensional matrix for biological experiments.

The reduction of dimensionality is achieved by SVD, which identifies an orthogonal basis set for both the row and column spaces of **X**. To do so, SVD decomposes the matrix **X** with the rank *r*

$$\mathbf{X} = \mathbf{U}\mathbf{\Sigma}\mathbf{V}^{T} \qquad \text{(Eq. 3)}$$

Upon this decomposition, the first *r* rows of **V** comprise an orthogonal basis set for the row space and the first *r* columns of **U** an orthogonal basis set for the column space. Rows and columns after *r* in **V** and **U** comprise the basis set for the null spaces of **X** and $\mathbf{X}^{T}$, respectively. The covariance of **X** and $\mathbf{X}^{T}$ is then defined as

$$\mathbf{X}\,\mathbf{X}^{T} = \mathbf{U}\,\mathbf{\Sigma}\,\mathbf{\Sigma}^{T}\,\mathbf{U}^{T} \qquad \text{(Eq. 4)}$$

$$\mathbf{X}^{T}\,\mathbf{X} = \mathbf{V}\,\mathbf{\Sigma}^{T}\,\mathbf{\Sigma}\,\mathbf{V}^{T} \qquad \text{(Eq. 5)}$$

Lastly then, to solve for **U** and **V**, we need to recognize that the columns of **V** and **U** comprise the eigenvectors for $\mathbf{X}^{T}\mathbf{X}$ and $\mathbf{X}\mathbf{X}^{T}$, respectively, in Jordan normal form. Finally, using SVD and introducing the pseudoinverse $\mathbf{X}^{-1}$, Eq. 2 becomes:

$$\mathbf{B} = \mathbf{X}^{-1}\,\mathbf{Y} = \mathbf{V}\,\mathbf{\Sigma}^{-1}\,\mathbf{U}^{T}\,\mathbf{Y} \qquad \text{(Eq. 6)}$$

In the context of PCA, the matrix **X** is decomposed into a sum of outer products [49]:

$$\mathbf{X} = \mathbf{t}_1\mathbf{p}_1^{T} + \mathbf{t}_2\mathbf{p}_2^{T} + \ldots + \mathbf{t}_r\mathbf{p}_r^{T} \qquad \text{(Eq. 7)}$$

where **t** is the scores vector and is equivalent to the columns of **U;** and **p** is the loadings vector equivalent to the rows of **V**.

Obviously, the above description of SVD and PCA applies also for the response vector **Y**. The decomposition of both the **X** and **Y** is called principal component regression

(PCR). The regression parameters between the scores vectors of **X** and **Y** determined in PCR allow the reduction in dimensionality described above. When we define **t** and **w** to be the scores vectors and **p** and **q** the loadings vectors associated with **X** and **Y**, respectively, the following regression equations are obtained:

$$\mathbf{t}\,\gamma = \mathbf{w} \qquad \text{(Eq. 8)}$$

where

$$\gamma = \mathbf{p}^T\mathbf{b}\mathbf{q}/(\mathbf{q}^T\mathbf{q}) \qquad \text{(Eq. 9)}$$

This description of X and Y by their scores vectors results in their representation by the basis set for the covariance of each matrix. While this regression solution addresses the linear projection problem, the current solution does not best capture the covariance between **X** and **Y**. PLSR accounts the maximization of the covariance capture between **X** and **Y** through a computational algorithm, described in more detail in the next section and section 3.2.8.

2.4.4. PLSR algorithm

This section is largely reiterated and modified from [50]. For clarity, we will first describe the implementation of PCA (or solution of SVD), which is performed via a computational technique called non-linear iterative partial least squares (NIPALS) algorithm. A principal component (PC) is calculated by [51]

1) equating vector $\mathbf{x_j}$ from **X** to $\mathbf{t_j}$
2) solving $\mathbf{p_j}^T = \mathbf{t_j}^T\mathbf{X}/(\mathbf{t_j}^T\mathbf{t_j})$
3) normalizing $\mathbf{p_j}^T$
4) solving for a new $\mathbf{t_j} = \mathbf{X}\,\mathbf{p_j}/(\mathbf{p_j}^T\mathbf{p_j})$
5) comparing $\mathbf{t_j}$ from step 2 and step 4 and repeat iteration if the difference is within a predetermined threshold.

Essentially, when combining steps 2 and 4, we result in the following eigenvalue problems:

$$\mathbf{t_j}\,(\mathbf{C\,I} - \mathbf{X\,X^T}) = 0 \qquad \text{(Eq. 10)}$$

$$\mathbf{p_j^T}(\mathbf{CI} - \mathbf{X^T X}) = 0 \qquad \text{(Eq. 11)}$$

where

$$\mathbf{C} = (\mathbf{p_j^T p_j})(\mathbf{t_j^T t_j}).$$

The PLSR NIPALS algorithm is described in [48] as follows:

1) define **w** as the first column of **Y**
2) Solve for $\mathbf{a} = \mathbf{X^T w} / (\mathbf{w^T w})$
3) Normalize **a**
4) Solve for $\mathbf{t} = \mathbf{X a}$
5) Solve for $\mathbf{c} = \mathbf{Y^T t} / (\mathbf{t^T t})$
6) Normalize **c**
7) Solve for $\mathbf{w} = \mathbf{Y c} / (\mathbf{c^T c})$
8) Compare **w** of step 7 to **w** of step 2. Repeat at step 2 if they are not equal.
9) Solve for $\mathbf{p} = \mathbf{X^T t} / (\mathbf{t^T t})$
10) Solve for $\mathbf{q} = \mathbf{Y^T w} / (\mathbf{w^T w})$
11) Perform the regression $\mathbf{Y} = \mathbf{w^T t} / (\mathbf{t^T t})$

The vectors **a** and **c** are the loadings associated with the variance-covariance matrices below, while **p** and **q** only relate directly to **X** and **Y** only:

$$\mathbf{w} \rightarrow \mathbf{Y\,Y^T\,X\,X^T}$$

$$\mathbf{c} \rightarrow \mathbf{Y^T\,X\,X^T\,Y}$$

$$\mathbf{t} \rightarrow \mathbf{X\,X^T\,Y\,Y^T}$$

$$\mathbf{a} \rightarrow \mathbf{X^T\,Y\,Y^T\,X}$$

2.5. References

1. Lauffenburger, D.A. and A.F. Horwitz, *Cell migration: a physically integrated molecular process.* Cell, 1996. **84**(3): p. 359-69.
2. Ridley, A.J., et al., *Cell migration: integrating signals from front to back.* Science, 2003. **302**(5651): p. 1704-9.

3. Pankov, R., et al., *A Rac switch regulates random versus directionally persistent cell migration.* J Cell Biol, 2005. **170**(5): p. 793-802.
4. Sabass, B., et al., *High resolution traction force microscopy based on experimental and computational advances.* Biophys J, 2008. **94**(1): p. 207-20.
5. Lo, C.M., et al., *Cell movement is guided by the rigidity of the substrate.* Biophys J, 2000. **79**(1): p. 144-52.
6. Peyton, S.R., et al., *The emergence of ECM mechanics and cytoskeletal tension as important regulators of cell function.* Cell Biochem Biophys, 2007. **47**(2): p. 300-20.
7. Zaman, M.H., et al., *Migration of tumor cells in 3D matrices is governed by matrix stiffness along with cell-matrix adhesion and proteolysis.* Proc Natl Acad Sci U S A, 2006. **103**(29): p. 10889-94.
8. Zaman, M.H., et al., *Computational model for cell migration in three-dimensional matrices.* Biophys J, 2005. **89**(2): p. 1389-97.
9. Dunn, G.A. and A.F. Brown, *A unified approach to analysing cell motility.* J Cell Sci Suppl, 1987. **8**: p. 81-102.
10. Mogilner, A., R. Wollman, and W.F. Marshall, *Quantitative modeling in cell biology: what is it good for?* Dev Cell, 2006. **11**(3): p. 279-87.
11. Chen, H.C., *Boyden chamber assay.* Methods Mol Biol, 2005. **294**: p. 15-22.
12. Liang, C.C., A.Y. Park, and J.L. Guan, *In vitro scratch assay: a convenient and inexpensive method for analysis of cell migration in vitro.* Nat Protoc, 2007. **2**(2): p. 329-33.
13. Maheshwari, G. and D.A. Lauffenburger, *Deconstructing (and reconstructing) cell migration.* Microsc Res Tech, 1998. **43**(5): p. 358-68.
14. Ferrer, J.M., et al., *Measuring molecular rupture forces between single actin filaments and actin-binding proteins.* Proc Natl Acad Sci U S A, 2008. **105**(27): p. 9221-6.
15. du Roure, O., et al., *Force mapping in epithelial cell migration.* Proc Natl Acad Sci U S A, 2005. **102**(7): p. 2390-5.
16. Janes, K.A. and M.B. Yaffe, *Data-driven modelling of signal-transduction networks.* Nat Rev Mol Cell Biol, 2006. **7**(11): p. 820-8.
17. Ideker, T., L.R. Winslow, and D.A. Lauffenburger, *Bioengineering and systems biology.* Ann Biomed Eng, 2006. **34**(7): p. 1226-33.
18. Bindschadler, M. and J.L. McGrath, *Sheet migration by wounded monolayers as an emergent property of single-cell dynamics.* J Cell Sci, 2007. **120**(Pt 5): p. 876-84.
19. Simpson, K.J., et al., *Identification of genes that regulate epithelial cell migration using an siRNA screening approach.* Nat Cell Biol, 2008.
20. Kumar, N., et al., *A high-throughput migration assay reveals HER2-mediated cell migration arising from increased directional persistence.* Biophys J, 2006. **91**(4): p. L32-4.
21. Wolf-Yadlin, A., et al., *Effects of HER2 overexpression on cell signaling networks governing proliferation and migration.* Mol Syst Biol, 2006. **2**: p. 54.
22. Wolf, K., et al., *Compensation mechanism in tumor cell migration: mesenchymal-amoeboid transition after blocking of pericellular proteolysis.* J Cell Biol, 2003. **160**(2): p. 267-77.
23. Harms, B.D., et al., *Directional persistence of EGF-induced cell migration is associated with stabilization of lamellipodial protrusions.* Biophys J, 2005. **88**(2): p. 1479-88.

24. Strack, R.L., et al., *A noncytotoxic DsRed variant for whole-cell labeling.* Nat Methods, 2008. **5**(11): p. 955-7.
25. Resch-Genger, U., et al., *Quantum dots versus organic dyes as fluorescent labels.* Nat Methods, 2008. **5**(9): p. 763-75.
26. Joslin, E.J., et al., *EGF-receptor-mediated mammary epithelial cell migration is driven by sustained ERK signaling from autocrine stimulation.* J Cell Sci, 2007. **120**(Pt 20): p. 3688-99.
27. Wolf, K., et al., *Multi-step pericellular proteolysis controls the transition from individual to collective cancer cell invasion.* Nat Cell Biol, 2007. **9**(8): p. 893-904.
28. Ewald, A.J., et al., *Collective epithelial migration and cell rearrangements drive mammary branching morphogenesis.* Dev Cell, 2008. **14**(4): p. 570-81.
29. Kumar, N., et al., *Multipathway model enables prediction of kinase inhibitor cross-talk effects on migration of Her2-overexpressing mammary epithelial cells.* Mol Pharmacol, 2008. **73**(6): p. 1668-78.
30. Burgess, B.T., J.L. Myles, and R.B. Dickinson, *Quantitative analysis of adhesion-mediated cell migration in three-dimensional gels of RGD-grafted collagen.* Ann Biomed Eng, 2000. **28**(1): p. 110-8.
31. Knight, M.M., et al., *Live cell imaging using confocal microscopy induces intracellular calcium transients and cell death.* Am J Physiol Cell Physiol, 2003. **284**(4): p. C1083-9.
32. Lutolf, M.P., et al., *Synthetic matrix metalloproteinase-sensitive hydrogels for the conduction of tissue regeneration: engineering cell-invasion characteristics.* Proc Natl Acad Sci U S A, 2003. **100**(9): p. 5413-8.
33. Friedl, P. 2008.
34. Dieterich, P., et al., *Anomalous dynamics of cell migration.* Proc Natl Acad Sci U S A, 2008. **105**(2): p. 459-63.
35. Demou, Z.N. and L.V. McIntire, *Fully automated three-dimensional tracking of cancer cells in collagen gels: determination of motility phenotypes at the cellular level.* Cancer Res, 2002. **62**(18): p. 5301-7.
36. Islam, M.A., *Einstein-Smoluchowski diffusion equation: A discussion.* Physica Scripta, 2004. **70**(2-3): p. 120-125.
37. Dunn, G.A., *Characterising a kinesis response: time averaged measures of cell speed and directional persistence.* Agents Actions Suppl, 1983. **12**: p. 14-33.
38. Alt, W. and G. Hoffmann, *Biological motion : proceedings of a workshop held in Königswinter, Germany, March 16-19, 1989*. Lecture notes in biomathematics ;. 1990, Berlin ; New York: Springer-Verlag. x, 604 p.
39. Othmer, H.G., S.R. Dunbar, and W. Alt, *Models of dispersal in biological systems.* J Math Biol, 1988. **26**(3): p. 263-98.
40. Uhlenbeck, G.E. and L.S. Ornstein, *On the theory of Brownian Motion.* Phys Rev, 1930. **36**: p. 823-41.
41. Dickinson, R.B. and R.T. Tranquillo, *Optimal Estimation of Cell-Movement Indexes from the Statistical-Analysis of Cell Tracking Data.* Aiche Journal, 1993. **39**(12): p. 1995-2010.
42. Friedl, P. and K. Wolf, *Tumour-cell invasion and migration: diversity and escape mechanisms.* Nat Rev Cancer, 2003. **3**(5): p. 362-74.

43. Kim, H.D., et al., *Epidermal growth factor-induced enhancement of glioblastoma cell migration in 3D arises from an intrinsic increase in speed but an extrinsic matrix- and proteolysis-dependent increase in persistence.* Mol Biol Cell, 2008. **19**(10): p. 4249-59.
44. Lodish, H.F., et al., *Molecular cell biology*. 5th ed. 2004, New York: W.H. Freeman and Company. 1 v. (various pagings).
45. Janes, K.A., et al., *A systems model of signaling identifies a molecular basis set for cytokine-induced apoptosis.* Science, 2005. **310**(5754): p. 1646-53.
46. Djoba Siawaya, J.F., et al., *An evaluation of commercial fluorescent bead-based luminex cytokine assays.* PLoS ONE, 2008. **3**(7): p. e2535.
47. Kumar, N., et al., *Modeling HER2 effects on cell behavior from mass spectrometry phosphotyrosine data.* PLoS Comput Biol, 2007. **3**(1): p. e4.
48. Hoskuldsson, A., *PLS Regression Methods.* J Chemometrics, 1988. **2**: p. 211-28.
49. Jolliffe, I.T., *Principal component analysis*. 2nd ed. Springer series in statistics. 2002, New York: Springer. xxix, 487 p.
50. Kumar, N., *A Computational and Experimental Study of HER2-Signaling Effects on Cellular migration and Proliferation*, in *Department of Chemical Engineering*. 2007, Massachusetts Institute of Technology: Cambridge, MA.
51. Geladi, P. and B. Kowalski, *Partial Least Squares Regression: A Tutorial.* Analytica Chimica Acta, 1986. **185**: p. 1-17.

CHAPTER 3

Cue-signal-response analysis of EGFR-mediated cell migration upon epithelial mesenchymal transition

In this chapter, systematic and quantitative analyses of signaling networks and novel 2D *in vitro* migratory phenotypes are combined with multivariate data-driven modeling to understand EGFR-mediated cell migration and to gain previously unidentified biological insights.

3.1. Introduction

Epithelial mesenchymal transition (EMT) is a cellular program allowing polarized, immotile epithelial cells, held by organized cell-cell junctions, convert to mesenchymal cells distinguished by their ability to migrate through extracellular matrices (ECMs) [1]. EMT was originally identified as a critical process in several stages of development, most notably in the formation of mesoderm from ectoderm and in the formation of neural crest during gastrulation [2, 3]. The changes in the cellular phenotype triggered by EMT is loosely defined as [4] (1) the changes in the morphology from a cobblestone-like collective of epithelial cells that maintain basement membrane-oriented apical-basal polarity to a spindle-shaped mesenchymal cells able to extend migratory protrusions, (2) the changes in gene expression and differentiation markers, from a cell-cell junction protein and cytokeratin signature to a profile of vimentin filaments, fibronectin, and integrins [5], (3) the changes in the migratory behavior from stationary, non-invasive epithelial cells to individual mesenchymal cells able to invade through extracellular matrices (ECMs) via the upregulation of ECM-degrading enzymes. Particularly, the ability to migrate and invade ECMs as individual cells is considered to be the most important characteristic of EMT and is of particular interest in this work.

More recently, EMT has been implicated in carcinoma progression where tumor cells must lose cell-cell adhesions, break away from the primary lesions, and acquire motility to disseminate as single cells for successful metastasis, the major cause of tumor fatalities [6]. While the critical role of EMT in carcinoma progression has intuitively been suggested for long, the lack of direct observation of the EMT process in primary human tumor samples *in vivo*, amongst many others, have contributed to the controversy of the role of EMT in carcinomas. Nevertheless, studies involving manipulation of E-cadherin-mediated cell-cell junctions and their effect on carcinoma progression and poor prognosis, as well as the correlation of EMT-inducing transcription factors with tumor invasion and metastasis, have more firmly established the potential role of EMT in tumor biology. Particularly, the partial loss of E-cadherin has been correlated with poor prognosis in various tumors; forced expression of E-cadherin in invasive carcinomas can impede their ability to invade and metastasize [7]. Moreover, the expression of Twist1, FOXC2, and Goosecoid – few of many transcription factors shown to induce EMT – have shown to be correlated with enhanced metastasis [8-10]. Thus, many recent publications have convincingly suggested the potential benefit of EMT markers and gene expression profiles as predictive signatures for carcinoma progression and metastasis [11, 12].

As described in chapter 1, the aberrant expression of the members of the ErbB receptor tyrosine kinase family and their associated ligand is also highly correlated with carcinoma progression, particularly with invasiveness and metastasis [13, 14]. Over-expression of the epidermal growth factor receptor (EGFR) is correlated with poor prognosis in many human cancers including non-small cell lung cancers, head and neck, pancreas, and breast cancers [15]. Activation of EGFR by its ligands, such as EGF, is known to regulate multiple biophysical processes involved in cell locomotion that require careful orchestration [16]. The key signaling pathways intimately involved in these biophysical processes are also often dysregulated in tumors and contribute to the enhancement of EGFR-mediated cell motility [17, 18]. However, the role of EGFR in regulating cell migration in the context of EMT is still unclear.

Due to the therapeutic potential of targeting EGFR, several small molecule or monoclonal antibody antagonists have been developed, however resulted in relatively low clinical success. Recent studies suggest that cells with low levels of epithelial markers and

high levels of mesenchymal protein expression display higher resistance against these inhibitors [11, 19]. Therefore, the decreased sensitivity of mesenchymal-like tumors to EGFR antagonists argues a potential role of EMT that is important for therapeutic targeting of EGFR [12]. It has been suggested that EMT bestows the cells the ability to bypass the EGFR dependency to activate the downstream signaling pathways necessary for tumor malignancy, such as PI3K, Ras, and MAPK pathways. Insulin-like growth factor-1 receptor (IGF-1R), fibroblast growth factor receptor (FGFR), and platelet-derived growth factor receptor (PDGFR) may play an increased role upon resistance to EGFR antagonists [19, 20].

Therefore, existing studies indicate a fundamental change in the EGFR signaling network upon EMT that requires detailed understanding for a more effective therapeutic targeting against tumor metastasis. This is further intrigued by the non-intuitive correlation between the roles of EGFR and EMT and their regulation of cell migration and invasiveness; namely, that the EMT is known to enhance cell motility, but renders cells less dependent on EGFR, whose activation is also known to regulate cell motility. While many growth factors and their activation are known to initiate and mediate the process of EMT [1, 4], the activation and processing of growth factor cues before and after EMT has not yet been investigated. In this study, we hypothesize that the signaling network, particularly the downstream pathways, are significantly rewired upon EMT. Specifically, upon processing the treatment of with EGF and other growth factor ligands, epithelial-like tumors confer a non-motile phenotype; the rewired signaling network of mesenchymal cells, however, is able to process the same cues to result in enhanced motility and invasion.

To investigate this hypothesis and understand the underlying signaling network rewiring, we utilized a recently established human mammary epithelial cell line model to represent the pre-EMT and post-EMT states. These cells (named HMLEs) were immortalized by introduction of genes encoding the SV40 large-T antigen, the telomerase catalytic subunit, and an H-Ras oncoprotein into primary human mammary epithelial cells [21]. In a recent study, HMLEs have been transduced with Twist1, which is known to induce EMT [8]. HMLEs expressing Twist have been shown to display mesenchymal morphology with loss of epithelial markers and gain of mesenchymal markers and have increased invasive potential over the control HMLEs.

Here, we employ these cells in a single cell and monolayer migration assay to show that surprisingly, both epithelial and mesenchymal cells inherently contain migratory potential. But active migration is displayed only in the preferred migratory context (epithelial cells as monolayers, and mesenchymal cells as single cells). Cell migration was not only EMT state-dependent but also growth factor-dependent as treatments with EGF, heregulin (HRG), IGF-1 (to activate EGFR, HER2, and IGF-1 receptor, respectively) displaying differential effects. We followed up with comprehensive signaling measurements of early activation upon growth factor treatments in these cell lines, which required a multivariate data-driven modeling approach due to the inherent heterogeneity of signaling profiles in the dataset. Partial least squares regression (PLSR) analysis identified signaling candidates that may play a more important role in the migration of either pre- and post-EMT states. Pharmacological inhibition of one of the EGFR downstream candidate, PKCδ, preliminarily validated the multivariate model by indicating that mesenchymal cells are more dependent on PKCδ than EGFR itself. These studies suggest a therapeutic potential for tailoring drug treatments to receptors and downstream targets according to the EMT marker profiles.

3.2. Materials and Methods

3.2.1. Reagents and antibodies

Bioplex phospho-bead-based ELISA kits against phospho-EGF receptor (pan-phospho-tyrosine), phospho-IGF-1 receptor (Tyr1131), phospho-Src (Tyr418), phospho-p38 (Thr180/Tyr182), phospho-Erk1/2 (Thr202/Tyr204, Thr185/Tyr187), phospho-HSP27 (Ser78), phospho-JNK (Thr183, Tyr185), phospho-Akt (Ser473), phospho-IRS-1 (Ser636/Ser639), phospho-GSK3α/β (Ser21/29) were purchased from Biorad Laboratories (Hercules, CA). Antibodies against phospho-PKCδ (Thr505), phospho-PLCγ (Tyr711), phospho-Met (Tyr1234/1235), phospho-Shc (Tyr239/240), phospho-β-catenin (Ser33/37, Tyr41), EGFR, IGF-1R, HER2, and GAPDH were purchased from Cell Signaling Technologies (Danvers, MA). The antibody against phospho-FAK (Tyr397) and phalloidin

were purchased from Invitrogen (Carlsbad, CA), and antibodies against E-cadherin, N-cadherin, and vimentin, as well as human recombinant insulin-like growth factor-1 were purchased from BD Biosciences (San Jose, CA). Human recombinant epidermal growth factor (EGF) and heregulin-β1 were purchased from Peprotech (Rocky Hill, NJ) and Sigma-Aldrich (St. Louis, MO), respectively. Rottlerin and AG1478 were purchased from Biomol (Plymouth Meeting, PA).

3.2.2. Cell culture

Immortalized human mammary epithelial cells (HMLEs) expressing either the empty control vector pBp or pBp-Twist (from herein referred to as Epithelial or Mesenchymal HMLEs) were obtained from Robert Weinberg's laboratory at the Whitehead Institute for Biomedical Research (Cambridge, MA). Cells were cultured in 50% Mammary Epithelial Basal Medium (MEBM; Lonza, Walkersville, MD), 25% Dulbecco's Modified Eagle Medium, and 25% Ham's F-12 media (Invitrogen, Carlsbad, CA) supplemented with a full MEGM SingleQuot containing bovine pituitary extract, EGF, insulin, hydrocortisone, and gentamycin & amphotericin-B (Lonza). Serum-free medium contained all of the components of the complete medium, except the bovine pituitary extract, EGF, and insulin.

3.2.3. Quantitative assessment of phosphorylation dynamics via Western Blotting and Bioplex Bead-based ELISA

Epithelial or Mesenchymal HMLEs were trypsinized, centrifuged and resuspended in fresh complete medium. Epithelial and Mesenchymal HMLEs were seeded in 6-well or 10 cm tissue culture plates, respectively, at a density of 60,000 cells/cm^2 or 6,000 cells/cm^2, respectively, in complete medium. Cells were grown overnight (approximately 16-18 hours) and serum-starved for 24 hours. Cells were stimulated either with 100 ng/ml EGF, 80 ng/ml HRG, or 100 ng/ml IGF-1 in serum-free media and washed with PBS after 5, 10, 30, or 60 minutes, and immediately lysed with the Bioplex lysis buffer (Biorad). Scraped lysates were clarified by centrifugation and protein concentration measured with a microplate BCA assay (Pierce Biotechnology; Rockford, IL). Lysates were aliquotted at equal protein concentrations and kept at -80°C.

For both Western blotting and Bioplex assays, assays were validated for its suitability for quantitation by assessing the linearity of the signal versus protein concentration curve (section 2.4.1). Lysates of both Epithelial and Mesenchymal cells stimulated with EGF and lysed after 5 minutes were serially diluted, and a curve relating assay signal of each phospho-site to protein concentration was generated (Figure 2-6 and data not shown). Some assays showed signal saturation at relatively low levels of protein (e.g. phospho-EGFR, phospho-Akt) while some assays required high amounts of protein for detectable signal (e.g. phospho-Src, phospho-p38, phospho-JNK). The lysate amount per well for the Bioplex assay and Western blotting were determined to be on the medium-high level of the linear range and were as follows: 20 μg per well for phospho-Src, phospho-p38, phospho-JNK; 5 μg for phospho-HSP27, phospho-IRS-1, phospho-GSK3α/β, phospho-Erk1/2, phospho-IGF1-R; 1 μg for phospho-Akt and phospho-EGFR. For Western blotting, 20 μg lysates were loaded per well of a 15-well gel. A stock lystate containing Epithelial cells treated with EGF or IGF-1 for 5 minutes served as a positive control for signal intensity comparison.

Manufacturer instructions were followed for the Bioplex assays. For Western blotting, lysates were boiled at 70°C for 10 minutes, loaded onto NuPage Novex Bis-Tris gels (Invitrogen) and transferred onto a nitrocellulose membrane. The membrane was blocked with Odyssey blocking buffer (Li-Cor Biosciences; Lincoln, NE) diluted with PBS and incubated with primary antibodies overnight at 4°C. GAPDH served as loading controls. Membranes were washed with PBS containing 0.1% Tween and incubated with Odyssey secondary antibodies conjugated to infrared dyes suited for imaging with the Odyssey imaging system (Li-Cor). Bands were quantified by densitometry using the Li-Cor Odyssey quantitation software. Signal density was normalized to the stock lysate controls loaded on each gel. All signaling data was eventually normalized to the 0 minute time point of Epithelial cells.

3.2.4. 2D cell migration assays

For fluorescent visualization and facilitated cell tracking, Epithelial and Mesenchymal cells were each incubated with 8 μM green-fluorescent CMFDA (Invitrogen) for 20 minutes and

washed twice with PBS before trypsinizing. For the sparse migration assay, labeled cells were seeded at 3,000 cells/cm^2 for both cell lines in 24-well tissue culture plates. For the monolayer migration assay, labeled cells and unlabeled cells were mixed at a 1:20 ratio and seeded at 60,000 cells/cm^2 for Epithelial cells and at 30,000 cells/cm^2 for Mesenchymal cells in 24-well tissue culture plates. This procedure creates a homogeneous monolayer with only a fraction of the cells labeled for facilitated cell tracking as described previously (section 2.3.1) [22, 23]. For both migration assays, cells were incubated overnight (16-18 hours) and serum-starved for 24 hours before growth factor stimulation. For inhibitor treatments, cells were pre-treated with either 0.1% DMSO or the inhibitor for 15 minutes before growth factor stimulation in the continued presence of the inhibitor.

Cells were placed on a Nikon TE2000 microscope (Nikon Instruments; Melville, NY) equipped with a Solent environmental chamber (Solent Scientific; Segensworth, United Kingdom) at 37°C and 5% CO_2. After 1 hour of growth factor stimulation, cells were imaged with a 4x DIC objective via brightfield and 488 nm excitation over 18 hours with 30 minute time intervals.

3.2.5. 3D collagen migration assay

As described previously [24], cells were mixed with pH-neutralized collagen I in serum-free medium (Inamed Biomaterials; Fremont, CA) at 500,000 cells/ml and 2.0 mg/ml final collagen concentration. The matrix-cell solution was placed on glass-bottom cell culture dishes (MatTek; Ashland, MA) and polymerized for 1 hour at 37ºC. The culture was immediately serum-starved for 24 hours and stimulated with 100 ng/ml EGF before imaging cells via brightfield microscopy at 10x magnification.

3.2.6. Quantitative cell migration analysis

Generated fluorescence movies were analyzed with Bitplane Imaris software (Zurich, Switzerland). Cells were tracked using the built-in 'Spots' function, which calculates the centroid of fluorescent objects. Cell tracks were generated using the 'Brownian Motion' algorithm and subsequently manually validated. Only cells that were in the imaging field for the complete 18 hours were initially taken into consideration, and only the last 12

hours were quantified, during which cell speeds exhibited steady-state levels (data not shown). For the sparse migration assays, only cells that did not exhibit physical contact with other cells were analyzed. Cells that did not exhibit movement were included in the analysis while cells that exhibited death, as assessed by release of green fluorescence, were not included in the analysis. Track coordinates were used in a custom-built Matlab code (section 2.3.4. and Appendix A) to deduce average cell speed for each cell by averaging the instantaneous cell speeds over the time interval.

3.2.7. Cell proliferation measurements

Epithelial and Mesenchymal cells were seeded in 6-well tissue culture plates at 50,000 cells per well and incubated overnight in complete medium. Cells were serum-starved for 24 hours and treated either with serum, 100 ng/ml EGF, 80 ng/ml HRG, or 100 ng/ml IGF-1 for 72 hours before trypsinizing and counting.

3.2.8. Immunofluorescence

Epithelial and Mesenchymal cells were seeded on glass coverslips at 60,000 or 30,000 cells/cm^2, respectively, in complete medium overnight and serum-starved for 24 hours. Cells were stimulated with EGF for 5 minutes before fixing with a PHEM fix solution (60 mM Pipes, 25 mM Hepes, 10 mM EGTA, 2 mM $MgSO_4$, pH 7.0) for 15 minutes. Cells were permeablized with 0.1% Triton-X for 3 minutes and blocked with a 10% BSA solution for 1 hour before treating them with primary, secondary antibodies, and phalloidin. Cells were imaged with the DeltaVision imaging system (Applied Precision; Issaquah, WA).

3.2.9. Partial Least Squares Regression Analysis

Detailed description of partial least squares regression (PLSR) analysis can be found in section 2.4. and elsewhere [25, 26]. Here, the PLSR model was generated using SIMCA-P 11.0 (Umetrics; Kinnelon, NJ) software package. Briefly, PLSR is used to solve the regression problem:

$$\mathbf{Y = Xb + e} \qquad \text{(Eq. 1)}$$

where **X** is a M x N rank deficient data matrix for M treatment conditions and N signaling metrics (e.g. phosphorylation of Erk1/2 at 5 min time point), **Y** is a M x P response matrix containing P unique response parameters. **b** is a M x 1 vector containing the regression coefficient and **e** is the residual. Here, M = 2 cell lines (Epithelial and Mesenchymal) x 4 growth factor treatments (serum-free, 100 ng/ml EGF, 80 ng/ml heregulin, 100 ng/ml IGF-1) = 8. **X** was populated by each column corresponding either the initial phosphorylation (T=0) or net phosphorylation over 60 minutes (Int) for each phosphosite. Hence, N = 2 metrics x 18 phosphosites = 36 columns. **Y** contained the cell speeds for monolayer migration in one column and for the sparse migration in the second column. To solve the regression problem, a non-iterative partial least squares (NIPALS) algorithm was used, the details of which are described in chapter 2. NIPALS algorithm decomposes a single M x N matrix into a sum of outer products as follows:

$$\mathbf{X} = \mathbf{t_1 p_1'} + \mathbf{t_2 p_2'} + \ldots + \mathbf{e} = \Sigma \mathbf{t_i p_i} + \mathbf{e} \qquad \text{(Eq. 2)}$$

Where $\mathbf{t_i}$ is the scores vector and $\mathbf{p_i}$ is the loadings vector representing the one-dimensional orthogonal basis set of the column and row spaces, respectively, in the principal components space. The algorithm is implemented to define two vectors, **w** and **c** such that the following is maximized:

$$[\mathrm{Cov}(\mathbf{t},\mathbf{u})]^2 = [\mathrm{Cov}(\mathbf{Xw},\mathbf{Yc})]^2 \qquad \text{(Eq. 3)}$$

where **t** and **u** are the scores vectors for **X** and **Y**, respectively. The loadings vectors for **X** and **Y** are called **p** and **q**, respectively, and are defined as

$$\mathbf{p} = \mathbf{X}^T\mathbf{t}/(\mathbf{t}^T\mathbf{t}) \text{ and } \mathbf{q} = \mathbf{Y}^T\mathbf{u}/(\mathbf{u}^T\mathbf{u}) \qquad \text{(Eq. 4)}$$

and the PLS regression vector **b'** is defined as

$$\mathbf{b'} = (\mathbf{u}^T\mathbf{t})/(\mathbf{t}^T\mathbf{t}) \qquad \text{(Eq. 5)}$$

As described previously [26], for the discriminant partial least squares (DPLSR) the following treatment vectors were created: Epithelial, Mesenchymal, EGF, HRG, and IGF. Depending on the treatments, the vectors were populated with 0s and 1s (e.g. for Mesenchymal EGF treatment, Epithelial = 0, Mesenchymal = 1, EGF = 1, HRG = 0, and IGF = 0) and were entered into SIMCA-P as Y-variables.

3.3. Results

3.3.1. Human mammary epithelial cell system exhibits an EMT-dependent single cell migration phenotype.

To identify the migration phenotype of cells prior to and subsequent to EMT, we utilized an immortalized human mammary epithelial cell line (HMLE) either expressing a control vector or a vector transcribing Twist, a transcription factor previously shown to induce EMT [8]. These cells expressed similar levels of EGFR and HER2, while the expression of IGF-1R was decreased significantly upon expression of Twist (Figure 3-1, A). For the assessment of the migratory phenotype of these two cell lines representing pre- and post-EMT states and referred to Epithelial and Mesenchymal cells hereafter, respectively, cells

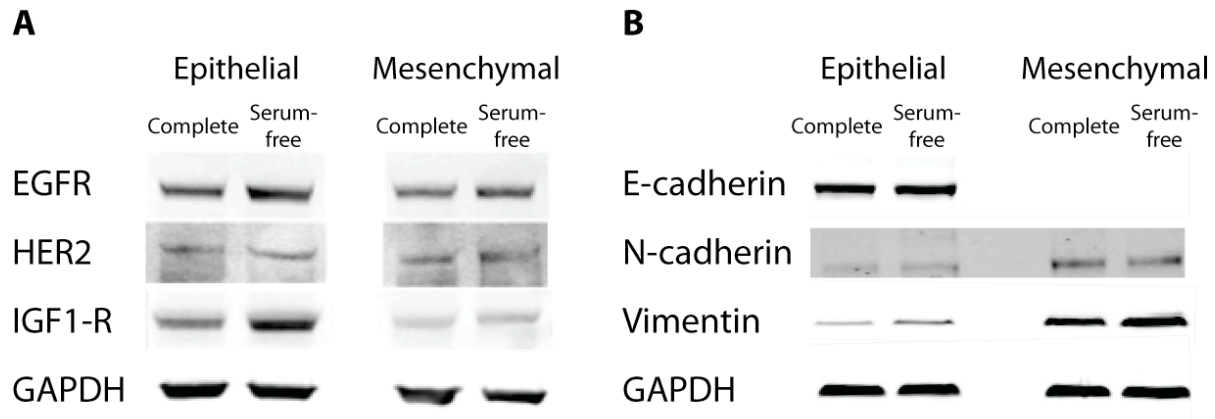

Figure 3-1 – Epithelial and Mesenchymal HMLEs display distinct receptor and EMT marker profiles. Western Blot for cell-surface receptors **(A)** and EMT markers **(B)** in Epithelial and Mesenchymal cells in complete medium or after serum-starvation for 24 hours. GAPDH was used as loading control.

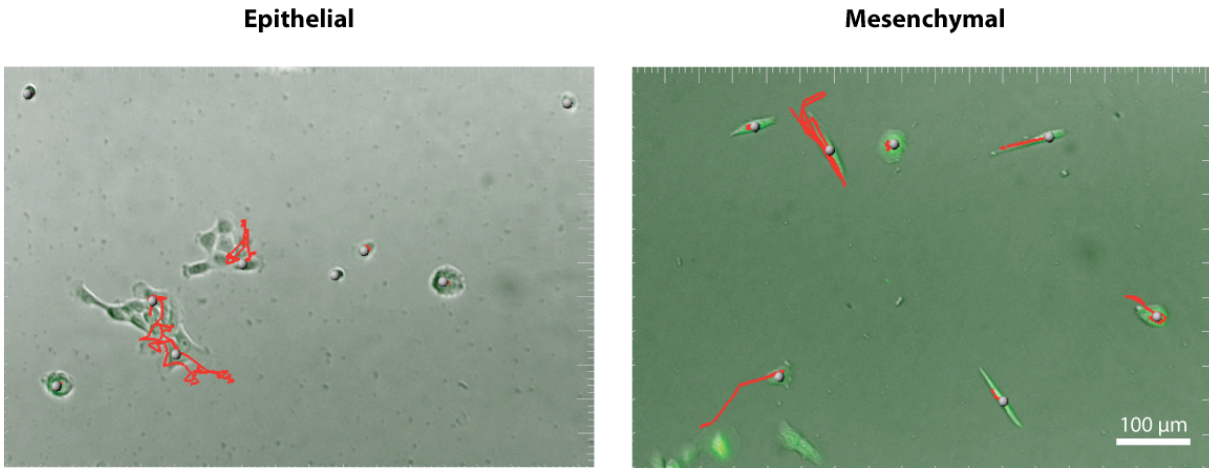

Figure 3-2 – Sparse cell migration assay reveals that HMLEs gain single cell migration potential upon EMT. CMFDA-labeled Epithelial (left) and Mesenchymal (right) cells were seeded sparsely, serum-starved for 24 hours, and stimulated with 100 ng/ml EGF. Cells were imaged 1 hour after stimulation and imaged for 18 hours using brightfield and fluorescence microscopy. Cell tracks (red) over 18 hours were generated after centroid calculation of fluorescent objects (grey spheres).

were seeded sparsely on tissue culture plastic and serum-starved. Although Mesenchymal underwent a slight morphological change upon serum-starvation, including a flatter morphology and the ability to form a monolayer when forced to confluency, serum-starvation did not significantly change the expression of E-cadherin as an epithelial marker, and N-cadherin and vimentin as mesenchymal markers, indicating that the EMT state was unaltered upon serum-starvation (Figure 3-1, B). When cells were then stimulated with saturating levels of EGF and imaged via time-lapse video microscopy (Figure 3-2), Mesenchymal cells exhibited significant movement as single cells over 18 hours while Epithelial cells that did not touch another cell during the full time of imaging tended to remain stationary.

This behavior was reproduced in a 3D cell migration assay where cells were sparsely embedded in a 3D collagen I matrix, serum-starved, and stimulated with EGF. Even more pronounced than in 2D assays, Mesenchymal cells exhibited high degree of invasive activity while Epithelial cells were not able to translocate within the 3D matrix (Figure 3-3). Hence, single cell migration and invasion behavior of the HMLEs in 2D and

3D, respectively, recapitulate the current understanding of EMT's role in enhancing migratory potential.

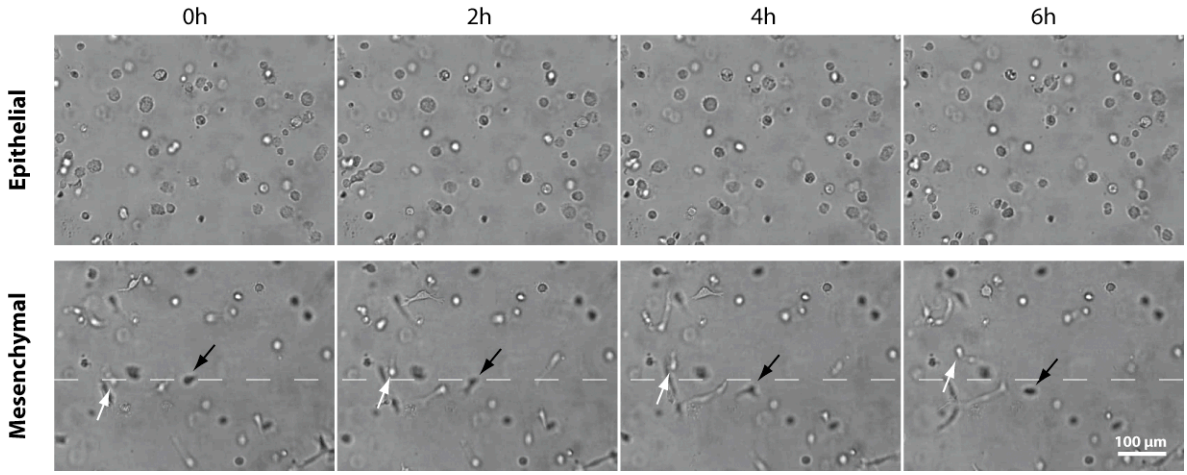

Figure 3-3 – EMT enables single cell invasion in 3D collagen I matrices. Epithelial (top) and Mesenchymal (bottom) HMLEs were sparsely embedded in collagen I matrices, serum-starved for 24 hours, and stimulated with 100 ng/ml. After 1 hour, cell movement was imaged for 6 hours via brightfield microscopy. Black and white arrows point to cells that moved from the dashed lines.

3.3.2. Collective migration is observed in Epithelial cells, not in Mesenchymal cells.

Interestingly, however, Epithelial cells that exhibited cell-cell contact at any time during the experiment exhibited significant movement. In particular, Epithelial cells that existed as islets, which was their preferred seeding state, exhibited a high degree of collective movement, whose displacements often surpassed the displacement of individual Mesenchymal cell migration (Figure 3-2, left).

To account for this phenomenon, we devised a second migration assay where both cell types were seeded confluently. Only a fraction of the cells were fluorescently labeled with a whole-cell dye for enhanced visualization of cell movement and subsequent quantitation. Since Mesenchymal cells were approximately twice the size of the Epithelial cells when attached to tissue culture plastic, twice as many Epithelial cells were seeded than Mesenchymal cells to achieve approximately similar confluency (data not shown). When cells were seeded, serum-starved, and stimulated with EGF, Epithelial cells displayed

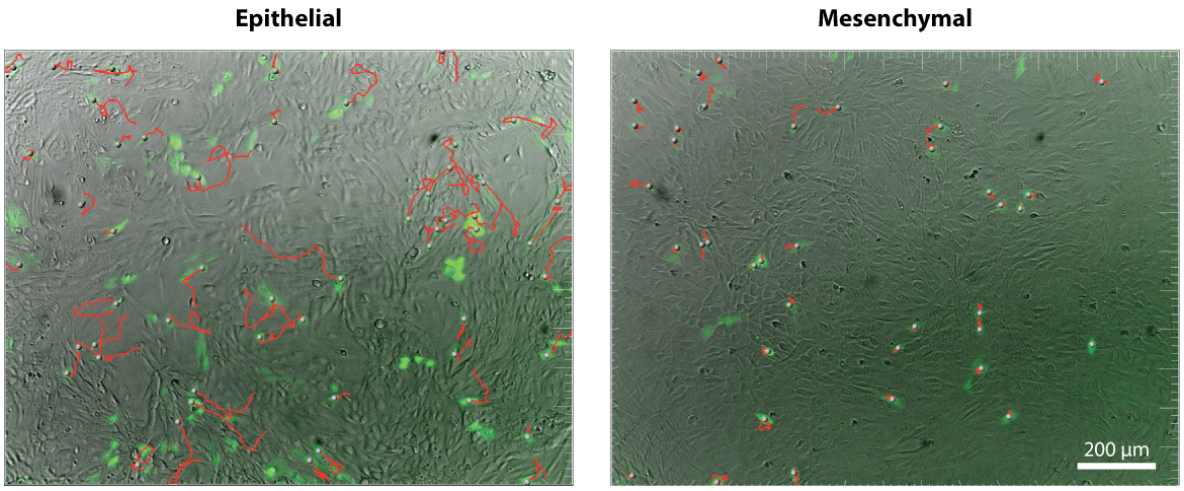

Figure 3-4 – Epithelial HMLEs prefer collective migration while Mesenchymal cells are immotile in a monolayer. Epithelial (left) and Mesenchymal (right) cells were seeded confluently, serum-starved for 24 hours, and stimulated with 100 ng/ml EGF. A fraction of cells were labeled with CMFDA. Cells were imaged 1 hour after stimulation and imaged for 18 hours using brightfield and fluorescence microscopy. Cell tracks (red) over 18 hours were generated after centroid calculation of fluorescent objects (grey spheres).

a great degree of collective cell movement within the monolayer while Mesenchymal cells did not move in a confluent monolayer (Figure 3-4). Although Epithelial collective movement eventually suspended with extremely over-confluent seeding densities, Epithelial cells were able to exhibit movement regardless of availability of cell-free space. Both Epithelial and Mesenchymal cells showed preference to migrate into cell-free spaces; Epithelial cells did so collectively, while only individual Mesenchymal cells preferred to migrate into free spaces (data not shown). This preferential collective movement by Epithelial cells was not an artifact of cells seeded on the tissue culture plastic, as cells exhibited similar behavior when seeded on a thin Matrigel layer intended to recapitulate the physiologically relevant basement membrane (data not shown).

Immunofluorescence for E-cadherin on both cell lines in a confluent monolayer showed that Epithelial cells maintained highly E-cadherin-rich cell-cell junctions, while Mesenchymal cells did not form E-cadherin-mediated cell-cell junctions (Figure 3-5). Hence, perhaps mediated by the maintenance of E-cadherin junctions, Epithelial cells were able to dynamically reorganize and migrate within the monolayer. The lack of such junctions may contribute to the lack of collective migration.

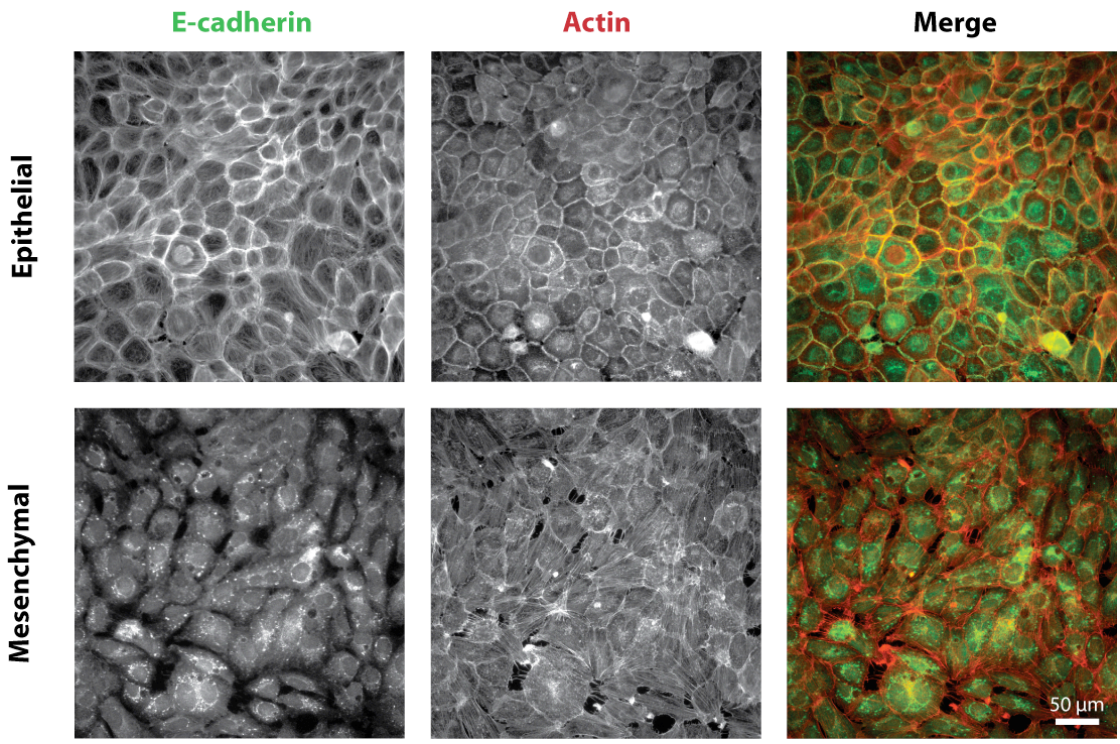

Figure 3-5 – Epithelial cells maintain E-cadherin junctions during collective migration while Mesenchymal cells lack them. Epithelial (top) or Mesenchymal (bottom) cells were seeded confluently on glass coverslips, serum-starved for 24 hours, stimulated with 100 ng/ml EGF, and fixed and stained for E-cadherin (left) and actin (middle).

In summary, using two types of migration assays, we were able to demonstrate that HMLEs are inherently migratory regardless of the EMT state. However, there were distinct migratory modes preferred by an EMT state: Mesenchymal cells demonstrated preference for sparse migration mode while they failed to exhibit migration in the monolayer migration assay. Epithelial cells, on the other hand, did not exhibit migration as single cells, but preferred to migrate in the collective mode. This collective movement is reminiscent of the recently observed 'non-invasive' movement of MCF-10A cells within an *in vitro* mammary acini Matrigel culture [27]. In conclusion, these two migratory modes captured by our assays were in agreement with our current understanding of physiologically relevant migratory behaviors before and after EMT.

3.3.3. Quantitative cell tracking reveals additional growth factor-dependent enhancement of cell speeds in each migratory mode.

The two migration assays in 2D have been performed with cells labeled with whole-cell dyes to facilitate cell tracking (all cells have been labeled in the sparse assay whereas only a fraction of cells have been labeled in the monolayer assay). After computer-assisted cell tracking, individual cell speeds were deduced from their tracks. Analysis of instantaneous cell speeds over the 18-hour imaging period indicated that cells reach steady-state after 6 hours of growth factor treatment (data not shown), particularly in the monolayer assay. Hence, only the cell tracks over the last 12 hours were quantified. For the sparse migration assay analysis, only cells were included that did not exhibit physical contact to another cell during the course of the experiment.

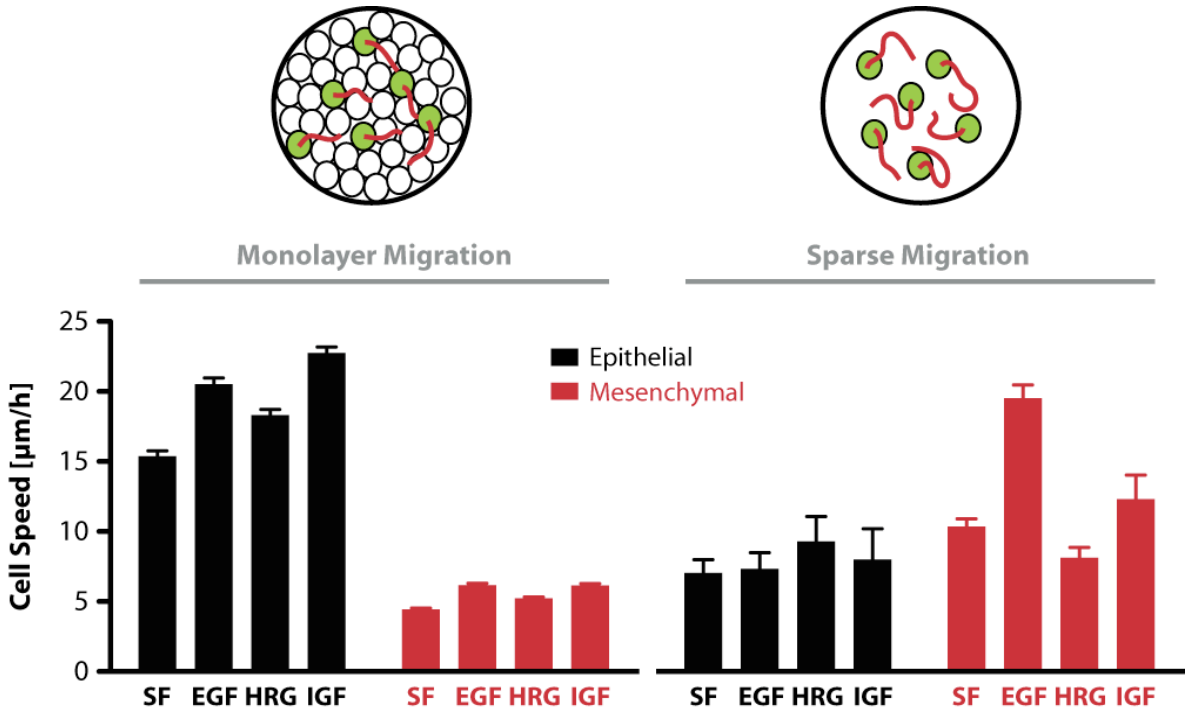

Figure 3-6 – Quantitative cell migration analysis displays growth factor- and EMT state-dependent cell speeds in monolayer and sparse migration modes. Fluorescent cells from images in Figures 3-2 (monolayer migration; left) and 3-4 (sparse migration; right) under EGF, heregulin (HRG), and IGF-1 treatments were tracked and their cell speeds calculated. Data shown as mean ± SEM.

To understand the effects of various growth factors on the two EMT state-dependent migratory modes via activation of similar EGFR downstream signaling pathways, we treated the cells either with no growth factor, saturating levels of EGF, HRG, or IGF-1 and quantified the cell speeds upon activation of the EGFR, HER2, or IGF-1R, respectively. As described above, Epithelial cells exhibited high cell speeds in the monolayer migration mode, even in the absence of growth factors at ~15 μm/h (Figure 3-6). EGF, HRG, and IGF-1 increased the cell speed by approximately 33%, 53%, and 20%, respectively. Mesenchymal cells exhibited very low levels of cell speeds (~5 μm/h) that were only insignificantly enhanced by growth factor treatment. In the sparse migration assay, both Epithelial and Mesenchymal cells showed small average cell speeds in the absence of growth factor or heregulin treatment (Figure 3-6). However, EGF treatment – and IGF-1 treatment to a certain extent – enhanced cell speeds only in Mesenchymal cells. Therefore, these results suggest that the degree of migration in both migratory modes is very growth factor- and EMT-dependent. As illustrated by the lack of Mesenchymal sparse migration upon HRG treatment, EMT causes the cells to respond differentially to growth factor treatments, which may be due to very differential activation in the signaling network.

3.3.4. Quantitative measurements of phosphorylation dynamics of EGF receptor downstream signaling pathways exhibit highly variable activation dynamics.

We hypothesized that the changes in EMT-mediated gene expression elicits a significant rewiring of the signaling network circuitry leading to the observed EMT-dependent migratory responses. However, while changes in overall expression of some proteins have been assessed in epithelial and mesenchymal tumors (e.g. PI3K, Akt [19]), a systematic network assessment of the changes in signaling activity due to EMT is still lacking. In particular, we sought to identify signals whose activation is associated with a particular EMT state and its corresponding migratory mode. To achieve this, we assessed the activation dynamics of 16 signals downstream of the EGF receptor upon growth factor treatment by measuring their phosphorylation levels (Figure 3-7). These 16 protein candidates have been chosen to include cell surface receptors and key intracellular nodes

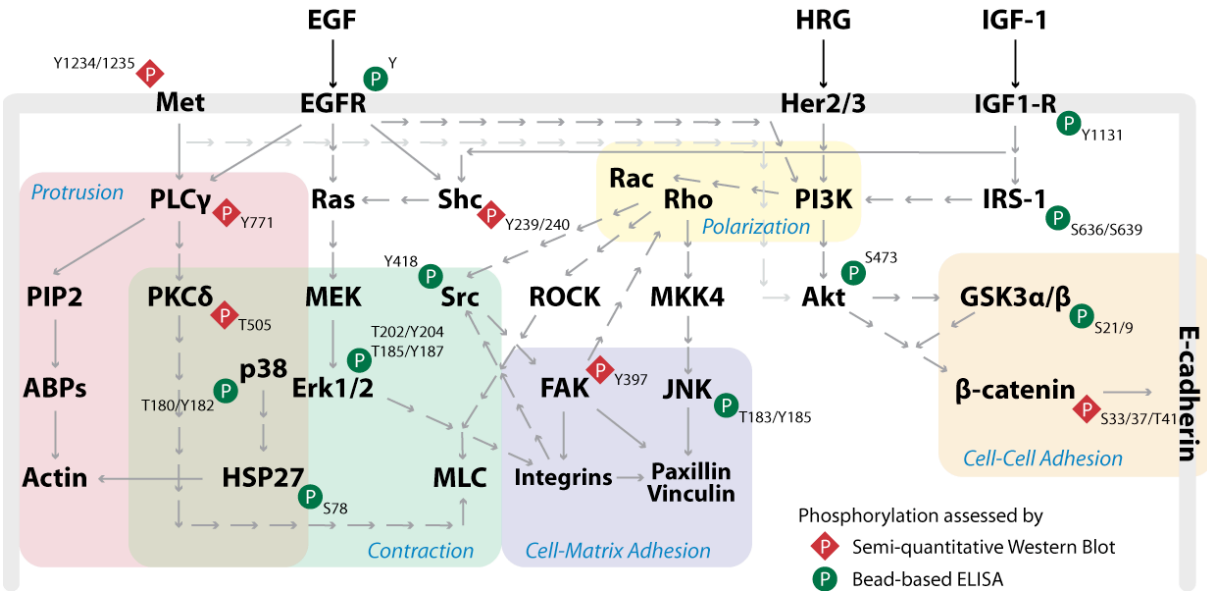

Figure 3-7 – Simplified schematic of the EGF receptor signaling network and candidates chosen for quantitative assessment. Method of quantitation and specific phospho-sites are listed next to the candidate.

associated with EGFR and are reported to be regulating various biophysical processes of cell migration in most cases [16, 17]. For example, as described in chapter 1, PLCγ has been implicated as an important switch for EGF receptor-mediated cell migration while FAK associates with focal adhesions and regulates the assembly and disassembly of adhesions. Erk has often been reported in regulating the overall migration process by its indirect interactions with integrins, Rho, as well as by its critical role in regulating proper rear release [16, 28]. On the other hand, candidates such as GSK3α/β or IRS-1 were less associated with migration. The availability of reagents for quantitative phosphorylation measurements also played a role in the choice of key intracellular regulators. Phosphorylation levels were measured via a quantitative bead-based ELISA or Western blotting after confirming each assay for its quantitative capability via validating the linearity of the assay (see sections 2.4.1. and 3.2.3.). Measured phospho-sites were previously reported to correlate with the activity of these proteins.

To assess whether the early activation profile of a signal upon growth factor treatment can provide correlative insights into the EMT state-dependent migratory behaviors, we lysed HMLEs at 0, 5, 10, 30, and 60 minutes after stimulation with saturating

levels of EGF, HRG, and IGF-1. Since the seeding conditions of these cells resulted in differential migratory behaviors, Epithelial cells were seeded in a confluent monolayer and Mesenchymal cells seeded sparsely to capture the more physiologically relevant migratory conditions for each cell line. The measurements of 18 phosphosites over 5 time points, 3 growth factor treatments and 2 cell lines, and 2-3 replicates yielded in a compendium of 1,250 measurements (Figure 3-8). Needless to say, the activation profiles and levels were highly variable across the individual signals but were also highly growth factor- and EMT state-dependent. Even initial phosphorylation levels were significantly different depending on the EMT state, with EGFR, Met receptor, Erk, Src, Shc, β-catenin, IRS-1, and p38 displaying significantly higher initial phosphorylation in Epithelial cells, but IGF-1R, Akt, GSK3α/β, PKCδ, PLCγ and JNK displaying higher levels in Mesenchymal cells. Despite the elevated expression of IGF-1R in Epithelial cells (Figure 3-1, A), the initial phosphorylation levels of IGF-1 receptor were slightly higher in Mesenchymal cells while IGF-1 stimulation eventually led to the expected higher activation in Epithelial cells (Figure 3-8). Also intriguing is that the EGFR activation was much greater in Epithelial cells (Figure 3-8) although the total EGF receptor levels were comparable, and cells were treated with same levels of EGF (Figure 3-1, A). This high activation of the EGFR may be required for co-activation of the Met receptor as its activation was only measured in EGF-treated Epithelial cells. Therefore, total receptor expression levels and their initial phosphorylation levels are not necessarily correlated in the context of EMT, and there are already receptor-level differences in activation between the EMT states and growth factor treatments.

Downstream signals display an even more heterogeneous response. While EGF-treatment induced simliar Shc phosphorylation peaks (for p66 and p52) regardless of the EMT state, activations of JNK, IRS-1, Src, HSP27, GSK3α/β, β-catenin, and p38 were cell type specific and corresponded with their initial phosphorylation levels (Figure 3-8). Activation of IRS-1, PKCδ, PLCγ, as well as EGFR canonical pathways Erk and Akt were more growth factor-dependent than EMT state-dependent. Hence, the first-pass observation of the key regulators across the EGF receptor pathway offers promising correlations, but it is unclear which signals most contribute to the differential, EMT state-dependent migratory responses. In fact, when evaluating the canonical EGF receptor pathways by observing

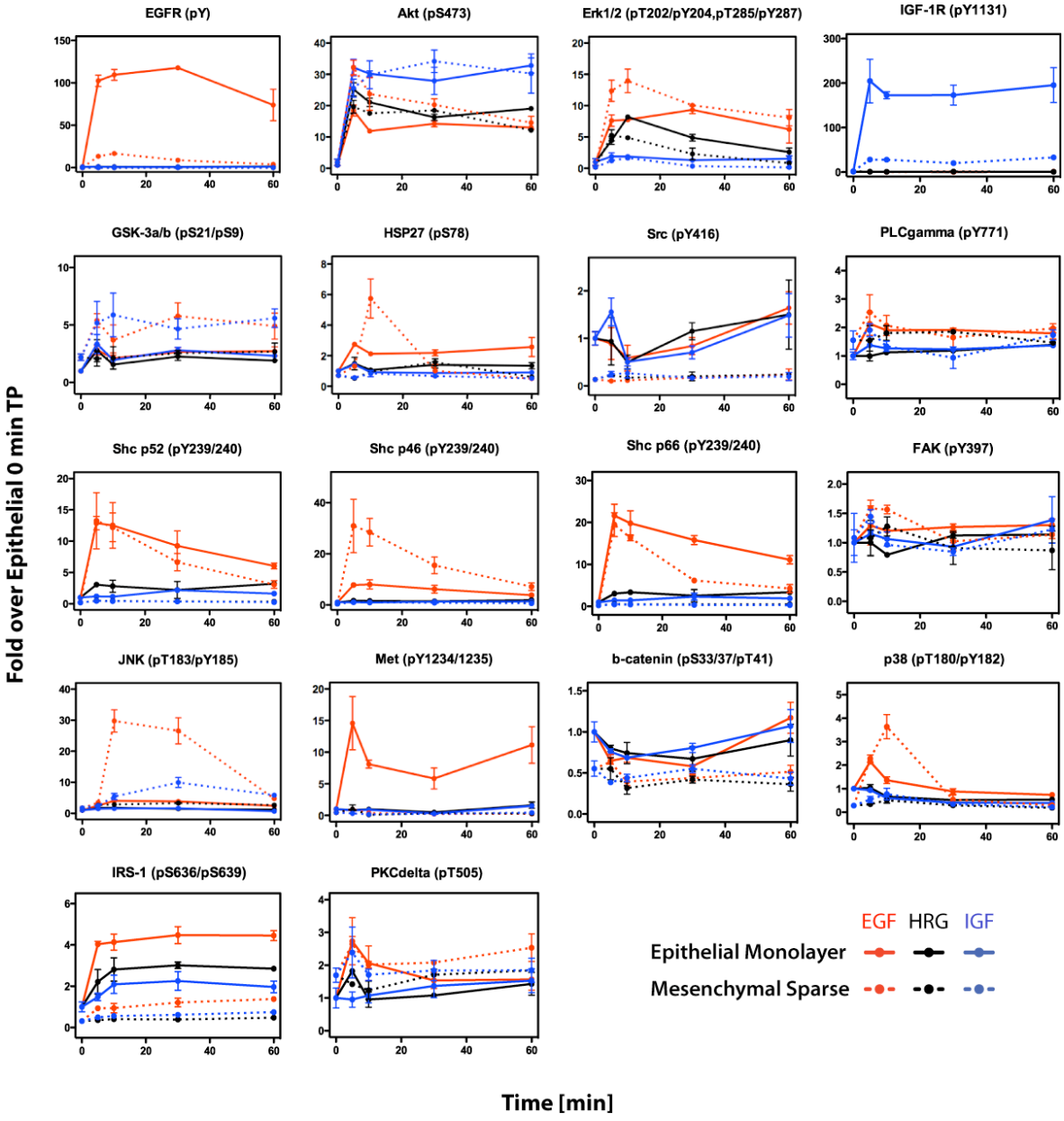

Figure 3-8 – Activation profiles of 18 phospho-sites of 16 proteins in the EGF receptor signaling network upon growth factor treatment, prior to and subsequent to EMT.
Epithelial (solid lines) and Mesenchymal (dashed lines) cells were lysed at indicated times after treatment with EGF, HRG, and IGF and subjected to either Western Blot or Bioplex bead-based ELISA analysis as indicated in Figure 3-7. Phosphorylation levels were normalized to the initial phosphorylation levels of Epithelial cells. Data shown as mean ± SEM.

the EGFR, Erk, and Akt phosphorylations alone – as often done when analyzing EGF receptor signaling – it is unclear how Erk and Akt transmit the high EGF receptor activation in Epithelial cells to result in high collective migration, since Erk activation was highest for EGF treatment and Akt activation demonstrated a large IGF-1-dependency in both cell types (Figure 3-8).

3.3.5. Multivariate computational analysis reveals robust signaling candidates important for Epithelial and Mesenchymal cell migration.

While we cannot effortlessly identify the important signals for a migratory mode, cells are able to integrate the activities of key regulatory nodes to generate a robust, EMT-dependent migratory response. We attempted to understand this cellular language by applying partial least squares regression (PLSR) to the signaling dataset to correlate the signaling activities to the migration speeds and to quantify the contribution of each key regulator to the migration speeds. As described in sections 2.4. and 3.2.9., PLSR calculates

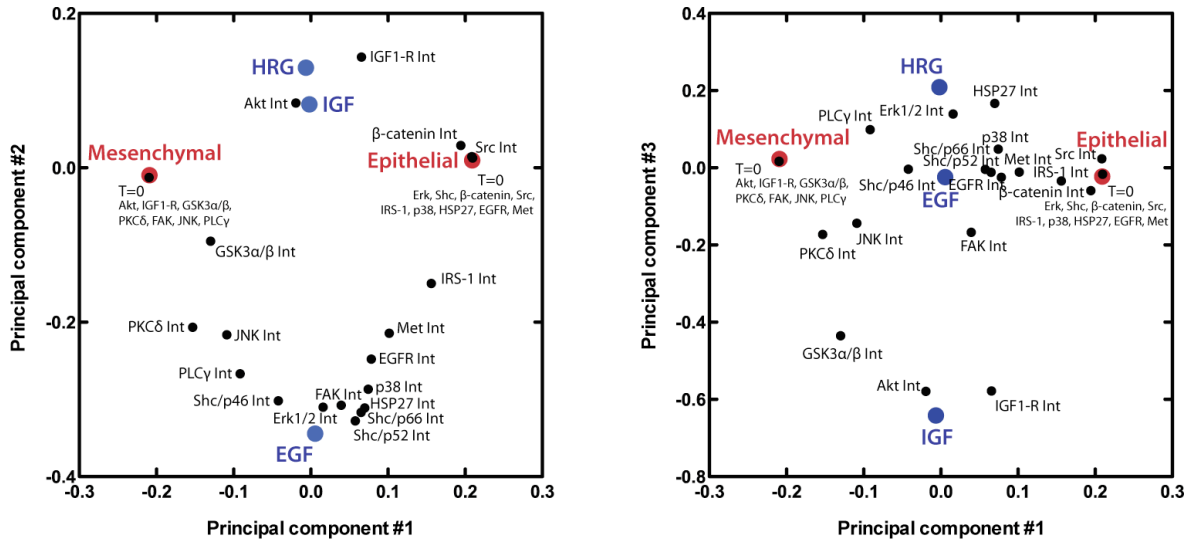

Figure 3-9 – DPLSR model relating signaling data to treatment conditions demonstrates PLSR's ability to separate multivariate signaling data according to their contributions to their treatments. First 3 PCs are depicted with PC 2 vs. PC 1 (left) and PC 3 vs. PC 1 (right). Signaling metrics included in the model were either the initial phosphorylations (T=0) or net activation (Int).

weighted linear combinations of the most informative subsets of signaling measurements by solving a matrix algebraic equation relating the signaling dataset (X-variables) obtained from all the experimental treatment conditions to the corresponding migration dataset (Y-variables) [25]. While performing this calculation, one ideally attempts to reduce the dimensionality of the multidimensional signaling dataset by identifying a lower dimensional, so-called principal component (PC) space in which most of the variance existent in the dataset is captured. This algorithm is performed such that the first PC captures the most informative co-variation existent in the dataset, the second PC the next most informative co-variation, etc. Important signals can then be identified when their coordinates on the PC axes co-vary with the coordinates of the response dataset. While the particular algorithm of PLSR applied here attempts to optimize for the predictability of migration speeds given these signaling measurements, we will focus the following report only on the identification of important signals that co-vary in the PC space.

As a proof of concept, we applied a slightly modified version of PLSR – discriminant PLSR (DPLSR) – to correlate the signaling dataset to a *de novo* treatment dataset (instead of the migration dataset). Here, Epithelial, Mesenchymal, EGF, HRG, and IGF matrices were populated according to our *a priori* treatment knowledge (see section 3.2.9.). In this model, DPLSR algorithm reduced the dimensionality of the signaling dataset by projecting the dataset onto a three-dimensional PC space. This 3-component model captures 80.6% of the variance existent in the data. Figure 3-9 shows the mapping of the loadings, or contributions, of measured signals and the treatments onto the principal component space. The loadings plots demonstrate that DPLSR is able to clearly separate the Epithelial and Mesenchymal cell lines (red) along PC 1 and the growth factor treatments (blue) along PC 2 and 3 while identifying the contributions of the signaling metrics – either the initial phosphorylation levels (T=0) or the net activation over 60 minutes (Int) – to the treatments. Depending on the magnitude of the initial phosphorylation, T=0 metrics were separated along PC 1 either to Epithelial and Mesenchymal cell lines. Most of the net activation signal metrics co-varied highly with EGF stimulation, presumably because our selection of key regulatory nodes were highly biased towards EGFR signaling. Moreover, signals were separated along PC 1 indicating their importance for the respective cell lines. Hence, this model is able to visually organize the contributions of the various signaling

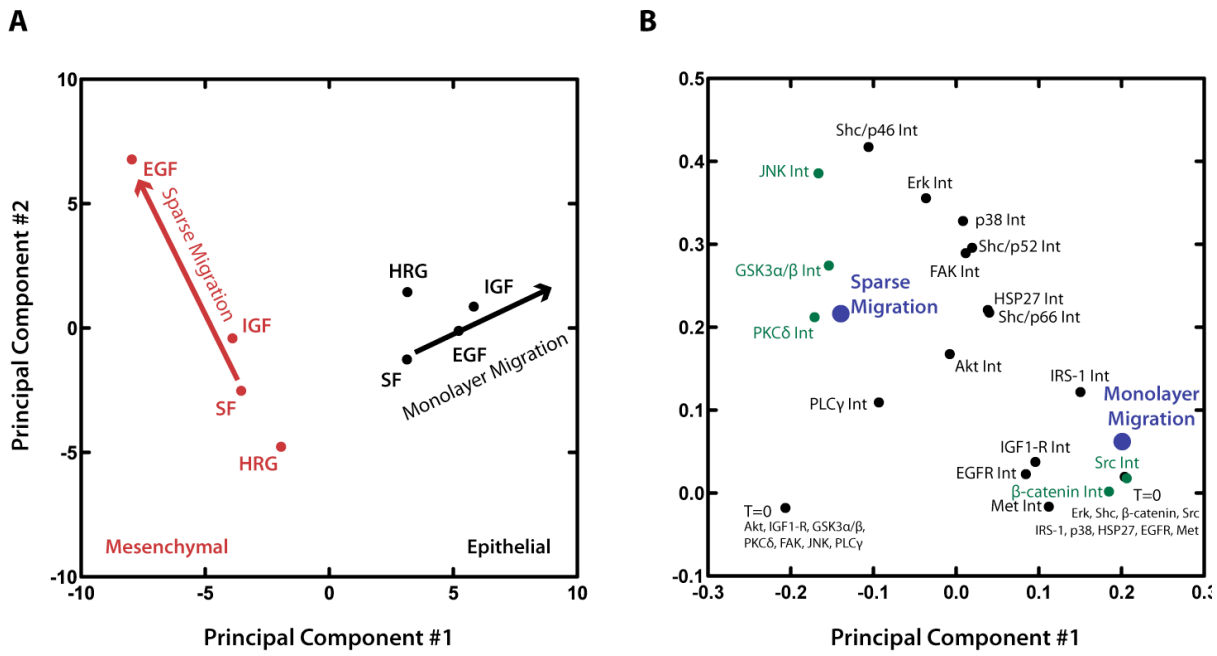

Figure 3-10 – PLSR migration model separates the EMT-dependent migration modes and identifies signaling candidates associated with them. Scores **(A)** and loadings **(B)** plots of the 2-component PLSR model with initial phosphorylation levels (T=0) and net activation (Int) as X variables and monolayer and sparse migration speeds as Y-variables. Red and black dots indicate Mesenchymal and Epithelial observations, respectively (A). Blue dots are response loadings, and green dots are most co-varying signaling metrics with the responses (B).

activities according to the growth factor stimulations and EMT-state. However, it did not take into account the EMT-state migration responses upon various growth factor treatments.

Hence, we generated the main PLSR model relating the signaling dataset to the migration responses by entering monolayer and sparse migration speeds as separate Y-variables. The resultant model is a 2-component PLSR model capturing 85% of the dataset variance. The contributions of each treatment conditions to the PC space are indicated by the scores plot (Figure 3-10, A). The mapping of the scores indicate that, again, the responses of the Epithelial and Mesenchymal cell lines are separated along PC 1 whereas the contributions of growth factor treatments are mapped along PC 2. When manually drawing vectors depicting increasing migration speeds, these 'response' vectors have orthogonal properties to each other indicating that this PLSR model appropriately separates the two migratory modes. The loadings plot (Figure 3-10, B) displays the

contributions of the signals and responses to the PC space. The sparse migration and monolayer migration responses (blue) are mapped according to their contributions in the scores plot. The signaling metrics (black and green) – initial phosphorylation (T=0) and net activation (Int) – are mapped according to their contributions, and their proximity to the responses indicates their co-variation with the responses. Highlighted in green are the signals that consistently co-vary most strongly with the respective migration responses. PKCδ, GSK3α/β, and JNK highly co-vary with the sparse migration response, while β-catenin and surprisingly, Src highly are identified to be co-varying with the monolayer migration response. This PLSR model therefore suggested candidates that are potentially more important and contributing to the respective EMT state-dependent migratory modes – a task that would have been difficult to identify by simply surveying the signaling data.

3.3.6. Cell proliferation is an Epithelial response and co-varies with monolayer migration.

In tumor progression, EMT is thought to increase the migratory potential, but also decrease the proliferative potential [1]. The current model suggests that only after the reverse Mesenchymal-Epithelial Transition, cells regain the potential to proliferate, in accordance with the existing antagonistic relationship between proliferation and cell migration. To at least preliminarily investigate this facet, we measured cell proliferation by cell counting after 72 hours (Figure 3-11, A). Cell counts were consistently higher for Epithelial cells with EGF increasing cell counts in both cell lines. However, HRG and IGF-1 stimulation only increased proliferation of Epithelial cells; IGF-1 was the major stimulatory factor.

When cell proliferation was added as a third Y-variable to the PLSR model, the 2-dimensional model captured only 70% of the variance existent in the dataset indicating that the measured signaling metrics could not adequately explain the proliferation behavior. This conclusion was reiterated by the non-orthogonal vectors in the scores plot – although they may have been caused by the inadequate visualization of 3 responses by a 2-dimensional model (Figure 3-11, B and C). Nevertheless, the proliferation vector was almost co-linear to the monolayer migration vector indicating that proliferation is indeed an Epithelial response – reiterated by the proximity of the proliferation loadings to the

monolayer migration loadings; this finding is in accordance with our understanding of the role of EMT in regulating proliferation. When proliferation response was entered as the only Y-variable in a new PLSR model, not many signaling metrics co-varied with the response suggesting that our biased selection of the key regulators were not proliferation-associated (data not shown). We therefore concluded that our compendium of signaling dataset was insufficient to describe cell proliferation, when added to migration responses.

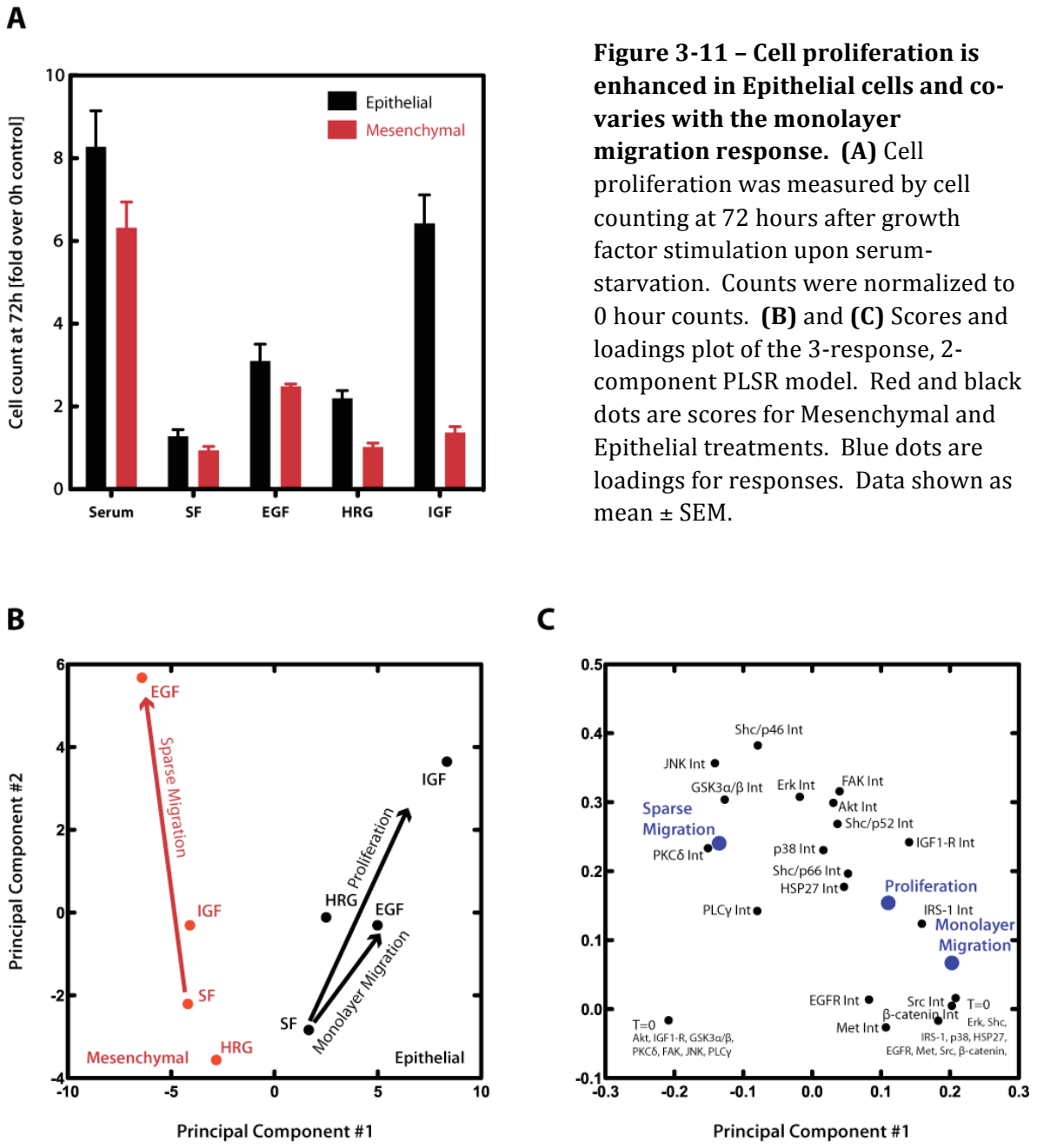

Figure 3-11 – Cell proliferation is enhanced in Epithelial cells and co-varies with the monolayer migration response. **(A)** Cell proliferation was measured by cell counting at 72 hours after growth factor stimulation upon serum-starvation. Counts were normalized to 0 hour counts. **(B)** and **(C)** Scores and loadings plot of the 3-response, 2-component PLSR model. Red and black dots are scores for Mesenchymal and Epithelial treatments. Blue dots are loadings for responses. Data shown as mean ± SEM.

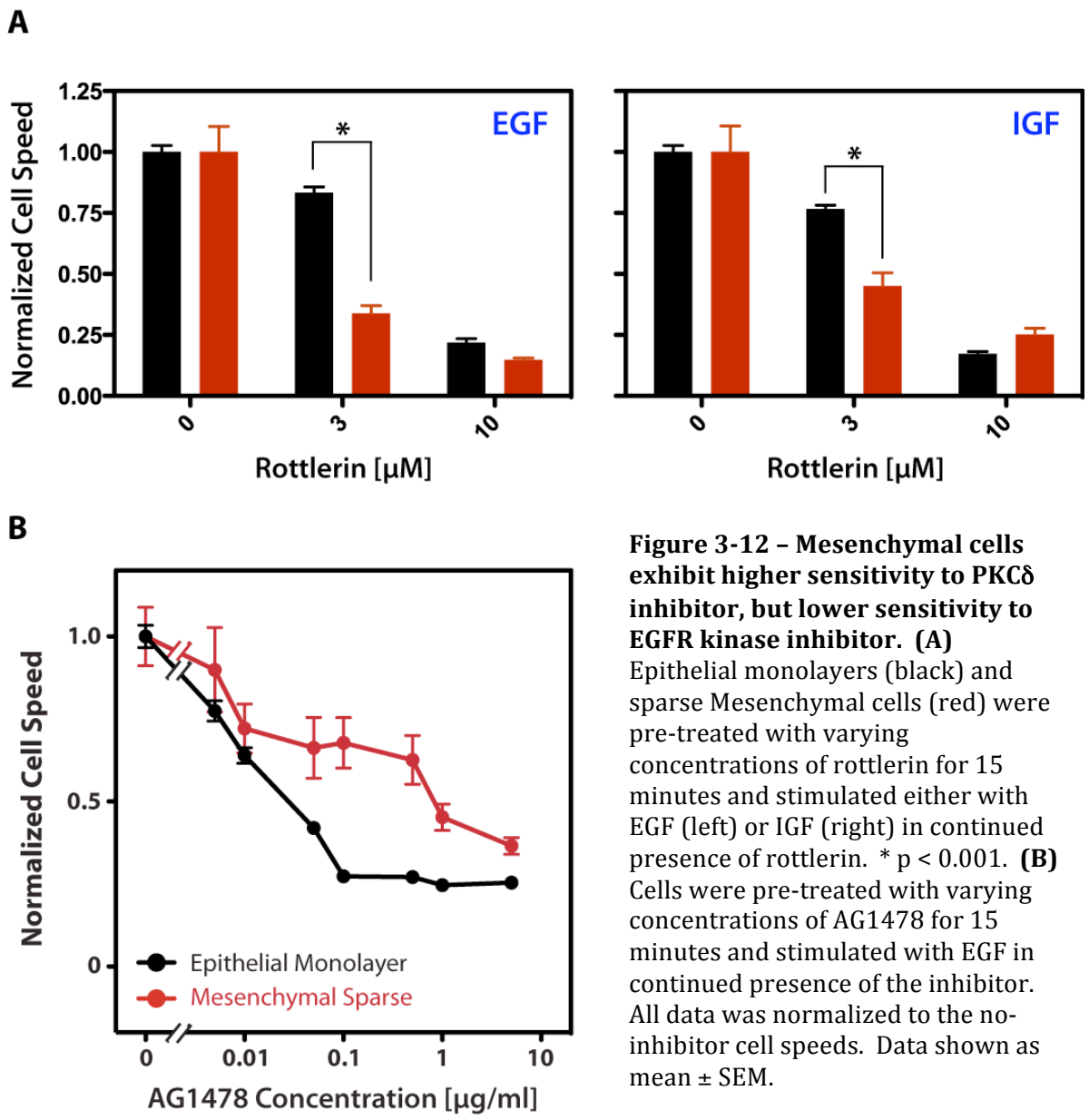

Figure 3-12 – Mesenchymal cells exhibit higher sensitivity to PKCδ inhibitor, but lower sensitivity to EGFR kinase inhibitor. (A) Epithelial monolayers (black) and sparse Mesenchymal cells (red) were pre-treated with varying concentrations of rottlerin for 15 minutes and stimulated either with EGF (left) or IGF (right) in continued presence of rottlerin. * $p < 0.001$. **(B)** Cells were pre-treated with varying concentrations of AG1478 for 15 minutes and stimulated with EGF in continued presence of the inhibitor. All data was normalized to the no-inhibitor cell speeds. Data shown as mean ± SEM.

3.3.7. Mesenchymal single cell migration displays greater dependency on PKCδ while Epithelial cells are highly dependent on EGFR.

To assess whether the candidates identified in the migration PLSR model did play a more important role in the EMT state-dependent migratory mode, we attempted to target the candidates with known pharmacological inhibitors. Of the identified candidates, we targeted PKCδ as the most interesting candidate to regulate Mesenchymal single cell

migration due to its intimate involvement in EGFR-mediated generation of acto-myosin contractility. PKCδ is downstream of the PLCγ pathway – which incidentally was also co-varying with Mesenchymal single cell migration – and is known to mediate phosphorylation of myosin light chains [29]. Epithelial and Mesenchymal cells were treated with 3 μM or 10 μM of rottlerin, a known pharmacological inhibitor against PKCδ, during stimulation with either EGF or IGF-1. Their monolayer or single cell migration speeds, respectively, were then measured during the first 12 hours of imaging (Figure 3-12, A). At 10 μM rottlerin, both Epithelial monolayer migration and Mesenchymal single cell migration was inhibited, but at a 3 μM rottlerin, only Mesenchymal single cell migration was drastically reduced to about 30% of the full migration speed while Epithelial cells retained 80% of their migration speeds. Hence, Mesenchymal cells displayed an increased sensitivity towards rottlerin and may therefore display a higher dependence on PKCδ consistent with the model predictions.

As alluded to in the introduction, it has been reported that epithelial tumors display higher sensitivity to EGFR kinase inhibitor treatments [12]. This phenomenon has not yet been confirmed *in vitro* in the context of cell migration. To assess the sensitivity of pre- and post-EMT HMLEs to an EGFR kinase inhibitor, cells were treated with varying concentrations of AG1478, a generic EGFR kinase inhibitor, and their respective migration speeds measured (Figure 3-12, B). As expected, Epithelial cells were highly affected by AG1478, with their speed reducing to the minimum of 30% at 0.1 μg/ml. Mesenchymal cells retained more than 60% of their cell speed at the same AG1478 level. These results suggest that Epithelial monolayer migration is highly dependent on the EGFR kinase activity; upon EMT, cells undergo appropriate transformations reducing their dependence on EGFR and amplifying their dependence on a downstream target, PKCδ, while gaining the ability to migrate invasively as single cells.

3.4. Discussion

Epithelial Mesenchymal Transition (EMT) has gained major attention as a critical process in the progression of carcinomas. While questions regarding the molecular processes of

the transition – which extracellular cues and gene expression changes mediated by these cues are involved in EMT – are being extensively addressed [4] and there is a general understanding of how properties of epithelial and mesenchymal tumors can be exploited for therapeutic purposes [12], a systematic assessment of the changes in the migratory phenotype and in the signaling network caused by these gene expression changes is still lacking. For this purpose, we employed two genetically identical cell lines representing the pre-EMT (Epithelial) and the post-EMT (Mesenchymal) states, where the EMT-like changes in the signaling network has been solely introduced by the expression of Twist [8]. Controlled experiments using these cell lines revealed intriguing and surprising migration behaviors. Epithelial and Mesenchymal cells display drastically opposite behaviors when seeded sparsely or in a confluent monolayer; namely that Mesenchymal cells only reveal their migratory potential as single cells whereas Epithelial cells disclose their migratory potential as a collective.

Collective migration has been observed previously in various settings and has been known to occur for various cell types *in vivo* and *in vitro*, most notably in development of model organisms and collective invasion of tumors [3, 30]. Very recently, during mammary branching morphogenesis, primary epithelial cells have been observed to migrate collectively in elongating mammary ducts into epithelial sheets in a 3D Matrigel culture upon treatment with FGF2 [31]. It was confirmed that these cells did not lose their epithelial characteristics, as assessed by consistent localization of E-cadherin and β-catenin to the cell-cell junctions. Interestingly, these cells also lacked in distinct cellular protrusions during migration, similiarly to our movies, perhaps suggesting a distinct mode of migration from the well-known fibroblast-like migration. More relevant to the context of our study, immortalized MCF-10A cells within in a Matrigel mammary acini culture displayed Erk1/2-dependent motile behavior without actually invading the surrounding Matrigel [27]. Individual cell movements were not correlated nor sheet-like indicating that cells migrated as autonomous units. We were able to observe similar non-correlated migration behavior in our monolayer assay although migration into free space required physical contact to neighboring cells causing them to be 'pulled' with the leading front. The phenomenon of monolayer migration was not an artifact of cells not being exposed to the

biochemical cues of the basement membrane since cells on Matrigel-layered surfaces exhibited the same behavior (data not shown). Interestingly, however, cells seeded on a thick Matrigel layer – presumably with a drastically lower stiffness – cells did not form a homogeneous monolayer, but a multicellular, string-like structure that did not seem to strongly adhere to the Matrigel surface (data not shown). Hence, substrate stiffness plays a large role in the organization of these cells as well. Nevertheless, although the 2-dimensionality of our assays did provide some artificial aspects, we captured the inherently migratory propensity to migrate – preferably as a collective – of cells of epithelial nature. But there is still a need for 3D in vitro models for the complete understanding of EMT-dependent morphology and dynamic organization.

On the other hand, the lack of collective migration behavior in mesenchymal cells or a loss of collective migration potential in general upon a transformation has not yet been observed, to the best of our knowledge. Particularly upon serum-starvation, Mesenchymal HMLEs inclined to increase the area covered by the cell and establish physical contact to the neighboring cell. However, this physical contact seemed to lack E-cadherin mediated junctions (Figure 3-5). Therefore, we surmise that the inability to form dynamic contacts may be impeding for dynamic reorganization within a monolayer. This was also supported by lower β-catenin phosphorylation in Mesenchymal cells (Figure 3-8), which is known to be involved in cadherin-junction disassembly and reassembly [32].

It was our initial goal to gain insight into the rewiring of the signaling network upon EMT, which effected the differential migratory behaviors. We have performed a biased signaling analysis by measuring the early activation profiles of candidates in the EGFR signaling network involved in migratory processes, which has previously not been performed. Here (Figure 3-7), we concentrated on (1) the classical EGFR migration pathways of Shc-Ras-Erk pathway necessary for overall cell migration [16], (2) the PLCγ-PKCδ pathways implicated in proper cell polarization and acto-myosin contractility [29], (3) the receptor-level cross-talk of EGFR and c-Met [33], (4) MAPK pathways subtly implicated in actin cytoskeletal processes including JNK and p38, the latter leading to activation of HSP27 [34], (5) classical migration pathways of FAK and Src, and (6) the IGF-1R related pathways including IRS-1, and lastly (7) the Akt related pathways including

GSK3α/β and β-catenin with the latter involved in degradation of E-cadherin [32]. This comprehensive analysis of the activation profiles revealed the vigorous, EMT state- and growth factor-dependent variations of signals, some intuitive and some surprising, and revealed a need for multivariate analysis clarifying the dense cellular terminology. For example, as previously mentioned Erk and Akt activations were similar in both cell lines although cells showed differential migratory behaviors. Interestingly, HRG treatments activated various signaling pathways, including Akt, Erk, and β-catenin, in both cell lines, but HRG treatments elicited a stimulatory effect on migration only in epithelial cells.

Nevertheless, the application of PLSR identified a set of candidates that most strongly co-varied with the migratory responses. Phosphorylations of β-catenin and Src have been identified to potentially play an increased role in Epithelial monolayer migration. β-catenin is known to form complexes with E-cadherin critical for cadherin-based cell-cell adhesions [32]. Phosphorylation at the Ser33/37/Tyr41 site is mediated by GSK3α/β and initiates β-catenin degradation when unassociated with E-cadherin. This degradation may cause dissociation of E-cadherin cell-cell adhesions to confer a more dynamic reorganization of cells within the monolayer. However, interestingly, GSK3α/β activity is highly correlated with Mesenchymal sparse migration in our model indicating that GSK3α/β activity may not be fully correlated with β-catenin phosphorylation. Nevertheless, correlation of β-catenin to Epithelial monolayer migration did not surprise us, and the lack of simple molecular interventions for β-catenin impeded us to further pursue this candidate.

The Src family of non-receptor tyrosine kinases is involved in many processes important to cell migration including a high-level of crosstalk with receptor tyrosine kinases as well as intimate involvement with actin dynamics and integrin-mediated adhesion pathways [35]. However, Src is also critical for cell proliferation and survival rendering its role in EMT state-dependent migration difficult. In particular, the application of available pharmacological inhibitors renders both cell lines non-migratory (data not shown), perhaps enhanced by their promiscuous nature. Hence, we concentrated on the candidates correlating with Mesenchymal sparse migration.

Currently available literature does not identify GSK3α/β and JNK as important proteins regulating cell migration. Therefore, we prioritized the assessment of PKCδ as an attempt to validate the insights provided by the PLSR model. PKCδ is downstream of the PLCγ pathway, which has also been identified to co-vary strongly with Mesenchymal cells, and is required for EGFR-mediated contractile force generation necessary for cell migration. Preliminary inhibition of PKCδ via application of its available pharmacological inhibitor, rottlerin, indicated that Mesenchymal cells are more sensitive to rottlerin than Epithelial cells in the context of their migration behaviors (Figure 3-12, A). Although this observation is very promising for our conclusions, recent reports place doubts about the use of rottlerin as a specific inhibitor [36]. However, interestingly rottlerin has rendered PKCδ specific inhibitory effects in many publications that also used RNAi approaches against PKCδ. Hence, here we provide caution that our results show promise but need more rigorous validation using either RNAi or dominant-negative constructs. Also interesting is that rottlerin has been shown to inhibit phosphorylation of GSK3β indicating. Perhaps, PKCδ inhibition leads to GSK3β inhibition or GSK3β could be the actual candidate that needs validation.

The PLSR approach integrated all available signaling data and weighted the contributions of each signal to the overall migratory phenomena, under the assumption that the migration responses can be described as a linear combination of the signaling activities of each component. This approach is limited in that signaling networks are not linearly wired, but are blessed with positive and negative feedback loops potentially rendering the multivariate analysis difficult. We nevertheless claim the usefulness of this model as a predictive one given a set of signaling measurements and surmise that the snapshot of a signaling state can be predictive of the long-term migratory responses. This capability of PLSR has not been investigated in this work primarily due to the fact that the differential migratory modes are highly EMT state-dependent: while the model was able to predict the preference of an EMT state for a migratory mode, the dataset did not provide with a migratory mode that conferred equal levels of monolayer migration and sparse migration. Thus, the current dataset was too limited to successfully train the model to predict the growth factor-dependent migration speeds in each migratory mode. Testing of

the predictability of this model using epithelial and mesenchymal tumor cell lines is an avenue for future research and would add significant potential for the use of multivariate modeling of our dataset.

Our preliminary validation does indicate that PLSR is able to isolate contributions of downstream signaling proteins and suggest a previously unidentified signal that Mesenchymal cells bestow more dependency on than the EGFR itself. Although activation of PKCδ is significantly higher in Mesenchymal cells, we suspect there may be an upstream cell surface receptor, other than the EGFR, that may be constitutively active upon EMT. Autocrine platelet-derived growth factor (PDGF) is upregulated in mesenchymal tumors [37] indicating that the PDGF receptor pathway may contribute to the dependency of mesenchymal cells to PKCδ. Measurement of this pathway is also an avenue for future research. In conclusion, if further validation holds true, we will have discovered a potential therapeutic target that is EMT state-dependent, further substantiating EMT markers as additional pre-indicators for therapeutic success.

3.5. References

1. Thiery, J.P., *Epithelial-mesenchymal transitions in development and pathologies.* Curr Opin Cell Biol, 2003. **15**(6): p. 740-6.
2. Duband, J.L., et al., *Epithelium-mesenchyme transition during neural crest development.* Acta Anat (Basel), 1995. **154**(1): p. 63-78.
3. Kimelman, D., *Mesoderm induction: from caps to chips.* Nat Rev Genet, 2006. **7**(5): p. 360-72.
4. Thiery, J.P. and J.P. Sleeman, *Complex networks orchestrate epithelial-mesenchymal transitions.* Nat Rev Mol Cell Biol, 2006. **7**(2): p. 131-42.
5. Zuk, A. and E.D. Hay, *Expression of beta 1 integrins changes during transformation of avian lens epithelium to mesenchyme in collagen gels.* Dev Dyn, 1994. **201**(4): p. 378-93.
6. Yang, J. and R.A. Weinberg, *Epithelial-mesenchymal transition: at the crossroads of development and tumor metastasis.* Developmental Cell, 2008. **14**(6): p. 818-29.
7. Perl, A.K., et al., *A causal role for E-cadherin in the transition from adenoma to carcinoma.* Nature, 1998. **392**(6672): p. 190-3.
8. Yang, J., et al., *Twist, a master regulator of morphogenesis, plays an essential role in tumor metastasis.* Cell, 2004. **117**(7): p. 927-39.
9. Hartwell, K.A., et al., *The Spemann organizer gene, Goosecoid, promotes tumor metastasis.* Proc Natl Acad Sci U S A, 2006. **103**(50): p. 18969-74.

10. Mani, S.A., et al., *Mesenchyme Forkhead 1 (FOXC2) plays a key role in metastasis and is associated with aggressive basal-like breast cancers.* Proc Natl Acad Sci U S A, 2007. **104**(24): p. 10069-74.
11. Frederick, B.A., et al., *Epithelial to mesenchymal transition predicts gefitinib resistance in cell lines of head and neck squamous cell carcinoma and non-small cell lung carcinoma.* Mol Cancer Ther, 2007. **6**(6): p. 1683-91.
12. Barr, S., et al., *Bypassing cellular EGF receptor dependence through epithelial-to-mesenchymal-like transitions.* Clin Exp Metastasis, 2008. **25**(6): p. 685-93.
13. Yarden, Y. and M.X. Sliwkowski, *Untangling the ErbB signalling network.* Nat Rev Mol Cell Biol, 2001. **2**(2): p. 127-37.
14. Bublil, E.M. and Y. Yarden, *The EGF receptor family: spearheading a merger of signaling and therapeutics.* Curr Opin Cell Biol, 2007. **19**(2): p. 124-34.
15. Grandis, J.R. and J.C. Sok, *Signaling through the epidermal growth factor receptor during the development of malignancy.* Pharmacol Ther, 2004. **102**(1): p. 37-46.
16. Wells, A., *Tumor invasion: role of growth factor-induced cell motility.* Adv Cancer Res, 2000. **78**: p. 31-101.
17. Lauffenburger, D.A. and A.F. Horwitz, *Cell migration: a physically integrated molecular process.* Cell, 1996. **84**(3): p. 359-69.
18. Ridley, A.J., et al., *Cell migration: integrating signals from front to back.* Science, 2003. **302**(5651): p. 1704-9.
19. Thomson, S., et al., *Kinase switching in mesenchymal-like non-small cell lung cancer lines contributes to EGFR inhibitor resistance through pathway redundancy.* Clin Exp Metastasis, 2008.
20. Chakravarti, A., J.S. Loeffler, and N.J. Dyson, *Insulin-like growth factor receptor I mediates resistance to anti-epidermal growth factor receptor therapy in primary human glioblastoma cells through continued activation of phosphoinositide 3-kinase signaling.* Cancer Res, 2002. **62**(1): p. 200-7.
21. Elenbaas, B., et al., *Human breast cancer cells generated by oncogenic transformation of primary mammary epithelial cells.* Genes Dev, 2001. **15**(1): p. 50-65.
22. Joslin, E.J., et al., *EGF-receptor-mediated mammary epithelial cell migration is driven by sustained ERK signaling from autocrine stimulation.* J Cell Sci, 2007. **120**(Pt 20): p. 3688-99.
23. Kumar, N., et al., *A high-throughput migration assay reveals HER2-mediated cell migration arising from increased directional persistence.* Biophys J, 2006. **91**(4): p. L32-4.
24. Kim, H.D., et al., *Epidermal growth factor-induced enhancement of glioblastoma cell migration in 3D arises from an intrinsic increase in speed but an extrinsic matrix- and proteolysis-dependent increase in persistence.* Mol Biol Cell, 2008. **19**(10): p. 4249-59.
25. Janes, K.A., et al., *A systems model of signaling identifies a molecular basis set for cytokine-induced apoptosis.* Science, 2005. **310**(5754): p. 1646-53.
26. Janes, K.A., et al., *Cue-signal-response analysis of TNF-induced apoptosis by partial least squares regression of dynamic multivariate data.* J Comput Biol, 2004. **11**(4): p. 544-61.
27. Pearson, G.W. and T. Hunter, *Real-time imaging reveals that noninvasive mammary epithelial acini can contain motile cells.* J Cell Biol, 2007. **179**(7): p. 1555-67.

28. Glading, A., et al., *Epidermal growth factor receptor activation of calpain is required for fibroblast motility and occurs via an ERK/MAP kinase signaling pathway.* J Biol Chem, 2000. **275**(4): p. 2390-8.
29. Iwabu, A., et al., *Epidermal growth factor induces fibroblast contractility and motility via a protein kinase C delta-dependent pathway.* J Biol Chem, 2004. **279**(15): p. 14551-60.
30. Wolf, K., et al., *Multi-step pericellular proteolysis controls the transition from individual to collective cancer cell invasion.* Nat Cell Biol, 2007. **9**(8): p. 893-904.
31. Ewald, A., et al., *Collective Epithelial Migration and Cell Rearrangements Drive Mammary Branching Morphogenesis.* Developmental Cell, 2008. **14**(4): p. 570-581.
32. Daugherty, R.L. and C.J. Gottardi, *Phospho-regulation of Beta-catenin adhesion and signaling functions.* Physiology (Bethesda, Md), 2007. **22**: p. 303-9.
33. Huang, P.H., et al., *Quantitative analysis of EGFRvIII cellular signaling networks reveals a combinatorial therapeutic strategy for glioblastoma.* Proc Natl Acad Sci U S A, 2007. **104**(31): p. 12867-72.
34. Huang, C., K. Jacobson, and M.D. Schaller, *MAP kinases and cell migration.* J Cell Sci, 2004. **117**(Pt 20): p. 4619-28.
35. Parsons, S.J. and J.T. Parsons, *Src family kinases, key regulators of signal transduction.* Oncogene, 2004. **23**(48): p. 7906-9.
36. Soltoff, S.P., *Rottlerin is a mitochondrial uncoupler that decreases cellular ATP levels and indirectly blocks protein kinase Cdelta tyrosine phosphorylation.* J Biol Chem, 2001. **276**(41): p. 37986-92.
37. Matei, D., et al., *Autocrine activation of PDGFRalpha promotes the progression of ovarian cancer.* Oncogene, 2006. **25**(14): p. 2060-9.

CHAPTER 4

Biophysical analysis of EGF-enhanced glioblastoma migration in 3D matrices

The 3D environment poses additional parameters to the migrating tumor cell that has not been systematically assessed (see section 1.4). This chapter is devoted to a quantitative biophysical analysis of cell migration evaluating the overall effect of the convolution of EGF-enhanced matrix proteolysis and cell motility machinery on cell speed and directional persistence.

4.1. Introduction

As discussed in detail in chapter 1, members of the ErbB receptor tyrosine kinase family and their associated ligands are aberrantly expressed in many cancers, including carcinomas and glioblastomas, and have become a major realm for therapeutic targeting [1, 2]. Their over-expression is often correlated with poor prognosis as they play a central role in tumor progression, especially in invasion and metastasis, which lead to cancer-related fatalities [3, 4]. Tumor invasion requires carefully orchestrated cell motility behavior, which is stimulated by epidermal growth factor (EGF) family ligands [5, 6]. Multiple biophysical processes involved in cell locomotion [7, 8] are regulated by EGF receptor (EGFR) activation [9]. In tumor cells, a number of key signaling pathways regulating these migration-related biophysical processes are dysregulated [10]. Glioblastoma multiforme is a particularly serious example of EGFR-related dysregulation of cell motility strongly correlated with poor disease prognosis [11-13].

Current models of tumor cell migration suggest that extracellular matrix proteolysis is critical for tumor cell migration in three-dimensional (3D) environments [14, 15], although certain cell types in some environments exhibit fascinating exceptions to such models [16]. Tumor cells move through their environment by extending their leading edge

and concomitantly secreting matrix-metalloproteinases locally that act pericellularly; this matrix-remodeling step allows directed cell locomotion upon cell contraction and rear release [14, 16]. In a wide range of contexts, tumor invasion requires matrix proteolysis mediated by proteinases such as the matrix metalloproteinase (MMP) and a metalloproteinase and disintegrin (ADAM) families [17, 18]. There are currently more than 20 known members of the MMP family alone, which differ by their preferred extracellular matrix substrate specificity. MMPs are highly upregulated in invasive tumors [19] and MMP expression is induced by EGF receptor activation in various cancers [20-22]. Although tumor cell migration can occur without matrix proteolysis in some circumstances [23], various studies have correlated MMP expression and activity with tumor invasion, including in glioblastomas [13, 24].

The effects of matrix proteolysis on cell migration processes may involve more than simply providing pathways for transit [25]. While matrix degradation may loosen steric barriers, it can simultaneously decrease the availability of matrix adhesion ligands or even expose new cryptic adhesion sites. Moreover, cell speed in 3D matrices is influenced by matrix stiffness, which in turn is partly determined by the matrix fiber network density and associated network pore size [15]. Local matrix degradation can produce a reduction in stiffness that can either increase or decrease in cell migration depending on environmental and cellular context. For these reasons as well as others [26], it is perhaps not surprising that the therapeutic success of matrix protease inhibitors has been mixed at best [27].

As noted earlier, there is increasing interest in the of ErbB inhibitors as cancer therapeutics– with specific focus on reducing motility in order to diminish invasiveness [28-30] in particular for treating glioblastoma [12, 31, 32]. However, the effects of ErbB signaling network activation on cell migration are complex and highly dependent on extracellular matrix conditions [9, 15, 33, 34]; even in absence of chemotactic concentration gradients, EGF stimulation can increase or decrease the speed of migration while simultaneously increasing or decreasing directional persistence of migration depending on the substratum. These two facets of migration are governed differentially by diverse molecular components and regulatory pathways [8]. Most studies, however, have utilized 2D assays and therefore have not integrated the additional effects of EGF-induced matrix proteolysis in 3D. Therefore, there is currently no effective basis to predict the net

effect of EGF stimulation on cell migration in 3D environments – in terms of the effects this factor has on intrinsic cell locomotion behavior and its modulation by extrinsic matrix-associated properties.

To address this problem, we utilized confocal imaging – whose development is described in section 2.3.2. – to generate time-lapse movies of individual EGF-responsive human glioblastoma cells migrating in 3D matrices and quantitatively analyzed cell tracks to obtain migration parameters, including cell speed and directional persistence across different collagen densities and with varying degrees of protease inhibition. We establish that EGF stimulation leads to increase in overall motility in 3D matrices mediated by an increase in cell speed and a matrix density-dependent increase in apparent directional persistence. In contrast, parallel analysis of cell migration on 2D substrates shows that cell-intrinsic effects of EGF are increased cell speed but *decreased* directional persistence. Thus, the observed increase in apparent directional persistence in 3D is mediated by cell-extrinsic matrix proteolysis. Detailed biophysical analysis of cell tracks indicated that low matrix proteolysis leads to characteristically unproductive motility confined by matrix steric hindrance. Quantitative modulation of EGF-induced matrix proteolysis using an MMP inhibitor correlated directly with 3D directional persistence in high matrix concentrations. Therefore, the importance of EGF-induced matrix proteolysis for cell migration is highly dependent on matrix properties, where overall increase in cell migration is accomplished by cell speed in low-barrier matrix environments but by protease-mediated directional persistence in high-barrier matrix environments. Our results offer potential implications for the efficacy of EGFR and MMP inhibitors in treatment of invasive cancers.

4.2. Materials and Methods

4.2.1. Cell Culture and stable transduction of eGFP

U87MG human glioblastoma cells were originally obtained from Webster Cavenee (Ludwig Institute for Cancer Research, San Diego, CA) and maintained in DMEM supplemented with

10% FBS. pML²-eGFP retroviral plasmid was used for retroviral packaging, infection, and subsequent FACS sorting of cells as described previously [35]. Morphology and migration properties of eGFP-expressing cells were similar to the parental cells for lower than 15 passages (data not shown). All experiments were performed with cells with less than 10 passages.

4.2.2. Cell culture on 2D collagen-coated surfaces and in 3D collagen matrices

For 2D migration assays, 24-well Visiplates (Perkin-Elmer; Waltham, MA) were coated with native bovine dermal type I collagen (Nutragen, Inamed Biomaterials; Fremont, CA) as described previously with other matrix molecules [33]. In short, dishes were acid-treated, incubated with varying concentrations of collagen for 2 hours, washed with PBS, and blocked with 1% BSA for 1 hour. After washing with PBS, GFP-expressing cells were seeded at 2,000 cells/well and serum-starved overnight (>16 hours) with serum-free DMEM supplemented with 0.5% BSA.

For 3D migration assays, cells were mixed with pH-neutralized collagen of varying concentrations at 200,000 cells/ml in serum-free media. The matrix-cell solution was placed on glass-bottom cell culture dishes (MatTek; Ashland, MA) and polymerized for 1 hour at 37ºC. The culture was immediately serum-starved overnight (>16 hours).
For both 2D and 3D cultures, 8 hours prior to imaging, cells were stimulated with 50 ng/ml human recombinant EGF (Invitrogen; Carlsbad, CA). All experiments were performed with 0.1% DMSO as control for future inhibitor studies. For studies of matrix proteolysis inhibition (Biomol International; Plymouth Meeting, PA), a broad inhibitor of matrix metalloproteinases, GM6001 was added simultaneously with EGF.

4.2.3. 2D and 3D time-lapse microscopy assays

To generate time-lapse movies of cells migrating in 3D matrices, 80 confocal images were taken with 1µm spacing in z every 15 minutes for 10 hours using a McBain spinning-disk confocal microscope (McBain Instruments; Simi Valley, CA) equipped with environmental control (37°C, 5% CO_2, humidity). The bottom of the field of view was consistently chosen to be 50 µm above the glass. The final dimensions of the field of view were 870 x 660 x 80

μm with 1.3 x 1.3 x 1 μm voxels. For 2D migration assays, cells were similarly imaged every 15 minutes for 10 hours using fluorescence excitation. The imaged field was 2,200 x 1,700 μm with 1.6 x 1.6 μm pixels. All movies with the slightest drifts in x, y, or z-direction as assessed by movement of stationary fluorescent objects were not included for further analysis.

4.2.4. Quantitative analysis of cell migration tracks

Imaris image analysis software (Bitplane, Zurich, Switzerland) was used to visualize the both 2D and 3D time-lapse images. The 'Spots' function was used to calculate centroids of fluorescent objects and to generate migratory tracks as described previously [15, 36]. All generated tracks were manually verified for its accuracy and modified when computational mistakes were present. If a cell exhibits any movement more than its own cell length during the course of the experiment in the field of view, it was identified as motile. Motile cell fraction was calculated as the ratio of number of motile cells to total number of cells tracked. Cells undergoing division or death (as identified as release of fluorescence) were not included in the analysis. 2D and 3D Wind-Rose plots were generated by randomly choosing 30 tracks from the motile population and overlaying the starting coordinates at the origin of the plots to graphically represent average cell dispersion during migration. Only tracks longer than 3 hours that migrated independently without physical contact with other cells were included in the calculation of cell speed and directional persistence.

As discussed in section 2.3.4., average individual cell speeds (S) were calculated from individual cell tracks by averaging the distances over the time interval. Mean squared displacements (MSD) at various time intervals (t) were calculated using the method of non-overlapping intervals [37] and directional persistence time (P) was obtained by fitting it to the persistent random walk model (PRW):

$$MSD = 2S^2P[t - P(1 - e^{-t/P})] \qquad \text{(Eq. 1)}$$

The random motility coefficient (RMC) for each cell was calculated as $RMC = S^2P/3$, bears the units of the diffusion coefficient, and quantifies cell dispersion from its starting point.

4.2.5. Confocal reflection microscopy

3D matrices were generated without cells by incubating pH-neutralized collagen at varying concentrations for 1 hour at 37°C. Confocal reflection images were taken with a Zeiss LSM 510 scanning confocal microscope (Carl Zeiss Microimaging; Thornwood, NY).

4.2.6. Quantitative measurements of MMP-1 release and MT1-MMP expression

Cells were seeded on 10 μg/cm^2 collagen-coated tissue culture dishes in serum-free media. After >16 hours, cells were stimulated with 50 ng/ml EGF. For MMP-1 release assay, media was collected after indicated times and was assayed with the Human MMP-1 Fluorokine MAP kit (R&D Systems; Minneapolis, MN) by following manufacturer's instructions. For assaying membrane-bound MT1-MMP expression, membrane-bound proteins were biotinylated using EZ-Link Sulfo-NHS-LC-LC-Biotin (Pierce Biotechnology; Rockford, IL) as described previously [38]. Cells were lysed and biotinylated proteins were precipitated using Neutravidin beads (Pierce Biotechnology). Precipitated lysates were subjected to standard Western blot analysis using an anti-MT1-MMP antibody (Santa Cruz Biotechnologies; Santa Cruz, CA) and the Odyssey detection system (LI-COR; Lincoln, NE). Densitometry of bands was performed with the Odyssey software.

4.2.7. Rac1 activity measurements

Rac1-GTP levels were measured using the G-LISA Rac1 specific activation assay (Cytoskeleton, Inc.; Denver, CO). For 2D samples, cells were seeded at 15,000 cells/cm^2 on 10 μg/cm^2 collagen-coated tissue culture dishes in serum-free media. For 3D samples, cells were seeded at 500,000 cells/ml gel in serum-free media. After >16 hours, cells were stimulated 50 ng/ml EGF and lysed at indicated times. For 3D samples, gels were homogenized in presence of lysis buffer and lysates clarified. Manufacturer instructions were followed for the remainder of the assay protocol. To normalize for total Rac1 levels, we subjected lysates to a semi-quantitative Western blot analysis using an anti-Rac1 antibody and an anti-GAPDH antibody (Millipore; Billerica, MA). Bands were detected and analyzed with the Odyssey detection system. Rac1-GTP levels were normalized internally and then to total Rac1 levels of the 2D serum-free levels.

4.2.8. FITC-collagen release assay

Matrix degradation assays were performed with a quenched FITC-labeled DQ-collagen Type I (Invitrogen; Carlsbad, CA) as described previously [38]. In short, parental cells were seeded at 500,000 cells/ml of pH-neutralized collagen (3.0 mg/ml) containing 5% (w/v) DQ-collagen in a 24-well plate. Cells were serum-starved >16 hours and stimulated with 50 ng/ml EGF in presence or absence of GM6001. Matrices were collected after 12 and 24 hours and centrifuged. Supernatant was collected and released fluorescence read with a SpectraMax M2e fluorescence plate reader (Molecular Devices; Sunnyvale, CA). All fluorescent values were normalized to no-cell control.

4.2.9. Rheometry of collagen gels

Elastic moduli of cell-free collagen gels were obtained using the AR2000 rheometer (TA Instruments, New Castle, DE). Collagen was pH-neutralized, placed in stainless steel washers of 2.0 cm diameter and 0.9 mm height on top of wetted parchment paper and polymerized for 1 hour at 37ºC. Washer was gently removed and placed on the rheometer for measurement of storage moduli (G') at 1 Hz and 0.87 μNm oscillatory torque using a 2 cm plate.

4.2.10. Statistical Analysis

All data is shown as mean ± s.e.m. unless otherwise noted. All experiments had 3 – 5 biological replicates unless otherwise noted. For migration experiments, N = number of motile cells. Depicted statistical significance was assessed by two-way analysis of variance (ANOVA) of log-transformed data values to obtain normal distributions as tested by Kolmogorov-Smirnov test. p-values represent significance across treatments. One-way ANOVA and two-tailed student's t-tests of log-transformed data values were performed where appropriate (Figure 1, F and see Text). To test significance of deviation of a single data point to trends in Figure 6, B and 6, C, one-way ANOVA was performed on data sets excluding the 1 μM GM6001 with and without the serum-free data point.

4.3. Results

4.3.1. EGF-stimulated 3D cell migration results from increased cell speed and matrix concentration-dependent increased directional persistence.

EGF increases tumor cell invasiveness via enhancement of intrinsic cell motility machinery and induction of matrix metalloproteinases (MMPs). As most previous *in vitro* studies were performed in 2D assays where matrix-degrading effects of MMPs are not applicable, the combined effects of these two factors on cell migration behavior have not yet been assessed. To quantify the effects of EGF stimulation on cell migration in 3D, we optimized a 3D culture system for cell tracking using highly invasive and EGF-responsive U87MG human glioblastoma cells seeded sparsely in type I collagen matrices. Our use of type I collagen provides a reasonably physiological model for at least some aspects of glioma cell migration: glioblastoma cells secrete high levels of their own extracellular matrix proteins *in vivo* and *in vitro* that are present both in normal brain and tumor microenvironment [39, 40] and type I collagen is found in perivascular regions of the brain [41] where glioblastoma invasion has been often noted [42, 43].

Since extracellular matrix concentrations influence cell migration by varying ligand density and matrix compliance [15, 34, 44] and the effects of matrix proteolysis have been predicted to depend on these factors [25], cells were seeded in collagen concentrations

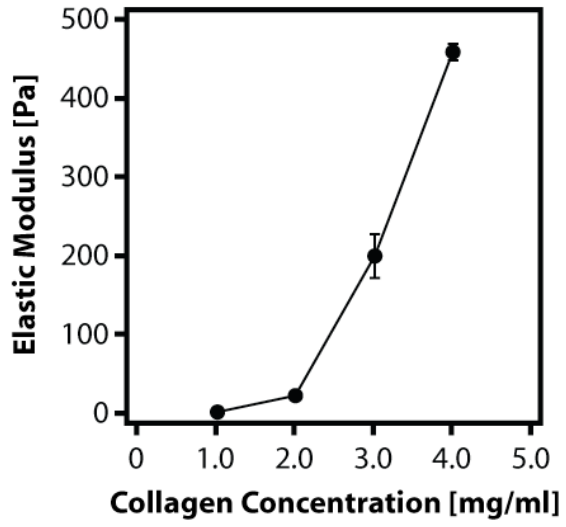

Figure 4-1 – Plate rheometry of varying concentrations of collagen used in this study indicate an almost 20-fold variation of elastic moduli. Cell-free collagen gels of 2 mm diameter were placed on a 2 mm plate rheometer and measured at 1 Hz oscillation to obtain G'. Figure reprinted from the Molecular Biology of the Cell [63].

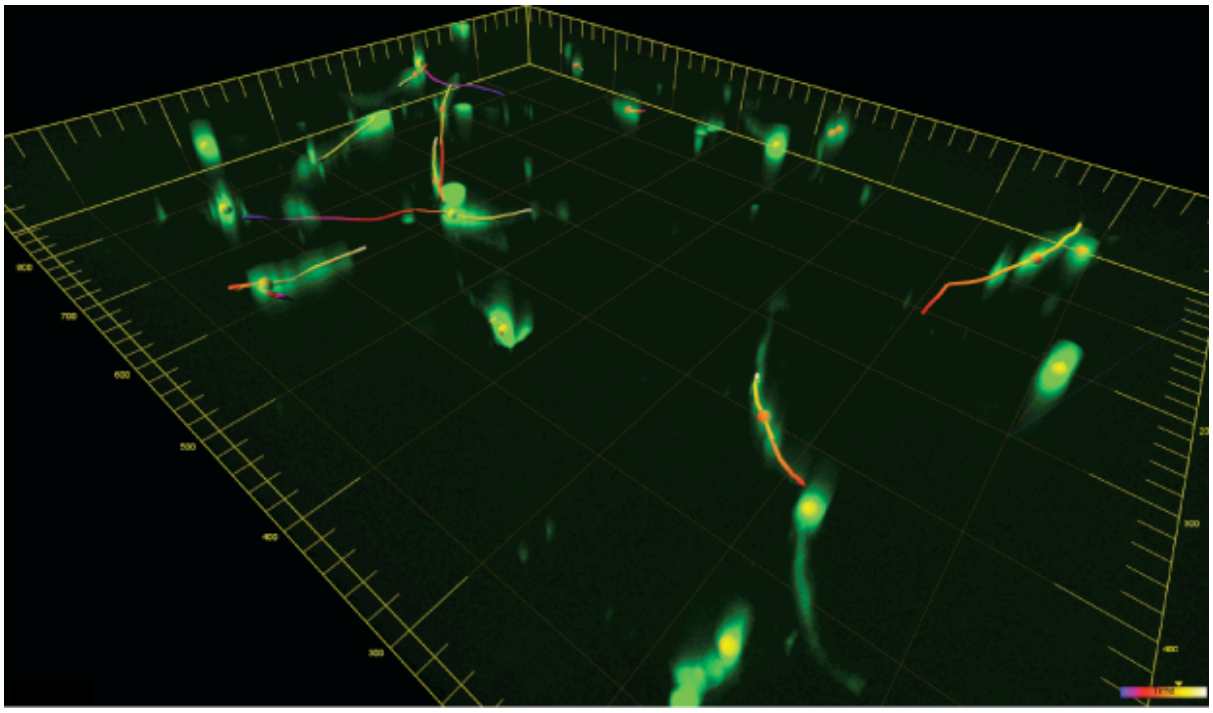

Figure 4-2 – Representative 3D time-lapse confocal microscopy image of U87MG cells displaying high degree of locomotion in collagen matrix. GFP-expressing U87MG cells were seeded in varying concentrations of collagen matrices and imaged over 10 hours with 15-minute intervals and cells tracked using Imaris tracking software. Yellow spheres indicate cell center and the tracks are color-coded according to their position in the 10 hour period (blue-red-yellow-white). Image dimensions: 870 μm x 660 μm x 80 μm (each large grid = 100 μm).

from 2.0 to 4.0 mg/ml, which corresponded to a 20-fold increase of elastic modulus (Figure 4-1). After serum-starvation, cells were uniformly stimulated with saturating levels of EGF for 8 hours and the movements of cells expressing cytoplasmic GFP were tracked for 10 hours using 3D time-lapse confocal microscopy as described previously [15].

Reconstructed real-time movies (Figure 4-2) showed cells with a range of migratory phenotype; a significant number of cells (50-70%) failed to locomote productively despite actively forming protrusions (Figure 4-3, B). This is likely due to the heterogeneity in the local matrix network, as well as intrinsic heterogeneity within the cell population. By analyzing the cell tracks of the motile population, we confirmed that EGF had a qualitatively stimulatory effect on the displacements of U87MG cell migration over the course of the experiment (Figure 4-3, A and B). As expected, the stimulatory effect was chemokinetic since EGF-induced migration failed to show preferential migration towards

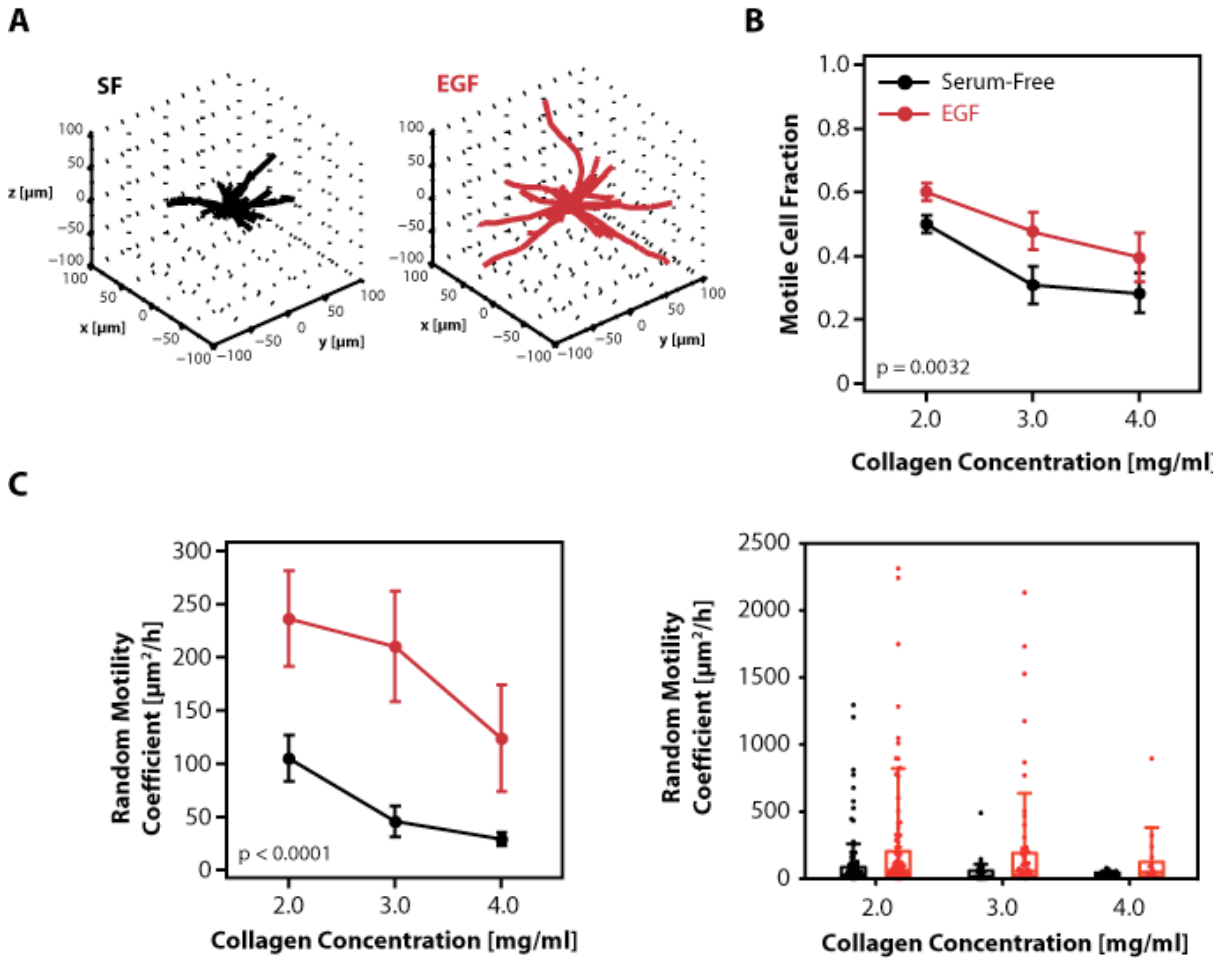

Figure 4-3 – EGF stimulation enhances 3D U87MG migration in varying collagen matrix concentrations. (A) Representative 3D Wind-Rose plots depicting migratory tracks over 10 hours of 40 random cells determined as motile in 3.0 mg/ml collagen matrix. Cells that moved more than its cell length were determined as motile. **(B)** Ratio of number of motile cells to total number of cells tracked in presence (red) or absence (black) of 50 ng/ml EGF. Cells that moved more than its cell length were determined as motile. **(C)** Cell dispersion quantified as random motility coefficient. Random motility coefficient of each cell is calculated from cell speed and persistence time of the persistent random walk model. Data shown as mean ± SEM (left) or in a box-and-whisker plot (edges representing 25th and 75th percentiles and whiskers representing 10th and 90th percentiles) overlaid with a distribution of each cell's random motility coefficient (right). N = 3 – 5 biological experiments (B). N = 18 – 105 motile cells (C) out of ~100 – 250 total cells tracked. p-value indicates statistics obtained from two-way analysis of variance across treatment conditions. Figure modified and reprinted from the Molecular Biology of the Cell [63].

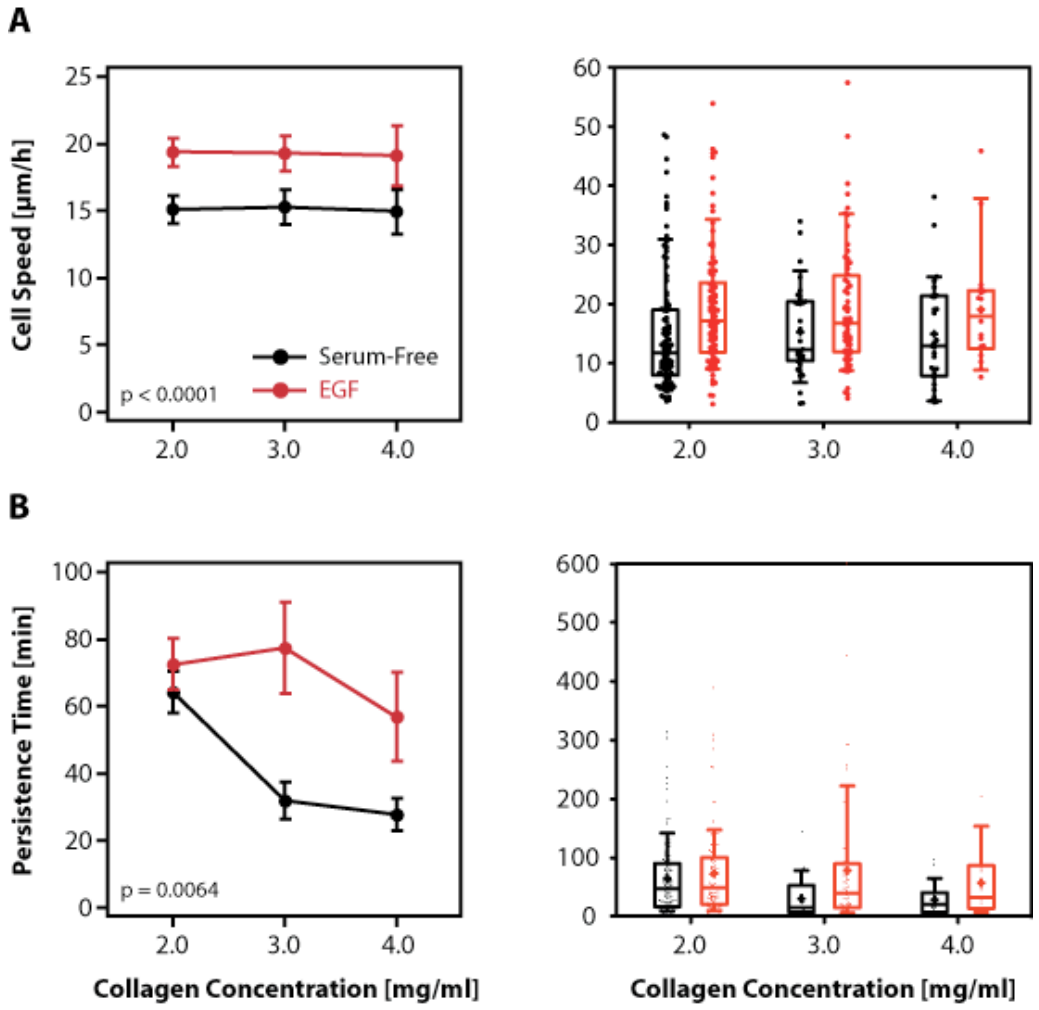

Figure 4-4 – EGF enhanced cell migration in 3D arises from increased cell speed and matrix-dependent increase in directional persistence. (A) Cell speeds of cells determined as motile. **(B)** Directional persistence time fitted from the persistent random walk model. High persistence times indicate directed movement whereas low persistence times indicate erratic movement according to the model. Data shown as mean ± SEM (left) or in a box-and-whisker plot (edges representing 25th and 75th percentiles and whiskers representing 10th and 90th percentiles; '+' indicates the mean and the bar the median) overlaid with a distribution of each cell's random motility coefficient (right). N = 18 – 105 motile cells out of ~100 – 250 total cells tracked. p-values indicate statistics obtained from two-way analysis of variance across treatment conditions. Figure modified and reprinted from the Molecular Biology of the Cell [63].

the top (Figure 4-3, A) and addition of EGF elicited an almost immediate protrusion response of cells in the bottom of the matrix (data not shown). We posit that the EGF concentration perceived by these cells is dominated by the exogenous treatment as blocking of the EGF receptor by an inhibitory antibody did not change motility in serum-

free media, and since TGF-α release by U87MG cells was found to be negligible (data not shown).

EGF-induced chemokinetic migration exhibited significant increase in the population of motile cells across measured matrix concentrations. Moreover, the motile fraction showed a significant dependence on matrix concentration ($p = 0.0012$, two-way ANOVA across matrix concentrations). Motile cells were analyzed further for their overall cell dispersion by calculating random motility coefficients for each individual cell – a parameter analogous to the diffusion coefficient of a single molecule. As reflected in Wind-Rose plots (Figure 4-3, A), cell dispersion was increased upon EGF treatment across all matrix concentrations (Figure 4-3, C) and depended on matrix concentration ($p = 0.017$).

As extensively described in section 2.3.3., chemokinetic cell movement has often been quantitatively characterized via its translational speed and directional persistence [45, 46]. These migratory attributes have previously been shown to be regulated by distinct intracellular mechanisms [47]. To determine the contributions of speed and persistence to overall increase in EGF-induced cell dispersion, we calculated average cell speed and applied the persistent random walk (PRW) model to cell tracks to obtain persistence time [37, 48, 49]. While cell speed describes the rate of translational locomotion, persistence time quantifies the extent of directionality changes over the course of locomotion. High persistence times indicate strongly directional movement and low persistence times are indicative of very random or erratic movement. In the presence of a homogeneous, isotropic migratory environment without physical barriers such as the 3D extracellular matrix or another cell, persistence times obtained from PRW model may describe the cell's intrinsic inclination for randomness or directionality. However, as discussed in section 2.3.5., cells in 3D extracellular matrices are obviously subjected to physical influences, such as steric obstructions. Keeping the model assumptions in mind, our purpose in employing the PRW model was merely to quantitatively describe persistence of cell tracks rather than to characterize intrinsic cell motility persistence [36].

As expected, cell speed increased significantly (approximately 33%) across all matrix concentrations upon EGF induction (Figure 4-4, A); matrix concentration did not influence cell speed of motile cells ($p = 0.95$). Interestingly, directional persistence (Figure

4-4, B) displayed a matrix concentration-specific response (p = 0.006) with a significant increase in response to EGF only at higher matrix concentrations (p = 0.003 and p = 0.04 for 3.0 and 4.0 mg/ml collagen, respectively) and not at low concentrations (p = 0.61 for 2.0

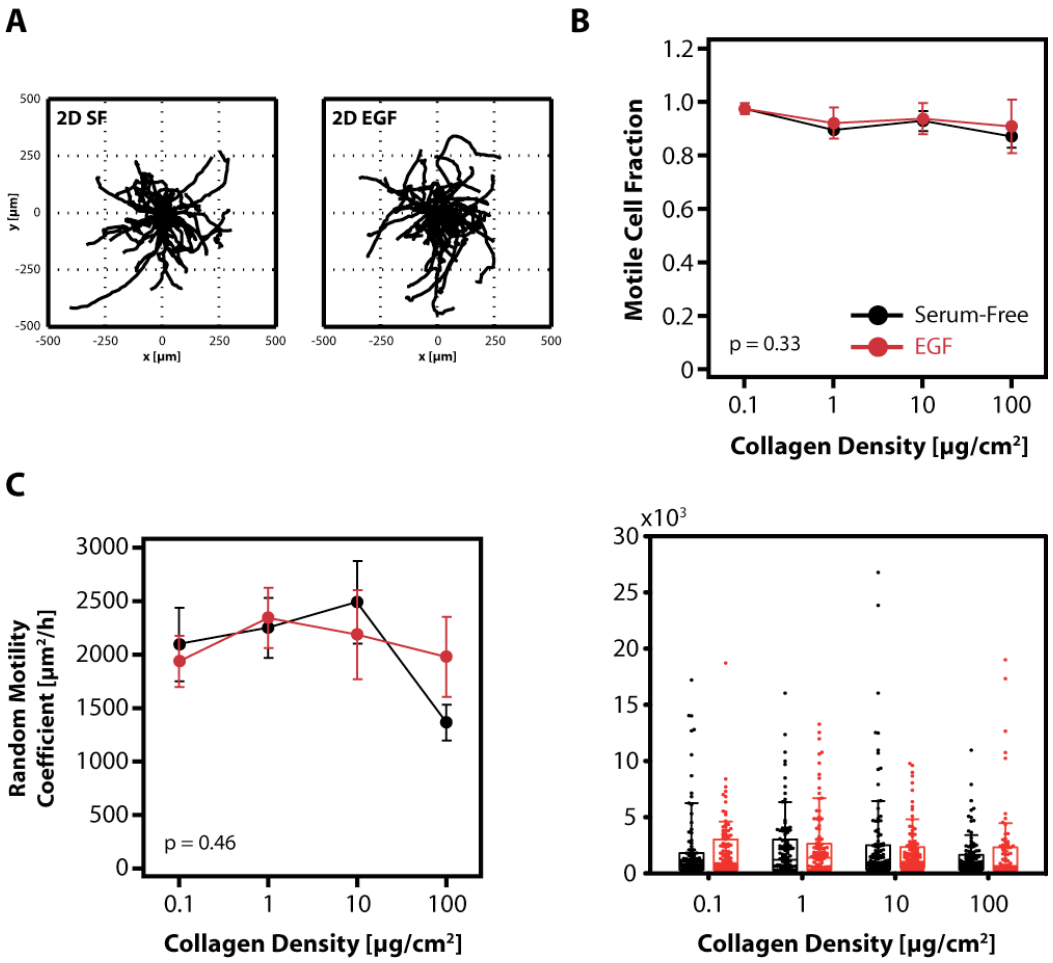

Figure 4-5 – EGF stimulation has little effect on U87MG cells on 2D, barrier-free surfaces. **(A)** Representative 2D Wind-Rose plots depicting migratory tracks over 10 hours of 40 random cells determined as motile on 10 µg/cm² collagen-coated 2D surfaces. **(B)** Motile fraction and **(C)** random motility coefficients obtained from 2D time-lapse microscopy analysis of U87MG cells migrating on collagen-coated surfaces of varying densities in presence (red) or absence (black) of 50 ng/ml EGF. Cells that moved more than its cell length were determined as motile. Data shown as mean ± SEM (left) or in a box-and-whisker plot (edges representing 25th and 75th percentiles and whiskers representing 10th and 90th percentiles) overlaid with a distribution of each cell's random motility coefficient (right). N = 3 biological experiments (B). N = 83-118 motile cells (C). p-values indicate statistics obtained from two-way analysis of variance across treatment conditions. Figure modified and reprinted from the Molecular Biology of the Cell [63].

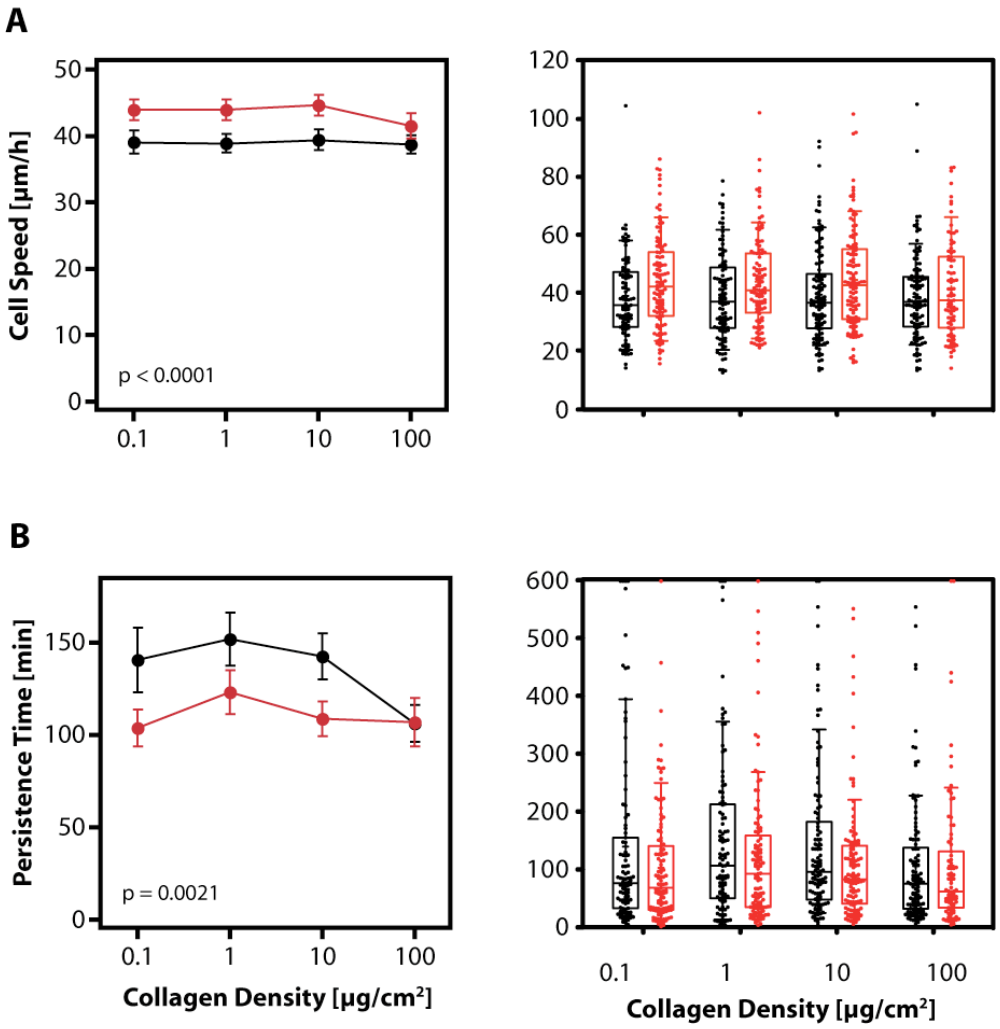

Figure 4-6 – EGF-stimulated cell-intrinsic migratory response is to increase cell speed, but to decrease directional persistence. (A) Cell speeds and **(B)** persistence times obtained from 2D time-lapse microscopy analysis of U87MG cells migrating on collagen-coated surfaces of varying densities in presence (red) or absence (black) of 50 ng/ml EGF. Cells that moved more than its cell length were determined as motile. Data shown as mean ± SEM (left) or in a box-and-whisker plot (edges representing 25th and 75th percentiles and whiskers representing 10th and 90th percentiles; '+' indicates the mean and the bar the median) overlaid with a distribution of each cell's random motility coefficient (right). N = 83-118 motile cells. p-values indicate statistics obtained from two-way analysis of variance across treatment conditions. Figure modified and reprinted from the Molecular Biology of the Cell [63].

mg/ml collagen). Hence, the EGF-induced increase in cell dispersion is environment specific and is mediated by an increase only in cell speed at low matrix concentrations, but predominantly by an increase in directional persistence in high matrix concentrations.

4.3.2. Cell-intrinsic response to EGF treatment is to increase cell speed, but decrease directional persistence

We hypothesized that the increase in cell speed and matrix density-dependent increase in directional persistence results from a combination of EGF-stimulated cell-intrinsic and matrix proteolytic effects. To determine the cell-intrinsic effects of EGF-stimulation on cell speed and directional persistence in absence of matrix proteolysis, we performed conventional 2D time-lapse microscopy assay to track migration of the same U87MG cells on collagen-coated surfaces in presence and absence of saturating levels of EGF. As expected, in absence of a much more viscous 3D surrounding, cells exhibited much greater motility and displacements (Figure 4-5, A and B). However, interestingly, 2D Wind-Rose plots showed that cell displacements were comparable and motile cell population were essentially unitary upon EGF treatment even across 1000-fold variation of matrix coating density (Figure 4-5, A and B). Quantitation of motile tracks showed that cell dispersion was not increased upon EGF stimulation (Figure 4-5, C). Parsing cell tracks into cell speed and directional persistence demonstrated that EGF stimulation led to a slight, but significant increase in cell speed in U87MG cells on 2D collagen-coated surfaces, while a significant decrease in persistence was observed across most matrix densities (Figures 4-6, A and B). This phenomenon was observed previously in fibroblasts on 2D matrix-coated surfaces [34] and was explained by the ability of homogeneous EGF stimulation to induce protrusions from all cell edges, which promotes a lower probability of forming a stable asymmetry for continued directional movement while inducing a greater motility [34]. Therefore, the cell-intrinsic response to EGF stimulation is to increase cell speed and decrease directional persistence. Cell speed was increased by EGF stimulation both in 2D and 3D environments suggesting that the EGF-induced cell intrinsic response holds true in 3D matrices. Interestingly, however, directional persistence was increased only in 3D matrix environment and decreased in a 2D barrier-free environment.

Rac1 has been proposed as a candidate switch for persistence, and Rac1 activity was inversely correlated with persistence [47]. We therefore asked whether Rac1 activity is differentially regulated in 2D and 3D environments and is responsible for the observed difference in EGF-stimulated directional persistence. We measured Rac1 activity of cells upon EGF stimulation in 2D and 3D environments to assess whether EGF stimulation had

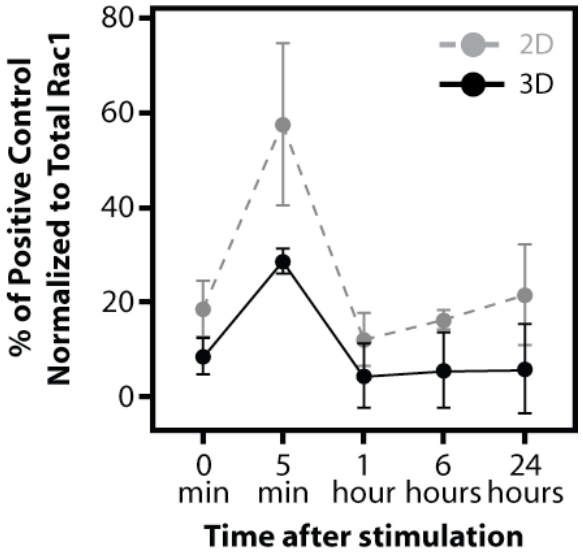

Figure 4-7 – Rac1 activation upon EGF stimulation is preserved in the 3D environment. Time course of Rac1-GTP levels of U87MG cells on collagen-coated 2D surfaces (grey) or in 3D collagen matrix (black) after stimulation with 50 ng/ml EGF using commercially available Rac-GTP ELISA normalized to total Rac1 levels measured by semi-quantitative immunoblot. Data shown as mean ± SEM. N = 2 biological replicates. Figure reprinted from Molecular Biology of the Cell [63].

differential effects on cell-intrinsic regulators of persistence. It is well established that EGF transiently stimulates Rac1 activity with a return to baseline activity observed after approximately 30 minutes [50, 51]. Quantitative time-courses of Rac1 activity displayed similar kinetics in both 2D and 3D environments with an early increase followed by a return to basal levels within an hour, although Rac1 activity was slightly lower in 3D environments (Figure 4-7). Therefore, the 3D environment does not significantly alter Rac1 response to EGF stimulation, and absolute activity levels of Rac1 may not explain regulation of EGF-induced directional persistence. We infer that the cell-intrinsic response to EGF stimulation is decreased directional persistence, perhaps partially mediated by a temporal increase in Rac1 activity. The increase in persistence in 3D matrices likely arises from mechanisms independent from the cell intrinsic response, such as matrix proteolysis mediated by expression of proteinases.

4.3.3. EGF stimulates MMP expression and matrix proteolysis, which is required for cell migration in 3D while preserving cell-intrinsic migration responses to EGF.

Before further exploring the underlying mechanism for increased directional persistence at high matrix concentrations, we assessed EGF-induced MMP expression and matrix proteolysis in 3D. We confirmed that EGF stimulates U87MG cells to express MMP specific to the type I collagen used in this study (Figure 4-8, A and B). The earliest measurable

differences were observed at 8 hours for MMP-1 with large differences measurable within 24h after stimulation. Thus, MMP upregulation could underlie the observed effects on EGF-induced 3D migration, which were performed 8 – 18 hours after stimulation.

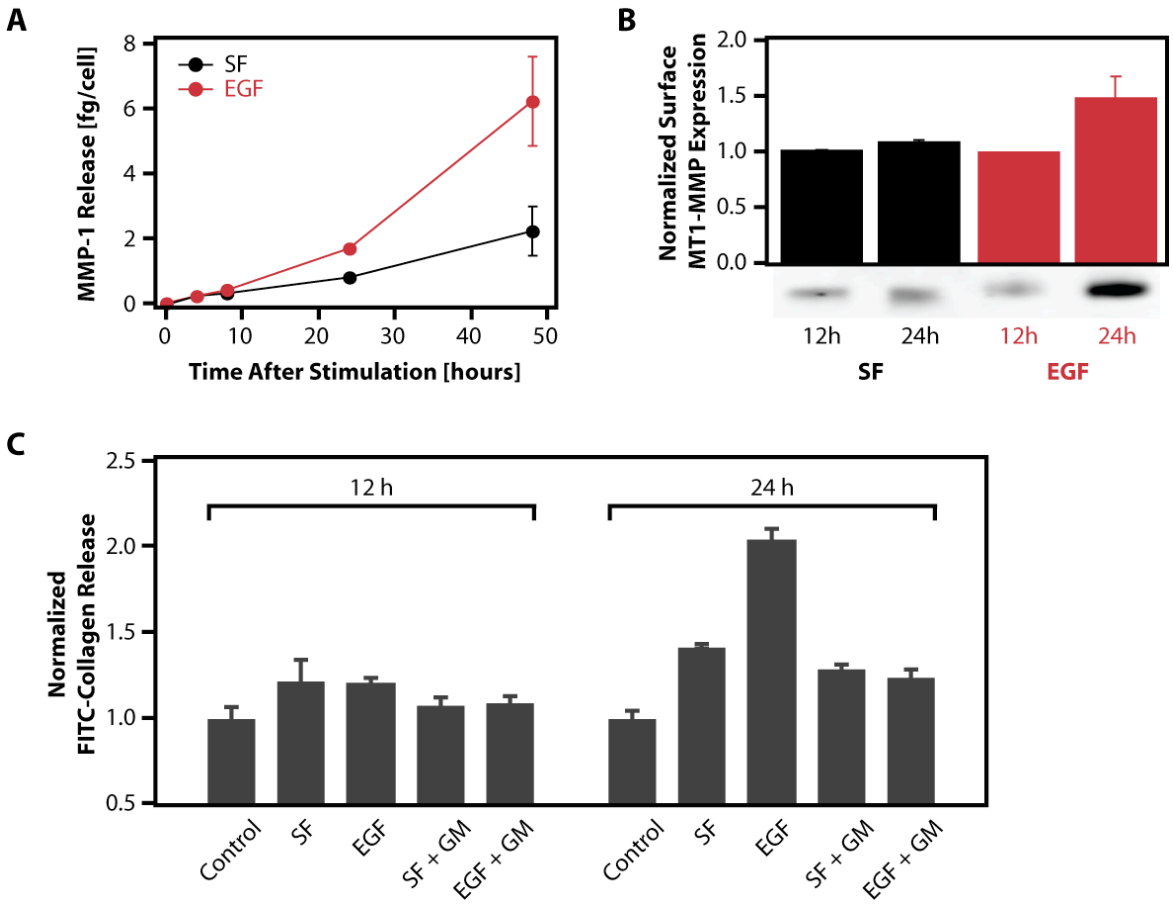

Figure 4-8 – EGF stimulation increases MMP release and 3D matrix degradation. (A) MMP-1 release was measured using a quantitative immunoprecipitation bead-based MMP-1 detection assay. Cells were seeded on surfaces coated with 10 μg/cm^2 collagen and serum-starved. Media was collected at various times after changing to serum-free media (SF) or to media containing 50 ng/ml EGF. **(B)** Cell surface MT1-MMP expression was measured by semi-quantitative densitometry of Western Blot for cell surface MT1-MMP. Cells were seeded on collagen I and serum-starved. Cell surface proteins were biotinylated and cells were lysed at indicated times after changing media to serum-free or EGF containing media. Cell surface proteins were precipitated with streptavidin beads and prepared for SDS-PAGE. **(C)** Bulk matrix degradation by U87MG cells in 3D collagen gels were measured using a FITC-collagen dequenching assay. Cells were embedded in a matrix consisting of 5% quenched FITC-labeled collagen and serum-starved. FITC-collagen released into media was quantified at indicated times after changing media to serum-free or EGF containing media. 1 μM GM6001 (GM), a broad matrix metalloproteinase inhibitor, was used as negative control. Figure reprinted from the Molecular Biology of the Cell [63].

We further confirmed the effects of MMP-1 and MT1-MMP upregulation on matrix proteolysis via a fluorimetric matrix proteolysis assay using a quenched FITC-labeled collagen (DQ-collagen) as previously described [23, 38]. Cells were embedded in matrices using 5% DQ-collagen in similar conditions as the migration assays. While even serum-free cells exhibited considerable bulk matrix proteolysis, EGF induced a significant increase in degradation by 24 hours (Figure 4-8, C).

To illustrate the importance of matrix proteolysis on EGF-induced 3D migration of U87MG cells in collagen, we measured 3D migration in presence of GM6001, a broad MMP inhibitor, which has also been shown to inhibit activity of urokinase plasminogen activator (uPA) [52]. Treatment with 1 μM of GM6001 was sufficient to significantly decrease matrix degradation below the baseline for serum-free levels (Figure 4-8, C). This level of inhibition was sufficient to decrease 3D motility by 10-fold (Figure 4-9, A) indicating that MMP activity is essential for U87MG migration in 3D collagen. In contrast, even 5 μM GM6001 was not sufficient to affect migratory behavior U87MG cells on 2D substrates, as cell speed and directional persistence was not significantly changed in presence of GM6001

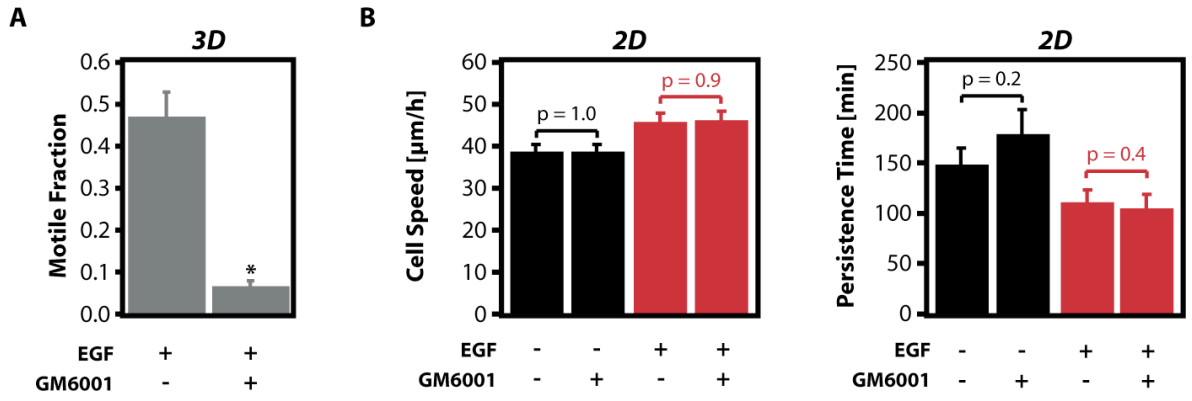

Figure 4-9 – Inhibition of MMPs does not affect 2D migration, but abrogates 3D migration. U87MG cells were seeded in **(A)** 3.0 mg/ml collagen matrices or **(B)** on 2D surfaces coated with 10 μg/cm^2 collagen were stimulated with 50 ng/ml EGF in presence or absence of 1 μM or 5 μM of a broad MMP inhibitor GM6001 for 3D and 2D experiments, respectively, for 6 hours and then tracked for 10 hours. **(A)** Cells that moved more than its cell length were determined as motile. N = 3-5 biological experiments, p = 0.002. **(B)** 2D cell speed (left) and persistence (right) were calculated for motile cells. Data shown as mean ± SEM. Figure reprinted from the Molecular Biology of the Cell [63].

(Figure 4-9, B). Inhibition of matrix proteolysis thus seems not to affect the cell-intrinsic responses to increase cell speed and decrease directional persistence upon EGF stimulation. These results support a model in which MMPs act as cell-extrinsic factors required for 3D migration.

4.3.4. Low matrix proteolysis results in cell migration characteristic of matrix confinement

To investigate the biophysical basis for EGF-induced matrix proteolysis as a cell-extrinsic factor in regulating directionally persistent migration in 3D matrices, we examined the relationship between matrix properties and cell migration more closely. An obvious function of matrix proteolysis is to clear steric barriers for successful cell migration. Confocal reflection micrographs of matrices of varying concentrations confirmed that matrix pore size decreases as density of matrix fibers increases with increasing concentration (Figure 4-10, A). While cell speed was relatively constant across matrix concentrations (Figure 4-4, A), the motile fraction, cell dispersion, and directional persistence all decreased with increasing matrix concentration, especially in serum-free conditions (Figure 4-3, B and C; Figure 4-4, B). In addition, the increase in 3D persistence at higher matrix concentration was observed mainly due to serum-free persistence decreasing with increasing matrix concentration (Figure 4-4, B), suggesting a role of matrix steric hindrance in regulating cell migration at low levels of matrix proteolysis. When examining the real-time cell tracks in detail, we found qualitatively that the untreated, high matrix concentration conditions contained an increased population of cells that displayed movement characteristic of matrix confinement. Figure 4-10, B shows an example of such cell displaying back-and-forth movements within a confined space over the course of the experiment. This type of movement may be categorized as 'erratic' and may display low persistence times, but does not display a true random walk for it is influenced by external confinement. Persistence time for each cell track is obtained from a non-linear model fit (see Eq. 1 in section 4.2.4.) under the assumption that each cell track arises without external physical influence as mentioned above. Goodness of fit of the cell track data to this model therefore serves as a quantitative indication for cell migration under these assumptions. We calculated the goodness of fit (R^2) of cells with low persistence times ($P <$

A

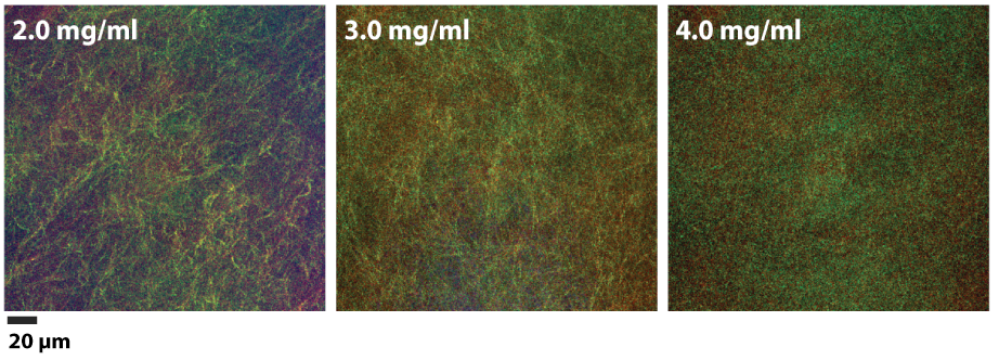
2.0 mg/ml
3.0 mg/ml
4.0 mg/ml
20 µm

B

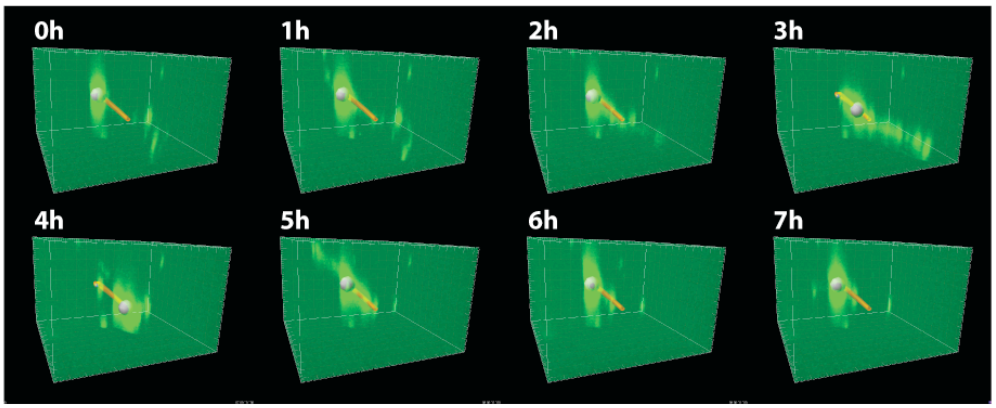
0h
1h
2h
3h
4h
5h
6h
7h

C

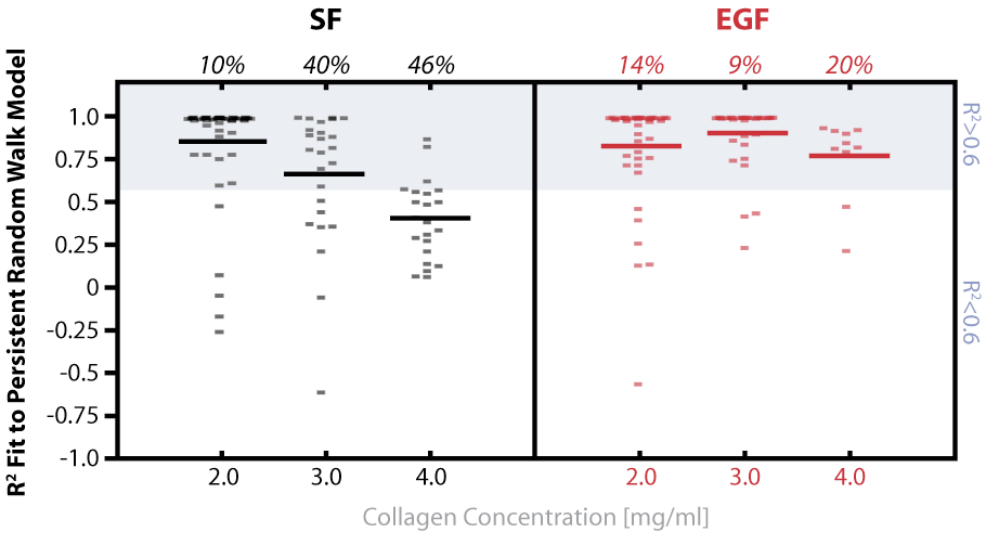
SF
EGF
10%
40%
46%
14%
9%
20%
R² Fit to Persistent Random Walk Model
1.0
0.75
0.5
0.25
0
-0.25
-0.5
-0.75
-1.0
R²>0.6
R²<0.6
2.0
3.0
4.0
2.0
3.0
4.0
Collagen Concentration [mg/ml]

Figure 4-10 – Concentration-dependent matrix-confined movement governs low persistent movement in unstimulated cells. (A) Confocal reflection micrographs of collagen matrices of varying concentrations. **(B)** Representative time-lapse images of an U87MG cell migrating with low persistence time in serum-free cells. White sphere and yellow line indicate the centroid of the cell and the migratory track, respectively. Dimensions of the box: 122 x 112 x 80 μm. **(C)** Scatter plot for goodness of fit (R^2) of cell migration tracks to the persistent random walk model. Only cells migrating in untreated, serum-free (left, black) or in 50 ng/ml EGF treatment (right, red) with P < 50 minutes were plotted. Lines indicate mean of the distribution and the percentage numbers on right indicate the percentile of cells with $R^2 < 0.6$ (threshold chosen as poor fit). Figure modified and reprinted from the Molecular Biology of the Cell [63].

50 min) across all matrix concentrations in an attempt to quantify matrix-confined movement for low persistent cells. Randomly migrating cells in high matrix concentrations and serum-free condition exhibited poor fits to the persistent random walk model where the fits became poorer with increasing matrix concentration (Figure 4-10, C). When arbitrarily defining a threshold for poor fit at $R^2 < 0.6$, 40-46% of these cells showed poor fit to PRW model whereas only 9-20% of randomly migrating cells in EGF showed a poor fit. These analyses suggest that low persistence under the two stimulation conditions are distinct in nature, with serum-free cells exhibiting migratory paths indicative of movement sterically hindered by the 3D matrix. Further, we conclude that EGF-induced increase in 3D directional persistence mediated by cell-extrinsic proteolysis arises from the ability to overcome steric hindrances posed by the 3D matrix.

4.3.5. 3D directional persistence correlates with matrix degradation activity

To establish direct correlation between directional persistence and matrix degradation, we set out to modulate matrix degradation activity with GM6001 quantitatively. Via the matrix degradation assay described above, the degree of bulk matrix degradation was measured in presence of EGF and varying levels of GM6001. The decrease in bulk matrix degradation correlated well with increasing levels of GM6001 (Figure 4-11; $R^2 = 0.96$ for linear fit). Matrix degradation measured in serum-free condition corresponded to levels between 0.01 and 0.1 μM GM6001.

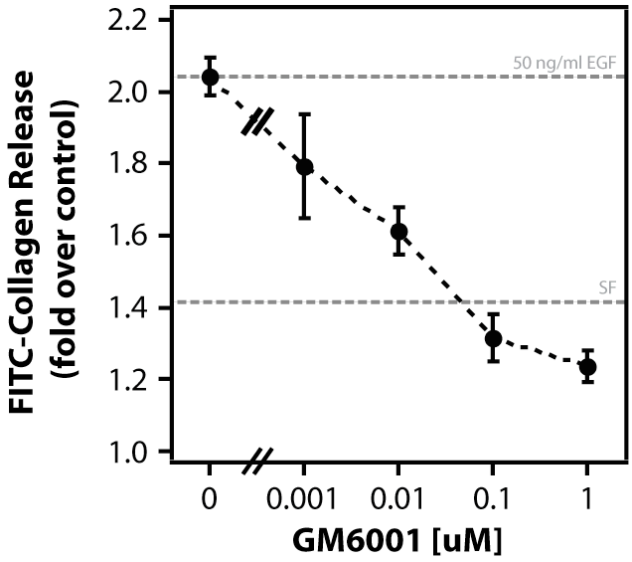

Figure 4-11 – Varying concentrations of MMP inhibitor GM6001 modulates matrix degradation. Bulk matrix degradation of U87MG cells was quantified in presence of varying concentrations of GM6001 and 50 ng/ml EGF as described above. Horizontal dashed lines indicate mean values of EGF control and serum-free control from Figure 4-8, C. $R^2 = 0.96$ for logarithmic fit. N = 3-5 biological experiments. Figure reprinted from the Molecular Biology of the Cell [63].

3D migration experiments were then performed using varying levels of GM6001, and motile fraction, cell speed, and persistence times were deduced as described above. Instead of plotting parameters against inhibitor levels, we plotted them against the experimentally determined matrix degradation activity in presence of GM6001 to illustrate more directly the effects of matrix degradation on 3D cell migration (Figure 4-12, A-C). Motile cell fraction and cell speeds displayed similar trends: both parameters were low at the lowest matrix degradation measured, but assumed maximum values once a threshold of matrix degradation was reached (Figure 4-12, A and B; $p = 0.13$ and $p = 0.32$, respectively, from one-way ANOVA of data points < 1 µM GM6001). Serum-free conditions (grey data points) for both motile fraction and cell speed were close to the EGF-induced data points (black data points), but deviated significantly from the trend ($p = 0.0008$ and $p = 0.044$, respectively; see section 4.2.10 for statistics). A better correlation to matrix degradation was observed with directional persistence for all data points including the serum-free condition (Figure 4-12, C, $R^2 = 0.92$). Small modulation of matrix degradation at 0.001 and 0.01 µM GM6001 modulated directional persistence significantly, indicating the importance of matrix proteolysis in generating directional persistence. Scatter plot of goodness of fit (R^2) to PRW model in presence of the inhibitors show a correlation between poor fit and matrix degradation, where number of cells exhibiting poor fit increases with increasing GM6001 levels (Figure 4-12, C). These results indicate that EGF-induced matrix

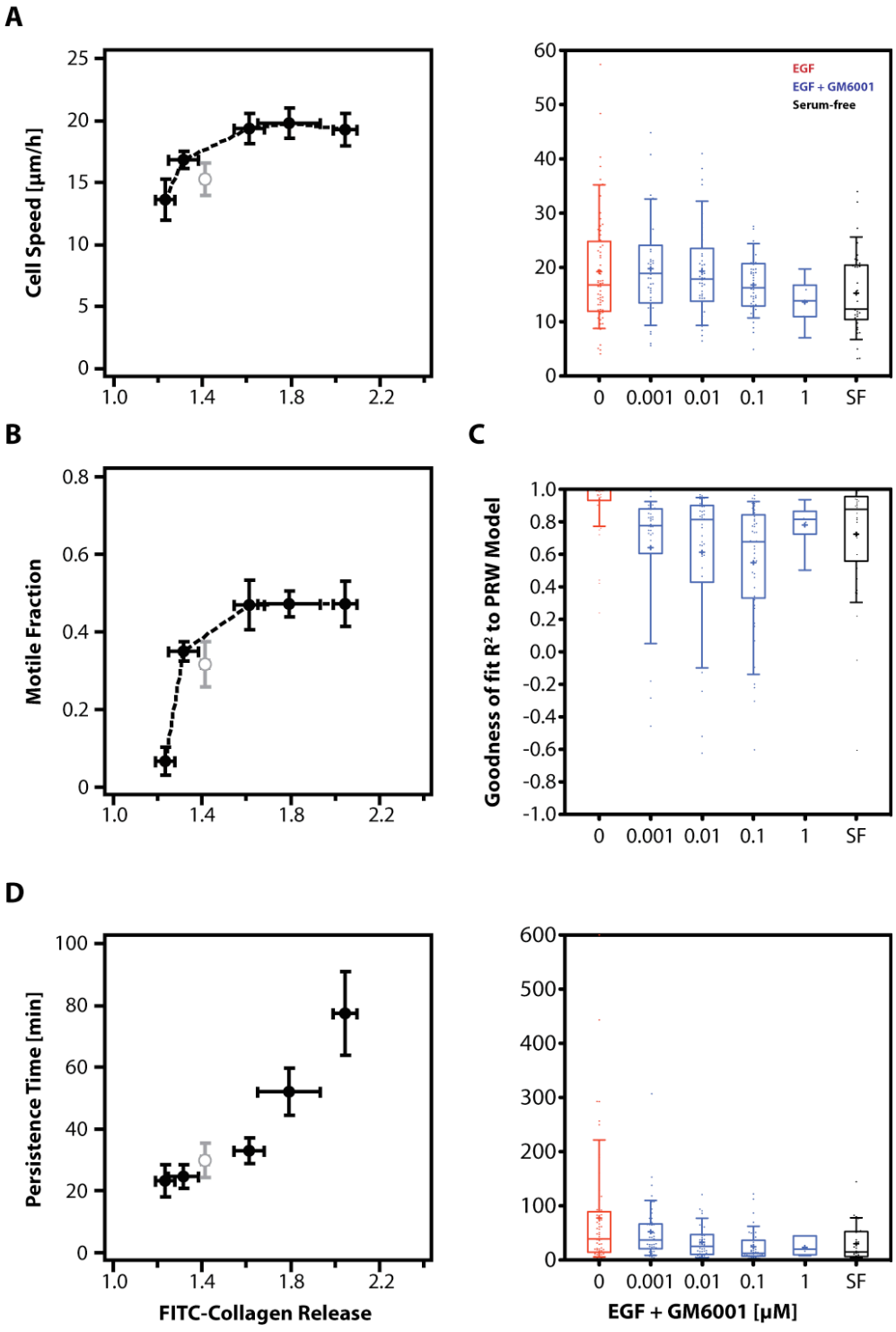

Figure 4-12 – Modulation of MMP activity results in correlated modulation of 3D directional persistence. **(A)** Cell speed, **(B)** motile fraction, **(C)** R^2 fit to PRW model and **(D)** persistence times of cells migrating in 3.0 mg/ml collagen matrices in presence of various

concentrations of GM6001 and 50 ng/ml EGF. Migration data was plotted against FITC-collagen release values determined in Figure 4-11. Data points in grey for (A), (B), (D) indicate migration data in serum-free condition at 3.0 mg/ml matrix concentration from Figure 4-3, B and 4-4, A. Data shown as mean ± SEM (A and D, left; and B) or in a box-and-whisker plot (edges representing 25th and 75th percentiles and whiskers representing 10th and 90th percentiles) overlayed with a distribution of each cell's random motility coefficient (A and D, right; and C). N = 3 biological samples for (B) and N = 7-64 motile cells for (A) and (C-D). R^2 = 0.92 for linear fit in (D). Figure modified and reprinted from the Molecular Biology of the Cell [63].

proteolysis regulates directional persistence in 3D matrices, particularly in high matrix concentrations. Once a threshold for matrix proteolysis is reached, further changes did not modulate cell speed significantly as shown in Figure 4-4, A and 4-12, A, suggesting that matrix proteolysis does not have a significant effect on the cell-intrinsic increase in cell speed of cells described as motile. These results and the inability of EGF to enhance directional persistence at low matrix concentrations (Figure 4-4, B) suggest that the relative contribution of EGF-induced cell speed and directional persistence to overall cell dispersion that is mediated by proteolysis is highly dependent on matrix properties.

4.4. Discussion

Tumor invasion involves complex interactions between intrinsic cell motility behavior and extrinsic factors in the extracellular matrix environment. In many tumor types, cell motility and invasion behavior are strongly influenced by EGF family ligands [5, 6], and multiple processes involved in cell locomotion [7, 8] are regulated by EGFR activation – including cell-intrinsic biophysical mechanisms [9] as well as proteolytic effects on cell-extrinsic matrix properties [20-22]. Since these various processes are regulated by diverse sets of molecular components and pathways [3], it is important to parse the relative contributions of EGF-induced effects on intrinsic cell behavior versus behavior governed by EGF-induced extrinsic matrix modulation.

To obtain cell speed and directional persistence of individual migrating cells driven by EGF-induced motility and matrix proteolysis, we generated real-time 3D movies of glioblastoma cell migration sparsely embedded in a 3D matrix. Detailed analysis of the cell

tracks and the application of the persistent random walk model lead us to conclude that the stimulatory effects of EGF arose from a concomitant increase in motility, cell speed, and matrix concentration-dependent directional persistence (Figure 4-3, B and C; Figure 4-4). Interestingly, translocation speed of moving cells was not significantly influenced by matrix density, while the overall motility was substantively affected since fraction of motile cells decreased with increasing matrix density. Although cell speed increased at all matrix concentrations assessed, EGF enhanced directional persistence only at high concentrations. Therefore, while cell speed was the sole contributor of EGF-induced cell dispersion at low concentrations, directional persistence was the predominant contributor at high concentrations. Analogous real-time 2D movies demonstrated that these cells exhibit increased cell speed but decreased directional persistence upon EGF stimulation (Figure 4-5, B and C; Figure 4-6), similar to the effect of EGF on fibroblasts [34]. The modest magnitude of these 2D effects are likely due to a background PDGF autocrine loop present in U87MG cells [53]. The crucial finding, nevertheless, is that EGF yields a qualitatively opposite effect on persistence in 3D versus 2D.

2D cell migration does not require MMP activity and matrix proteolysis; cell migration was unaffected upon treatment with an MMP inhibitor (Figure 4-9) while 3D cell migration is dependent on matrix proteolysis. Therefore, we hypothesized that, while cell speed is increased as part of the cell-intrinsic, proteolysis-independent programming in both environments, the observed dimensionality-dependent regulation of directional persistence arises from extrinsic sources: when embedded in a 3D proteolysis-dependent environment, EGF induces an integrated cell-intrinsic (to lower persistence) and cell-extrinsic response (to enhance persistence), where the cell-extrinsic response dominates. This idea was supported by highly matrix concentration-dependent cell dispersion and directional persistence in unstimulated conditions (Figure 4-3, C; Figure 4-4, B; Figure 4-10, A). Further detailed analysis of unstimulated cell migration indicates that low persistent movement is governed by matrix confinement (Figure 4-10, C), supporting that the cell-extrinsic response arises from EGF-induced matrix proteolysis, whose role is to clear extracellular steric barriers to enhance cell migration. Quantitative modulation of matrix proteolysis using a broad MMP inhibitor demonstrated a high correlation between matrix proteolysis and directional persistence (Figure 4-12, D) confirming that the cell-

extrinsic increase in directional persistence is modulated by matrix proteolysis. Translocational speed of motile cells, however, was not affected by modulation of matrix proteolysis once a proteolysis threshold was reached, consistent with the matrix concentration-independent cell speed response measured in Figure 4-4, A. Taken together, we conclude that matrix proteolysis governs directional persistence in high matrix concentration and that overall contribution of matrix proteolysis to cell dispersion mediated through directional persistence, and not cell speed, is dependent on matrix concentration.

Interestingly, neither 2D nor 3D cell speed exhibited a significant dependence on matrix properties despite a variation of 1000-fold ligand density or 20-fold matrix stiffness (Figure 4-1). Such variation has been demonstrated to strongly influence epithelial and fibroblast-like cell migration [15, 44, 54]. We hypothesize here that U87MG cells may not follow such migratory patterns, or more likely, that the matrix property variations were not sufficient to display a change in cell speed. Nevertheless, independence of cell speed on matrix ligand density or stiffness facilitated our ability to parse the effects of matrix steric hindrance and proteolytic degradation on directional persistence.

We focused our study on a human glioblastoma line due to its highly invasive and migratory properties in *in vitro* collagen matrices and physiological responsiveness to EGF; amplification and overexpression of EGFR are observed in 50% of glioblastoma patients and correlate with poor prognosis [55]. Surgical resection of high-grade glioblastomas is ineffective as they display a diffuse, single-cell invasion pattern, which was modeled by our *in vitro* migration assay. Our assays illustrated that MMP activity is critically important for invasion consistent with the prominent portrayal of MMPs in the literature as therapeutic targets for glioblastoma treatment. Furthermore, parsing of cell-intrinsic and proteolysis-mediated cell-extrinsic effects may be facilitated by our results suggesting that U87MG cells do not appear to undergo mesenchymal-amoeboid transition in presence of high levels of MMP inhibitors as described previously in fibrosarcomas and breast carcinomas [23]. This result, however, could be due to higher matrix densities and smaller pore sizes used in our study here compared to previous work. While the bulk matrix elastic moduli involved in these studies were comparable to those of the brain [56], the native brain environment lacks high concentrations of fibrillar collagens [40]. Nonetheless, the glioblastoma invasion

environment, including the perivascular space, is reported to contain laminin, fibronectin, and collagens [41], much of which is secreted by the tumor cells themselves. In our experiments, U87MG cells were seeded in the collagen matrix for a total of 24 hours before imaging, making it likely that the cells had conditioned their environment by secreting matrix proteins. In addition, glioblastomas are reported to express $\alpha_2\beta_1$, fibrillar collagen binding integrins; the β_1 subunit has plays an important role in glioblastoma biology [57]. U87MG cells expressed collagen I specific proteinases (Figure 4-8, A and B) and MMP-2 (data not shown).

The scope of this study was to identify the net effect of EGF stimulation in regulating motility and proteolysis-mediated migratory behavior. Thus, questions, such as what the detailed molecular mechanism of the signaling pathways downstream of EGF inducing protease release are, as well as how these cell-intrinsic and extrinsic regulation of persistence convoluted to give rise to an increase in persistence, were left as interesting avenues for future research. Many downstream components of the EGF receptor have been shown to induce expression and activation of MMPs and other proteinases while activating the intrinsic motility machinery. They include downstream effectors such as PI3K, Rac1 and MAPK, and transcription factors like AP-1 [58-61]. High spatial and temporal resolution imaging studies of cell protrusion and matrix degradation in presence of molecular manipulations could be powerful in parsing the mechanisms of directional persistence regulation. Most interestingly, it has been suggested that activated MMP-1 acts on collagen fibrils by moving along the fiber in a biased diffusion while acting as a molecular ratchet tethered to the cell surface [62]. This directed proteolysis of molecular scale might significantly contribute to polarized cell protrusions in presence of the 3D extracellular matrix, effectively governing 3D migration persistence. EGF-induced increase in MMP-1 release could intensify this effect, which contributes to the increase in directional persistence in high matrix concentration environment.

4.5. References

1. Bublil, E.M. and Y. Yarden, *The EGF receptor family: spearheading a merger of signaling and therapeutics.* Curr Opin Cell Biol, 2007. **19**(2): p. 124-34.
2. Yarden, Y., *The EGFR family and its ligands in human cancer. signalling mechanisms and therapeutic opportunities.* Eur J Cancer, 2001. **37 Suppl 4**: p. S3-8.
3. Wells, A., *Tumor invasion: role of growth factor-induced cell motility.* Adv Cancer Res, 2000. **78**: p. 31-101.
4. Yarden, Y. and M.X. Sliwkowski, *Untangling the ErbB signalling network.* Nat Rev Mol Cell Biol, 2001. **2**(2): p. 127-37.
5. Wells, A., *EGF receptor.* Int J Biochem Cell Biol, 1999. **31**(6): p. 637-43.
6. Wells, A., et al., *Growth factor-induced cell motility in tumor invasion.* Acta Oncol, 2002. **41**(2): p. 124-30.
7. Lauffenburger, D.A. and A.F. Horwitz, *Cell migration: a physically integrated molecular process.* Cell, 1996. **84**(3): p. 359-69.
8. Ridley, A.J., et al., *Cell migration: integrating signals from front to back.* Science, 2003. **302**(5651): p. 1704-9.
9. Maheshwari, G., et al., *Biophysical integration of effects of epidermal growth factor and fibronectin on fibroblast migration.* Biophys J, 1999. **76**(5): p. 2814-23.
10. Condeelis, J., R.H. Singer, and J.E. Segall, *The great escape: when cancer cells hijack the genes for chemotaxis and motility.* Annu Rev Cell Dev Biol, 2005. **21**: p. 695-718.
11. Huang, J., et al., *Transactivation of the epidermal growth factor receptor by formylpeptide receptor exacerbates the malignant behavior of human glioblastoma cells.* Cancer Res, 2007. **67**(12): p. 5906-13.
12. Lal, A., et al., *Mutant epidermal growth factor receptor up-regulates molecular effectors of tumor invasion.* Cancer Res, 2002. **62**(12): p. 3335-9.
13. VanMeter, T.E., et al., *The role of matrix metalloproteinase genes in glioma invasion: co-dependent and interactive proteolysis.* J Neurooncol, 2001. **53**(2): p. 213-35.
14. Wolf, K. and P. Friedl, *Functional imaging of pericellular proteolysis in cancer cell invasion.* Biochimie, 2005. **87**(3-4): p. 315-20.
15. Zaman, M.H., et al., *Migration of tumor cells in 3D matrices is governed by matrix stiffness along with cell-matrix adhesion and proteolysis.* Proc Natl Acad Sci U S A, 2006. **103**(29): p. 10889-94.
16. Wolf, K. and P. Friedl, *Molecular mechanisms of cancer cell invasion and plasticity.* Br J Dermatol, 2006. **154 Suppl 1**: p. 11-5.
17. Mochizuki, S. and Y. Okada, *ADAMs in cancer cell proliferation and progression.* Cancer Sci, 2007. **98**(5): p. 621-8.
18. Yana, I. and M. Seiki, *MT-MMPs play pivotal roles in cancer dissemination.* Clin Exp Metastasis, 2002. **19**(3): p. 209-15.
19. Nakada, M., Y. Okada, and J. Yamashita, *The role of matrix metalloproteinases in glioma invasion.* Front Biosci, 2003. **8**: p. e261-9.
20. Alper, O., et al., *Epidermal growth factor receptor signaling and the invasive phenotype of ovarian carcinoma cells.* J Natl Cancer Inst, 2001. **93**(18): p. 1375-84.
21. Ellerbroek, S.M., L.G. Hudson, and M.S. Stack, *Proteinase requirements of epidermal growth factor-induced ovarian cancer cell invasion.* Int J Cancer, 1998. **78**(3): p. 331-7.

22. Rooprai, H.K., et al., *The effects of exogenous growth factors on matrix metalloproteinase secretion by human brain tumour cells.* Br J Cancer, 2000. **82**(1): p. 52-5.
23. Wolf, K., et al., *Compensation mechanism in tumor cell migration: mesenchymal-amoeboid transition after blocking of pericellular proteolysis.* J Cell Biol, 2003. **160**(2): p. 267-77.
24. Binder, D.K. and M.S. Berger, *Proteases and the biology of glioma invasion.* J Neurooncol, 2002. **56**(2): p. 149-58.
25. Zaman, M.H., P. Matsudaira, and D.A. Lauffenburger, *Understanding effects of matrix protease and matrix organization on directional persistence and translational speed in three-dimensional cell migration.* Ann Biomed Eng, 2007. **35**(1): p. 91-100.
26. Martin, M.D. and L.M. Matrisian, *The other side of MMPs: protective roles in tumor progression.* Cancer Metastasis Rev, 2007. **26**(3-4): p. 717-24.
27. Matrisian, L.M., G.W. Sledge, Jr., and S. Mohla, *Extracellular proteolysis and cancer: meeting summary and future directions.* Cancer Res, 2003. **63**(19): p. 6105-9.
28. Kumar, N., et al., *Multi-Pathway Model Enables Prediction of Kinase Inhibitor Cross-Talk Effects on Migration of Her2-Overexpressing Mammary Epithelial Cells.* Mol Pharmacol, 2008.
29. Rosano, L., et al., *Combined targeting of endothelin A receptor and epidermal growth factor receptor in ovarian cancer shows enhanced antitumor activity.* Cancer Res, 2007. **67**(13): p. 6351-9.
30. Willmarth, N.E. and S.P. Ethier, *Autocrine and juxtacrine effects of amphiregulin on the proliferative, invasive, and migratory properties of normal and neoplastic human mammary epithelial cells.* J Biol Chem, 2006. **281**(49): p. 37728-37.
31. Huang, P.H., et al., *Uncovering therapeutic targets for glioblastoma: a systems biology approach.* Cell Cycle, 2007. **6**(22): p. 2750-4.
32. Lamszus, K., et al., *Inhibition of glioblastoma angiogenesis and invasion by combined treatments directed against vascular endothelial growth factor receptor-2, epidermal growth factor receptor, and vascular endothelial-cadherin.* Clin Cancer Res, 2005. **11**(13): p. 4934-40.
33. Harms, B.D., et al., *Directional persistence of EGF-induced cell migration is associated with stabilization of lamellipodial protrusions.* Biophys J, 2005. **88**(2): p. 1479-88.
34. Ware, M.F., A. Wells, and D.A. Lauffenburger, *Epidermal growth factor alters fibroblast migration speed and directional persistence reciprocally and in a matrix-dependent manner.* J Cell Sci, 1998. **111 (Pt 16)**: p. 2423-32.
35. Bear, J.E., et al., *Negative regulation of fibroblast motility by Ena/VASP proteins.* Cell, 2000. **101**(7): p. 717-28.
36. Harley, B.A., et al., *Micro-Architecture of Three-Dimensional Scaffolds Influences Cell Migration Behavior via Junction Interactions.* Biophys J, 2008. **In press**.
37. Dickinson, R.B. and R.T. Tranquillo, *Optimal Estimation of Cell-Movement Indexes from the Statistical-Analysis of Cell Tracking Data.* Aiche Journal, 1993. **39**(12): p. 1995-2010.
38. Wolf, K., et al., *Multi-step pericellular proteolysis controls the transition from individual to collective cancer cell invasion.* Nat Cell Biol, 2007. **9**(8): p. 893-904.

39. Han, J. and J.C. Daniel, *Biosynthesis of type VI collagen by glioblastoma cells and possible function in cell invasion of three-dimensional matrices.* Connect Tissue Res, 1995. **31**(2): p. 161-70.
40. Nakada, M., et al., *Molecular targets of glioma invasion.* Cell Mol Life Sci, 2007. **64**(4): p. 458-78.
41. Gladson, C.L., *The extracellular matrix of gliomas: modulation of cell function.* J Neuropathol Exp Neurol, 1999. **58**(10): p. 1029-40.
42. Bellail, A.C., et al., *Microregional extracellular matrix heterogeneity in brain modulates glioma cell invasion.* Int J Biochem Cell Biol, 2004. **36**(6): p. 1046-69.
43. Giese, A., et al., *Cost of migration: invasion of malignant gliomas and implications for treatment.* J Clin Oncol, 2003. **21**(8): p. 1624-36.
44. Palecek, S.P., et al., *Integrin-ligand binding properties govern cell migration speed through cell-substratum adhesiveness.* Nature, 1997. **385**(6616): p. 537-40.
45. Cukierman, E., et al., *Taking cell-matrix adhesions to the third dimension.* Science, 2001. **294**(5547): p. 1708-12.
46. Kumar, N., et al., *A high-throughput migration assay reveals HER2-mediated cell migration arising from increased directional persistence.* Biophys J, 2006. **91**(4): p. L32-4.
47. Pankov, R., et al., *A Rac switch regulates random versus directionally persistent cell migration.* J Cell Biol, 2005. **170**(5): p. 793-802.
48. Dunn, G.A., *Characterising a kinesis response: time averaged measures of cell speed and directional persistence.* Agents Actions Suppl, 1983. **12**: p. 14-33.
49. Gail, M.H. and C.W. Boone, *The locomotion of mouse fibroblasts in tissue culture.* Biophys J, 1970. **10**(10): p. 980-93.
50. Wang, H., et al., *Phospholipase Cgamma/diacylglycerol-dependent activation of beta2-chimaerin restricts EGF-induced Rac signaling.* Embo J, 2006. **25**(10): p. 2062-74.
51. Yip, S.C., et al., *The distinct roles of Ras and Rac in PI 3-kinase-dependent protrusion during EGF-stimulated cell migration.* J Cell Sci, 2007. **120**(Pt 17): p. 3138-46.
52. Fukuda, S., et al., *Focal cerebral ischemia induces active proteases that degrade microvascular matrix.* Stroke, 2004. **35**(4): p. 998-1004.
53. Ma, D., et al., *Autocrine platelet-derived growth factor-dependent gene expression in glioblastoma cells is mediated largely by activation of the transcription factor sterol regulatory element binding protein and is associated with altered genotype and patient survival in human brain tumors.* Cancer Res, 2005. **65**(13): p. 5523-34.
54. Gupton, S.L. and C.M. Waterman-Storer, *Spatiotemporal feedback between actomyosin and focal-adhesion systems optimizes rapid cell migration.* Cell, 2006. **125**(7): p. 1361-74.
55. Shinojima, N., et al., *Prognostic value of epidermal growth factor receptor in patients with glioblastoma multiforme.* Cancer Res, 2003. **63**(20): p. 6962-70.
56. Georges, P.C., et al., *Matrices with compliance comparable to that of brain tissue select neuronal over glial growth in mixed cortical cultures.* Biophys J, 2006. **90**(8): p. 3012-8.
57. Paulus, W., et al., *Diffuse brain invasion of glioma cells requires beta 1 integrins.* Lab Invest, 1996. **75**(6): p. 819-26.
58. Kajanne, R., et al., *EGF-R regulates MMP function in fibroblasts through MAPK and AP-1 pathways.* J Cell Physiol, 2007. **212**(2): p. 489-97.

59. Mamoune, A., et al., *DU145 human prostate carcinoma invasiveness is modulated by urokinase receptor (uPAR) downstream of epidermal growth factor receptor (EGFR) signaling.* Exp Cell Res, 2004. **299**(1): p. 91-100.
60. Van Meter, T.E., et al., *Induction of membrane-type-1 matrix metalloproteinase by epidermal growth factor-mediated signaling in gliomas.* Neuro Oncol, 2004. **6**(3): p. 188-99.
61. Zhuge, Y. and J. Xu, *Rac1 mediates type I collagen-dependent MMP-2 activation. role in cell invasion across collagen barrier.* J Biol Chem, 2001. **276**(19): p. 16248-56.
62. Saffarian, S., et al., *Interstitial collagenase is a Brownian ratchet driven by proteolysis of collagen.* Science, 2004. **306**(5693): p. 108-11.
63. Kim, H.-D., et al., *Epidermal growth factor-induced enhancement of glioblastoma cell migration in 3D arises from an intrinsic increase in speed but an extrinsic matrix- and proteolysis-dependent increase in persistence.* Mol Biol Cell, 2008. **19**(10): p. 4249-59.

CHAPTER 5

Role of microarchitecture in quasi-3D fibroblast migration in collagen-glycosaminoglycan scaffolds

Experimental model systems determine the physiological relevance of discoveries. It has been recently suggested that 1-D or 'quasi-3D' constructs may provide a better model system for cell migration studies. In this chapter, physical properties of the porous scaffolds are varied to find surprising effects regarding the regulatory role of construct microarchitecture on fibroblast migration.

5.1. Introduction

Cell motility is critical in many physiological and pathological processes as well as in tissue engineering applications. Cell migration is modulated by a complex, spatio-temporally integrated set of biophysical mechanisms that are influenced not only by the biochemistry of extracellular and intracellular signaling, but also by the biophysics of the surrounding extracellular environment [3, 4]. Efforts in studying the effect of the extracellular environment on cell migratory behavior have led to an improved understanding of how substrate features, especially substrate stiffness, affect migration through changes in cytoskeletal organization and applied traction forces [5-7]. However, the vast majority of studies probing cell-substrate interactions have done so using artificial two-dimensional surfaces. As a result, our understanding of the critical biochemical and biophysical parameters that affect cell motility in three-dimensional (3D) environments is quite limited. Extending such studies to the third dimension requires considering the *in vivo* extracellular environment in which cell behavior is regulated.

As discussed in chapter 1, one of the main components of the 3D *in vivo* extracellular environment is the extracellular matrix (ECM), a complex network of structural matrix protein fibers and glycosaminoglycans [4]. In addition to providing biochemical stimuli,

the ECM provides three-dimensional microstructural and mechanical cues, both of which have been shown to significantly influence 3D cell migration in recent computational and experimental studies [8, 9]. Additionally, heterogeneities within the 3D ECM, such as steric hindrances imposed on cell movement by the dense ECM network, may introduce geometry-dependent effects on migratory behavior [10, 11]; the fiber thickness and the pore size of an analog of this in vivo ECM microenvironment may play a role in regulating migratory behavior. Manipulation of ECM geometries on 2D substrata using lithographic and micro-printing techniques have demonstrated that microstructural guidance affects cell migration and its related cellular functions [12, 13]. Such 'contact guidance' by the extracellular matrix has been demonstrated *in vivo* in recent intravital imaging studies of carcinoma cells in the mammary fat pad. These studies show preferential chemotactic movement of invasive carcinoma cells along thick collagen fibers towards blood vessels [14]. In the lymph node paracortex, the porous micro-architecture of collagen and fibronectin bundles ensheathed by fibroblastic reticular cells has been shown to significantly influence T-cell migration behavior and is believed to facilitate colocalization of T-cells with dendritic cells [15]. Contact guidance cues have also been observed governing T-cell motility through composite macroporous poly(ethylene glycol) (PEG) hydrogel scaffolds infused with collagen *in vitro* [16]. These studies indicate that *in vivo* and *in vitro* ECM geometries and micro-architecture play a significant role in modulating cell migration. However, it is still unknown how specific parameters of an ECM microstructure influence cell migration, especially in physiologically relevant 3D ECM analogs.

3D tissue engineering constructs provide a powerful model system for studying cell migration. For tissue engineering purposes, understanding extracellular influences on cell motility within physiologically relevant three-dimensional constructs can aid the design of future bioactive constructs since an initially acellular scaffold must be rapidly cellularized either *in vitro* or *in vivo*. Controlling cell motility via modulation of the local engineered extracellular environment process is also a critical stepping-stone in the development of the next generation of bioactive tissue engineering scaffolds. A homologous series of controlled scaffold microenvironments provides an ideal construct to explore the individual influence of specific extracellular cues on cell motility.

Three-dimensional tissue engineering scaffolds are analogs of the extracellular matrix present in all tissues and organs. The scaffold acts as a physical support structure and insoluble regulator of cell activity. Notably, scaffold microstructure (porosity, mean pore size, pore shape, interconnectivity, specific surface area) [2, 17, 18] and mechanical properties (Young's modulus) [19-22] have been shown to significantly influence cell behaviors such as adhesion, growth and differentiation and to affect the bioactivity of scaffolds used for *in vivo* tissue regeneration applications [23-25]. However, quantitative study of individual cell behavior within a three-dimensional scaffold construct requires understanding the local extracellular environment of the individual cells through accurate compositional, microstructural, and mechanical characterization. The lack of standardized three-dimensional constructs with well-characterized and independently variable mechanical, compositional, and microstructural properties have previously made it difficult to draw quantitative conclusions concerning the independent effect of the specific extracellular features on cell behavior.

In this investigation, we use highly porous collagen-glycosaminoglycan (CG) scaffolds fabricated through a freeze drying, or lyophilization, process as a model ECM system [1]. These low-density, open-cell foams are biodegradable, are characterized by an interconnected pore network defined by fibers of collagen-GAG coprecipitate termed struts, and provide an ideal environment for *in vitro* cell behavior studies. CG scaffolds have previously been shown to possess physiologically relevant pore sizes, degradation rates, and chemical compositions when used to induce *in vivo* regeneration of skin and peripheral nerves [24, 25]. We have recently developed improved fabrication methods that enable production of CG scaffolds with a uniform, equiaxed, polygonal pores of controlled pore size [2, 26]. The microstructure and mechanical behavior of these scaffolds have previously been characterized [2, 26-28], allowing a series of standardized and well-defined microstructural environments to be presented to individual cells within the scaffold. Most significant for this investigation, the average pore size and strut modulus (and so the scaffold modulus) can be varied independently of one other.

Manipulation of CG scaffold microstructural (pore size) and mechanical (scaffold Young's modulus) properties was used to address the question of how cell migration is influenced by the surrounding microenvironment and what the critical microstructural

cues that affect migratory behavior within a physiologically relevant ECM analog are. By quantifying 3D migratory behavior of NR6 mouse fibroblasts in CG scaffolds of varying pore sizes, we found that cell migration is dependent on the pore size of the CG scaffold. Independent variation of scaffold strut modulus found a biphasic relationship between cell speed and strut modulus, and confirmed that the microstructural (pore size) dependence of cell migration is not due to deviations in scaffold strut flexural rigidity with changing pore size. Finally, more in-depth analysis of individual migration tracks revealed that an increased density of junction points between the scaffold struts (termed junction density) is correlated with increased cell speed and changes in cell persistence. Our results also show that cell speed is significantly higher along the struts versus at the strut junctions regardless of pore size. Our findings, on the whole, establish the relevance of junctional microstructure in guiding and enhancing cell migration for both exploratory and design purposes.

5.2. Materials and Methods

5.2.1. Cell culture

Cell migration assays were performed with NR6 mouse fibroblasts, a cell line derived from the Swiss 3T3 fibroblast line [29]. Cells were maintained in MEM-α supplemented with 2 mM L-glutamine, 7.5% fetal bovine serum, 100 U/ml penicillin and 100 μg/ml streptomycin, 0.1 mM non-essential amino acids, and 1 mM sodium pyruvate (Complete medium; all components from Invitrogen, Carlsbad, CA).

5.2.2. Collagen-GAG scaffold fabrication and crosslinking

Collagen-glycosaminoglycan (CG) scaffolds were fabricated from a suspension consisting of type I collagen (0.5% wt) isolated from bovine tendon (Integra LifeSciences, Plainsboro, NJ) and chondroitin 6-sulfate (0.05% wt) isolated from shark cartilage (Sigma-Aldrich, St. Louis, MO) in a solution of 0.05M acetic acid (pH 3.2) via a lyophilization process described previously [2, 25, 26]. In short, the aqueous suspension of precipitated collagen-GAG is

solidified at a constant cooling rate from room temperature to a final freezing temperature, resulting in a continuous, interpenetrating network of ice crystals surrounded by the CG co-precipitate. Sublimation of the ice crystals produces the highly porous scaffold structure defined by individual fibers of CG, termed struts. Final freezing temperatures of -10°C, -20°C, -30°C, and -40°C were used to produce scaffolds of different mean pore sizes (96, 110, 121, and 151 μm, respectively, Table 5-1). These scaffolds have previously been found to be microstructurally uniform with equiaxed pores throughout the scaffold defined by struts of uniform thickness along their length [2, 28]. Finally, scaffolds were crosslinked using the dehydrothermal-based (DHT) process at 105°C for 24 hours, as previously described [25] and cut into 6mm diameter disks. To vary scaffold strut modulus independently of pore size, we further crosslinked scaffolds of 96 μm mean pore size with varying ratios of 1-ethyl-3-(3-dimethylaminopropyl)carbodiimide (EDAC) to N-hydroxysuccinimide (NHS) (Sigma-Aldrich) to scaffold protein (COOH) as previously described [1]. A series of four DHT and EDAC crosslinking treatments were used: DHT 105^{o}C for 24 hours (DHT105/24), 1:1:5 EDAC:NHS:COOH ratio (EDAC1:1:5), 5:2:5 EDAC:NHS:COOH ratio (EDAC5:2:5), and 5:2:1 EDAC:NHS:COOH ratio (EDAC5:2:1). Scaffold elastic moduli have been shown to be independent of variations in scaffold mean pore size, and individual strut elastic moduli have been previously determined via atomic force microscopy of individual struts (Table 5-2) [1].

5.2.3. Fluorescent labeling of CG scaffolds

For multi-channel imaging of fluorescent cells and scaffolds (Figure 5-1, A), dry scaffolds disks were fluorescently labeled by hydrating the scaffold with 5 μg/ml AlexaFluor 633 carboxylic acid succinimidyl ester (Invitrogen) in phosphate buffered saline (PBS) (Invitrogen) for 1 hour at room temperature. Scaffolds were washed three times with PBS before seeding them with cells and imaging cells at 488 nm excitation as described below and AlexaFluor 633 labeled scaffolds at the 647 nm excitation via confocal microscopy.

5.2.4. 3D time-lapse confocal microscopy assay

NR6 fibroblasts were fluorescently labeled with 10 μM CellTracker Green CMFDA (Invitrogen) in complete medium for 20 minutes, washed twice with PBS, trypsinized, and

resuspended in complete medium. $2.5x10^5$ cells in 10 µl complete medium were seeded onto each side of an unlabeled scaffold disk pre-hydrated in complete medium to a final concentration of $5x10^5$ cells per scaffold. Cells were allowed to attach to the scaffold in an ultra-low attachment 6-well plate (Corning, Inc., Corning, NY) for an hour before the addition of complete medium and incubation for 12 hours [30]. Cell movement was imaged with a PerkinElmer RS-3 confocal microscope at 25x magnification and 488 nm excitation by collecting a 15-minute interval time-lapse series of 100 µm z-stacks with 1 µm spacing over 10 hours for a final field of view of 364 x 246 x 100 µm.

5.2.5. Single cell tracking and quantitative analysis of cell migration

Centroids of fluorescent cells were computed with Imaris (Bitplane, St. Paul, MN) using the built-in 'spots' function, and tracks of individual cells were generated with 'autoregressive motion' tracking algorithms as described previously and discussed in section 2.3.4. (Figure 5-1, B) [8]. Cells that migrate out of the field for more than 5 hours as well as cells undergoing division or blebbing were ignored from further analysis. Cells that moved more than 10 µm over 10 hours were considered motile and their tracks were included in the quantitative analysis. Presented results were robust to the choice of the distance (data not shown). 3D Wind-Rose plots were generated by randomly choosing 40 tracks from the motile population and overlaying the starting coordinates at the origin of the plots to graphically represent average cell dispersion during migration. Average individual cell speeds (S) were calculated from individual cell tracks by averaging the distances over the time interval. Mean squared displacements (MSD) at various time intervals (t) were calculated using the method of non-overlapping intervals [31] and directional persistence time (P) was obtained by fitting it to the persistent random walk model:

$$MSD = 2S^2P[t - P(1 - e^{-t/P})] \qquad \text{(Eq. 1)}$$

Cell speed data from N > 3 biological replicates was represented using box-and-whisker plots where the edges of the boxes represent the 25th and 75th percentile and the error bars represent the 10th and 90th percentile. The line dividing the box represents the median and

the large dot represents the mean of the distribution. Statistical significance ($p < 0.05$) was determined via students' t-test for motile fraction data and via Komogorov-Smirnov test for non-normally distributed data sets, such as cell speed and persistence data.

5.2.6. Cell turning time analysis

Cell tracks were independently analyzed for 'turning' behavior, indicative of migration at a strut junction, versus 'straight' migration behavior, indicative of migration along a strut. Consistently erratic movement over mostly relatively short distances was classified as turning behavior, whereas directional movement with relatively large distances (approximately greater than two cell lengths) was classified as straight motion. Time points that belonging to turning behavior were quantified as 'time spent turning.'

5.2.7. Cellular solids modeling

The complex geometry of scaffolds is difficult to replicate exactly. We have previously used a tetrakaidecahedral unit cell (a fourteen-sided polyhedron) to model the geometry of the CG scaffolds [1, 2, 27, 28, 32]. The tetrakaidecahedron (Figure 5-3, A) packs to fill space and approximates the structural features of low-density foams observed through experiment [32]. The dimensionless measure of total edge length per (unit volume)$^{1/3}$ for the tetrakaidecahedron is nearly identical to that observed for many random cellular structures [33], suggesting that it gives a good representation of the contact guidance cues (individual scaffold struts) provided by the CG scaffold and has been successfully used to model CG scaffold specific surface area and permeability [2, 27]. For scaffolds with variable pore size (d) but constant relative density (ρ^*/ρ_s), the ratio of the scaffold strut thickness and length (l, t) can be described by Eq. 2 [32]:

$$\frac{t_1}{l_1} = \frac{t_2}{l_2} \qquad \text{(Eq. 2)}$$

where t_1 and l_1 are the thickness and length of the struts in scaffold 1 and t_2 and l_2 are those for scaffold 2, which has a different pore size but constant relative density compared to

scaffold 1. Note that the relative density of the scaffold (the density of the scaffold divided by that of the solid CG in the struts) is:

$$\frac{\rho^*}{\rho_s} = \frac{Vol_{solid}}{Vol_{foam}} \propto \frac{l \cdot t^2}{l^3} \propto \left(\frac{t}{l}\right)^2 \qquad \text{(Eq. 3)}$$

The CG scaffold pore microstructure is defined by an interconnected series of CG struts that meet at strut junctions. The spacing between (D_{jxn}) and density of strut junctions (ρ_{jxn}, number of strut junctions per unit cell divided by the volume of a unit cell) within the CG scaffold microstructure can be calculated from the scaffold pore size and tetrakaidecahedral unit cell model geometry:

$$D_{jxn} = l = \frac{d}{2.785} \qquad \text{(Eq. 4)}$$

$$\rho_{jxn} = \frac{6(jxns/UC)}{11.31 \cdot \left(\frac{d}{2.785}\right)^3 (vol/UC)} = \frac{11.459}{d^3} \qquad \text{(Eq. 5)}$$

5.3. Results

5.3.1. Cell migration in three-dimensional CG scaffolds surprisingly decreases as pore size increases.

CG scaffolds exhibit pore sizes that are significantly larger than the characteristic dimension of NR6 fibroblasts (Figure 5-1, A); hence, the cells are not exposed to steric hindrance such as in a dense network of ECM fibers. Rather, cells are forced to migrate along scaffold struts, a phenomenon known as contact guidance. To specifically address the question of how scaffold pore size affects cell migration behavior, we seeded NR6 mouse fibroblasts in CG scaffolds with pore sizes ranging from 96 μm to 151 μm and

T_f, °C	Pore Size, μm	Relative Density	Motile Fraction	Cell speed, μm/hr
-10	151 ± 32	0.0062 ± 0.0005	0.31	6.38 ± 0.50
-20	121 ± 23	0.0061 ± 0.0003	0.36	7.96 ± 0.52
-30	110 ±18	0.0059 ± 0.0003	0.41	9.43 ± 0.53
-40	96 ± 12	0.0058 ± 0.0003	0.69	11.98 ± 0.61

Table 5-1 – T_f varies scaffold pore size, but not relative density. Mean pore size and relative density of the DHT cross-linked CG scaffold variants [2]; motile fraction and cell speed for NR6 fibroblasts within the scaffold variants. Data expressed as Mean ± StDev. Table reprinted from [45] with permission from the Biophysical Society.

tracked single cell migration using 3D time-lapse confocal microscopy. A 10 hour series of 3D volume stacks of fluorescently labeled cells in unlabeled scaffolds was generated, 3D coordinates of centroids of individual cells were determined over time, and individual tracks generated (Figure 5-1, B). Tracks from at least 3 biological replicates show that cells migrating in scaffolds with larger pore sizes exhibit less cell dispersion (Wind-Rose plot, Figure 5-2, A) and are less motile (Figure 5-2, B) than cells migrating in scaffolds with smaller pores. Further quantitation of these tracks shows that cell speed of the motile fraction significantly decreases with increasing scaffold pore size (Table 5-1, Figure 5-2, C); cell speed is reduced almost by half from about 12 μm/h to 6 μm/h over the pore size range from 96 μm to 151 μm.

5.3.2. Changes in strut flexural rigidity are not responsible for dependence of cell speed on scaffold pore size

Previous studies of cell motility on 2D substrates [5] and within 3D gel constructs [8] show that substrate mechanical properties can strongly influence cell motility. We studied whether the influence of scaffold pore size on cell motility was due to changes in differences in scaffold mechanical properties with pore size. Specifically, mechanical features of the individual scaffold struts was considered; cells migrating within the CG scaffolds obtain mechanical cues from the individual struts they are attached to rather than from the network of struts that defines the scaffold microstructure. Previous assessment of the scaffold microstructural and mechanical properties showed that macroscopic scaffold

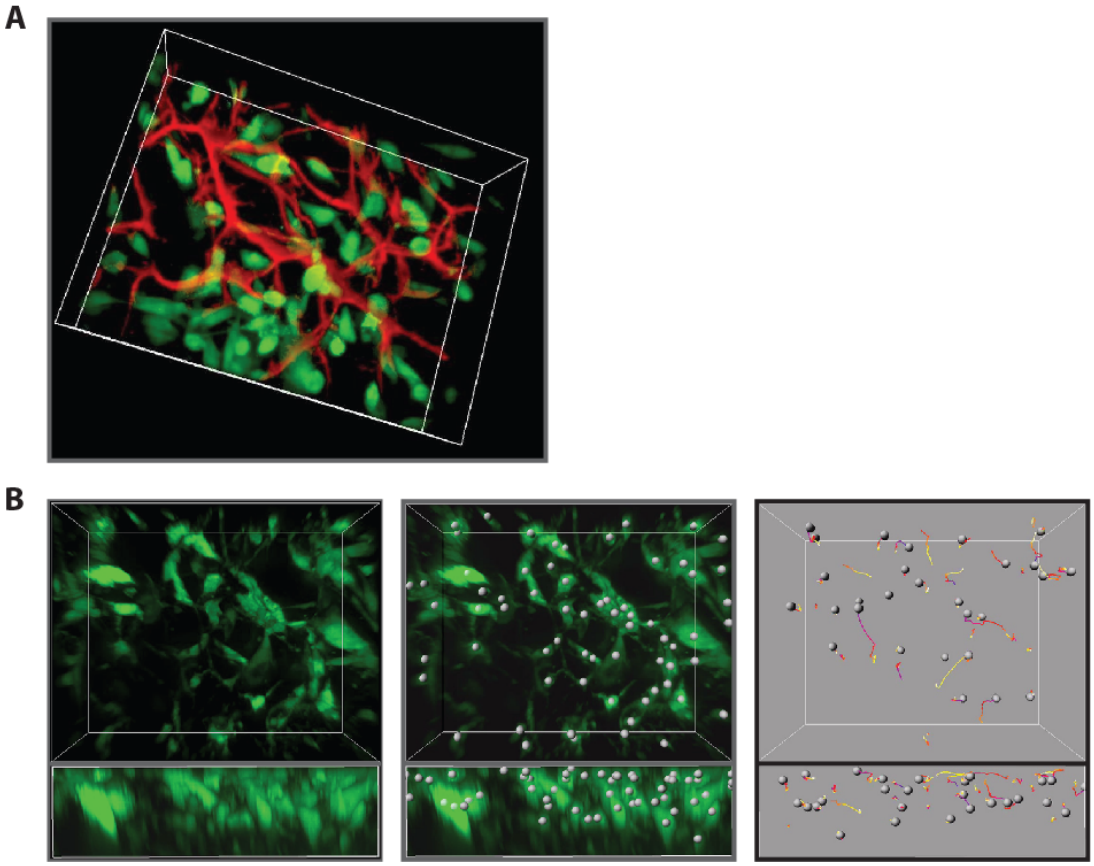

Figure 5-1 – Sparsely seeded NR6 fibroblasts in a three-dimensional, highly porous collagen-glycosaminoglycan scaffold. (A) 3D confocal micrograph of the porous microstructure of a CG scaffold (red) seeded with labeled NR6 cells (green). Note that the scaffold pore size is significantly larger than the dimension of a NR6 fibroblast. **(B)** X-Y and X-Z projections (top and bottom boxes, respectively) of individual cells tracked during migration in a CG scaffold. After capturing images via 3D time-lapse confocal microscopy (left), centroids of fluorescent NR6 cells are computed (center) and individual cell tracks generated (right). Cell tracks are color-mapped from blue to white indicating the beginning to the end of the movement. The mean pore size of CG scaffolds depicted is 96 μm and the 3D image dimensions are 364 x 246 x 100 μm. Figure reprinted from [45] with permission from the Biophysical Society.

Young's modulus (E^*) and relative density (ρ^*/ρ_s) are independent of pore size [1] and that the individual struts within a scaffold had a consistent size and modulus [1, 28]. These results suggest that the scaffold strut modulus (E_s) is uniform for the scaffolds with different pore sizes. While the strut moduli (E_s) and scaffold relative density (ρ^*/ρ_s) are constant for the scaffolds of different pore size, scaffolds with larger pore size have slightly longer ($l_{151\mu m} > l_{96\mu m}$) and thicker ($t_{151\mu m} > t_{96\mu m}$) struts (Eq. 3)(Figure 5-3, A). Hence, the

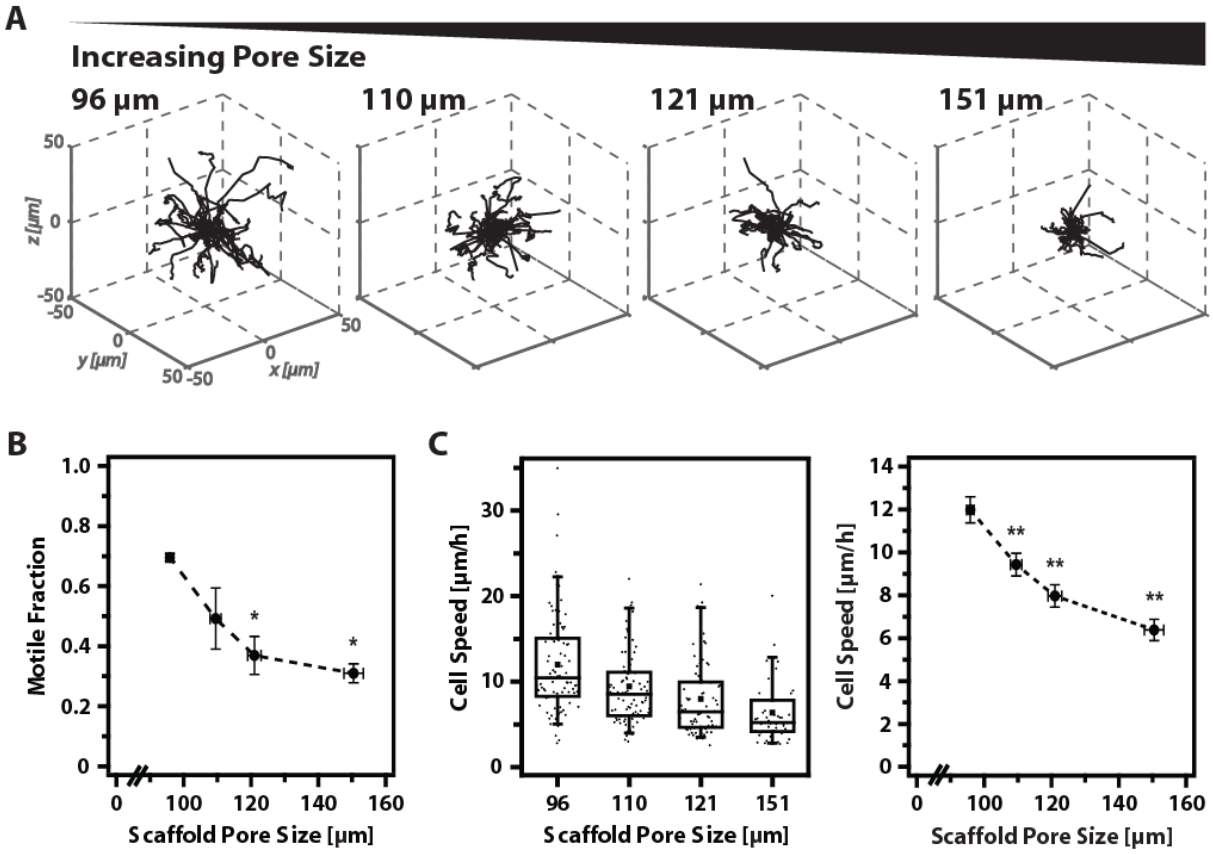

Figure 5-2 – Cell migration behavior decreases with increasing mean scaffold pore size. Tracks of NR6 cells migrating in CG scaffolds with 4 distinct mean scaffold pore sizes (96 – 151 µm) were determined using 3D time-lapse confocal microscopy. **(A)** 3D Wind-Rose plots of randomly chosen cell tracks (40 per condition) graphically represent the average cell dispersion from its starting point. Decreased dispersion is seen as scaffold mean pore size increases, from left to right. **(B)** Fraction of cells determined as motile (see section 5.2.5.) from 3 biological samples were plotted against mean scaffold pore size. Total number of cells tracked, N = 163, 203, 229, 131. **(C)** Box-and-whisker plot of cell speed of each individual cell determined as motile. Mean and standard error of the dataset is plotted as a summary (right) N = 50, 73, 94, 90, from left to right. Statistical significance (*, **) is determined by pair-wise Kolmogorov-Smirnov test for non-normally distributed data sets. Figure reprinted from [45] with permission from the Biophysical Society.

moment of inertia ($I = \pi \cdot t^4/64$) increases with increasing pore size due to a larger strut thickness, translating to a larger strut flexural rigidity ($E_s \cdot I$) with increasing pore size. The flexural rigidity is a measure of how difficult it is for the cell to bend or buckle the strut it is attached to; the flexural rigidity of the scaffold with the largest pore size (151 µm) was calculated to be greater than the scaffold with the smallest (96 µm) pore size by a factor of 6.1 (data not shown).

Crosslinking Treatment	Scaffold Strut Elastic Moduli, MPa	Motile Fraction	Cell speed, μm/hr
DHT (Standard)	5.28 ± 0.25	0.69	10.84 ± 0.54
EDAC1:1:5	10.6 ± 0.50	0.75	12.53 ± 0.42
EDAC5:2:5	11.8 ± 0.56	0.86	15.35 ± 0.56
EDAC5:2:1	38.0 ± 1.8	0.77	12.25 ± 0.64

Table 5-2 – Scaffold crosslinking modification varies strut elastic moduli. Young's moduli of individual, hydrated scaffold struts within CG scaffolds crosslinked via DHT and EDAC/NHS techniques (96 mm pore size) [1]; motile fraction and cell speed for NR6 fibroblasts within the scaffold variants. Data expressed as Mean ± StDev. Figure reprinted from [45].

Contractile fibroblasts have previously been observed to buckle CG scaffold struts [30] so strut flexural rigidity may be a more relevant biophysical parameter to consider for affecting cell behavior than material modulus alone [34]. To test the mechano-sensitive hypothesis that strut flexural rigidity may be responsible for the observed influence of scaffold pore size on cell motility, we experimentally increased strut flexural rigidity by further crosslinking CG scaffolds of constant microstructure (pore size: 96 μm) with EDAC chemistry thereby increasing strut elastic moduli by a factor of 7.2, across a range from 5.3 MPa to 38.0 MPa (Table 5-2); this range was chosen to cover the increase in strut flexural rigidity (factor 6.1) due to changes in scaffold pore size in order to test whether the pore size-dependent effect on cell motility was grounded in mechanical considerations. Migration of NR6 fibroblasts in the series of DHT- and EDAC-crosslinked scaffolds of constant pore size (96 μm) was tracked and the average cell speed was plotted against scaffold strut modulus (Table 5-2, Figure 5-3, B). The migration speed exhibited a subtle biphasic behavior with strut modulus, increasing significantly from 11 to 15 μm/hour for strut moduli between 5 and 12 MPa and then decreasing significantly back to 12 μm/hour for strut moduli of 39 MPa. The expected decrease in cell speed with increasing strut elastic moduli, thereby also increasing strut flexural rigidity, according to the mechano-sensitive hypothesis was not observed, suggesting that the affect of scaffold pore size on cell motility was not due to local changes in strut mechanical properties.

5.3.3. Cellular solids modeling and directional persistence analysis suggest a correlation between junction geometry and pore-size dependent regulation of cell speed

Cellular solids analysis was further used to consider potential local contact guidance cues that may explain the influence of pore size on cell motility. CG scaffolds consist of struts that meet at strut junctions, whose number per unit volume (ρ_{jxn}) and distance between (D_{jxn}) are dependent on the mean scaffold pore size. While the tetrakaidecahedral unit cell was used to quantify the change, the strut junction spacing (D_{jxn}, distance between strut junctions) increases with increasing pore size (Eq. 4) and the strut junction density (ρ_{jxn}, number of junctions per unit volume) decreases with increasing pore size (Eq. 5), regardless of the cellular solids unit cell chosen. Using these relationships, the pore-size dependent cell speed data replotted against junction spacing and especially junction density shows a high degree of correlation (linear regression, $R^2 = 0.901$ and $R^2 = 0.998$, respectively) and suggests that migratory behavior may be governed by the junction geometry of the scaffold (Figure 5-4, A).

To test this novel hypothesis we utilized the persistent random walk (PRW) model to determine persistence times for individual cell tracks within the scaffolds; the persistence times quantify the degree of directionally-productive (termed directional or straight) rather than erratic (termed turning) cell locomotion (Figure 5-4, B). As discussed in section 2.3.5., although the PRW model assumes a homogeneous, isotropic environment (*i.e.*, a gel rather than a scaffold structure), we applied this model here only as a descriptive model in attempt to correlate directionally-productive motion to cell migration along struts. Cells migrating in scaffolds with larger pore sizes exhibit greater persistence times indicating more directional motion. In contrast, persistence times of cells migrating in scaffolds with smaller pore sizes and greater junction density are significantly lower.

5.3.4. Analysis of turning movement confirms that increased cell speed is linked with movement at strut junctions

In an attempt to further correlate cell speed and localization of cells in the scaffold, each cell locomotion path was analyzed in detail by assigning local migration behavior into turning or directional movement categories. Turning movement is correlated to migration

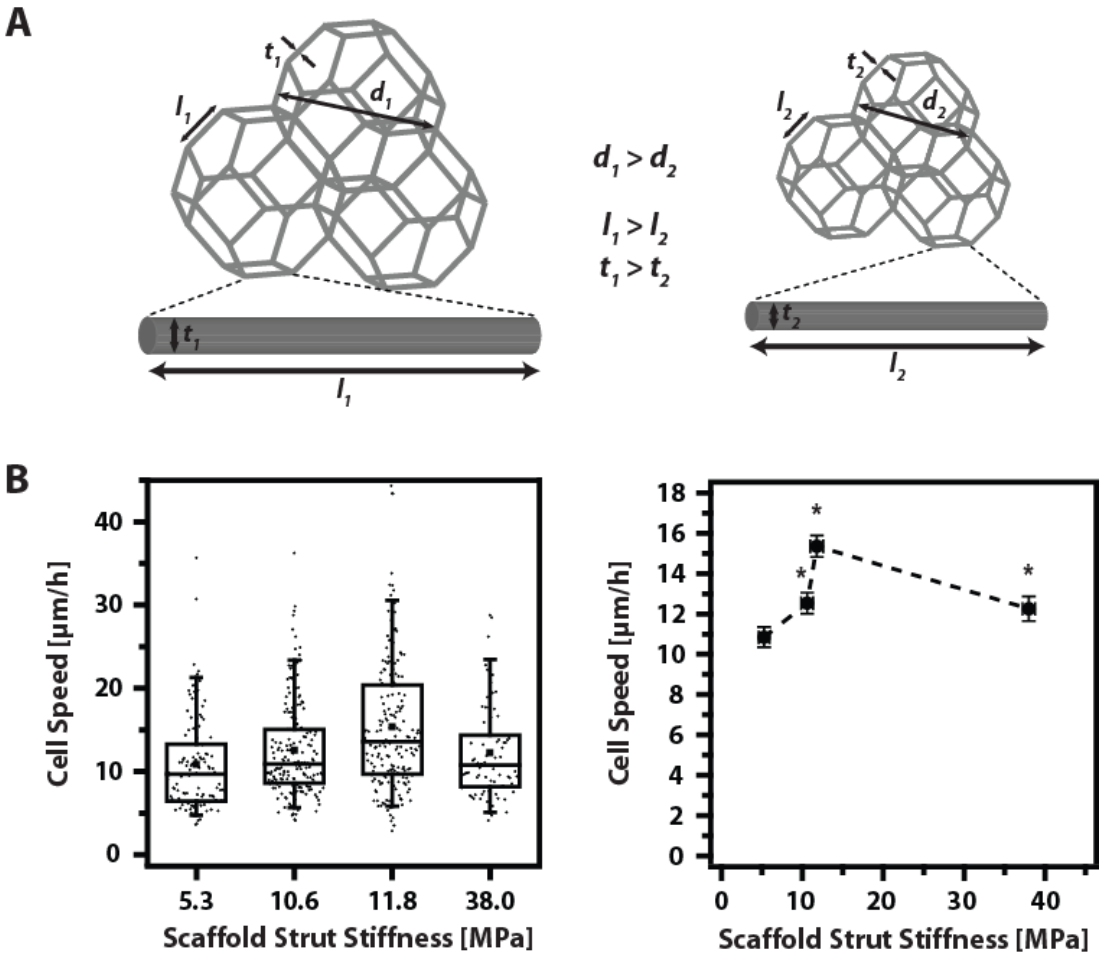

Figure 5-3 – A subtle biphasic relationship is observed between cell migration speed and CG scaffold strut modulus; pore size-dependent variation in cell speed is not explained by variation in scaffold strut flexural rigidity. (A) Tetrakaidecahedral unit cell model for CG scaffold. For a series of scaffolds with a constant relative density, those with larger pore sizes, d_1 (left), exhibit struts that are longer and thicker than a scaffold with smaller pore sizes, d_2 (right). The longer/thicker struts have a greater flexural rigidity ($Es \cdot I$) than the shorter/thinner struts, and would deform less under a constant cell-applied traction force. If changes in strut $Es \cdot I$ explain the pore size-dependent effect on cell motility, cell speed would be expected to decrease with increasing strut modulus. **(B)** Average speed of NR6 cells migrating in scaffolds with a constant microstructure (pore size: 96 μm) but with varying strut modulus (over the same range as due to changes in strut $Es \cdot I$) shown via box-and-whisker (left) and mean and standard error (right) plots. N = 116, 188, 191, 79. Distinct from decreasing cell speed with increasing modulus as predicted if the pore size-dependent effects on motility were due to changes in strut $Es \cdot I$, a subtle biphasic relationship is seen between cell speed and substrate modulus. Statistical significance (*, **) is determined by pair-wise Kolmogorov-Smirnov test for non-normally distributed data sets. Figure reprinted from [45] with permission from the Biophysical Society.

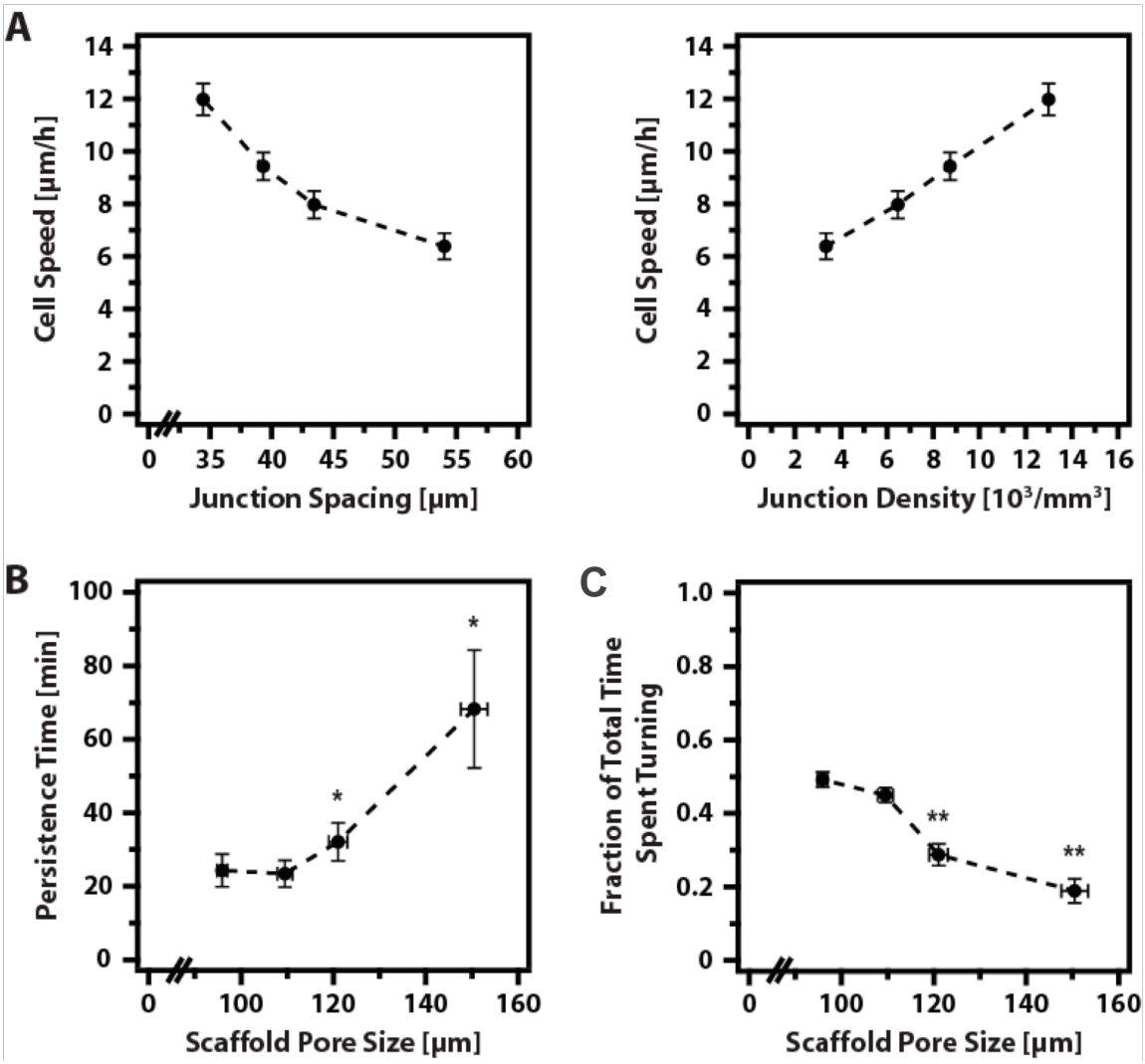

Figure 5-4 – Cell migration appears to be influenced by strut junctions within the scaffold microstructure. (A) Cell speed is replotted against junction spacing (left) and junction density (right), pore-size dependent parameters calculated from the tetrakaidecahedral unit cell model. **(B)** Persistence times of individual cells migrating in scaffolds of varying pore sizes were calculated from the persistent random walk model; for scaffolds with decreasing strut junction density (increasing distance between strut junctions), cells were observed to have increasing persistence times. **(C)** Cell turning was categorized as short, erratic movement and is indicative of migration at junctions. The time spent turning as opposed to moving directionally was determined for each distinct cell track and normalized against the total time spent migrating. The fraction of time cell spent turning was observed to significantly decrease with increasing pore size (decreasing strut junction density, increasing distance between strut junctions). All data is shown in ±SEM. Figure reprinted from [45] with permission from the Biophysical Society.

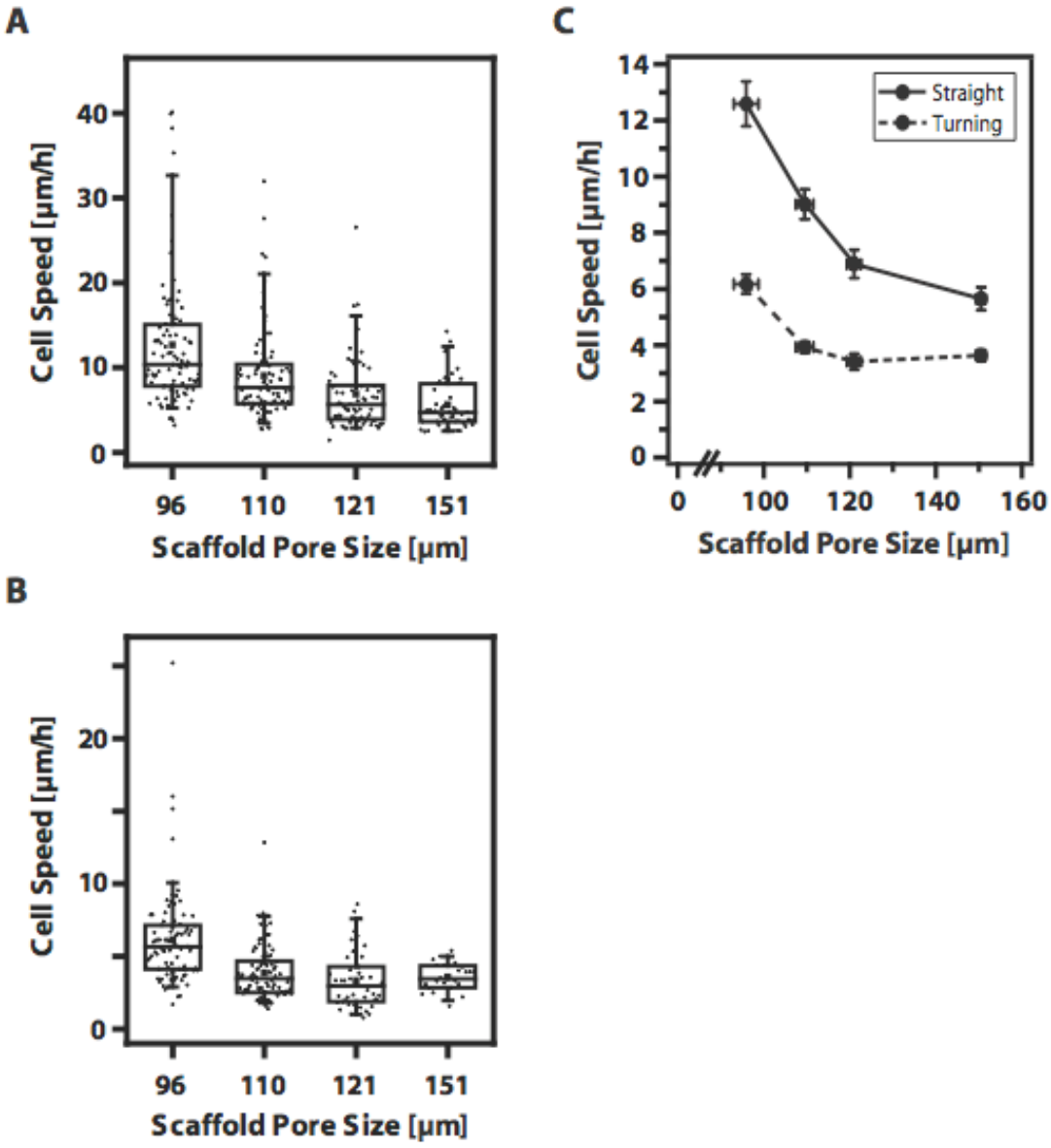

Figure 5-5 – Cell migration speed is significantly influenced by the presence of strut junctions. Average migration speed was determined within each cell track for the periods of time the cell spent **(A)** migrating directionally ("straight," along the strut) versus **(B)** migrating erratically ("turning," at strut junctions). A pore size-dependent effect is observed on cells migrating along the struts or at the junctions; cells are observed to migrate slower as pore size increases (strut junction density decreases, distance between junctions increases) **(C)** Summarized mean and SEM plot of **(A)** and **(B)**. Regardless of scaffold pore size, cell migration speed is significantly faster along the struts ('Straight') than at strut junctions ('Turning'), suggesting that strut junctions play a key role in regulating cell motility through 3D, fibrillar ECM structures. Figure reprinted from [45] with permission from the Biophysical Society.

at strut junctions and directional movement to migration along struts (see section 5.2.6.). Only a small fraction of cells were able to 'jump' from one strut to another (data not shown) validating our binary characterization. The time periods for each individual cell track in these two categories were quantified and normalized to the total track time for each cell path, enabling an overall population-averaged plot of the fraction of total time spent turning by cells within each scaffold variant (Figure 5-4, C). This analysis shows that cells spend almost 50% of their time turning in the smallest pore size scaffold (that with the largest ρ_{jxn}), and that the proportion of their movement time devoted to turning decreases steadily and substantively as scaffold pore size increases (decreasing ρ_{jxn}). In the largest pore size, cells migrate with only 20% of their time spent turning and consequently 80% of their time spent continuing directional movement. Further analysis of cell locomotion during turning versus directional movement showed that cell migration speed along struts (Figure 5-5, A) or at strut junctions (Figure 5-5, B) decreases with increasing pore size. Interestingly, the migration speed along the struts in the 151 mm scaffolds is less than half that for the 96 mm scaffolds. Cell migration speed is significantly faster along the struts than at strut junctions in each scaffold regardless of pore size (Figure 5-5, C). These results suggest a potential mechanistic explanation for our initially counter-intuitive observation that cell motility decreases as scaffold pore size increases (Figure 5-2), as will be described in detail in the following section.

5.4. Discussion

Collagen-glycosaminoglycan (CG) scaffolds have found useful application as ECM analogs for regeneration of a variety of tissue types [24, 25, 35]. Here, we took advantage of the uniform pore microstructure of these standardized, well-characterized CG scaffolds along with the ability to independently vary their pore size and strut modulus to assess how these parameters affect cell motility. Through a comprehensive, quantitative analysis of individual migration tracks of fibroblasts we observed that NR6 fibroblast migration was significantly influenced by the scaffold pore size and scaffold strut modulus (Figures 5-2 and 5-3). The subtle biphasic dependence of scaffold strut modulus (E_s) on cell migration

speed (Figure 5-3) correlates well with previous experimental and computational studies of cell motility in dense, three-dimensional materials with high degree of steric hindrances [8, 9]. However, the strong dependence of cell migration on pore size was not expected, since cells were not exposed to steric hindrance in the porous CG scaffold variants. The role of strut flexural rigidity in influence cell motility was tested and discounted as a mechanism for explaining the influence of scaffold pore size on cell motility (Figure 5-3).

A quantitative, theoretical analysis using cellular solids modeling revealed that decreasing mean scaffold pore size leads to increase in number of strut junctions, which are points in the scaffold microstructure where two or more struts meet. Strut junctions are discrete areas of significantly different extracellular morphology compared to an individual strut. With the average strut length of order 30 – 60 μm for the different scaffolds used in this investigation, motile cells as well as sessile cells extending processes along individual struts are expected to – and have been observed to – regularly encounter multiple strut junctions during the 10 hour imaging period of this experiment. If cell motility were influenced by strut junctions, it is likely the change in the extracellular morphology at the junctions that is responsible for this effect.

We therefore examined the possibility that there may be significant differences between cell migration behavior at strut junctions versus along the struts. Multiple struts branching out in 3D allow cells to probe multiple paths before deciding on a single path for migration. Fibroblast lamellipodia at the leading edge of the migrating cell are known to extend directed, local protrusions as well as synchronous transverse protrusions that probe for new adhesion sites and direct migration, playing a central role in path finding and mechanotransduction during motility [36, 37]; transverse lamellipodia protrusions may be especially significant here when considering strut junctions, as they allow the cell to navigate the strut junction complex by sampling more of the surrounding scaffold microstructure through its cell surface adhesion receptors than simple forward and backward probing. Such probing movements at the junctions are likely characterized by the erratic 'turning' movement of the entire cell observed experimentally.

Unfortunately, we found that direct, simultaneous visualization of cells and scaffold with confocal microscopy for purposes of correlating a cell's speed and behavior with its location on the scaffold was not possible. Specifically, fluorescent labeling of the scaffold

may alter the ligand distribution on the scaffold surface, and long-term two-channel image acquisition generated significant cell phototoxicity. Hence, indirect measures of scaffold localization were used to infer geographical information about the cells. Persistence times for individual cell movement (Figure 5-4, B, left) indicated that cell migration in scaffolds with lower junction density (larger pore size) exhibited greater persistence times with more directional motion (correlative to migration along individual struts). On the other hand, persistence times of cells migrating in scaffolds with greater junction densities (smaller pore size) were indicative of erratic movement, likely occurring more often at junctions that have the potential for cells to adhere to multiple struts (Figure 5-4, B, left). To support these findings, each cell locomotion path was analyzed and categorized as erratic turning movement, corresponding to movement at strut junctions, versus directional movement, corresponding to movement along struts (Figure 5-4, B, right). Indeed, cells migrating in scaffolds with higher junction density spent more time turning at strut junctions than those migrating in scaffolds with lower junction density. These findings led to the speculation that strut junction geometry is responsible for the initially non-intuitive increase in speed of cells migrating in scaffolds with smaller pore sizes.

Results that cells exhibit enhanced motility due to scaffold junctions was counter-intuitive at first, since the cells are given an opportunity to be 'indecisive' at junctions, usually leading to a reduction in net locomotion whereas struts only provide two opposite directions to migrate raising the probability to exhibit high cell locomotion. Previous *in vivo* contact guidance studies have shown cells migrating along single ECM fibers through a dense ECM network at high speeds up to 3 μm/min [14, 38]. However, these *in vivo* ECM fibers are much thicker than the struts in the CG scaffolds used here (order 3 – 5 μm), and due to the surrounding dense ECM structure *in vivo*, those cells were exposed to significantly greater surface area (increased ligand exposure). It is well known that migration behavior is governed by ligand density and the ability to form ligand-receptor interactions on 2D substrata [39-41] and in 3D ECM gels [8]. A single strut of our scaffold, providing almost a one-dimensional line to the cell, may not supply sufficient ligand density for movement with enhanced migration speed. However, strut junctions that present increased local ligand density may provide the necessary adhesion sites for increased migratory speed. In combination, multiple struts with options for movements in several

directions may lead to a more erratic movement, but not to a reduction in cell speed, which was shown in our data (Figure 5-4, B and C). There are no previous studies establishing relationships between dimensionality and cell speed, but this study may indicate that in absence of steric hindrance (i.e. $n < 3$), increase in dimensionality could lead to increase in migration response.

Nevertheless, when interpreting these findings, it is to be noted that the average cell speed for motile cells was calculated as an average over the entire 10 hour migration period; therefore, cell speed incorporates continuous, directional migration (along the struts) as well as turning behavior at the strut junctions. The influence of strut junction on cell speed likely manifests itself in one of two ways: increasing the migration speed along the struts between the junctions, or increasing the speed of the cell movements at the strut junctions. One could hypothesize that cells move at a constant rate along the struts but more rapidly at the strut junctions because they are attaching to several struts at once and therefore the cell is shifting rapidly over small distances [36]. Because cells spend a greater fraction of time turning (at the junctions) in scaffolds with smaller pore sizes, rapid movement at strut junctions could be responsible for the increased overall average cell speed. However, if this were the case, cells in the smaller pore size scaffold would also show decreased dispersion in the Wind-Rose plot due to the decreased time of directional movement, but in fact the opposite is the case (Figure 5-2, A). Therefore, strut junctions rather appear to increase cell motility by increasing the cell speed between junctions along the struts. Further analysis of the motility of cells along the struts at strut junctions confirmed this hypothesis (Figure 5-5); while cells in scaffolds with increased junction densities had an increased migration speed during turning, they showed a significantly greater increase in migration speed along the struts during directional motion. These results suggest that strut junctions play a central role in regulating cell motility in 3D scaffolds.

The ability to vary the scaffold and strut modulus independent of other scaffold properties through chemical crosslinking allowed us to rule out that the pore size-dependent decrease in cell migration speed seen in Figure 5-2 may be due to pore size-dependent changes in the scaffold mechanical properties (strut flexural rigidity). En route, we were able to identify that individual cell migration behavior is biphasically dependent

on strut elastic modulus (E_s; Figure 5-3, B). Such biphasic dependence on substrate rigidity has been previously reported only in isotropic, homogeneous 2D and 3D network systems [8, 9, 19]. These experiments looking at the effect of changes in scaffold strut modulus independent of microstructure on cell motility (Figure 5-3, B) were performed using scaffolds with the highest junction density (pore size 96 μm). Whether the biphasic dependence on stiffness would hold if scaffold modulus was varied in scaffolds of lower junction density is yet to be investigated.

While we report a biphasic relationship between cell migration speed and scaffold strut modulus (E_s), when contemplating cell mechanosensing mechanisms in a porous biomaterial a more detailed descriptor of the local microenvironment may be required. Details of such mechanosensing mechanisms are currently being studied [34], but a physiological read-out of substrate compliance or stiffness is likely through the cell's ability to sense the deformation of its underlying substrate in response to a constant applied traction force. Dermal fibroblasts, as well as a number of other cell types, have been observed to contract CG scaffolds, significantly deforming the macroscopic shape of scaffold samples as well as buckling the individual scaffold struts to which they are attached [28, 30, 42]. The applied contractile force generated by a single fibroblast has been calculated to be on the order of 25 nN [28]. Significantly, dermal fibroblasts are observed to apply a constant average contractile force per cell independent of the scaffold system stiffness [43], suggesting the cell may sense underlying substrate stiffness or compliance through its deformation; these results suggest that strut flexural rigidity is the more appropriate variable to consider when describing scaffold mechanical properties and considering cell behavior. However, since the CG scaffold strut dimensions were found to be uniform throughout each scaffold variant [28] therefore leading to a constant moment of inertia, the flexural rigidity of the CG scaffold struts can be adequately described by the strut modulus.

Results of our study complement those from previous studies that cell migratory behavior is non-trivially affected by multiple parameters and properties of the ECM [8, 9]. Our study not only highlighted the complex dependence of cell motility on matrix modulus in a highly porous ECM system consisting of struts and junctions, but also demonstrated the previously unexplored importance of the ECM microstructure in governing cell

migration behavior. These findings were made possible by the ability to independently vary the mechanical and microstructural properties of the CG scaffolds. These scaffolds, comprised of naturally derived ECM components, serve as highly tunable substrates for porous and fibrous ECM systems relevant to tissue engineering applications and physiology. Other substrates, such as tissue samples or naturally derived *in vitro* ECM gels are ill-suited for establishing quantitative relationship between migratory behavior and parameters of the 3D ECM microstructure due to their complex and unpredictable microstructure. Synthetic biomaterials [44] may allow subtle architectural control, but independent parsing of mechanical and geometrical properties have not yet been described. Our findings in this report have implications in design of tissue engineering substrates that require extensive migratory behavior; for example a scaffold with an engineered higher strut junction density may accelerate cell in-growth into the initially acellular structure, a critical requirement for the development of large, porous implants for regenerative medicine applications. In addition, the specific influence of construct parameters such as chemical composition, degradation characteristics, as well as the influence of environmental factors such as soluble additive content (i.e. growth factor, cytokine), cell culture conditions, and exogenous loading is unknown and is an area for future application of this CG scaffold system.

5.5. References

1. Harley, B.A., et al., *Mechanical Characterization of Collagen-GAG Scaffolds.* Acta Biomater, 2007. **3**(4): p. 463-474.
2. O'Brien, F.J., et al., *The effect of pore size on cell adhesion in collagen-GAG scaffolds.* Biomaterials, 2005. **26**(4): p. 433-41.
3. Lauffenburger, D.A. and A.F. Horwitz, *Cell migration: a physically integrated molecular process.* Cell, 1996. **84**(3): p. 359-69.
4. Friedl, P., K.S. Zanker, and E.B. Brocker, *Cell migration strategies in 3-D extracellular matrix: differences in morphology, cell matrix interactions, and integrin function.* Microsc Res Tech, 1998. **43**(5): p. 369-78.
5. Lo, C.M., et al., *Cell movement is guided by the rigidity of the substrate.* Biophys J, 2000. **79**(1): p. 144-52.
6. Munevar, S., Y.L. Wang, and M. Dembo, *Distinct roles of frontal and rear cell-substrate adhesions in fibroblast migration.* Mol Biol Cell, 2001. **12**(12): p. 3947-54.

7. Wang, H.B., et al., *Focal adhesion kinase is involved in mechanosensing during fibroblast migration.* Proc Natl Acad Sci U S A, 2001. **98**(20): p. 11295-300.
8. Zaman, M.H., et al., *Migration of tumor cells in 3D matrices is governed by matrix stiffness along with cell-matrix adhesion and proteolysis.* Proc Natl Acad Sci U S A, 2006. **103**(29): p. 10889-94.
9. Zaman, M.H., et al., *Computational model for cell migration in three-dimensional matrices.* Biophys J, 2005. **89**(2): p. 1389-97.
10. Wolf, K., et al., *Compensation mechanism in tumor cell migration: mesenchymal-amoeboid transition after blocking of pericellular proteolysis.* J Cell Biol, 2003. **160**(2): p. 267-77.
11. Zaman, M.H., P. Matsudaira, and D.A. Lauffenburger, *Understanding effects of matrix protease and matrix organization on directional persistence and translational speed in three-dimensional cell migration.* Ann Biomed Eng, 2007. **35**(1): p. 91-100.
12. Brock, A., et al., *Geometric determinants of directional cell motility revealed using microcontact printing.* Langmuir, 2003. **19**(5): p. 1611-7.
13. Lehnert, D., et al., *Cell behaviour on micropatterned substrata: limits of extracellular matrix geometry for spreading and adhesion.* J Cell Sci, 2004. **117**(Pt 1): p. 41-52.
14. Condeelis, J. and J.E. Segall, *Intravital imaging of cell movement in tumours.* Nat Rev Cancer, 2003. **3**(12): p. 921-30.
15. Bajenoff, M., et al., *Stromal cell networks regulate lymphocyte entry, migration, and territoriality in lymph nodes.* Immunity, 2006. **25**(6): p. 989-1001.
16. Stachowiak, A.N. and D.J. Irvine, *Inverse opal hydrogel-collagen composite scaffolds as a supportive microenvironment for immune cell migration.* J biomed Mater Res A, In Press, 2007.
17. Nehrer, S., et al., *Matrix collagen type and pore size influence behaviour of seeded canine chondrocytes.* Biomaterials, 1997. **18**(11): p. 769-76.
18. Wake, M.C., C.W. Patrick, Jr., and A.G. Mikos, *Pore morphology effects on the fibrovascular tissue growth in porous polymer substrates.* Cell Transplant, 1994. **3**(4): p. 339-43.
19. Peyton, S.R. and A.J. Putnam, *Extracellular matrix rigidity governs smooth muscle cell motility in a biphasic fashion.* J Cell Physiol, 2005. **204**(1): p. 198-209.
20. Grinnell, F., et al., *Differences in the regulation of fibroblast contraction of floating versus stressed collagen matrices.* J Biol Chem, 1999. **274**(2): p. 918-923.
21. Engler, A.J., et al., *Matrix Elasticity Directs Stem Cell Lineage Specification.* Cell, 2006. **126**(4): p. 677-689.
22. Yeung, T., et al., *Effects of substrate stiffness on cell morphology, cytoskeletal structure, and adhesion.* Cell Motil. Cytoskeleton, 2005. **60**: p. 24-34.
23. Capito, R.M. and M. Spector, *Scaffold-Based Articular Cartilage Repair.* IEEE Eng. Med. Biol. Mag., 2003. **22**(5): p. 42-50.
24. Harley, B.A., et al., *Optimal degradation rate for collagen chambers used for regeneration of peripheral nerves over long gaps.* Cells Tissues Organs, 2004. **176**(1-3): p. 153-65.
25. Yannas, I.V., et al., *Synthesis and characterization of a model extracellular matrix that induces partial regeneration of adult mammalian skin.* Proc. Natl. Acad. Sci. USA, 1989. **86**(3): p. 933-937.

26. O'Brien, F.J., et al., *Influence of freezing rate on pore structure in freeze-dried collagen-GAG scaffolds.* Biomaterials, 2004. **25**(6): p. 1077-86.
27. O'Brien, F.J., et al., *The effect of pore size on permeability and cell attachment in collagen scaffolds for tissue engineering.* Technol Health Care, 2007. **15**(1): p. 3-17.
28. Harley, B.A., et al., *A new technique for calculating individual dermal fibroblast contractile forces generated within collagen-GAG scaffolds.* Biophys J, In Press, 2007.
29. Pruss, R.M. and H.R. Herschman, *Variants of 3T3 cells lacking mitogenic response to epidermal growth factor.* Proc Natl Acad Sci U S A, 1977. **74**(9): p. 3918-21.
30. Freyman, T.M., et al., *Fibroblast contraction of a collagen-GAG matrix.* Biomaterials, 2001. **22**(21): p. 2883-2891.
31. Dickinson, R.B. and R.T. Tranquillo, *Optimal Estimation of Cell-Movement Indexes from the Statistical-Analysis of Cell Tracking Data.* Aiche Journal, 1993. **39**(12): p. 1995-2010.
32. Gibson, L.J. and M.F. Ashby, *Cellular Solids: Structure and Properties*. 2nd ed. 1997, Cambridge, U.K.: Cambridge University Press.
33. Kraynik, A.M., D.A. Reinelt, and F. van Swol, *Structure of random monodisperse foam.* Phys. Rev., 2003. **67**: p. 031403.
34. Vogel, V. and M. Sheetz, *Local force and geometry sensing regulate cell functions.* Nat Rev Mol Cell Biol, 2006. **7**(4): p. 265-75.
35. Yannas, I.V., *Tissue and Organ Regeneration in Adults*. 2001, New York: Springer.
36. Galbraith, C.G., K.M. Yamada, and J.A. Galbraith, *Polymerizing actin fibers position integrins primed to probe for adhesion sites.* Science, 2007. **315**(5814): p. 992-5.
37. Suter, D.M. and P. Forscher, *Transmission of growth cone traction force through apCAM-cytoskeletal linkages is regulated by Src family tyrosine kinase activity.* J Cell Biol, 2001. **155**(3): p. 427-38.
38. Sidani, M., et al., *Probing the microenvironment of mammary tumors using multiphoton microscopy.* J Mammary Gland Biol Neoplasia, 2006. **11**(2): p. 151-63.
39. DiMilla, P.A., K. Barbee, and D.A. Lauffenburger, *Mathematical model for the effects of adhesion and mechanics on cell migration speed.* Biophys J, 1991. **60**(1): p. 15-37.
40. Huttenlocher, A., M.H. Ginsberg, and A.F. Horwitz, *Modulation of cell migration by integrin-mediated cytoskeletal linkages and ligand-binding affinity.* J Cell Biol, 1996. **134**(6): p. 1551-62.
41. Palecek, S.P., et al., *Integrin-ligand binding properties govern cell migration speed through cell-substratum adhesiveness.* Nature, 1997. **385**(6616): p. 537-40.
42. Torres, D.S., et al., *Tendon cell contraction of collagen-GAG matrices in vitro: effect of cross-linking.* Biomaterials, 2000. **21**(15): p. 1607-1619.
43. Freyman, T.M., et al., *Fibroblast contractile force is independent of the stiffness which resists the contraction.* Experimental Cell Research, 2002. **272**(2): p. 153-162.
44. Lutolf, M.P. and J.A. Hubbell, *Synthetic biomaterials as instructive extracellular microenvironments for morphogenesis in tissue engineering.* Nat Biotechnol, 2005. **23**(1): p. 47-55.
45. Harley, B.A., Kim, H.-D., et al., *Microarchitecture of three-dimensional scaffolds influences cell migration behavior via junction interactions*. Biophys J, 2008. **95**(8): p. 4013-24.

CHAPTER 6

Conclusions

In closing, we discuss the research results in the context of the field of cell migration research, future areas of research based on this thesis, as well as the current role and future of quantitative biology as a discipline in advancing biological sciences.

6.1. Significance and contributions

The overall goal of this thesis was to elucidate mechanisms of epidermal growth factor receptor (EGFR)-mediated cell migration in the context of microenvironmental cues, focusing on the epithelial-mesenchymal transition (EMT) and the 3D extracellular matrix (ECM). The multivariate nature of these cue-signal-response problems compelled the need for carefully controlled quantitative methods while still being able to tie the results and interpretations to relevant *in vivo* biology. Taking this approach, we assumed that the absolute levels of proteins or activities and the migratory parameter values are of biological relevance. Under these assumptions, we struck a balance between creating novel, stringently controlled experimental systems and maintaining physiological relevance. Mathematical analysis under these conditions resulted in discovering previously unknown mechanistic insights potentially useful for therapeutic opportunities. In this section, we discuss the contributions made to the field of cell migration biology and the field of quantitative modeling.

6.1.1. Contributions to EMT cell biology and potential targeted therapy

The interest in the role of EMT in cancer metastasis has been accelerated by seminal work by Robert Weinberg identifying the upregulation of an inducer of EMT, Twist, to be critical in tumor progression and metastasis [1]. Cellular transformations and changes in gene expression caused by EMT had been well studied previously due to the critical role EMT

plays during development. However, precisely which changes contribute to the enhancement in the invasive phenotype upon EMT was still unelucidated.

Due to the importance of the invasion microenvironment contributing to the EMT phenotype, a hypothesis-driven single-pathway approach was ill suited to efficiently discover the differential processing of growth factor cues into a migratory response. Instead, the quantitative multi-pathway measurement and analysis of signaling network combined with data-driven mathematical approach yielded novel insights without an *a priori* hypothesis. Furthermore, due to the careful design of the experimental system containing genetically identical cell line and the robust quantitation of migratory phenotype, we identified novel migratory phenotypes, while maintaining the interpretations of the results relevant to *in vivo* biology.

Our finding that epithelial cells confer increased dependency on EGFR itself was known prior to our study [2]. However, the discovery of the shift of dependency of mesenchymal cells on a downstream regulator of a biophysical process of cell migration was new, potentially suggesting a novel therapeutic target.

Currently, due to the inefficiency of single cancer therapeutics, more combined therapeutics against the ErbB family of receptor tyrosine kinases are being explored [3]. As explained previously, *in vivo* tumors are genetically and phenotypically heterogeneous, rendering single target therapy inefficient. Hence, our results may indicate the opportunity of combined receptor-level and downstream signal targeting for a more comprehensive targeting of tumors, in conjunction with EMT markers for tailoring customized therapies.

6.1.2. Contributions to 3D cell migration biology

A further therapeutic opportunity arises from the understanding of the invasive mechanism, but in a more phenomenological perspective. Namely, just as a car requires both the gas pedal and the steering wheel to reach its destination, the cell requires careful control of cell speed and directional persistence. Recent studies indicate that these two parameters may be under regulation of differential pathways. In addition, our studies indicate that the 3D ECM properties play an integral role for regulating the directional persistence, while cell speed is mainly under the intrinsic control, especially at small changes of matrix ligand density. Therefore, our results indicate that targeting of matrix

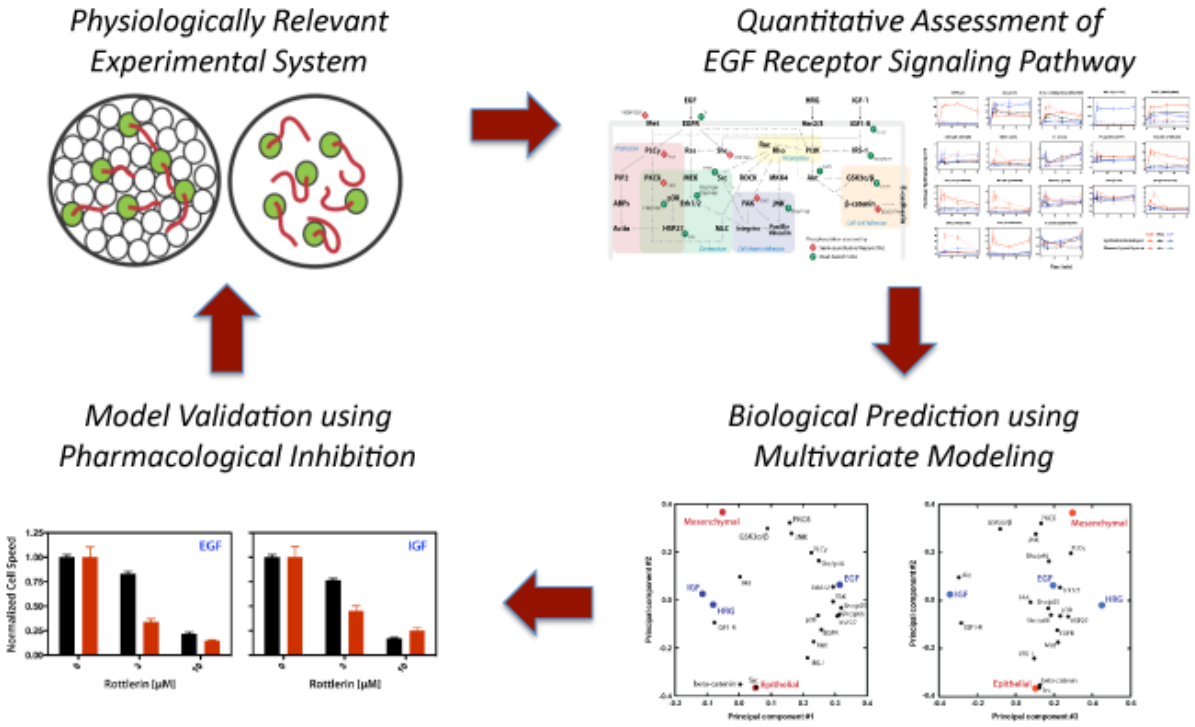

Figure 6-1 – Work flow of chapter 3. Figure illustrates the paradigm of 'measure, mine, model, and manpulate' emphasizing the importance of the physiologically relevant experimental system.

proteolysis may be efficient in certain matrix properties and not others, which may in part explain the failure of MMP inhibitors in metastasis therapy [4].

Until now, much of 3D cell migration research has been focused purely on the elucidation of the phenomenological cell biology and the biophysical aspects of cell migration [5-7]. To our knowledge, our work is novel in the attempt to link the biochemical stimulation to biophysical effects in a biological setting. We demonstrate that our model system is useful in elucidating the effects of other molecular interventions or biological functions of a gene.

6.1.3. Contributions to bioengineering

The work provided in chapter 3 follows the bioengineering paradigm of measuring, mining, modeling, and manipulating [8] (Figure 6-1). We further posit that the pertinence of measurement is the first and foremost factor in the design of this paradigm. We used data-

driven modeling to identify novel biological insights, but in a manner such that biology is the leading principle for our study. This is particularly important considering the overall goal of bioengineering model is the application – the development of robust therapeutics in biological systems in this case.

The persistent random walk model was also used in the context of the biological meaning, not as an academic exercise. We have demonstrated that the violation of model assumptions due to the 3D ECM environment can lead to interesting insights and can serve as an additional parameter (Figure 4-10, C). Here, we emphasize again the pertinence of measurements for biological phenomenon.

6.2. Future directions and concluding remarks

6.2.1. Systems analysis of EGFR-mediated 3D cell migration

Due to the biophysical nature of the migratory process, the study of cell migration is inherently multivariate. From a cell-centric perspective, even the 2D environment provides the ECM ligand density and mechanical properties as cues in addition to the soluble cytokines. Previous studies indicate that activities of key intracellular regulators depend on the ECM ligand densities, especially for highly bioactive ECMs such as fibronectin [9]. These experimental and computational studies also indicate that the crosstalk between the EGFR and integrin signaling networks contribute to the overall migratory speed. Therefore, even without the consideration of matrix remodeling, which presumably is absent in a 2D environment, the cell integrates multiple cues into a robust response.

The 3D environment introduces the consideration of matrix stiffness and sterics, as well as topological parameters as additional variables [6, 7]. As described in chapter 1, mechanical stiffness has been shown to regulate levels and activities of migration-related signals [10]. Recent unpublished work indicates that cells forced to elongate and to migrate along 1-D substrates express different levels of migration-related signals, which suggests a cellular sensory mechanism of contact guidance cues. Most intriguingly, the

impact of matrix remodeling responses from matrix secretion to matrix degradation is greatly pronounced in a 3D environment, as they lead to variation of matrix parameters and cause a response-cue feedback (Figure 6-2).

The work in chapter 4 began to provide an understanding of the biophysical balance between certain biophysical processes of cell migration by linking EGF cues and matrix cues to the migratory response. While the activation profile of Rac1 did not vary greatly between 2D and 3D environments, recent studies suggests that there are distinct differences in phosphorylation levels of Erk, Src, and FAK that are dependent on the extracellular matrix [11, 12]. Hence, it is reasonable to suggest that their activation profiles upon growth factor or cytokine treatment might differ significantly in a 3D environment. Whether the signaling changes in observed in 3D *in vitro* systems resembles the ones the *in vivo* environment is still unclear as comparative *in vivo* measurements remain challenging. Nevertheless, the work provided in chapter 4 and many other 3D systems, including the 3D mammary acini cultures, do urge the study of cell biology in 3D model systems.

Hence, the development of a systems model of EGFR-mediated cell migration in a 3D matrix could provide novel and interesting insights into the migratory processes beyond the biophysical balance. A systems model further enables the quantitative development of

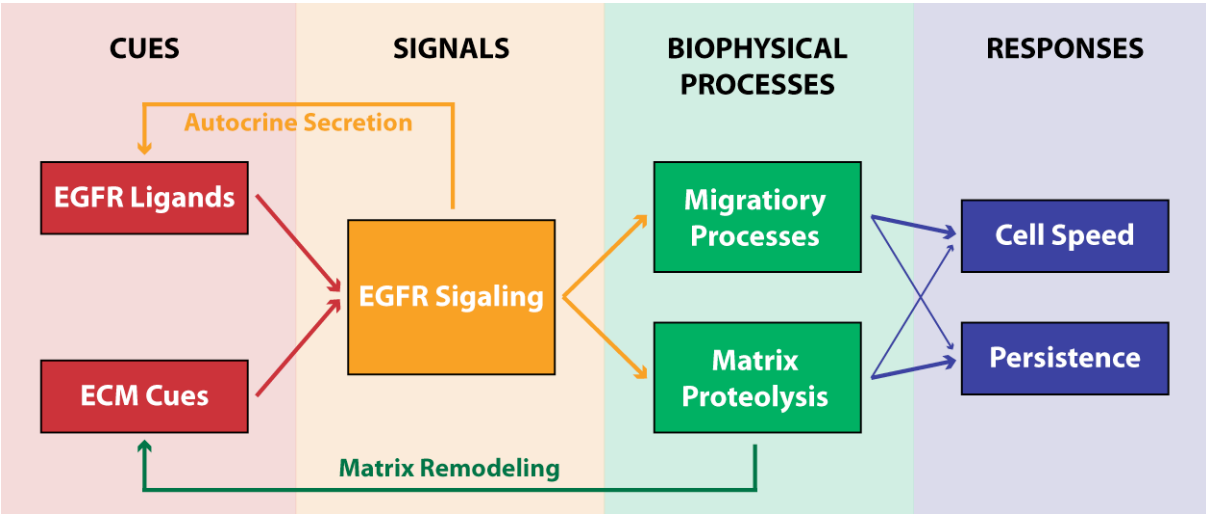

Figure 6-2 – Cue-signal-response system of EGFR-mediated cell migration in 3D environments. Depicted are the components of the cue-signal-response system with arrows indicating influences. Highlighted are the positive feedback loops caused by matrix remodeling and autocrine growth factor secretion.

predictions for migratory parameters upon molecular interventions that could be of use for the development of therapeutics.

However, there exist significant challenges in the development of quantitative systems models of EGFR-mediated cell migration in 3D matrices. The most prominent is difficulty in generating quantitative measurements of activation dynamics of key intracellular regulators. Traditional methods of signaling measurements as used in this thesis, such as Western Blot or ELISAs rely heavily on the accurate measurements of protein concentration in cell lysates. However, the overwhelming presence of ECM proteins in cell lysates generated from 3D culture often prevents the accurate measurement of protein concentrations. Proper normalization methodologies for 3D cultures are currently being addressed. Additional difficulties include the low cell numbers in a 3D cell culture and the costs associated with the ECM culture. The lack of high-throughput technologies for generating lysates as well as multiple protein measurements (largely due to the higher sensitivity required when challenged with low cell numbers in 3D cultures) is even more detrimental for 3D migration studies due to the increased number of variables. To address this problem, we are currently holding promise in the use of quantitative mass spectrometry methodologies [13, 14].

6.2.2. Cell signaling analysis of EGFR-mediated migration in a co-culture model

Although evolutionary paradigm of tumors in its tumor microenvironment has been known [15], the role of stromal cells – a major constituent of the tumor microenvironment and the major contributor to the heterogeneity of tumors – has been downplayed in this thesis. There are several methods to assess the role of stromal cells in regulating cell function. One is the use of primed media of stromal cell culture to treat cells of interest, with the obvious disadvantage of not knowing the constituents of the primed media. Another is the study of co-culturing stromal cells with the cells in question [16]. In addition to the ability to investigate the effect of the added cells on cell response, the co-culture often is accepted to be a more physiologically relevant system. For example, the extracellular environment of glioblastoma invasion is highly rich neurons and glial cells. The co-culture of neurons and glioblastomas in a 3D matrix could aid in creating a more physiologically relevant system. One challenge is the assessment of cell signaling dynamics in co-cultures since cell

lysates do not distinguish protein levels arising from different cell types. One interesting perspective is provided by stable isotope labeling by amino acids and quantitative mass spectrometry [17], which could aid in differentially labeling cell types and quantifying signaling dynamics of each cell type. While this experiment is non-trivial, the insights gained in the signaling activities due to the presence of stromal cells could aid in understanding the effects of the microenvironment on the migratory process.

6.2.3. Perspective ahead: *in vivo* quantitative biology

Recent developments in quantitative technologies, both for the measurement of protein levels and cellular response measurements, enhance the promise of quantitation in advancing biological knowledge. While the development of novel, physiologically relevant *in vitro* model systems is critical in the field of quantitative biology, the most effective and applicable use of data-driven modeling approaches – with the perspective of the tumor invasion microenvironment – lies in the ability to measure *in vivo* cell signaling and responses. While the use of primary cells instead of cell lines constitutes *in vivo* measurements and their quantitative assessments have found success [18], the use of robust quantitation for *in vivo* observations is still at its infancy with little tools available. Most promising for migration-related *in vivo* measurements are intravital imaging technologies able to observe tumor cell movement and its interactions with the invasion microenvironment [19, 20]. Second harmonic imaging allows for label-free imaging of ECMs, useful for quantitation of correlative parameters between the tumor cell and the ECM. For example, the specific location of cells in question, respective to an organ, can be very informative as the distribution of receptor levels vary greatly within an organ [21]. Furthermore, numerous publications cite the ability of intravital imaging technologies to quantify using fluorescence, magnetic resonance, and radioisotopes [22]. In addition, great attention is being paid to the development of imaging probes suited for quantitation. One exciting example is the development of a photoactivatable, color-switching fluorescent protein probe [23]. Use of such constructs can aid in quantifying random motility coefficients by tracking a subpopulation of cells upon careful molecular interventions.

Strides are also being made in the development of non-invasive molecular intervention technologies. Emergence of *in vivo* RNAi screens could help in discovery of

candidates correlative to a phenotype, and may also hold promise in quantitative modulation of individual signals. This type of approach may aid in quantitative reconstruction of *in vivo* signaling pathways.

Hence, the future holds great promise in the use of quantitative data-driven models derived from purely *in vivo* reagents and measurements. Such approaches will not only benefit the scientific community by providing a bridge between quantitatively minded basic scientists and clinical researchers and by advancing translational research. The future of quantitative biology gives hope to relevant personalized medicine and more comprehensive and predictive insights into the dynamics of tumor biology currently hidden.

6.3. References

1. Yang, J., et al., *Twist, a master regulator of morphogenesis, plays an essential role in tumor metastasis.* Cell, 2004. **117**(7): p. 927-39.
2. Barr, S., et al., *Bypassing cellular EGF receptor dependence through epithelial-to-mesenchymal-like transitions.* Clin Exp Metastasis, 2008. **25**(6): p. 685-93.
3. Amit, I., R. Wides, and Y. Yarden, *Evolvable signaling networks of receptor tyrosine kinases: relevance of robustness to malignancy and to cancer therapy.* Mol Syst Biol, 2007. **3**: p. 151.
4. Overall, C.M. and O. Kleifeld, *Towards third generation matrix metalloproteinase inhibitors for cancer therapy.* Br J Cancer, 2006. **94**(7): p. 941-6.
5. Friedl, P. and E.B. Brocker, *The biology of cell locomotion within three-dimensional extracellular matrix.* Cell Mol Life Sci, 2000. **57**(1): p. 41-64.
6. Zaman, M.H., et al., *Computational model for cell migration in three-dimensional matrices.* Biophys J, 2005. **89**(2): p. 1389-97.
7. Zaman, M.H., et al., *Migration of tumor cells in 3D matrices is governed by matrix stiffness along with cell-matrix adhesion and proteolysis.* Proc Natl Acad Sci U S A, 2006. **103**(29): p. 10889-94.
8. Parker, C.N., et al., *Measure, mine, model, and manipulate: the future for HTS and chemoinformatics?* Drug Discov Today, 2006. **11**(19-20): p. 863-5.
9. Kharait, S., et al., *Decision tree modeling predicts effects of inhibiting contractility signaling on cell motility.* BMC Syst Biol, 2007. **1**: p. 9.
10. Peyton, S.R., et al., *The emergence of ECM mechanics and cytoskeletal tension as important regulators of cell function.* Cell Biochem Biophys, 2007. **47**(2): p. 300-20.
11. Cukierman, E., et al., *Taking cell-matrix adhesions to the third dimension.* Science, 2001. **294**(5547): p. 1708-12.
12. Damianova, R., et al., *Three-dimensional matrix induces sustained activation of ERK1/2 via Src/Ras/Raf signaling pathway.* Cell Biol Int, 2008. **32**(2): p. 229-34.

13. Wolf-Yadlin, A., et al., *Multiple reaction monitoring for robust quantitative proteomic analysis of cellular signaling networks.* Proc Natl Acad Sci U S A, 2007. **104**(14): p. 5860-5.
14. Zhang, Y., et al., *Time-resolved mass spectrometry of tyrosine phosphorylation sites in the epidermal growth factor receptor signaling network reveals dynamic modules.* Mol Cell Proteomics, 2005. **4**(9): p. 1240-50.
15. Pienta, K.J., et al., *Ecological therapy for cancer: defining tumors using an ecosystem paradigm suggests new opportunities for novel cancer treatments.* Transl Oncol, 2008. **1**(4): p. 158-64.
16. Grant-Tschudy, K.S. and C.R. Wira, *Effect of oestradiol on mouse uterine epithelial cell tumour necrosis factor-alpha release is mediated through uterine stromal cells.* Immunology, 2005. **115**(1): p. 99-107.
17. Mann, M., *Functional and quantitative proteomics using SILAC.* Nat Rev Mol Cell Biol, 2006. **7**(12): p. 952-8.
18. Cosgrove, B.D., et al., *An inducible autocrine cascade regulates rat hepatocyte proliferation and apoptosis responses to tumor necrosis factor-alpha.* Hepatology, 2008. **48**(1): p. 276-88.
19. Kedrin, D., et al., *Imaging tumor cell movement in vivo.* Curr Protoc Cell Biol, 2007. **Chapter 19**: p. Unit 19 7.
20. Provenzano, P.P., K.W. Eliceiri, and P.J. Keely, *Multiphoton microscopy and fluorescence lifetime imaging microscopy (FLIM) to monitor metastasis and the tumor microenvironment.* Clin Exp Metastasis, 2008.
21. Caric, D., et al., *EGFRs mediate chemotactic migration in the developing telencephalon.* Development, 2001. **128**(21): p. 4203-16.
22. Graves, E.E., R. Weissleder, and V. Ntziachristos, *Fluorescence molecular imaging of small animal tumor models.* Curr Mol Med, 2004. **4**(4): p. 419-30.
23. Gurskaya, N.G., et al., *Engineering of a monomeric green-to-red photoactivatable fluorescent protein induced by blue light.* Nat Biotechnol, 2006. **24**(4): p. 461-5.

CHAPTER 7

APPENDICES

Listed here are the MATLAB codes for analyzing wound healing images (7.1 Appendix A) and applying the persistent random walk model to cell track coordinates (7.2 Appendix B).

7.1. Appendix A – WoundGUI.m

This file requires the WoundGUI.fig file for the graphical user interface (not included).

```
function varargout = woundgui(varargin)
% WOUNDGUI M-file for woundgui.fig

% Begin initialization code - DO NOT EDIT
gui_Singleton = 1;
gui_State = struct('gui_Name',       mfilename, ...
                   'gui_Singleton',  gui_Singleton, ...
                   'gui_OpeningFcn', @woundgui_OpeningFcn, ...
                   'gui_OutputFcn',  @woundgui_OutputFcn, ...
                   'gui_LayoutFcn',  [] , ...
                   'gui_Callback',   []);
if nargin && ischar(varargin{1})
    gui_State.gui_Callback = str2func(varargin{1});
end

if nargout
    [varargout{1:nargout}] = gui_mainfcn(gui_State, varargin{:});
else
    gui_mainfcn(gui_State, varargin{:});
end
% End initialization code - DO NOT EDIT

% --- Executes just before woundgui is made visible.
function woundgui_OpeningFcn(hObject, eventdata, handles, varargin)
% This function has no output args, see OutputFcn.
% hObject    handle to figure
% eventdata  reserved - to be defined in a future version of MATLAB
% handles    structure with handles and user data (see GUIDATA)
% varargin   command line arguments to woundgui (see VARARGIN)

% Choose default command line output for woundgui
handles.output = hObject;

% Update handles structure
guidata(hObject, handles);
```

```
% UIWAIT makes woundgui wait for user response (see UIRESUME)
% uiwait(handles.figure1);

handles.load_final = 0;
handles.filetype = '.bmp';
set(handles.workdir,'String',pwd);
set(handles.savedir,'String',pwd);

axes(handles.fig_beg); % Select the proper axes
imshow(ones(512,512));
axes(handles.fig_mid);
imshow(ones(512,512));
axes(handles.fig_end);
imshow(ones(512,512));

addpath(pwd,'-begin');

guidata(hObject, handles);

% --- Outputs from this function are returned to the command line.
function varargout = woundgui_OutputFcn(hObject, eventdata, handles)
% varargout  cell array for returning output args (see VARARGOUT);
% hObject    handle to figure
% eventdata  reserved - to be defined in a future version of MATLAB
% handles    structure with handles and user data (see GUIDATA)

% Get default command line output from handles structure
varargout{1} = handles.output;

function workdir_Callback(hObject, eventdata, handles)
% hObject    handle to workdir (see GCBO)
% eventdata  reserved - to be defined in a future version of MATLAB
% handles    structure with handles and user data (see GUIDATA)

% --- Executes during object creation, after setting all properties.
function workdir_CreateFcn(hObject, eventdata, handles)
% hObject    handle to workdir (see GCBO)
% eventdata  reserved - to be defined in a future version of MATLAB
% handles    empty - handles not created until after all CreateFcns called

if ispc && isequal(get(hObject,'BackgroundColor'),
get(0,'defaultUicontrolBackgroundColor'))
    set(hObject,'BackgroundColor','white');
end

% --- Executes on button press in workdirbrowse.
function workdirbrowse_Callback(hObject, eventdata, handles)
% hObject    handle to workdirbrowse (see GCBO)
% eventdata  reserved - to be defined in a future version of MATLAB
% handles    structure with handles and user data (see GUIDATA)
workdir_text = uigetdir;
if isstr(workdir_text) == 1
    set(handles.workdir,'String',workdir_text);
end

function frames_Callback(hObject, eventdata, handles)
% hObject    handle to frames (see GCBO)
```

```
% eventdata  reserved - to be defined in a future version of MATLAB
% handles    structure with handles and user data (see GUIDATA)

% --- Executes during object creation, after setting all properties.
function frames_CreateFcn(hObject, eventdata, handles)
% hObject    handle to frames (see GCBO)
% eventdata  reserved - to be defined in a future version of MATLAB
% handles    empty - handles not created until after all CreateFcns called

if ispc && isequal(get(hObject,'BackgroundColor'),
get(0,'defaultUicontrolBackgroundColor'))
    set(hObject,'BackgroundColor','white');
end

function interval_Callback(hObject, eventdata, handles)
% hObject    handle to interval (see GCBO)
% eventdata  reserved - to be defined in a future version of MATLAB
% handles    structure with handles and user data (see GUIDATA)

% --- Executes during object creation, after setting all properties.
function interval_CreateFcn(hObject, eventdata, handles)
% hObject    handle to interval (see GCBO)
% eventdata  reserved - to be defined in a future version of MATLAB
% handles    empty - handles not created until after all CreateFcns called

if ispc && isequal(get(hObject,'BackgroundColor'),
get(0,'defaultUicontrolBackgroundColor'))
    set(hObject,'BackgroundColor','white');
end

% --- Executes on selection change in imageenc_popup.
function imageenc_popup_Callback(hObject, eventdata, handles)
% hObject    handle to imageenc_popup (see GCBO)
% eventdata  reserved - to be defined in a future version of MATLAB
% handles    structure with handles and user data (see GUIDATA)
 val = get(hObject,'Value');
switch val
    case 1
        handles.filetype = '.bmp';
    case 2
        handles.filetype = '.tif';
    case 3
        handles.filetype = '.jpg';
end
guidata(hObject,handles);

% --- Executes during object creation, after setting all properties.
function imageenc_popup_CreateFcn(hObject, eventdata, handles)
% hObject    handle to imageenc_popup (see GCBO)
% eventdata  reserved - to be defined in a future version of MATLAB
% handles    empty - handles not created until after all CreateFcns called

if ispc && isequal(get(hObject,'BackgroundColor'),
get(0,'defaultUicontrolBackgroundColor'))
    set(hObject,'BackgroundColor','white');
end

% --- Executes on button press in loadbutton.
```

```
function loadbutton_Callback(hObject, eventdata, handles)
% hObject    handle to loadbutton (see GCBO)
% eventdata  reserved - to be defined in a future version of MATLAB
% handles    structure with handles and user data (see GUIDATA)

cd(get(handles.workdir,'String'));
filename = dir(num2str(['*' handles.filetype]));
handles.nframes = length(filename);

if handles.nframes > 0
    for z = 1:handles.nframes
        [handles.I_orig(:,:,:,z), handles.map] = imread(filename(z).name);
        handles.I_fill(:,:,:,z) = imfill(handles.I_orig(:,:,:,z));
    end

    set(handles.frames,'String',num2str(handles.nframes));
    pixels = size(handles.I_orig);
    set(handles.pixel_row,'String',num2str(pixels(1)));
    set(handles.pixel_column,'String',num2str(pixels(2)));

    handles.load_final = 1;
    set(handles.message,'String','');

    axes(handles.fig_beg); % Select the proper axes
    imshow(handles.I_fill(:,:,:,1));
    set(handles.frame_beg_n,'String','1');
    axes(handles.fig_mid);
    imshow(handles.I_fill(:,:,:,ceil(handles.nframes./2)));
    set(handles.frame_mid_n,'String',num2str(ceil(handles.nframes./2)));
    axes(handles.fig_end);
    imshow(handles.I_fill(:,:,:,handles.nframes));
    set(handles.frame_end_n,'String',num2str(handles.nframes));

    set(handles.frame_beg_n,'String',1);
    set(handles.frame_mid_n,'String',num2str(ceil(handles.nframes./2)));
    set(handles.frame_end_n,'String',num2str(handles.nframes));

    set(handles.message,'String','Images Loaded');
    set(handles.savedir,'String',get(handles.workdir,'String'));

    handles.full_update = 0;
    handles.approx_update = 0;
    handles.linear_final = 0;
    handles.crop_final = 0;
    handles.binary_final = 0;
    handles.linear_restore = 0;
    handles.binary_restore = 0;
else
    set(handles.message,'String',['No ' handles.filetype ' Image Files
Detected']);
end

guidata(hObject,handles);

% --- Executes on button press in restore.
function restore_Callback(hObject, eventdata, handles)
% hObject    handle to restore (see GCBO)
% eventdata  reserved - to be defined in a future version of MATLAB
```

```
% handles    structure with handles and user data (see GUIDATA)

% --- Executes on button press in pushbutton7.
function pushbutton7_Callback(hObject, eventdata, handles)
% hObject    handle to pushbutton7 (see GCBO)
% eventdata  reserved - to be defined in a future version of MATLAB
% handles    structure with handles and user data (see GUIDATA)

% --- Executes on slider movement.
function thresh_slider_Callback(hObject, eventdata, handles)
% hObject    handle to thresh_slider (see GCBO)
% eventdata  reserved - to be defined in a future version of MATLAB
% handles    structure with handles and user data (see GUIDATA)

set(handles.thresh,'String',num2str(get(handles.thresh_slider,'Value')));

% --- Executes during object creation, after setting all properties.
function thresh_slider_CreateFcn(hObject, eventdata, handles)
% hObject    handle to thresh_slider (see GCBO)
% eventdata  reserved - to be defined in a future version of MATLAB
% handles    empty - handles not created until after all CreateFcns called

if isequal(get(hObject,'BackgroundColor'),
get(0,'defaultUicontrolBackgroundColor'))
    set(hObject,'BackgroundColor',[.9 .9 .9]);
end

function thresh_Callback(hObject, eventdata, handles)
% hObject    handle to thresh (see GCBO)
% eventdata  reserved - to be defined in a future version of MATLAB
% handles    structure with handles and user data (see GUIDATA)

val = str2double(get(handles.thresh,'String'));
min = get(handles.thresh,'Min');
max = get(handles.thresh,'Max');
default = 0.15;

if isnumeric(val) & length(val)==1 & val >= min & val <= max
    set(handles.thresh_slider,'Value',val);
elseif isnumeric(val) & length(val)==1 & val <= min
    set(handles.thresh_slider,'Value',min);
    set(handles.thresh,'String',min);
elseif isnumeric(val) & length(val)==1 & val >= max
    set(handles.thresh_slider,'Value',max);
    set(handles.thresh,'String',max);
else
    set(handles.thresh_slider,'Value',default);
    set(handles.thresh,'String',default);
end

% --- Executes during object creation, after setting all properties.
function thresh_CreateFcn(hObject, eventdata, handles)
% hObject    handle to thresh (see GCBO)
% eventdata  reserved - to be defined in a future version of MATLAB
% handles    empty - handles not created until after all CreateFcns called

if ispc && isequal(get(hObject,'BackgroundColor'),
get(0,'defaultUicontrolBackgroundColor'))
```

```
    set(hObject,'BackgroundColor','white');
end

% --- Executes on button press in begin_crop.
function begin_crop_Callback(hObject, eventdata, handles)
% hObject    handle to begin_crop (see GCBO)
% eventdata  reserved - to be defined in a future version of MATLAB
% handles    structure with handles and user data (see GUIDATA)


% --- Executes on button press in final_crop.
function final_crop_Callback(hObject, eventdata, handles)
% hObject    handle to final_crop (see GCBO)
% eventdata  reserved - to be defined in a future version of MATLAB
% handles    structure with handles and user data (see GUIDATA)

% --- Executes on button press in skip_crop.
function skip_crop_Callback(hObject, eventdata, handles)
% hObject    handle to skip_crop (see GCBO)
% eventdata  reserved - to be defined in a future version of MATLAB
% handles    structure with handles and user data (see GUIDATA)

if handles.binary_final == 1;
    handles.I_crop = handles.I_final;
    handles.crop_final = 1;
else
    set(handles.message,'String','Binarization Missing');
end

guidata(hObject,handles);

function savedir_Callback(hObject, eventdata, handles)
% hObject    handle to savedir (see GCBO)
% eventdata  reserved - to be defined in a future version of MATLAB
% handles    structure with handles and user data (see GUIDATA)

% --- Executes during object creation, after setting all properties.
function savedir_CreateFcn(hObject, eventdata, handles)
% hObject    handle to savedir (see GCBO)
% eventdata  reserved - to be defined in a future version of MATLAB
% handles    empty - handles not created until after all CreateFcns called

if ispc && isequal(get(hObject,'BackgroundColor'),
get(0,'defaultUicontrolBackgroundColor'))
    set(hObject,'BackgroundColor','white');
end

% --- Executes on button press in savedir_browse.
function savedir_browse_Callback(hObject, eventdata, handles)
% hObject    handle to savedir_browse (see GCBO)
% eventdata  reserved - to be defined in a future version of MATLAB
% handles    structure with handles and user data (see GUIDATA)
savedir_text = uigetdir;
if isstr(savedir_text) == 1
    set(handles.savedir,'String',savedir_text);
end

function pixel_row_Callback(hObject, eventdata, handles)
```

```
% hObject    handle to pixel_row (see GCBO)
% eventdata  reserved - to be defined in a future version of MATLAB
% handles    structure with handles and user data (see GUIDATA)
% --- Executes during object creation, after setting all properties.
function pixel_row_CreateFcn(hObject, eventdata, handles)
% hObject    handle to pixel_row (see GCBO)
% eventdata  reserved - to be defined in a future version of MATLAB
% handles    empty - handles not created until after all CreateFcns called

if ispc && isequal(get(hObject,'BackgroundColor'),
get(0,'defaultUicontrolBackgroundColor'))
    set(hObject,'BackgroundColor','white');
end

function pixel_column_Callback(hObject, eventdata, handles)
% hObject    handle to pixel_column (see GCBO)
% eventdata  reserved - to be defined in a future version of MATLAB
% handles    structure with handles and user data (see GUIDATA)

% --- Executes during object creation, after setting all properties.
function pixel_column_CreateFcn(hObject, eventdata, handles)
% hObject    handle to pixel_column (see GCBO)
% eventdata  reserved - to be defined in a future version of MATLAB
% handles    empty - handles not created until after all CreateFcns called

if ispc && isequal(get(hObject,'BackgroundColor'),
get(0,'defaultUicontrolBackgroundColor'))
    set(hObject,'BackgroundColor','white');
end

function csvname_Callback(hObject, eventdata, handles)
% hObject    handle to csvname (see GCBO)
% eventdata  reserved - to be defined in a future version of MATLAB
% handles    structure with handles and user data (see GUIDATA)

% --- Executes during object creation, after setting all properties.
function csvname_CreateFcn(hObject, eventdata, handles)
% hObject    handle to csvname (see GCBO)
% eventdata  reserved - to be defined in a future version of MATLAB
% handles    empty - handles not created until after all CreateFcns called

if ispc && isequal(get(hObject,'BackgroundColor'),
get(0,'defaultUicontrolBackgroundColor'))
    set(hObject,'BackgroundColor','white');
end

% --- Executes on button press in savebutton.
function savebutton_Callback(hObject, eventdata, handles)
% hObject    handle to savebutton (see GCBO)
% eventdata  reserved - to be defined in a future version of MATLAB
% handles    structure with handles and user data (see GUIDATA)

set(handles.message,'String','');
time_format = 0;

if handles.crop_final == 1
    pixels = size(handles.I_crop);
    totalarea = pixels(1).*pixels(2);
```

```
    for z = 1:handles.nframes
        handles.area(z) = totalarea - bwarea(handles.I_crop(:,:,:,z));
    end

    if isempty(get(handles.csvname,'String')) == 1
        set(handles.csvname,'String','data');
    end

    figure(1);
    orig_movie = immovie(handles.I_orig,handles.map);
    figure(1);
    bw_movie = immovie(handles.I_final,handles.map);
    movie2avi(orig_movie,[get(handles.savedir,'String') '\'
get(handles.csvname,'String') '_orig' '.avi'],'compression','none');
    movie2avi(bw_movie,[get(handles.savedir,'String') '\'
get(handles.csvname,'String') '_bw' '.avi'],'compression','none');

    x = linspace(0,handles.nframes - 1,handles.nframes);

    val = str2double(get(handles.interval,'String'));
    if isnumeric(val) & length(val)==1
        if val > 0
            time_format = 1;
            time = x.*val;
        end
    else
        set(handles.interval,'String','');
    end

    figure(1);
    if time_format == 1
        plot(time,handles.area./handles.area(1));
        title('Normalized Wound Area vs. Time');
        xlabel('Time [min]');
        ylabel('Normalized Wound Area');
    else
        plot(x,handles.area./handles.area(1));
        title('Normalized Wound Area vs. Frame');
        xlabel('Frame #');
        ylabel('Normalized Wound Area');
    end

    % Export data in a csv-file.
     if time_format == 1
        export(:,1) = x';
        export(:,2) = time';
        export(:,3) = handles.area'./handles.area(1);
    else
        export(:,1) = x';
        export(:,2) = handles.area'./handles.area(1);
    end

    expfile = [get(handles.savedir,'String') '\'
get(handles.csvname,'String') '.csv'];
    dlmwrite(expfile,export,',');
    set(handles.message,'String','Data Successfully Saved');
else
```

```
    set(handles.message,'String','Image Cropping Missing');
end

% --- Executes on button press in approx.
function approx_Callback(hObject, eventdata, handles)
% hObject    handle to approx (see GCBO)
% eventdata  reserved - to be defined in a future version of MATLAB
% handles    structure with handles and user data (see GUIDATA)

if get(hObject,'Value') == 1;
    set(handles.full,'Value',0);
end
if get(hObject,'Value') == 0 && get(handles.full,'Value') == 0
    set(handles.approx,'Value',1);
end

% --- Executes on button press in full.
function full_Callback(hObject, eventdata, handles)
% hObject    handle to full (see GCBO)
% eventdata  reserved - to be defined in a future version of MATLAB
% handles    structure with handles and user data (see GUIDATA)

if get(hObject,'Value') == 1;
    set(handles.approx,'Value',0);
end
if get(hObject,'Value') == 0 && get(handles.approx,'Value') == 0
    set(handles.full,'Value',1);
end

% --- Executes on button press in update_2.
function update_2_Callback(hObject, eventdata, handles)
% hObject    handle to update_2 (see GCBO)
% eventdata  reserved - to be defined in a future version of MATLAB
% handles    structure with handles and user data (see GUIDATA)

if handles.full_update == 0 && get(handles.full,'Value') == 1 &&
get(handles.approx,'Value') == 0 && handles.load_final == 1
    % Background subraction full
    for z = 1:handles.nframes
        background(:,:,:,z) =
imopen(handles.I_fill(:,:,:,z),strel('disk',100,4));
        background2(:,:,:,z) = imadjust(background(:,:,:,z),[],[0 0.7]);
        I_back(:,:,:,z) =
imsubtract(handles.I_fill(:,:,:,z),background2(:,:,:,z));
        handles.I_contrast(:,:,:,z) = imadjust(I_back(:,:,:,z));
        n = ceil(100.*z./handles.nframes);
    end
    % set(handles.progress,'String',' ');
    % set(handles.percent,'String',' ');
    handles.full_update = 1;
    set(handles.message,'String','Background Subtraction Complete');
elseif handles.approx_update == 0 && get(handles.full,'Value') == 0 &&
get(handles.approx,'Value') == 1  && handles.load_final == 1
    background =
imopen(handles.I_fill(:,:,:,handles.nframes),strel('disk',100,4));
    background2 = imadjust(background,[],[0 0.7]);
    for z = 1:handles.nframes
        I_back(:,:,:,z) = imsubtract(handles.I_fill(:,:,:,z),background2);
```

```
        handles.I_contrast(:,:,:,z) = imadjust(I_back(:,:,:,z));
        n = ceil(100.*z./handles.nframes);
    end
    % set(handles.progress,'String',' ');
    % set(handles.percent,'String',' ');
    handles.approx_update = 1;
    set(handles.message,'String','Background Subtraction Complete');
else
    set(handles.message,'String','Load Image Files First');
end

if handles.load_final == 1
    axes(handles.fig_beg); % Select the proper axes

imshow(handles.I_contrast(:,:,:,str2num(get(handles.frame_beg_n,'String'))));
    axes(handles.fig_mid);

imshow(handles.I_contrast(:,:,:,str2num(get(handles.frame_mid_n,'String'))));
    axes(handles.fig_end);

imshow(handles.I_contrast(:,:,:,str2num(get(handles.frame_end_n,'String'))));
end

guidata(hObject,handles);

% --- Executes on button press in update_3.
function update_3_Callback(hObject, eventdata, handles)
% hObject    handle to update_3 (see GCBO)
% eventdata  reserved - to be defined in a future version of MATLAB
% handles    structure with handles and user data (see GUIDATA)

if handles.full_update == 1 || handles.approx_update == 1
    for z = 1:handles.nframes
        I_filter(:,:,:,z) = imadjust(handles.I_contrast(:,:,:,z),[0
get(handles.index_slider,'Value')],[0 1],get(handles.gamma_slider,'Value'));
        handles.I_noise(:,:,:,z) = medfilt2(I_filter(:,:,:,z),[5 5]);
    end
    set(handles.message,'String','');

    axes(handles.fig_beg); % Select the proper axes

imshow(handles.I_noise(:,:,:,str2num(get(handles.frame_beg_n,'String'))));
    axes(handles.fig_mid);

imshow(handles.I_noise(:,:,:,str2num(get(handles.frame_mid_n,'String'))));
    axes(handles.fig_end);

imshow(handles.I_noise(:,:,:,str2num(get(handles.frame_end_n,'String'))));
    handles.linear_final = 1;
    handles.linear_restore = 0;
    set(handles.message,'String','Linear Scaling Complete');
else
    set(handles.message,'String','Background Subtraction Missing');
end

guidata(hObject,handles);

% --- Executes on button press in restore_3.
```

```
function restore_3_Callback(hObject, eventdata, handles)
% hObject    handle to restore_3 (see GCBO)
% eventdata  reserved - to be defined in a future version of MATLAB
% handles    structure with handles and user data (see GUIDATA)

if handles.full_update == 1 || handles.approx_update == 1
    axes(handles.fig_beg); % Select the proper axes

imshow(handles.I_contrast(:,:,:,str2num(get(handles.frame_beg_n,'String'))));
    axes(handles.fig_mid);

imshow(handles.I_contrast(:,:,:,str2num(get(handles.frame_mid_n,'String'))));
    axes(handles.fig_end);

imshow(handles.I_contrast(:,:,:,str2num(get(handles.frame_end_n,'String'))));
    set(handles.message,'String','');
    handles.linear_restore = 1;
else
    set(handles.message,'String','Background Subtraction Missing');
end
guidata(hObject,handles);

% --- Executes on slider movement.
function index_slider_Callback(hObject, eventdata, handles)
% hObject    handle to index_slider (see GCBO)
% eventdata  reserved - to be defined in a future version of MATLAB
% handles    structure with handles and user data (see GUIDATA)

set(handles.index,'String',num2str(get(handles.index_slider,'Value')));

% --- Executes during object creation, after setting all properties.
function index_slider_CreateFcn(hObject, eventdata, handles)
% hObject    handle to index_slider (see GCBO)
% eventdata  reserved - to be defined in a future version of MATLAB
% handles    empty - handles not created until after all CreateFcns called

if isequal(get(hObject,'BackgroundColor'),
get(0,'defaultUicontrolBackgroundColor'))
    set(hObject,'BackgroundColor',[.9 .9 .9]);
end

function index_Callback(hObject, eventdata, handles)
% hObject    handle to index (see GCBO)
% eventdata  reserved - to be defined in a future version of MATLAB
% handles    structure with handles and user data (see GUIDATA)

val = str2double(get(handles.index,'String'));
min = get(handles.index,'Min');
max = get(handles.index,'Max');
default = 0.5;

if isnumeric(val) & length(val)==1 & val >= min & val <= max
    set(handles.index_slider,'Value',val);
    set(handles.index,'String',num2str(val));
elseif isnumeric(val) & length(val)==1 & val <= min
    set(handles.index_slider,'Value',min);
    set(handles.index,'String','0.0');
elseif isnumeric(val) & length(val)==1 & val >= max
```

```
    set(handles.index_slider,'Value',max);
    set(handles.index,'String','1.0');
else
    set(handles.index_slider,'Value',default);
    set(handles.index,'String',default);
end

% --- Executes during object creation, after setting all properties.
function index_CreateFcn(hObject, eventdata, handles)
% hObject    handle to index (see GCBO)
% eventdata  reserved - to be defined in a future version of MATLAB
% handles    empty - handles not created until after all CreateFcns called

if ispc && isequal(get(hObject,'BackgroundColor'),
get(0,'defaultUicontrolBackgroundColor'))
    set(hObject,'BackgroundColor','white');
end

% --- Executes on slider movement.
function gamma_slider_Callback(hObject, eventdata, handles)
% hObject    handle to gamma_slider (see GCBO)
% eventdata  reserved - to be defined in a future version of MATLAB
% handles    structure with handles and user data (see GUIDATA)

set(handles.gamma,'String',num2str(get(handles.gamma_slider,'Value')));

% --- Executes during object creation, after setting all properties.
function gamma_slider_CreateFcn(hObject, eventdata, handles)
% hObject    handle to gamma_slider (see GCBO)
% eventdata  reserved - to be defined in a future version of MATLAB
% handles    empty - handles not created until after all CreateFcns called

if isequal(get(hObject,'BackgroundColor'),
get(0,'defaultUicontrolBackgroundColor'))
    set(hObject,'BackgroundColor',[.9 .9 .9]);
end

function gamma_Callback(hObject, eventdata, handles)
% hObject    handle to gamma (see GCBO)
% eventdata  reserved - to be defined in a future version of MATLAB
% handles    structure with handles and user data (see GUIDATA)

val = str2double(get(handles.gamma,'String'));
min = get(handles.gamma,'Min');
max = get(handles.gamma,'Max');
default = 0.7;

if isnumeric(val) & length(val)==1 & val >= min & val <= max
    set(handles.gamma_slider,'Value',val);
    set(handles.gamma,'String',num2str(val));
elseif isnumeric(val) & length(val)==1 & val <= min
    set(handles.gamma_slider,'Value',min);
    set(handles.gamma,'String','0.0');
elseif isnumeric(val) & length(val)==1 & val >= max
    set(handles.gamma_slider,'Value',max);
    set(handles.gamma,'String','1.0');
else
    set(handles.gamma_slider,'Value',default);
```

```
    set(handles.gamma,'String',default);
end

% --- Executes during object creation, after setting all properties.
function gamma_CreateFcn(hObject, eventdata, handles)
% hObject    handle to gamma (see GCBO)
% eventdata  reserved - to be defined in a future version of MATLAB
% handles    empty - handles not created until after all CreateFcns called

if ispc && isequal(get(hObject,'BackgroundColor'),
get(0,'defaultUicontrolBackgroundColor'))
    set(hObject,'BackgroundColor','white');
end

% --- Executes on button press in update_5.
function update_5_Callback(hObject, eventdata, handles)
% hObject    handle to update_5 (see GCBO)
% eventdata  reserved - to be defined in a future version of MATLAB
% handles    structure with handles and user data (see GUIDATA)

% Specify Image Region of Interest
set(handles.message,'String','');

if handles.binary_final == 1
    rect = getrect(handles.fig_beg);
    axes(handles.fig_beg);


rectangle('Position',[rect(1),rect(2),rect(3),rect(4)],'LineWidth',2,'EdgeCol
or',[1 0 0]);
    axes(handles.fig_mid);

rectangle('Position',[rect(1),rect(2),rect(3),rect(4)],'LineWidth',2,'EdgeCol
or',[1 0 0]);
    axes(handles.fig_end);

rectangle('Position',[rect(1),rect(2),rect(3),rect(4)],'LineWidth',2,'EdgeCol
or',[1 0 0]);

    handles.coord = rect;
else
    set(handles.message,'String','Binarization Missing');
end

guidata(hObject,handles);

% --- Executes on button press in restore_5.
function restore_5_Callback(hObject, eventdata, handles)
% hObject    handle to restore_5 (see GCBO)
% eventdata  reserved - to be defined in a future version of MATLAB
% handles    structure with handles and user data (see GUIDATA)

if handles.binary_final == 1
    axes(handles.fig_beg); % Select the proper axes

imshow(handles.I_final(:,:,:,str2num(get(handles.frame_beg_n,'String'))));
    axes(handles.fig_mid);
```

```
imshow(handles.I_final(:,:,:,str2num(get(handles.frame_mid_n,'String'))));
    axes(handles.fig_end);

imshow(handles.I_final(:,:,:,str2num(get(handles.frame_end_n,'String'))));
else
    set(handles.message,'String','Binarization Missing');
end

% --- Executes on button press in final_5.
function final_5_Callback(hObject, eventdata, handles)
% hObject    handle to final_5 (see GCBO)
% eventdata  reserved - to be defined in a future version of MATLAB
% handles    structure with handles and user data (see GUIDATA)

handles.I_crop = [];

if handles.binary_final == 1
    for z = 1:handles.nframes
        handles.I_crop(:,:,:,z) =
imcrop(handles.I_final(:,:,:,z),handles.coord);
    end
    axes(handles.fig_beg); % Select the proper axes
    imshow(handles.I_crop(:,:,:,str2num(get(handles.frame_beg_n,'String'))));
    axes(handles.fig_mid);
    imshow(handles.I_crop(:,:,:,str2num(get(handles.frame_mid_n,'String'))));
    axes(handles.fig_end);
    imshow(handles.I_crop(:,:,:,str2num(get(handles.frame_end_n,'String'))));

    handles.crop_final = 1;
else
    set(handles.message,'String','Binarization Missing');
end

guidata(hObject,handles);

% --- Executes on button press in update_4.
function update_4_Callback(hObject, eventdata, handles)
% hObject    handle to update_4 (see GCBO)
% eventdata  reserved - to be defined in a future version of MATLAB
% handles    structure with handles and user data (see GUIDATA)

% Binarization
if handles.linear_final == 1;
    for z = 1:handles.nframes
        level = graythresh(handles.I_noise(:,:,:,z)) -
get(handles.thresh_slider,'Value');
        I_bw(:,:,:,z) = im2bw(handles.I_noise(:,:,:,z),level);
        I_erode(:,:,:,z) = bwmorph(I_bw(:,:,:,z),'erode');
        handles.I_final(:,:,:,z) = bwmorph(I_erode(:,:,:,z),'dilate',2);
    end
    axes(handles.fig_beg); % Select the proper axes

imshow(handles.I_final(:,:,:,str2num(get(handles.frame_beg_n,'String'))));
    axes(handles.fig_mid);

imshow(handles.I_final(:,:,:,str2num(get(handles.frame_mid_n,'String'))));
    axes(handles.fig_end);
```

```
imshow(handles.I_final(:,:,:,str2num(get(handles.frame_end_n,'String'))));
    handles.binary_final = 1;
    handles.binary_restore = 0;
    set(handles.message,'String','Binarization Complete');
else
    set(handles.message,'String','Linear Scaling Missing');
end

guidata(hObject,handles);

% --- Executes on button press in restore_4.
function restore_4_Callback(hObject, eventdata, handles)
% hObject    handle to restore_4 (see GCBO)
% eventdata  reserved - to be defined in a future version of MATLAB
% handles    structure with handles and user data (see GUIDATA)

if handles.linear_final == 1;
    axes(handles.fig_beg); % Select the proper axes

imshow(handles.I_noise(:,:,:,str2num(get(handles.frame_beg_n,'String'))));
    axes(handles.fig_mid);

imshow(handles.I_noise(:,:,:,str2num(get(handles.frame_mid_n,'String'))));
    axes(handles.fig_end);

imshow(handles.I_noise(:,:,:,str2num(get(handles.frame_end_n,'String'))));
    set(handles.message,'String','');
    handles.binary_restore = 1;
else
    set(handles.message,'String','Linear Scaling Missing');
end

guidata(hObject,handles);

% --- Executes on button press in automate.
function automate_Callback(hObject, eventdata, handles)
% hObject    handle to automate (see GCBO)
% eventdata  reserved - to be defined in a future version of MATLAB
% handles    structure with handles and user data (see GUIDATA)

% No Background subtraction done yet.
 if handles.load_final == 1
    if handles.full_update == 0 && handles.approx_update == 0
        if get(handles.full,'Value') == 1 && get(handles.approx,'Value') == 0
            % Background subraction full
            for z = 1:handles.nframes
                background(:,:,:,z) =
imopen(handles.I_fill(:,:,:,z),strel('disk',100,4));
                background2(:,:,:,z) = imadjust(background(:,:,:,z),[],[0
0.7]);
                I_back(:,:,:,z) =
imsubtract(handles.I_fill(:,:,:,z),background2(:,:,:,z));
                handles.I_contrast(:,:,:,z) = imadjust(I_back(:,:,:,z));
                n = ceil(100.*z./handles.nframes);
            end
            % set(handles.progress,'String',' ');
            % set(handles.percent,'String',' ');
            handles.full_update = 1;
```

```
            set(handles.message,'String','Background Subtraction Complete');
        elseif handles.approx_update == 0 && get(handles.full,'Value') == 0
&& get(handles.approx,'Value') == 1
            background =
imopen(handles.I_fill(:,:,:,handles.nframes),strel('disk',100,4));
            background2 = imadjust(background,[],[0 0.7]);
            for z = 1:handles.nframes
                I_back(:,:,:,z) =
imsubtract(handles.I_fill(:,:,:,z),background2);
                handles.I_contrast(:,:,:,z) = imadjust(I_back(:,:,:,z));
                n = ceil(100.*z./handles.nframes);
            end
            % set(handles.progress,'String',' ');
            % set(handles.percent,'String',' ');
            handles.approx_update = 1;
            set(handles.message,'String','Background Subtraction Complete');
        end
    end
    if handles.linear_final == 0
        for z = 1:handles.nframes
            I_filter(:,:,:,z) = imadjust(handles.I_contrast(:,:,:,z),[0
get(handles.index_slider,'Value')],[0 1],get(handles.gamma_slider,'Value'));
            handles.I_noise(:,:,:,z) = medfilt2(I_filter(:,:,:,z),[5 5]);
        end
        handles.linear_final = 1;
        set(handles.message,'String','Linear Scaling Complete');
    end
    if handles.binary_final == 0
        for z = 1:handles.nframes
            level = graythresh(handles.I_noise(:,:,:,z)) -
get(handles.thresh_slider,'Value');
            I_bw(:,:,:,z) = im2bw(handles.I_noise(:,:,:,z),level);
            I_erode(:,:,:,z) = bwmorph(I_bw(:,:,:,z),'erode');
            handles.I_final(:,:,:,z) = bwmorph(I_erode(:,:,:,z),'dilate',2);
        end
        handles.binary_final = 1;
        set(handles.message,'String','Binarization Complete');
    end
    axes(handles.fig_beg); % Select the proper axes

imshow(handles.I_final(:,:,:,str2num(get(handles.frame_beg_n,'String'))));
    axes(handles.fig_mid);

imshow(handles.I_final(:,:,:,str2num(get(handles.frame_mid_n,'String'))));
    axes(handles.fig_end);

imshow(handles.I_final(:,:,:,str2num(get(handles.frame_end_n,'String'))));
else
    set(handles.message,'String','Load Image Files First');
end

guidata(hObject,handles);

function frame_beg_n_Callback(hObject, eventdata, handles)
% hObject    handle to frame_beg_n (see GCBO)
% eventdata  reserved - to be defined in a future version of MATLAB
% handles    structure with handles and user data (see GUIDATA)
```

```
if handles.full_update == 0 && handles.approx_update == 0
    axes(handles.fig_beg); % Select the proper axes
    imshow(handles.I_fill(:,:,:,str2num(get(handles.frame_beg_n,'String'))));
elseif handles.linear_final == 0 || handles.linear_restore == 1
    axes(handles.fig_beg); % Select the proper axes

imshow(handles.I_contrast(:,:,:,str2num(get(handles.frame_beg_n,'String'))));
elseif handles.binary_final == 0 || handles.binary_restore == 1
    axes(handles.fig_beg); % Select the proper axes

imshow(handles.I_noise(:,:,:,str2num(get(handles.frame_beg_n,'String'))));
elseif handles.binary_final == 1
    axes(handles.fig_beg);

imshow(handles.I_final(:,:,:,str2num(get(handles.frame_beg_n,'String'))));
end

% --- Executes during object creation, after setting all properties.
function frame_beg_n_CreateFcn(hObject, eventdata, handles)
% hObject    handle to frame_beg_n (see GCBO)
% eventdata  reserved - to be defined in a future version of MATLAB
% handles    empty - handles not created until after all CreateFcns called

if ispc && isequal(get(hObject,'BackgroundColor'),
get(0,'defaultUicontrolBackgroundColor'))
    set(hObject,'BackgroundColor','white');
end

function frame_mid_n_Callback(hObject, eventdata, handles)
% hObject    handle to frame_mid_n (see GCBO)
% eventdata  reserved - to be defined in a future version of MATLAB
% handles    structure with handles and user data (see GUIDATA)

if handles.full_update == 0 && handles.approx_update == 0
    axes(handles.fig_mid); % Select the proper axes
    imshow(handles.I_fill(:,:,:,str2num(get(handles.frame_mid_n,'String'))));
elseif handles.linear_final == 0 || handles.linear_restore == 1
    axes(handles.fig_mid); % Select the proper axes

imshow(handles.I_contrast(:,:,:,str2num(get(handles.frame_mid_n,'String'))));
elseif handles.binary_final == 0 || handles.binary_restore == 1
    axes(handles.fig_mid); % Select the proper axes

imshow(handles.I_noise(:,:,:,str2num(get(handles.frame_mid_n,'String'))));
elseif handles.binary_final == 1
    axes(handles.fig_mid);

imshow(handles.I_final(:,:,:,str2num(get(handles.frame_mid_n,'String'))));
end

% --- Executes during object creation, after setting all properties.
function frame_mid_n_CreateFcn(hObject, eventdata, handles)
% hObject    handle to frame_mid_n (see GCBO)
% eventdata  reserved - to be defined in a future version of MATLAB
% handles    empty - handles not created until after all CreateFcns called

if ispc && isequal(get(hObject,'BackgroundColor'),
get(0,'defaultUicontrolBackgroundColor'))
```

```
    set(hObject,'BackgroundColor','white');
end

function frame_end_n_Callback(hObject, eventdata, handles)
% hObject    handle to frame_end_n (see GCBO)
% eventdata  reserved - to be defined in a future version of MATLAB
% handles    structure with handles and user data (see GUIDATA)

if handles.full_update == 0 && handles.approx_update == 0
    axes(handles.fig_end); % Select the proper axes
    imshow(handles.I_fill(:,:,:,str2num(get(handles.frame_end_n,'String'))));
elseif handles.linear_final == 0 || handles.linear_restore == 1
    axes(handles.fig_end); % Select the proper axes

imshow(handles.I_contrast(:,:,:,str2num(get(handles.frame_end_n,'String'))));
elseif handles.binary_final == 0 || handles.binary_restore == 1
    axes(handles.fig_end); % Select the proper axes

imshow(handles.I_noise(:,:,:,str2num(get(handles.frame_end_n,'String'))));
elseif handles.binary_final == 1
    axes(handles.fig_end);

imshow(handles.I_final(:,:,:,str2num(get(handles.frame_end_n,'String'))));
end

% --- Executes during object creation, after setting all properties.
function frame_end_n_CreateFcn(hObject, eventdata, handles)
% hObject    handle to frame_end_n (see GCBO)
% eventdata  reserved - to be defined in a future version of MATLAB
% handles    empty - handles not created until after all CreateFcns called

if ispc && isequal(get(hObject,'BackgroundColor'),
get(0,'defaultUicontrolBackgroundColor'))
    set(hObject,'BackgroundColor','white');
end
```

7.2. Appendix B – Persistent random walk model analysis

Analysis of 2D and 3D tracks occur through different, but similar MATLAB codes. In this appendix, we include only the analysis files for 3D tracks. prw3D.m is the execution file.

7.2.1. prw3D.m

```
% 3D migration analysis by Hyung-Do Kim
% Purpose: Quantitation of cell migration trajectories from coordinate data

clear;
addpath(pwd,'-begin');
datadir = uigetdir;
cd(datadir);

% Enter experiment name
```

```
expname = input('\nEnter the experiment name: \n','s');
mkdir('Figures');
mkdir('Tiffs');

% Input file format: .txt
% Input text file:
filename = input('\nEnter the text file: \n','s');
data = load(filename);

% Enter time interval
interval_i = input('\nEnter the time interval in minutes: \n');
interval = interval_i./60;

% Enter image conversion factor and convert
global conversion
conversion=input('\nEnter the um/pixel conversion factor: \n');
data = data.*conversion;

% Calculate mean square displacement using non-overlapping intervals
msdnonoverlap3D;
fprintf('\nMSD calculation completed\n');
wait = input('Press Enter to continue','s');

% Fit speed and persistence using generalized nonlinear least-squares
% regression
prwfit3D;

% Make arrays of data and Save data into csv file.
% First save .mat file with variables
save([expname '.mat'],'n_cells','cell','xx','yy','zz','distance','msd',...
    'sigma_msd_cell','int_counter','avg_total_msd','max_msd','interval',...
    'Scalc','Sfit','Pcalc','Pfit','Calcresnorm','Fitresnorm','Pmisfit',...
    'speed_mean','speed_median','speed_sem','speed_max','speed_min',...

'persistence_mean','persistence_median','persistence_sem','persistence_max',.
..
    'persistence_min','CI_mean','CI_median','CI_sem','CI_max','CI_min',...
    'mu', 'mu_mean','meanpathlength','meanpathlength_mean','total_int');

% CSV file of individual cell data
% Row of parameters
csvname = [expname '_ind.csv'];
parind = ['Cell #,' 'Number of Intervals,' 'Calc. Speed Mean [um/hr],' 'Calc.
Speed SEM [um/hr],' 'Fit Persistence [min],'...
    'Fitting Residuals,' 'Chemotactic Index,' 'Total Path Length [um],'
'Total Displacement [um],' ...
    'Random Motility C. [um^2/hr],' 'Mean Path Length [um]'];
fid = fopen(csvname, 'wt');
fprintf(fid, '%s', parind);
fclose('all');
% Data
indM = [[1:n_cells]' total_int' Scalc(:,1) Scalc(:,2) Pcalc(:,1).*60
Calcresnorm(:,1) CI(:,1) ...
    total_cell_path_length' total_cell_displacement' mu(:,1)
meanpathlength(:,1)];
dlmwrite(csvname, indM, '-append','roffset',1);
clear indM;
```

```
% CSV file of pooled data set
% Column of parameters
csvname = [expname '_pool.csv'];
parpool = ['Number of cells,','Speed Mean [um/hr],','Speed SEM [um/hr],',...
    'Speed Median [um/hr],','Speed Max [um/hr],','Speed Min [um/hr],',...
    'Persistence Mean [min],','Persistence SEM [min],','Persistence Median
[min],',...
    'Persistence Max [min],','Persistence Min [min],','Persistence
Misfit,','CI Mean,','CI SEM,',...
    'CI Median,','CI Max,','CI Min,','Random Motility C [um^2/hr],','Mean
Path Length [um],'];
fid = fopen(csvname, 'wt');
fprintf(fid, '%s', parpool);
fclose('all');
% Data
poolM = [n_cells speed_mean speed_sem speed_median speed_max speed_min
persistence_mean.*60 ...
    persistence_sem.*60 persistence_median.*60 persistence_max.*60
persistence_min.*60 Pmisfit(1) CI_mean CI_sem ...
    CI_median CI_max CI_min mu_mean meanpathlength_mean];
dlmwrite(csvname, poolM, '-append','roffset',1);
clear poolM
```

7.2.2. msdnonoverlap3D.m

```
% msdnonoverlap.m - Hyung-Do Kim 3.1.2006
% For 3D x,y,z coordinates

% Calculates time interval-dependent mean-squared-displacements from cell
% trajectory coordinates by the method of non-overlapping intervals (see
% Dickinson and Tranquillo, AIChE J, 1993)

% Code provides the mean-squared displacement data for individual cells and
% population of cells in the experiment, including the SEM for each cell's
% MSD to track error propagation through a total experiment cell mean.  It
% also calculates other cell path parameters and plots MSD vs Time interval

% Store number of time points and number of cells tracked.
nt = size(data,1);
n_cells = size(data,2)./3;

% Counter for total number of displacements per interval length
int_counter = zeros(nt - 1,1);

% Counter for total time points of a track
tp_counter = zeros(1,nt);

% loop to separate the raw data into individual cells
for i = 1:n_cells

    % reads the X and Y coordinates of a single cell
    cell{i} = data(:,3*i-2:3*i);

    % Find all non-zero entries and truncates all zeros off the input data
    I = find(cell{i}(:,1));
    cell{i} = cell{i}(I,1:3);
```

```
    % Add the number of time points of this track to the time-point-counter
    tp_counter(size(cell{i},1)) = tp_counter(size(cell{i},1)) + 1;

    % x- and y- coordinates cells
    x{i} = cell{i}(:,1);
    y{i} = cell{i}(:,2);
    z{i} = cell{i}(:,3);
    % Calculate displacements in x and y direction in r.t. first time point.
    xx{i}= x{i}-x{i}(1);
    yy{i}= y{i}-y{i}(1);
    zz{i}= z{i}-z{i}(1);

    % Number of possible intervals in current track.
    total_int(i) = length(x{i}) - 1;

    % Vector of number of nonoverlapping intervals for each interval length
(t).
    v_nonoverlapint = floor(total_int(i)./(1:total_int(i))');

    % Loop for all possible time points for displacement measurements
    for j = 1:total_int(i)

        % Loop all possible starting points for a given time period
        % columns are time values; rows are distances traveled in that time
        for k = 1:v_nonoverlapint(j)
            distance{i}(k,j) = (x{i}(1 + j*k) - x{i}(1 + j*(k-1)))^2 + ...
                (y{i}(1+j*k) - y{i}(1 + j*(k-1)))^2 + (z{i}(1 + j*k) - ...
                z{i}(1 + j*(k-1)))^2;
        end

        % Mean squared displacement data for cell{i}
        msd{i}(j,1) = sum(distance{i}(:,j))/v_nonoverlapint(j);
        % Number of intervals for time period i for cell{b}
        msd{i}(j,2) = v_nonoverlapint(j);
        % Same in vector format
        msd_v(j,2*i-1) = sum(distance{i}(:,j))/v_nonoverlapint(j);
        msd_v(j,2*i) = v_nonoverlapint(j);

        % Finds non-zero distance measurements for a given cell and time
        % interval length
        J = find(distance{i}(:,j));

        % Puts these distances in a vector for determination of variance
        cov_distance{j} = distance{i}(J,j);

        % individual cell SEM for the MSD
        sigma_msd_cell{i}(j) =
cov(cov_distance{j})/sqrt(length(cov_distance{j}));

        % count the total number of intervals for time period j summed for
        % all cells
        int_counter(j) = int_counter(j) + v_nonoverlapint(j);

    end

    % Calculate path information for this cell
    % Total path length
    total_cell_path_length(i) = (sum((distance{i}(:,1)).^0.5))';
```

```
    % Total cell displacement
    total_cell_displacement(i) = (distance{i}(1,total_int(i)))^0.5;
    % Chemotactic Index
    CI(i,1) = total_cell_displacement(i)./total_cell_path_length(i);

end

% Plot MSD vs time interval in a subplot
if n_cells > 25
    columns = 10;
else
    columns = 5;
end

scrsz = get(0,'ScreenSize');
figure('Position',[scrsz(3)/6 scrsz(4)/6 scrsz(3)/1.4 scrsz(4)/1.4],...
    'Name','MSD vs. Time Plot Window','NumberTitle','off')
rows = ceil(n_cells./columns);
if n_cells < columns
    for i = 1:n_cells
        subplot(1,n_cells,i);
        plot(1:total_int(i),msd{i}(:,1),'xk');
        title(['Cell #',num2str(i)]);
    end
else
    for i = 1:rows
        for j = 1:columns
            if (i - 1).*columns + j > n_cells
                break
            end
            subplot(rows,columns,(i - 1).*columns + j);
            plot(1:total_int((i - 1).*columns + j),msd{(i - 1).*columns +
j}(:,1),'xk');
            title(['Cell #',num2str((i - 1).*columns + j)]);
        end
    end
end

saveas(gcf,[pwd '\Figures\' expname '_MSDplot.fig']);
saveas(gcf,[pwd '\Tiffs\' expname '_MSDplot'],'tif');

% Calculate mean-square displacements averaged across all cells (weigh
% individual cell by time periods contributed to total)
for i = 1:n_cells
    avg_total_msd(:,i) = msd_v(:,2*i-1).*msd_v(:,2*i)./int_counter;
end
% Average total MSD for each time interval
avg_total_msd = sum(avg_total_msd,2);
% Maximum averaged total MSD
max_msd = max(avg_total_msd);
```

7.2.3. prwfit.m

```
% prwfit.m - Hyung-Do Kim 3.2.2006
% modified from Lisa Joslin 4.23.2004, originally adapted from Gargi
% Maheshwari
```

```
% Fits the mean squared displacement data obtained from msdnonoverlap.m to
% the persistent random walk model to obtain S and P.  Two methods are
% used: calculate S from MSD then fit P; fit both S and P.  The first
% method usually fares better.
% Plots trajectory, speed at each time point, theoretical curves given S
% and P, and the MSD scatter
% For pooled data set, the program plots the Wind-Rose plot, Persistence
% vs. CI plot, S/P plot of each cell, and the histogram of S and P
% distribution.

global Scalc z
Scalc = [];
Sfit = [];
Pcalc = [];
Pfit = [];

% Fitted P over maximum P counter
Pmisfit = zeros(1,2);

for z = 1:n_cells
    % Convert intervals to hours
    time = interval.*[1:total_int(z)]';

    % Method 1 - Calculate speed and fit persistence

    % Calculate speed from distance values
    Scalc(z,1) = sqrt(msd{z}(1,1))/interval; % Mean

    % Find non-zero values for distances for covariance calculations
    J = find(distance{z}(:,1));
    cov_speed = sqrt(distance{z}(J,1))./interval;

    Scalc(z,2) = std(cov_speed)/sqrt(length(cov_speed));

    % One-parameter least-squares fit for P
    % guess P to be the time interval
    P_0 = interval;
    % Upper and lower bound for P: total duration of exp, 0, respectively
    [Pcalc(z,1),Calcresnorm(z,1)] = lsqcurvefit(@prwfuncalc, P_0, time,
msd{z}(:,1), 0, nt.*interval,optimset('Display','off'));

    % If P is larger than experiment duration, fitting may be faulty.
    if Pcalc(z) > nt.*interval
        Pcalc(z) = nt.*interval
        Pmisfit(1) = Pmisfit(1) + 1;
    end

    % Method 2 - Fit both speed and persistence
    Par_0 = [5 interval];
    [Par,Fitresnorm(z,1)] = lsqcurvefit(@prwfunfit, Par_0, time, msd{z}(:,1),
[0 0], [1000 nt.*interval],optimset('Display','off'));
    Sfit(z,1) = Par(1);
    Pfit(z,1) = Par(2);

    % If P is larger than experiment duration, fitting may be faulty.
    if Pfit(z) > nt.*interval
        Pfit(z) = nt.*interval
        Pmisfit(2) = Pmisfit(2) + 1;
```

```
    end
end

% Plot the fitting of data for checking and trajectory paths and speed at
% each time point

% One does not have to see all individual plots:
seeplot = input(['Would you like to look at ' num2str(n_cells) ' individual
cell plots? '],'s');
if (seeplot == 'y') || (seeplot == 'Y')
    plotthem = 1;
else
    plotthem = 0;
end

temp_counter = 0;
for i = 1:n_cells
    time = interval.*[1:total_int(i)]';
    % Calculate fitted curves
    model_calc = 2.*Scalc(i,1).^2.*Pcalc(i).*(time - Pcalc(i).*(1 - exp(-
time./Pcalc(i))));
    model_fit = 2.*Sfit(i,1).^2.*Pfit(i).*(time - Pfit(i).*(1 - exp(-
time./Pfit(i))));

    % Plot calculated Speed/fitted Persistence Curve
    figure('Position',[scrsz(3)/6 scrsz(4)/6 scrsz(3)/1.4 scrsz(4)/1.4],...
        'Name',['Model fitting to MSD data - Cell #'
num2str(i)],'NumberTitle','off')
    subplot(2,2,3);
    plot(time,msd{i}(:,1),'xk',time,model_calc,'-r');
    title(['Calc. S = ' num2str(Scalc(i,1)) ' um/h - Fit P = '
num2str(Pcalc(i,1).*60) ' min']);
    xlabel('Time interval [h]');
    ylabel('Mean Squared Displacement [um]');

    % Plot fitted speed/fitted persistence curve
    subplot(2,2,4);
    plot(time,msd{i}(:,1),'xk',time,model_fit,'-r');
    title(['Fit S = ' num2str(Sfit(i,1)) ' um/h - Fit P = '
num2str(Pfit(i,1).*60) ' min']);
    xlabel('Time interval (hr)');
    ylabel('Mean Squared Displacement (um)');

    % Plot cell trajectory
    subplot(2,2,1);
    plot3(xx{i}, yy{i},zz{i},'k.-');
    title('Cell trajectory');
    xlabel('x [um]');
    ylabel('y [um]');
    zlabel('z [um]');
    grid on;

    % Plot speed at each time interval curve
    subplot(2,2,2);
    Splot = sqrt(distance{i}(:,1))./interval;
    plot(time,Splot,'xb');
    title('Speed at each time interval');
    xlabel('Time [h]');
```

```
    ylabel('Speed [um/h]');

    saveas(gcf,[pwd '\Figures\' expname '_celln_' num2str(i) '.fig']);
    saveas(gcf,[pwd '\Tiffs\' expname '_celln_' num2str(i)],'tif');

    if plotthem == 0
        close(gcf)
    else
    % Wait after 10 plots.
        if round(i./10) == i./10
            fprintf(['Cells # ' num2str(temp_counter.*10 + 1) ' - '
num2str(i)]);
            temp_counter = temp_counter + 1;
            wait = input('\nPress Enter to continue','s');
        end
    end
end

% Wait for plots to be looked at
if plotthem == 1
    if round(i./10) == i./10
    else
        fprintf(['Cells # ' num2str(temp_counter.*10 + 1) ' - ' num2str(i)]);
        wait = input('\nPress Enter to continue','s');
    end
end

% Calculate basic statistics of speed and persistence across all cells
speed_mean = mean(Scalc(:,1));
speed_median = median(Scalc(:,1));
speed_sem = std(Scalc(:,1))./sqrt(length(Scalc(:,1)));
speed_max = max(Scalc(:,1));
speed_min = min(Scalc(:,1));
persistence_mean = mean(Pcalc(:,1));
persistence_median = median(Pcalc(:,1));
persistence_sem = std(Pcalc(:,1))./sqrt(length(Pcalc(:,1)));
persistence_max = max(Pcalc(:,1));
persistence_min = min(Pcalc(:,1));
CI_mean = mean(CI(:,1));
CI_median = median(CI(:,1));
CI_sem = std(CI(:,1))./sqrt(length(CI(:,1)));
CI_max = max(CI(:,1));
CI_min = min(CI(:,1));

% Plot Wind-Rose plot of all trajectories
figure;
for i = 1:n_cells
    plot3(xx{i},yy{i},zz{i});
    hold on;
end
hold off;
title(['Wind-Rose plot: S = ' num2str(speed_mean) ' +- '
num2str(speed_sem)...
    ' um/hr - P = ' num2str(persistence_mean.*60) ' +- '
num2str(persistence_sem.*60) ' min']);
axis([-100 100 -100 100 -100 100]);
xlabel('x [um]');
ylabel('y [um]');
```

```
zlabel('z [um]');
grid on;

saveas(gcf,[pwd '\Figures\' expname '_windrose.fig']);
saveas(gcf,[pwd '\Tiffs\' expname '_windrose'],'tif');

% Visualize Speed and Persistence distribution of all cells
% First, produce lines that show mean speed and persistence
S_Line = zeros(2,1) + speed_mean;
P_Line = zeros(2,1) + persistence_mean.*60;

figure;
% x axis: Speed, y axis: Persistence
plot(Scalc(:,1), Pcalc(:,1).*60, 'ok', S_Line,
linspace(0,persistence_max.*60,2),...
    '-r', linspace(0,speed_max,2), P_Line, '-b');
legend('Single Cells', 'Mean Persistence', 'Mean Speed',2);
xlabel('Speed [um/hr]');
ylabel('Persistence [min]');
axis([0 speed_max 0 persistence_max.*60]);
title('Scatter Plot: Speed and Persistence per cell');

saveas(gcf,[pwd '\Figures\' expname '_SPscatter.fig']);
saveas(gcf,[pwd '\Tiffs\' expname '_SPscatter'],'tif');

% A good way to check persistence values is to compare Chemotactic Index
% and Persistence Times
figure;
plot(CI,Pcalc(:,1).*60, 'ko');
xlabel('Chemotactic Index');
ylabel('Persistence [min]');
title('Persistence vs. Chemotactic Index Plot');

saveas(gcf,[pwd '\Figures\' expname '_PvsCI.fig']);
saveas(gcf,[pwd '\Tiffs\' expname '_PvsCI'],'tif');

% Generate histograms of speed and persistence
% Parameters for maximum bin edge and bin numbers to make histogram pretty
if speed_max > 100
    Smax_h = ceil(speed_max./10).*10;
    Sbins = 21;
elseif speed_max > 50
    Smax_h = round(speed_max./10).*10 + 5;
    Sbins = Smax_h./5 + 1;
elseif speed_max > 20
    Smax_h = ceil(ceil(speed_max)./2).*2;
    Sbins = Smax_h./2 + 1;
else
    Smax_h = ceil(speed_max);
    Sbins = Smax_h + 1;
end
if persistence_max.*60 > 100
    Pmax_h = ceil(persistence_max.*60./10).*10;
    Pbins = 20 + 1;
elseif persistence_max.*60 > 50
    Pmax_h = round(persistence_max.*60./10).*10 + 5;
    Pbins = Pmax_h./5 + 1;
elseif persistence_max.*60 > 20
```

```
    Pmax_h = ceil(ceil(persistence_max.*60./2)).*2
    Pbins = Pmax_h./2 + 1;
else
    Pmax_h = ceil(persistence_max.*60);
    Pbins = Pmax_h + 1;
end
if CI_max > 0.5
    CImax_h = ceil(CI_max.*10)./10;
    CIbins = CImax_h./0.05 + 1;
else
    CImax_h = ceil(ceil(CI_max.*100)./2).*2./100;
    CIbins = CImax_h./0.02 + 1;
end
% Create bin vectors
Sbinv = linspace(0,Smax_h,Sbins);
Sgenbinv = linspace(0,150,31);
Pbinv = linspace(0,Pmax_h,Pbins);
Pgenbinv = linspace(0,360,19);
CIbinv = linspace(0,CImax_h,CIbins);
CIgenbinv = linspace(0,1,21);


% Count according to bins
Hist_S = histc(Scalc(:,1),Sbinv)./n_cells;
Histgen_S = histc(Scalc(:,1),Sgenbinv)./n_cells;
Hist_P = histc(Pcalc(:,1).*60,Pbinv)./n_cells;
Histgen_P = histc(Pcalc(:,1).*60,Pgenbinv)./n_cells;
Hist_CI = histc(CI(:,1),CIbinv)./n_cells;
Histgen_CI = histc(CI(:,1),CIgenbinv)./n_cells;

% Plot histogram
figure('Position',[scrsz(3)/6 scrsz(4)/6 scrsz(3)/1.2 scrsz(4)/1.8],...
    'Name','Histogram Plot','NumberTitle','off')
subplot(2,3,1);
bar(Sbinv,Hist_S,'histc');
title('Speed Distribution');
xlabel('Speed [um/h]');
ylabel('Fraction of Total Cells');
axis([0 Smax_h 0 1]);
subplot(2,3,4);
bar(Sgenbinv,Histgen_S,'histc');
xlabel('Speed [um/h]');
ylabel('Fraction of Total Cells');
axis([0 155 0 1]);
subplot(2,3,2);
bar(Pbinv,Hist_P,'histc');
title('Persistence Distribution');
xlabel('Persistence [min]');
ylabel('Fraction of Total Cells');
axis([0 Pmax_h 0 1]);
subplot(2,3,5);
bar(Pgenbinv,Histgen_P,'histc');
xlabel('Persistence [min]');
ylabel('Fraction of Total Cells');
axis([0 380 0 1]);
subplot(2,3,3);
bar(CIbinv,Hist_CI,'histc');
title('Chemotactic Index Distribution');
```

```
xlabel('Chemotactic Index');
ylabel('Fraction of Total Cells');
axis([0 CImax_h 0 1]);
subplot(2,3,6);
bar(CIgenbinv,Histgen_CI,'histc');
xlabel('Chemotactic Index');
ylabel('Fraction of Total Cells');
axis([0 1.05 0 1]);

saveas(gcf,[pwd '\Figures\' expname '_SPCIhist.fig']);
saveas(gcf,[pwd '\Tiffs\' expname '_SPCIhist'],'tif');

% Calculate few more parameters
mu(:,1) = (1/3).*Scalc(:,1).^2.*Pcalc(:,1);
meanpathlength = Scalc(:,1).*Pcalc(:,1);
mu_mean = (1/3).*speed_mean.^2.*persistence_mean;
meanpathlength_mean = speed_mean.*persistence_mean;
```

7.2.4. prwfuncalc.m

```
function f = prwfuncalc(P, time)

global Scalc z

f = 2*(Scalc(z,1))^2*P*[time - P*(1-exp(-time/P))];
```

7.2.5. prwfunfit.m

```
function f = prwfunfit(Par, time)

f = 2*Par(1)^2*Par(2)*[time - Par(2)*(1-exp(-time/Par(2)))];
```